Exploring H I Asymmetries in Real and Simulated Galaxies

Nadine A. N. Hank

Supervisors: A/Prof. S.-L. Blyth and Dr. N. Deg

Dissertation presented for the degree of

Master of Science

in the

Department of Astronomy

Faculty of Science

University of Cape Town

September 2020

Abstract

In the ΛCDM model of the Universe, galaxy-galaxy interactions and mergers are considered key drivers in their evolution. These dynamical events lead to peculiar and disturbed morphologies, which can be studied using morphometric statistics. The rotational 2D asymmetry parameter, adopted from optical studies, has recently been used to quantify asymmetries in the HI images of galaxies. This is useful since HI disks typically extend further than the stellar disks and are more sensitive to distortions from interactions. Asymmetries can also manifest in the 1D spectral domain, distorting the shape of the global HI profiles of galaxies. The shape of this profile is determined predominantly by the kinematics of the galaxy, and the HI spatial distribution to a lesser extent. By using archival HI data and simulations, we have begun investigating the systematics and uncertainties of using the 1D and 2D asymmetry parameters for merger studies.

In this thesis, we present a new 1D measure of lopsidedness and examine the applicability of two different 2D asymmetry measures. We investigate the evolution of 2D asymmetry of the gas and stellar distributions in a simulated major merger event and demonstrate that the gas distribution registers the interaction before the stellar distribution is affected. We also find that the outer asymmetry of both distributions is considerably higher post-merger, whereas the intensity-weighted asymmetry returns to pre-merger values. We then explore how well the 1D and 2D parameters agree with visual classifications of asymmetry for a sample of 115 WHISP galaxies and observe that the 1D folding difference lopsidedness and the 2D intensity-weighted asymmetry parameters compare well with the visual classification of asymmetries in the HI profiles and images respectively. We examine the relationship between the 1D and 2D asymmetries in WHISP and find that the 1D folding difference lopsidedness and the 2D intensity-weighted asymmetry yield the strongest linear correlation between spectral and morphological asymmetries, with $r = 0.53$ after inclination cuts have been applied. Lastly, we investigate the location of interacting galaxies in asymmetry parameter space and find that the joint use of 1D and 2D parameters can separate most interacting galaxies from the non-interacting sample.

A portion of the work presented in this thesis (see §5.1.1) has been published in:

Deg N., Blyth S. L., **Hank N.**, Kruger S., Carignan C., 2020, Monthly Notices of The Royal Astronomical Society, 495, 1984.

Plagiarism Declaration

I, Nadine Alexandria Nomhle Hank, know the meaning of plagiarism and declare that all work in the dissertation, save for that which is properly acknowledged, is my own.

Signed by candidate

2020-09-14

Nadine A. N. Hank
Student number: HNKNAD001

Date signed

Acknowledgements

The completion of this thesis was made possible through the support and encouragement of a number of people. First and foremost, I would like to thank my supervisors, A/Prof. Sarah Blyth and Dr. Nathan Deg, for many constructive discussions and for always finding the time to read and provide quick feedback on multiple drafts of conference abstracts, presentations and thesis chapters. I also wish to thank them for their continued support and patience during the final stages of the writing process.

I am indebted to my family for their love and unwavering support throughout my postgraduate studies. I would like to especially thank my mother for her advice, for proof-reading my introduction and discussion chapters, and for pushing me when I needed it. Additionally, many thanks to my brother Andrew for helping with many of my "TEXnical" issues and for providing an alternative work environment on occasion.

To my friends at UCT and in Jo'burg, who have supported and encouraged me throughout the more challenging times of this journey, I am grateful. Special thanks are extended to Claire Lowry, who has always been available to provide a non-astronomer's opinion on any presentation or writing of mine.

I gratefully acknowledge the South African Radio Astronomy Observatory (SARAO) for providing generous funding during my MSc degree. This work has made use of numerical simulations, which were performed by N. Deg at the Centre for High Performance Computing, and data from the WHISP survey. The WHISP survey was carried out at the Kapteyn Astronomical Institute by J. Kamphuis, D. Sijbring and Y. Tang under the supervision of T.S. van Albada, J.M. van der Hulst and R. Sancisi.

Contents

List of Figures

List of Tables

Chapter 1

Introduction

In the preface to the *Atlas of Peculiar Galaxies* (hereafter referred to as Arp's Atlas, Arp 1966), Halton Arp noted that every galaxy is in some way peculiar, and that a thorough analysis of these anomalous features is necessary to understand the dynamical processes that govern the evolution of galaxies over cosmic time. These remarks are still of great relevance 54 years later. It is now widely accepted that the majority of galaxies in the Universe do not exist in isolation, but in gravitationally bound groups and clusters where they interact with neighbouring galaxies as well as the surrounding environment. In turn, these interactions affect various galaxy properties such as stellar mass, morphology, gas content and consequently star formation.

According to the Λ-cold dark matter (ΛCDM) cosmological model, galaxies are predicted to have formed in a 'bottom up' scenario through accretion and the sequential merging of dark matter haloes (White & Rees 1978; White & Frenk 1991). This suggests that galaxy mergers, within this cosmological framework, are an inescapable process in galaxy evolution.

1.1 The role of mergers in galaxy evolution

Galaxy-galaxy interactions and mergers can drive galaxy evolution in multiple ways. Some of these include the growth of mass (e.g. Somerville & Davé 2015, and references therein), induced star formation (Mihos & Hernquist 1996; Barnes 2004; Kim et al. 2009; Saitoh et al. 2009; Pearson et al. 2019), depositing gas (Barnes & Hernquist 1992; Hopkins et al. 2013; Hayward et al. 2013), the triggering of active galactic nuclei (Sanders & Mirabel 1996; Ellison et al. 2019), and changes to galaxy morphology (e.g. Toomre 1977; Steinmetz & Navarro 2002; Abruzzo et al. 2018). Therefore, it is important to study galaxy mergers as they have been shown, observationally and theoretically, to transform a galaxy's morphology, thus playing an integral role in its evolution.

The rate of galaxy mergers is expected, from cosmological simulations (Gottlöber et al. 2001; Genel et al. 2009; Fakhouri et al. 2010), to have been higher in the past when the Universe was smaller. Thus, quantifying the galaxy merger rate over time allows us

to compare observations to theoretical predictions. From an observational perspective, mergers have been identified either through close galaxy pairs or through disturbed morphologies. In the case of the former, 3D or 2D projected distance is used to identify galaxies in close proximity that are likely to merge (e.g. Patton et al. 2000; Bundy et al. 2004; Robotham et al. 2014; Mundy et al. 2017; Bok et al. 2019). With the latter, disturbed morphologies are present in both ongoing mergers and recent post-mergers. These are identified either through visual inspection or using non-parametric morphology measurements (e.g. Conselice 2003; Lotz et al. 2008a; Jogee et al. 2009; Bluck et al. 2012). Both techniques are essential as they are able to identify merger candidates at different stages of the merger process.

The final merger remnant depends on the mass ratios, impact parameters and orientation of the progenitors. Mergers between galaxies of unequal mass (minor mergers) are far more common, and generally contribute to galaxy mass growth, where the smaller galaxy is essentially cannibalised. In contrast, mergers between galaxies of roughly equal mass (major mergers) are less common, but strongly affect the merger remnant's final morphology. For example, a merging spiral galaxy may be transformed into an elliptical galaxy (e.g. Toomre 1977; Steinmetz & Navarro 2002). While a major merger is ongoing, the morphology may show distortions in the gas and stellar disks, and exhibit extended tidal tails and connecting bridges between the progenitors (see Figure 1.1 for an example of a late-stage major merger).

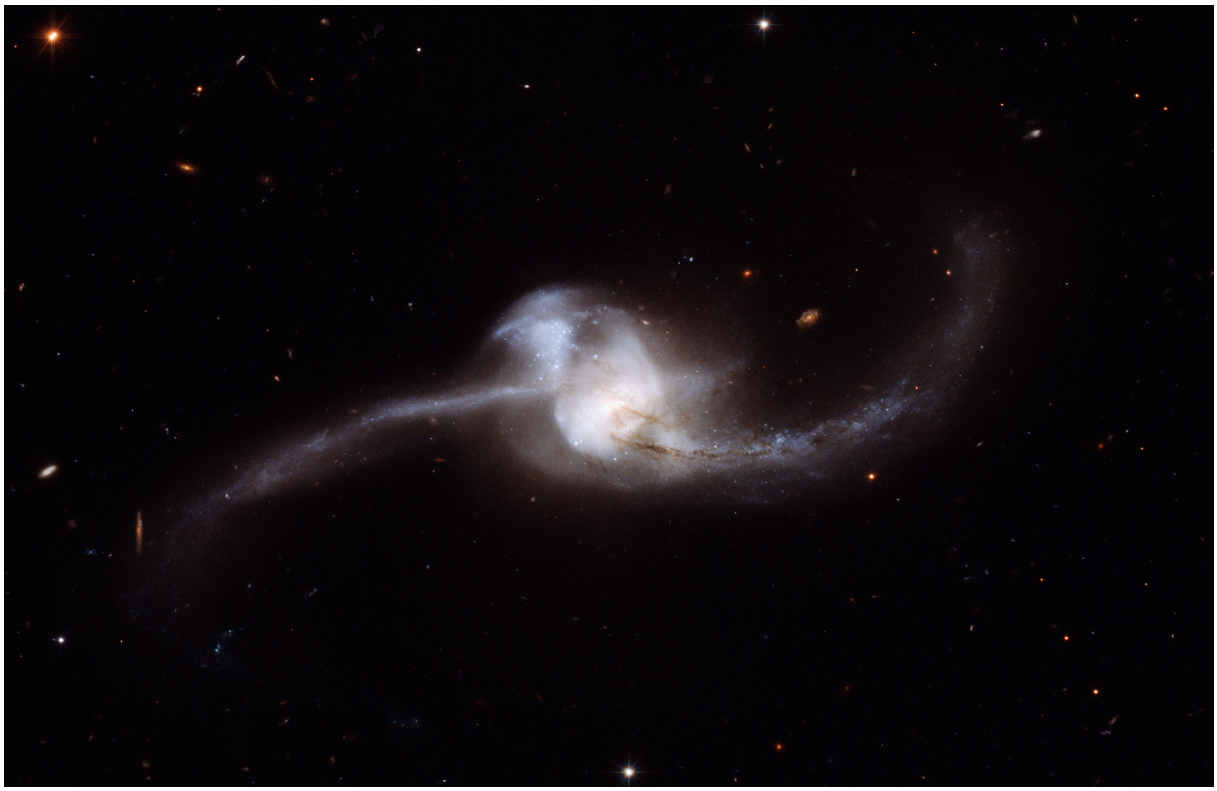

Figure 1.1: Optical image of advanced galaxy merger NGC 2623 (Arp 243). Image credit: NASA, ESA and A. Evans (Stony Brook University, New York, University of Virginia & National Radio Astronomy Observatory, Charlottesville, USA).

1.2 Galaxy simulations

Numerical simulations have served as an invaluable tool in studying the formation and evolution of galaxies over the history of the Universe. In general, there are three classes of numerical simulations that probe galaxy evolution: cosmological, zoom and equilibrium simulations. Each of these simulations probes different scales and processes, and have their own set of advantages for studying galaxy interactions over cosmic time. Some of the simulations belonging to the first two classes are illustrated in Figure 1.2 from Vogelsberger et al. (2020).

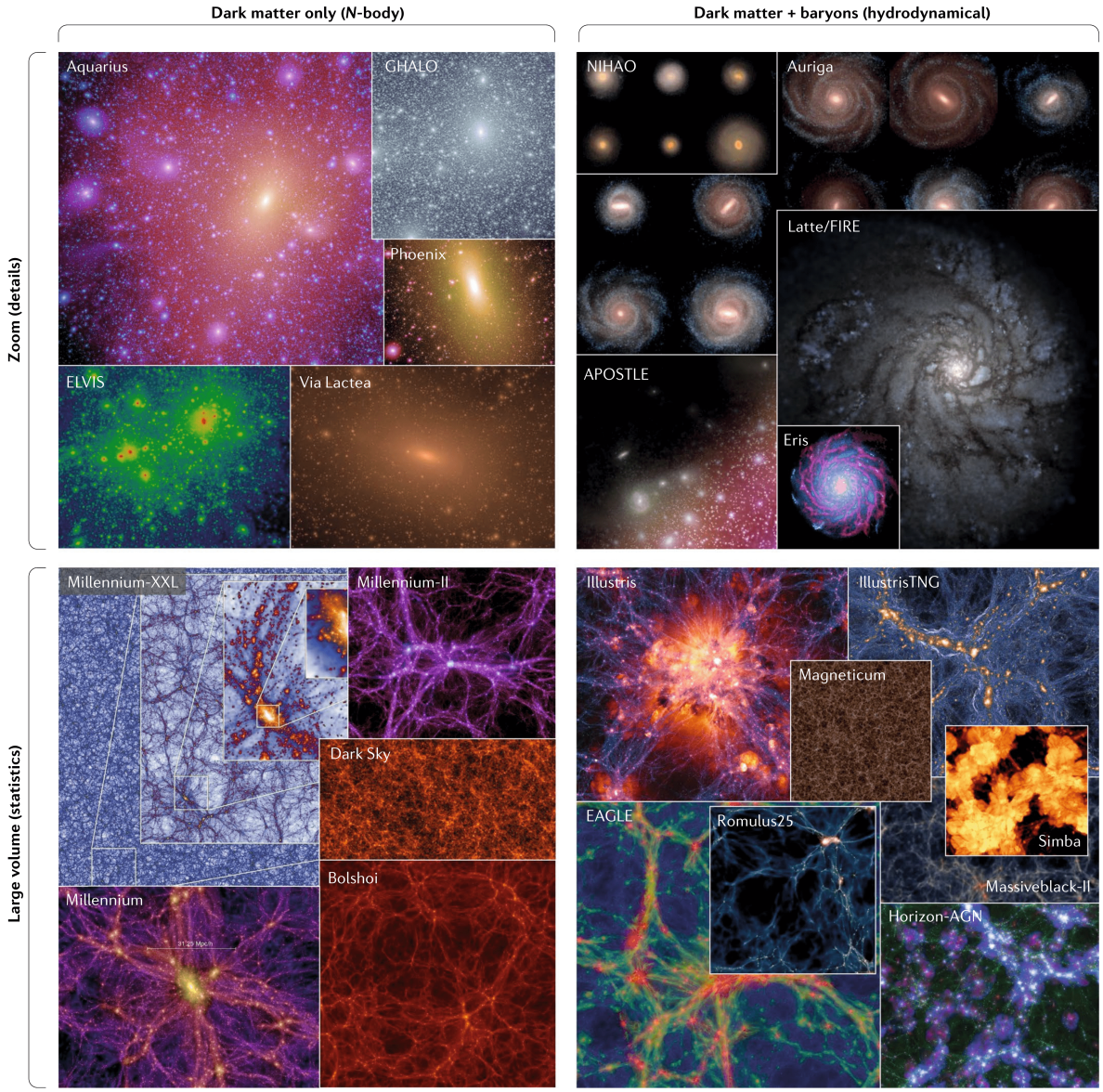

Figure 1.2: Visual representation of various cosmological N-body (left column) and hydrodynamical (right column) simulations, taken from Vogelsberger et al. (2020). The bottom row shows the large-scale projection of density distributions, and the top row shows a number of simulations on the galactic scale. References and further details on each of the simulations shown above are provided in Table 2 of Vogelsberger et al. (2020).

1.2.1 Cosmological simulations

Cosmological simulations provide an important comparison to observations and offer insight into the physics underpinning galaxy evolution in a cosmological framework. In particular, these simulations are useful for understanding the role of mergers in galaxy mass assembly using a large statistical sample of galaxies where the merger histories are known. They can also be used to make predictions about various galaxy populations in the Universe at different epochs.

Initially, large volume cosmological simulations such as Millennium (Springel et al. 2005), Bolshoi (Klypin et al. 2011) and Dark Sky (Skillman et al. 2014), consisted of dark matter only. The incorporation of baryonic matter in cosmological simulations (e.g. Illustris, Vogelsberger et al. 2014; EAGLE, Schaye et al. 2015; SIMBA, Davé et al. 2019) is essential in order to reliably compare results from these simulations to large observational surveys. This inclusion is done using two approaches: semi-analytic models (Henriques et al. 2009; Lu et al. 2011; Ruiz et al. 2015; Lagos et al. 2018) or full hydrodynamical simulations (Schaye et al. 2015; Crain et al. 2015; Pillepich et al. 2018). In brief, semi-analytic models paint baryonic physics onto dark matter-only simulations, whereas hydrodynamical simulations attempt to include baryonic physics into the simulations themselves. Due to the trade-off between realism and computational efficiency, semi-analytic and dark matter-only simulations are able to reach higher particle resolutions and cosmological volumes than full hydrodynamical simulations. Regardless of the method chosen, the inclusion of baryonic matter increases the computational cost of the simulation.

Many of the astrophysical processes that occur on sub-galactic scales, such as star formation, formation of supermassive black holes, stellar feedback as well as feedback from active galactic nuclei, etc., cannot be directly modelled and so subresolution, or subgrid, models are used to implement these processes in cosmological simulations. In order to investigate these processes, higher particle resolutions are required than are typically achieved by large volume cosmological simulations, necessitating the use of so-called 'zoom' simulations.

1.2.2 Zoom simulations

To address the issue of limited resolution in cosmological simulations, smaller volume, high resolution, zoom simulations have been used in recent years. As the name suggests, these simulations employ a 'zoom-in' technique, in which a sub-volume of a cosmologically representative region is evolved at a higher resolution than the surrounding simulation box. This allows for the region of interest to be studied in greater detail without compromising the cosmological context. With zoom simulations, physical processes can be resolved in greater detail.

Zoom simulations are able to probe scales ranging from clusters down to individual galaxies (e.g. FIRE, Hopkins et al. 2013; Wetzel et al. 2016; APOSTLE, Sawala et al.

2016; Auriga, Grand et al. 2017). In the context of mergers, zoom simulations allow for an exploration of high mass ratio mergers and the effects of mergers on morphology at various redshifts (e.g. Abruzzo et al. 2018). Due to the nature of zoom simulations, often involving multiple interactions along with environmental effects, it is difficult to perform a controlled exploration of the parameter space of a single merger or galaxy-galaxy interaction event. Such explorations require the use of equilibrium simulations.

1.2.3 Small-scale equilibrium simulations

Idealised (non-cosmological) simulations have been vital for understanding specific galaxy interactions and how they drive galaxy evolution. For example, Toomre & Toomre (1972) used such simulations to convincingly demonstrate that many of the morphological irregularities observed in Arp's Atlas were the result of tidal interactions between galaxies. Equilibrium simulations allow us to study galaxy mergers via controlled experiments and enable the investigations into the impact of various factors on an interaction, from the orientation and orbital parameters of the interaction, to the gas fraction and mass ratio of the interacting galaxies (e.g. Cox et al. 2008; Lotz et al. 2010a,b; Gajda et al. 2018; Semczuk et al. 2018; Namumba et al. 2019).

Despite the loss in realism with regards to a cosmological context, these idealised interaction and merger scenarios allow for the study of various physical processes in greater detail. For example, Privon et al. (2013) modelled NGC 2623, one of the galaxies featured on the Toomre sequence of merging galaxies (Toomre 1977), using test particle simulations. Figure 1.3 shows the morphological evolution of the system in the simulation. While the 0 Myr image, shown in the top right panel of the figure, matches current observations, as seen in Figure 1.1, some of the apparent signatures of the merger such as the tidal arms will disappear with time (see the 85 and 170 Myr panels of Figure 1.3). The high time resolution in these types of simulations is critical for understanding how a single merger can affect a galaxy's morphology. Historically, studies of galaxy morphology using this class of simulations have focussed on optical properties (e.g. Cox et al. 2008; Lotz et al. 2010a; Privon et al. 2013). More recently, the gas distributions have also been investigated using equilibrium simulations.

Mapelli et al. (2008) employed idealised simulations to investigate various astrophysical processes which could possibly be the cause of the lopsidedness observed in NGC 891, an edge-on spiral galaxy. They considered three mechanisms: accretion of cold gas from cosmological filaments, a flyby interaction, and ram pressure from the intergalactic medium. By comparing their results from the simulations with properties of the investigated galaxy, they determined that a flyby interaction with a nearby galaxy was the most likely cause for disrupting the morphology of NGC 891.

More recently, Namumba et al. (2019) used equilibrium simulations to investigate if the disturbed morphology and kinematics observed in IC 10, a blue compact dwarf galaxy in the Local Group, could be explained by an interaction between the galaxy and M31.

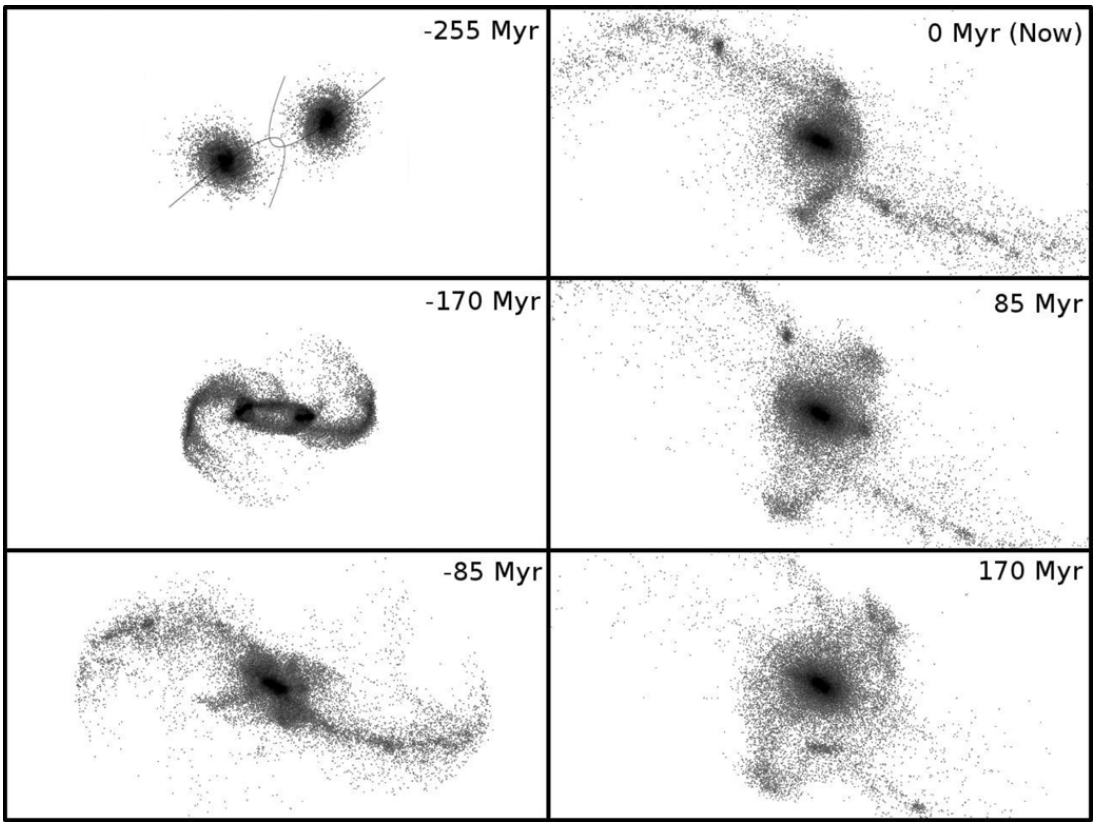

Figure 1.3: Modelled evolution of the stellar distribution of NGC 2623 as a function of time. Figure is taken from Privon et al. (2013). The scale of each panel is 75 kpc by 50 kpc. Time of each snapshot relative to now is provided in the top right corner of each panel.

Using these simulations, they were able to exclude a possible interaction between IC 10 and M31. In summary, equilibrium simulations are vital in helping to uncover which processes were involved (or not) in influencing the morphologies of interacting galaxies. In particular, they are one of the few tools available to compare directly to observations of real, individual galaxies.

1.3 Neutral atomic hydrogen

Hydrogen, the most abundant element in the Universe, is typically detected in its neutral state (HI) using the 21 cm line which was first predicted by H.C. van der Hulst in 1944. The 21 cm emission line is a result of the hyperfine spin flip transition between the energy levels of the ground state of a hydrogen atom. These energy levels are determined by the spin configuration of the electron and the central proton. If the electron transitions from a parallel to an anti-parallel spin configuration, a photon is emitted at a wavelength of $\lambda = 21.1$ cm, which lies in the radio wavelength range and can thus be detected with radio telescopes. Despite instrumental limitations at the time, the line was first detected in the Milky Way by Ewen & Purcell (1951) and Muller & Oort (1951). Shortly thereafter, the first extragalactic detection was observed in the Magellanic clouds by Kerr & Hindman (1953).

1.3.1 HI in galaxies

HI provides the raw fuel for eventual star formation and comprises a significant mass component of a galaxy. It extends beyond the stellar disk (Meurer et al. 1996; Broeils & Rhee 1997; Boomsma et al. 2008; Wang et al. 2013, see Figure 1.4), and is more sensitive to interactions and other disruptive processes (e.g. Combes et al. 1980; Yun et al. 1994). Studies of the HI in galaxies can provide insight into the processes governing galaxy evolution since it is susceptible to being spatially and dynamically disturbed. Due to the large spatial extent, HI disks can show signs of ongoing interactions before the stellar disk is affected.

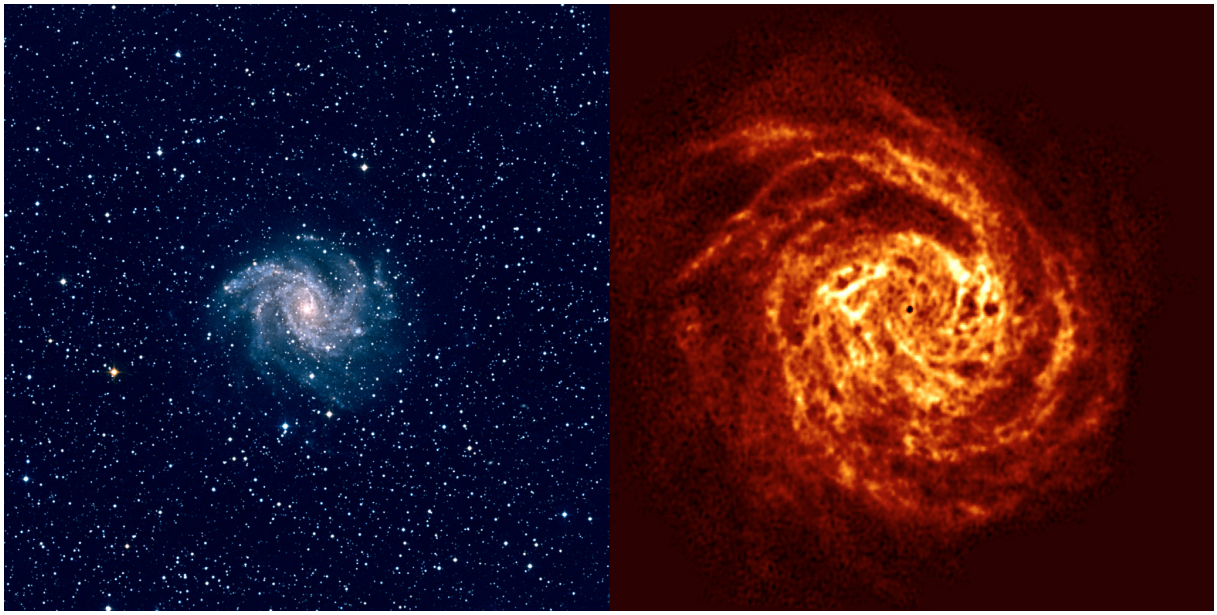

Figure 1.4: Comparison of the colour composite optical image (left) and the deep total HI image (right) of NGC 6946 (Arp 29), taken from Boomsma et al. (2008). The optical image is from the Digitized Sky Survey and the HI map is from 192 h integration on the Westerbork Radio Synthesis Telescope (WSRT). Both images are presented on the same scale.

Until now, HI observations of spatially resolved galaxies have been limited to relatively small samples (a few hundred) in the local Universe (e.g. WHISP*, THINGS†, VIVA‡, HALOGAS§, ATLAS^{3D}, BlueDisks, and LVHIS¶; see van der Hulst et al. 2001; Walter et al. 2008; Chung et al. 2009; Heald et al. 2011; Cappellari et al. 2011; Wang et al. 2013; Koribalski et al. 2018) due to unfeasibly long observing time requirements on synthesis telescopes (radio interferometers). Nevertheless, these surveys have provided a wealth of information about the gas distributions and dynamics of galaxies at low redshift. Orders of magnitude more HI detections of spatially unresolved galaxies have been obtained with

* The Westerbork HI survey of Irregular and Spiral Galaxies
† The HI Nearby Galaxy Survey
‡ the VLA Imaging of Virgo in Atomic Gas survey
§ The Hydrogen Accretion in Local Galaxies Survey
¶ The Local Volume HI Survey

HI surveys on single dish radio telescopes (e.g. HIPASS[‖], ALFALFA[**] and NIBLES[††]; see Barnes et al. 2001; Haynes et al. 2018; van Driel et al. 2016). Surveys such as these have enabled statistical studies of the gas content and scaling relations of galaxies in the local Universe.

Upcoming HI surveys on the Square Kilometre Array (SKA) pathfinders, including MeerKAT, ASKAP and WSRT/APERTIF, will enable us to explore the evolution of the gas in galaxies using much larger samples in the local Universe and beyond. For example, the MeerKAT International GHz tiered extragalactic exploration (MIGHTEE, Jarvis et al. 2016) survey and the Widefield ASKAP L-band Legacy All-sky Blind survey (WALLABY, Koribalski et al. 2020) will spatially resolve hundreds to thousands of galaxies in HI, while the Looking at the Distant Universe with the MeerKAT Array (LADUMA, Blyth et al. 2016) survey will detect the HI profiles of galaxies out to high redshift ($z < 1.4$). This will provide a means to trace galaxy interactions via HI beyond the local Universe, for the first time.

1.4 Deviations from symmetry

As previously mentioned, morphological transformations in the gas and/or stellar distributions of galaxies are often indicative of external processes at play. While previous sections have focussed on galaxy mergers, it should be emphasised that environmental processes such as ram-pressure stripping (Gunn & Gott 1972), accretion of cold gas from the surrounding intergalactic medium (e.g. Bournaud et al. 2005; Sancisi et al. 2008), as well as galaxy-galaxy interactions in dense environments which do not result in mergers (galaxy harassment and flyby interactions, Moore et al. 1996; Mapelli et al. 2008) can result in morphological asymmetries. While these asymmetries are most clearly observed in the spatial distributions of galaxies, they can also manifest in the HI velocity fields and integrated spectra.

Extragalactic studies with asymmetry as a focal point of the research date back to the 1970s. Peterson & Shostak (1974) studied the HI line profiles of 23 galaxies from Arp's Atlas in order to establish if the asymmetries observed in the spatial stellar distributions of these galaxies were reflected in their HI profiles. The authors found that a general correlation existed between a deviation from symmetry in the shape of the HI profiles and the degree of "morphologic abnormality" assigned to the galaxy through visual inspection of the optical images. However, they also noted that there were a number of galaxies with relatively undisturbed stellar morphologies but asymmetric HI profiles due to perturbations in the HI velocity fields.

Having investigated the spatial HI distributions of approximately 20 spiral galaxies, Baldwin et al. (1980) were the first to discern that large-scale morphological asymmetries

[‖] The HI Parkes All Sky Survey
[**] The Arecibo Legacy Fast ALFA Survey
[††] The Nançay Interstellar Baryons Legacy Extragalactic Survey

were not just a feature observed in stellar disks. They used the term 'lopsided' to refer to a galaxy whose stellar and/or gas distribution is disproportionately skewed on one side of the galaxy, such that the ratio of projected surface density of the two sides exceeds 2:1. They identified four galaxies in their sample fitting this description and proposed a kinematic model in which the observed lopsidedness is connected to off-centred elliptical orbits.

Richter & Sancisi (1994) qualitatively examined the global HI of ~1700 disk galaxies obtained through single dish surveys. They estimated that at least 50% of the inspected profiles displayed some degree of spectral asymmetry, suggesting that asymmetries are far more common than previously assumed. In these influential studies, it was recognised that quantitative techniques which could be applied to large galaxy samples in a consistent and coherent manner were required.

1.4.1 Quantifying spectral asymmetries

In the majority of the literature, asymmetries in the HI line spectrum of a galaxy have been calculated in two ways: using a ratio of velocity differences in the profile, or the ratio of the integrated flux in two halves of the profile. The former technique was first implemented by Tifft & Cocke (1988), who calculated the difference between the velocity found to divide the area under the profile in half (v_A), and the lower and upper velocities measured at 20% of the peak flux density (v_l and v_h respectively). This asymmetry index is expressed either as a negative or positive value depending on the value of v_A relative to the systemic velocity (v_{sys}) of the profile:

$$A_{vel} = \begin{cases} \dfrac{-(v_A - v_l)}{(v_h - v_A)} \leq -1, & \text{if } v_A > v_{sys} \\ \dfrac{(v_h - v_A)}{(v_A - v_l)} \geq 1, & \text{if } v_A < v_{sys} \end{cases} \tag{1.1}$$

Richter & Sancisi (1994) used A_{vel} in order to calibrate a subsample of galaxies in their study for comparison, and found great agreement between their qualitative and quantitative results.

The second technique, which has been used more extensively in recent literature, measures the spectral asymmetry by calculating the ratio of areas under the profile at velocities less than and greater than the systemic velocity (Haynes et al. 1998):

$$A_{l/h} = \frac{\int_{v_l}^{v_{sys}} S dv}{\int_{v_{sys}}^{v_h} S dv}, \tag{1.2}$$

where S is the flux density contained within the specified velocity bounds and v_l (v_h) corresponds to the lower (upper) velocities measured at either 20% or 50% of the peak

flux density on either side of v_{sys}. It is common convention for this formulation of the 1D asymmetry to be expressed as a value greater than 1, and so it is quoted as:

$$A_{1D} = \begin{cases} A_{l/h}, & \text{if } A_{l/h} \geq 1 \\ \dfrac{1}{A_{l/h}}, & \text{if } A_{l/h} < 1 \end{cases} \tag{1.3}$$

This statistic has been widely used in the literature, and depending on the threshold used, various studies find a high proportion of asymmetric spectra. Haynes et al. (1998) analysed a sample of 78 isolated spiral galaxies and found 45% of them had $A_{1D} > 1.1$, which they classified as asymmetric. Matthews et al. (1998) examined a sample of 30 late-type spiral galaxies and found that 77% displayed some degree of asymmetry.

To better understand the underlying drivers of asymmetry, various studies have focussed on the spectral asymmetry and the rate of its occurrence in samples based on environment. For example, Espada et al. (2011) used a refined HI sample of isolated galaxies from the Analysis of the interstellar Medium of Isolated GAlaxies (AMIGA Verdes-Montenegro et al. 2005) project to study the distribution of A_{1D} in order to quantify the intrinsic asymmetry of disk galaxies. They found that the distribution was well represented by a half-Gaussian with a standard deviation of $\sigma = 0.13$ and classified a galaxy as asymmetric if the measured A_{1D} value exceeded the 2σ level of their HI refined sample ($A_{1D} > 1.26$). With this defined threshold, they discovered that only 9% and 2% of galaxies in their isolated sample measured $A_{1D} > 2\sigma$ and 3σ (1.39) respectively. Furthermore, when comparing their results to other studied samples of field galaxies, they found statistically different intrinsic σ and higher asymmetry rates for the field samples. The authors noted that this was likely due to the inclusion of interacting systems in those samples, and that this result suggests that the effects from denser environments are responsible for the increased rate of HI asymmetry.

Recent studies have used the Espada et al. (2011) 2σ and 3σ thresholds to calculate rates of HI asymmetry in their samples. For example, Scott et al. (2018) investigated a sample of 43 late-type galaxies with HI detections in the galaxy cluster Abell 1367 and found that 40% measured $A_{1D} > 1.26$. They also found that 31% of the late-type galaxies with $A_{1D} > 1.26$ are members of groups or pairs, suggesting that galaxy-galaxy interactions are partially responsible for the high rate of HI asymmetry in their sample.

Watts et al. (2020) studied a sample of 562 galaxies from the extended GALEX Arecibo SDSS Survey (xGASS, Catinella et al. 2018). The authors found that satellite galaxies were generally more asymmetric than central galaxies, and furthermore that central galaxies in groups were slightly more asymmetric than isolated central galaxies. They also found that asymmetric galaxies, when compared to symmetric counterparts with similar stellar mass and signal-to-noise (S/N) ratios, had lower gas fractions, suggesting that gas removal processes might be responsible for the observed asymmetry rates in the xGASS sample.

In order to probe whether galaxy mergers give rise to HI asymmetries, Bok et al. (2019) compared samples of close galaxy pairs and isolated galaxies selected from the ALFALFA survey. They found a significant difference between the distributions of A_{1D} for the samples, and observed a rate of 27% of asymmetric (i.e. $A_{1D} > 1.26$) galaxies in the close pair sample, in comparison to 18% in the isolated sample.

1.4.2 Quantifying morphological asymmetries

Various methods have been used to quantify morphological asymmetries in the last 25 years. One such method is the use of the normalised amplitude of the $m = 1$ Fourier component (see Jog & Combes 2009, and references therein for a comprehensive review on the use of this method). This technique has been used in optical (Reichard et al. 2008), near-infrared (Rix & Zaritsky 1995; Zaritsky & Rix 1997; Bournaud et al. 2005) and HI (Angiras et al. 2006, 2007; van Eymeren et al. 2011; Reynolds et al. 2020) studies. One key result of this Fourier analysis is that asymmetry is quantitatively larger and more frequent in the HI than in the stellar distribution (Jog & Combes 2009).

Another method is the use of the CAS system, which is a set of morphometric statistics explored in Conselice (2003). The parameters are the concentration of stellar light (C), the asymmetric distribution of this light (A) and its clumpiness (S). Other non-parametric morphological measurements include the Gini parameter (Abraham et al. 2003), a measure adopted from Economics which has been used in astronomy to quantify the distribution of flux over pixels in an image, and M_{20} (Lotz et al. 2004), which is defined as the relative contribution of the brightest 20% of pixels to the second-order moment image.

The 2D rotational asymmetry, introduced by Schade et al. (1995), Abraham et al. (1996) and Conselice et al. (2000), is expressed as

$$A_{2D} = \frac{\sum_{i,j} |I(i,j) - I_{180}(i,j)|}{2\sum_{i,j} |I(i,j)|} - B_{180}, \tag{1.4}$$

where $I(i,j)$ is the pixel flux value in the galaxy image, $I_{180}(i,j)$ is the pixel flux value in the 180° rotated image and B_{180} is the average asymmetry of the background. This statistic has been frequently used to study disturbed optical morphologies (e.g. Conselice 2003; Lotz et al. 2008a; Jogee et al. 2009; Bluck et al. 2012).

In recent years, asymmetry and other non-parametric morphologies have been used to study the HI morphology of nearby galaxies. Holwerda et al. (2011a,b) were the first to do this, and examined the morphologies of THINGS and WHISP galaxies respectively. Using a variety of morphometric statistics, they found that the asymmetry parameter was the most promising at identifying interacting galaxies. Following from this, Giese et al. (2016) studied the same sample of WHISP galaxies as Holwerda et al. (2011b) and simulated galaxies in order to better understand the observational effects, such as S/N, resolution and inclination, on the non-parametric morphological measurements. They were able to

determine a set of reliable resolution and inclination limits for the use of these statistics in large surveys.

Wang et al. (2013) studied a sample of 23 nearby galaxies with high HI mass fractions and compared them with a control sample of 19 galaxies. Having studied a variety of HI properties in both samples, they found little to no difference in the overall asymmetry distributions of the populations. However, they observed that the outermost regions of the HI-rich galaxies tended to be more asymmetric. Lelli et al. (2014) developed a modified outer asymmetry parameter (see §2.2.2 for more details) that is more sensitive to low surface brightness regions on the outskirts of galaxies. They found that the newly defined 'outer asymmetry' was able to distinguish between samples of starburst dwarf galaxies and irregular galaxies, and that the outer HI regions of the starburst dwarf galaxies studied were generally more asymmetric than those of the irregular galaxies.

In addition to these observational studies, non-parametric morphologies have also been used to analyse galaxies in cosmological simulations. For instance, Abruzzo et al. (2018) studied optical morphologies in the MUFASA simulations (Davé & Rafieferantsoa 2016) at cosmic noon ($z \sim 2-4$). The authors found that the complex morphologies of galaxies, in addition to confusion between central galaxies and satellites, made it difficult to successfully identify galaxy mergers at high redshifts using these statistics.

1.4.3 Relating asymmetries in 1D and 2D

Despite the growing body of literature on galaxy asymmetries, there has been little quantitative analysis on the connection between the 1D spectral and 2D morphological asymmetries in HI. Since the global HI profile's shape is determined largely by the internal kinematics of the galaxy and the spatial HI distribution to a lesser extent, it is possible for perturbations in the velocity field to induce spectral asymmetries, without the spatial distribution being considerably affected.

Kornreich et al. (2000) considered 9 spiral galaxies and examined the relationship between A_{1D} and a bisector method of calculating the morphological asymmetry in both HI and R-band images. They found no correlation between the 1D and 2D measures but noted that the 2D rotational asymmetry, which they did not consider, is fundamentally different to their bisector method.

More recently, Reynolds et al. (2020) investigated the morphological, kinematic and spectral HI asymmetries in galaxy samples from three different surveys. They introduced a number of new 1D and 2D asymmetry statistics and found a moderate level of correlation between the various 1D and 2D measures. Further details can be found in Chapter 6 of this thesis.

1.5 Thesis outline

Many of the studies briefly discussed suggest a pertinent role for the use of asymmetries as a tool to probe galaxy-galaxy interactions and other evolutionary processes. However, there are a number of outstanding questions that I aim to address in this thesis:

- How long-lived is the asymmetry signature of an interaction in the stellar and gaseous components of a galaxy?
- How well do various spectral and morphological asymmetry measures correspond to visual classifications?
- Given the abundance of HI spectra relative to the number of spatially resolved HI images of galaxies, how well can the spectral asymmetry track the asymmetries in 2D?
- Are interacting galaxies generally more asymmetric than non-interacting galaxies in HI, and what are the best measures to determine this?

I will explore these questions using idealised merger simulations and data from the WHISP survey. This work is particularly topical given the large samples of HI data which are starting to be produced by the SKA pathfinder telescopes.

The remaining 5 chapters of this thesis are organised in the following manner. Chapter 2 details four parameters, two of which were introduced in §1.4, that are used to quantify the spectral and morphological asymmetries in the 1D velocity profiles and 2D images respectively. Chapter 3 describes the data used in this work. The first part of Chapter 4 focusses on the simulated data and investigates the behaviour of the 2D parameters measured for the gas and stellar distributions over the duration of the merger event. The second part of the chapter explores varying the inclination and viewing angle of the gas distribution at two separate stages of the merger, and what effect these changes have on the measured 1D and 2D parameters. Chapter 5 uses visual classifications of the degree of asymmetry in the global HI profiles and integrated HI images of galaxies in the WHISP sample to investigate which of the 1D and 2D parameters is in best agreement with visually assigned degrees of asymmetry. I then explore the linear correlation between the 1D and 2D parameters and identify optimal inclination limits to be imposed on a sample. I also examine if galaxies which have visually been classified as interacting occupy a specific region of the asymmetry parameter space, and identify several selection criteria which are able to generally separate interacting galaxies from the non-interacting galaxy sample. Chapter 6 provides a discussion and summary of the results presented in Chapters 4 and 5, and concludes with an outlook for future work.

Chapter 2

Measuring asymmetries in 1D and 2D

Before we proceed with describing the various non-parametric measurements available for quantifying the asymmetry in a galaxy image or velocity profile, it is important to make the distinction between lopsidedness and asymmetry. These terms have been used interchangeably in the literature, particularly in research pertaining to the HI global profiles of galaxies, as mentioned in Chapter 1. However, there is a subtle difference in the definitions of these terms, as well as their approach to measuring a deviation from symmetry. In this work, we adopt the nomenclature used by Holwerda et al. (2011b), who use the following definitions:

- lopsidedness is a measure of axi-symmetry about a specified axis. In the 2D domain, Fourier decompositions have been used to quantify the lopsidedness in Hα velocity and velocity dispersion fields (e.g. Shapiro et al. 2008; Bloom et al. 2017, 2018) as well as galaxy images across a range of wavelengths (e.g. Rix & Zaritsky 1995; Zaritsky & Rix 1997; Bournaud et al. 2005; Angiras et al. 2006, 2007; Reichard et al. 2008; van Eymeren et al. 2011; Reynolds et al. 2020). With reference to the 1D global HI profile, lopsidedness refers to how asymmetric the profile is when mirrored about a specified velocity. The quantified definition of 1D lopsidedness was briefly discussed in §1.4.1.
- asymmetry is a measure of the point-symmetry of an object. As mentioned in §1.4.2, this 2D parameter is defined as the level of asymmetry in the light distribution of a galaxy when rotated 180° about a chosen centre of rotation (Schade et al. 1995; Abraham et al. 1996; Conselice et al. 2000).

Based on these definitions, this chapter focusses on the parameters used in this thesis to measure the lopsidedness in 1D global HI profiles and the asymmetry in 2D integrated HI maps of galaxies. Two parameters are described for each dimension: one which has been well-established in the literature (§2.1.1 and §2.2.1), and an alternative which could more effectively quantify the asymmetry/lopsidedness (§2.1.2 and §2.2.2). The steps taken below to compute all parameters for the data were performed using Python.

2.1 The 1D case: lopsidedness

The subject of characterising the lopsidedness in the 1D global HI profile of galaxies has been studied extensively over the last 3 decades. These profiles, which can be obtained using single dish radio telescopes, are somewhat in abundance relative to their partner 2D HI images, which require observations with interferometers. The steps described in this section are performed on spectra which are assumed to rest on a flat baseline. More information is provided in §3.2.3 for spectra which are not in this form.

2.1.1 Measuring 1D global profile lopsidedness

The 1D lopsidedness parameter, described by Equations 1.2 and 1.3, is often quoted as a number greater than 1 in the literature. However, it can be expressed as a number between 0 and 1 using the following expression (Peterson & Shostak 1974; Matthews et al. 1998; Deg et al. 2020):

$$L = \frac{\left| \int_{v_{sys}}^{v_h} S_v dv - \int_{v_l}^{v_{sys}} S_v dv \right|}{\int_{v_l}^{v_h} S_v dv}. \tag{2.1}$$

In this work we will use Equation 2.1 to calculate the lopsidedness, following the method outlined in Haynes et al. (1998). Below describes the steps taken for a single profile.

1. **Locate and determine the number of peaks.** The first step is to locate and determine the number of peaks in the profile. Using the literature value of the systemic velocity ($v_{sys,lit}$) as an initial guide, the code searches for the channels on either side of $v_{sys,lit}$ which result in the steepest positive and negative slopes. For simulated HI profiles, 1000 km s^{-1} is the default value used for $v_{sys,lit}$. These slopes are used to determine the turning points of the profile. We classified a profile as having a single peak if the difference in velocity between the peaks is less than half the literature value of the line width at 50% flux density, hereafter referred to as w_{50}.
2. **Determine profile velocity parameters $v_{l_{20}}$, $v_{h_{20}}$, w_{20} and w_{50}.** Once the peaks are found, they are used to calculate 50% and 20% of the peak flux density. The profile is then interpolated to determine v_l and v_h, the "low" and "high" velocities corresponding to the fractional peaks. The interpolation is done because these velocities tend to lie between channels. Once v_l and v_h have been calculated for 50% and 20% the peak flux, the profile widths for the measured flux densities are calculated using $w_k = v_{h_{(k)}} - v_{l_{(k)}}$, where k is 50% or 20%. This is shown in Figure 2.1 for a single peak profile (UGC 2034) and a double-horn profile (UGC 5721).
3. **Calculate the systemic velocity, v_{sys}.** At the 50% and 20% intensity levels, $v_{mid} = (v_l + v_h)/2$ is calculated. We measure v_{sys} as the average of $v_{mid_{20}}$ and $v_{mid_{50}}$.

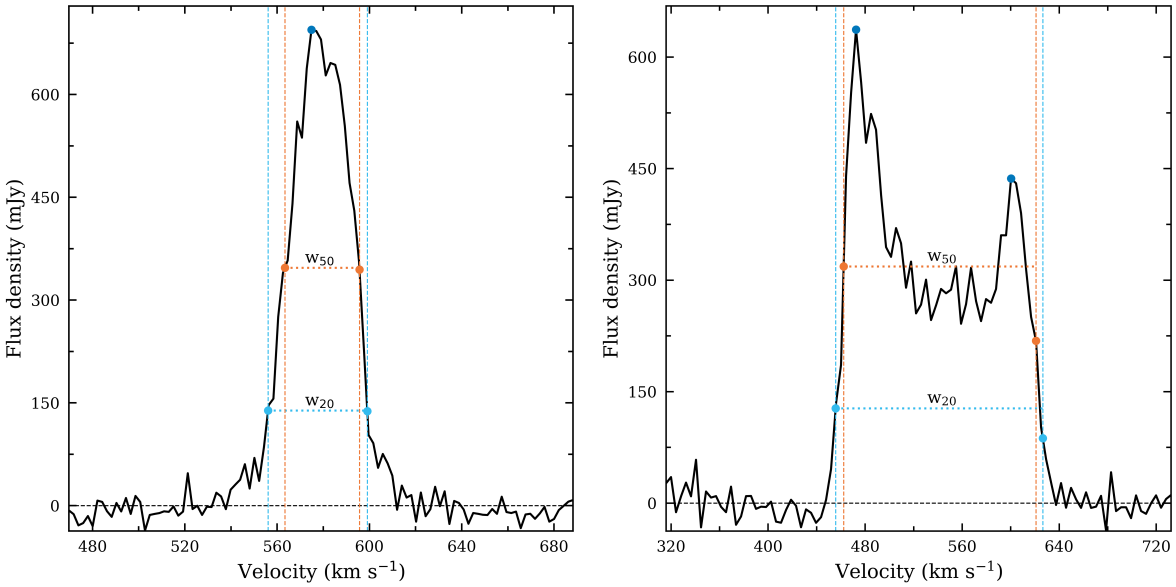

Figure 2.1: Global HI spectra of UGC 2034 (left) and UGC 5721 (right). The dark blue circle markers indicate the peaks of the profile, orange markers the positions on the profile at 50% the peak flux, and cyan markers the positions on the profile at 20% the peak flux. The vertical dashed lines correspond to the upper and lower velocities at the measured fractional flux densities.

4. **Calculate the rms noise in the spectrum.** We then calculate the rms noise in the profile using sections of the spectrum outside the HI line profile. These sections are chosen based on the number of channels beyond the v_{20} points. If there are n channels to the left of $v_{l_{20}}$ and m channels to the right of $v_{h_{20}}$, $n/10$ and $m/10$ channels are excluded from the start and end of the spectrum respectively, as well as $n/4$ and $m/4$ channels closest to $v_{l_{20}}$ and $v_{h_{20}}$ where there may still be some HI emission. This is done to avoid over-estimating the noise in the spectrum, which is calculated as the standard deviation of these regions.

5. **Calculate *L*.** At this stage, we are fully equipped to calculate the lopsidedness parameter, hereafter referred to as L or the L parameter, for the HI profile. Using the interpolated data to allow for easier integration, the area to the left and right of the systemic velocity is calculated up to $v_{l_{20}}$ and $v_{h_{20}}$. Due to the S/N ratio of the archival data sample, for which two profiles are shown in Figure 2.1, the flux values at v_{20} are well above the rms noise of the profiles, so we do not expect any additional asymmetry to be introduced by integrating to the 20% intensity level as opposed to 50%. Furthermore, we want to include as much of the profile as possible when computing the lopsidedness. The L parameter is calculated using Equation 2.1, by taking the absolute difference of the areas on both sides of the systemic velocity and dividing by the sum of the areas. This result is shown in the left panel of Figure 2.2 for WHISP galaxy UGC 5721. The vertical dashed blue lines show v_l and v_h at 20% the peak flux density and the black dotted line shows v_{sys}. The shaded regions show the areas on either side of v_{sys} integrated across w_{20}.

6. **Calculate σ_L.** The final step is to calculate the associated error of the L parameter. We use the same technique implemented by Bok et al. (2019). Gaussian noise with a mean of zero and standard deviation equal to the rms noise calculated in step 4 is added to the profile and L is recalculated by repeating steps 1-5. This is done since the peak fluxes, and thus v_l, v_{sys} and v_h, will change in the new profile. This is repeated 100 times and the estimated uncertainty in L is taken as the standard deviation of the 100 measurements.

2.1.2 The *folding difference* method

The L parameter discussed in the previous section has been shown in the literature (eg. Haynes et al. 1998; Espada et al. 2011) to reliably quantify the overall lopsidedness in a 1D global HI profile. However, one of the difficulties with the current formulation of L is that small-scale asymmetries that occur over a few channels are suppressed in the calculation since it only considers the ratio of the overall difference in the areas of two halves of the profile to the sum of those areas. This is likely to occur in the central region of a double-horn profile where there is a central dip. This region has lower flux densities in comparison to the horns of the profile, and as a result contributes less to the total area of the profile. This means that asymmetries in the inner regions of double-horn profiles, which would be visually apparent, are often suppressed due to the low areal contribution of these regions.

One possible way to give weight to these small-scale asymmetries is to localise the comparison of the halves of a profile. Consider the following equation:

$$\mathcal{L} = \frac{\sum_{i=1}^{N} |S_{v_l}(i) - S_{v_h}(i)|\Delta v}{\sum_{i=1}^{N} |S_{v_l}(i) + S_{v_h}(i)|\Delta v} \tag{2.2}$$

where i is the velocity channel, N is the number of symmetric channel pairs contained between the profile edges (inclusive) and the central channel containing v_{sys}, S_{v_l} and S_{v_h} are the HI flux densities measured in channel i on the left and right sides of the profile respectively, and Δv is the velocity channel width. As opposed to Equation 2.1 which calculates the lopsidedness in a continuous manner since it employs interpolation, Equation 2.2 utilises a discrete approach by considering the contribution from symmetric channel pairs about the central channel. One can think of this method as "folding" the HI profile at v_{sys}, as shown in the right panel of Figure 2.2, and comparing the difference in the flux density of the overlaid velocity channels. As intended, Equation 2.2 bears resemblance to Equation 1.4, which was introduced in Chapter 1 as one of the ways to measure the 2D asymmetry in a galaxy image. Although it is similar in equation form to the 2D asymmetry, it should be noted that the "folding difference" asymmetry (hereafter referred to as $\mathcal{L}$) is still, based on the definitions stated at the start of this chapter, a measure of lopsidedness.

The panels in Figure 2.2 show the difference in the approaches taken to measure L and $\mathcal{L}$ for a moderately asymmetric HI profile. In the left panel of the figure, the blue dashed lines correspond to $v_{l_{20}}$ and $v_{h_{20}}$, and the black dotted line to the measured v_{sys}. For illustrative and descriptive purposes, the velocity channels shown in both panels between $v_{l_{20}}$ and $v_{h_{20}}$ have been grouped and so each grouped channel with a marker is representative of three velocity channels in the spectrum. Paired channels are represented by the same markers in the left panel and have been overlaid in the right panel.

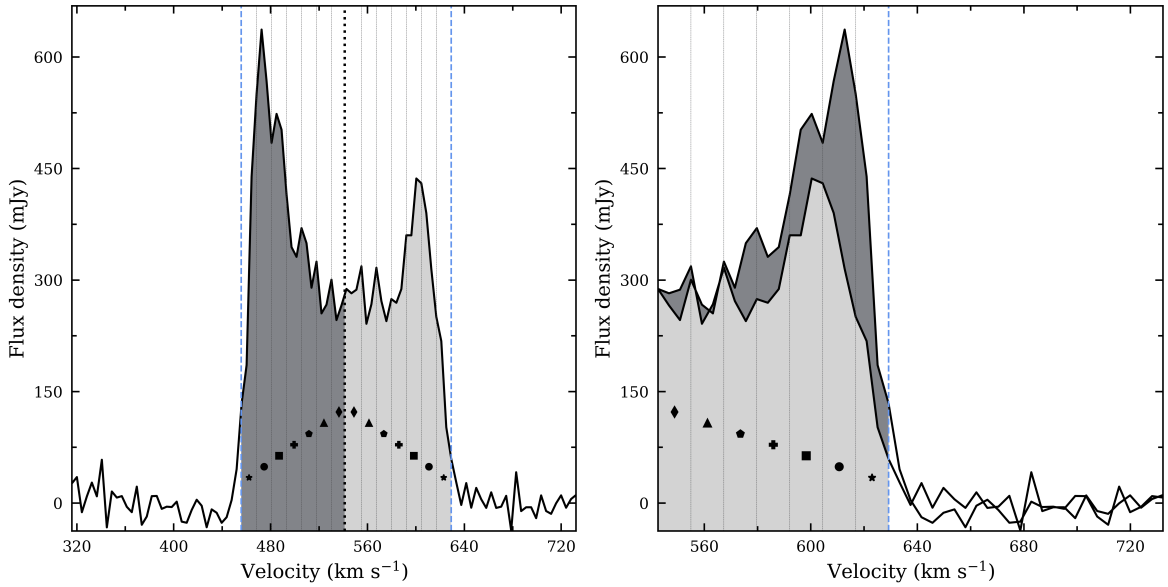

Figure 2.2: Illustration of the differences in calculating L and $\mathcal{L}$ using the HI spectrum of WHISP galaxy UGC 5721. The dotted black line corresponds to the calculated systemic velocity and the blue dashed lines correspond to the upper and lower velocities at 20% the peak flux. The shaded light and dark grey regions shown in the left panel are used to calculate L. The sum of the differences between the light and dark grey profile halves is used to calculate $\mathcal{L}$.

In this work, L and $\mathcal{L}$ were calculated together since both methods require the same information about the HI profile: the number of peaks, $v_{l_{20}}$, $v_{h_{20}}$, and v_{sys}. As such, the steps below describe the process of measuring $\mathcal{L}$, with the aid of Figure 2.2, and steps performed in both methods have been summarised to avoid repetition.

1–3. **Calculate $v_{l_{20}}$, $v_{h_{20}}$, v_{sys} and the channel indices corresponding to these velocities.** These steps are the same as those described in §2.1.1. Additionally, the "folding difference" method requires the channel indices corresponding to these velocities. These velocities often do not lie at a specific channel value - recall that interpolation was implemented to calculate $v_{l_{20}}$ and $v_{h_{20}}$ - and so the closest channel to the velocity value of interest is chosen.

4. **Calculate rms noise in the spectrum**. This is identical to step 4 of §2.1.1.

5. **Determine the number of channel pairs, N.** In order to calculate $\mathcal{L}$, we want to consider profile halves of equal width in velocity. For most HI profiles in our sample,

the number of channels contained within w_{20} is odd, resulting in the central channel being excluded when determining N. However, it is possible that there may be an uneven number of channels on either side of the channel corresponding to v_{sys}, where one profile half has an extra channel. In such a case, the central channel is included on the side with fewer channels.

6. **Calculate $\mathcal{L}$.** The code begins by considering the profile edge channel pair, represented by ★ markers in Figure 2.2, and ends with the pair closest to the central channel (shown by ♦ markers). The $\mathcal{L}$ parameter is calculated using Equation 2.2, by summing the absolute difference in flux between the channels in each pair and dividing by the sum of the total flux in each channel pair. In summary, for each channel pair, the absolute difference in flux between the channels and the sum of their flux are calculated. The sum of the former for all channels is then divided by the sum of the latter.
7. **Calculate $\sigma_{\mathcal{L}}$.** This follows the same process described in step 6 in §2.1.1: for 100 realisations, Gaussian noise with a mean of zero and σ = rms noise is added to the profile and steps 1-6 are repeated to measure $\mathcal{L}$ for the new profile.

For symmetric profiles, there should be no considerable difference in the values for L and $\mathcal{L}$; while there will be small differences between the flux values of paired channels, these are not expected to result in a large value for $\mathcal{L}$ if the total difference in channels is small in comparison to the total sum of flux in these channels. Similarly for severely asymmetric profiles, L and $\mathcal{L}$ should not significantly differ in their values, especially for profiles where one half of the profile contains considerably more HI flux than the other half*.

It should be noted that the $\mathcal{L}$ parameter is a precursor to the 1D asymmetry statistic used in Deg et al. (2020). The authors demonstrate that the parameter can be calculated using either v_{sys} or the velocity that minimises the measured lopsidedness, which they refer to as the 'velocity of symmetry'. They also show that for low S/N spectra, a background subtraction term is necessary to circumvent inflated values due to noise. As the data used in this work, which are discussed in Chapter 3, have sufficient S/N, the background term is small. In order to compare the values of L and $\mathcal{L}$ in a consistent manner, both parameters are calculated at v_{sys}.

2.2 The 2D case: asymmetry

We now proceed to the 2D domain and present how the 2D asymmetry, introduced in Chapter 1 and governed by Equation 1.4, has been measured in this thesis. In a scenario where the background noise and the emission not associated with a galaxy have been masked out in a galaxy image, the B_{180} term is negligible and Equation 1.4 reduces to

* Such examples are WHISP galaxies UGC 4862 and UGC 5351, whose global HI profiles are provided in Appendix B.

$$A = \frac{\sum_{i,j} |I(i,j) - I_{180}(i,j)|}{2\sum_{i,j} |I(i,j)|}. \tag{2.3}$$

The conditions of the data used in this work, which are discussed in more detail in §3, allow us to make use of Equation 2.3. As such, the methods of calculating the 2D asymmetries described in this section are specific to this data set and are performed on galaxy images which are assumed to have had their background noise masked out and we refer the reader to Conselice et al. (2000) for more information on how the asymmetry of the background, B_{180}, is calculated.

2.2.1 Minimising asymmetry: the centre of symmetry

The task of computing A with a specified centre of rotation (CoR) is fairly straightforward: the initial galaxy image is rotated 180° about the CoR and subtracted from the initial image, after which the sum of the flux in the residual image is divided by twice the sum of the flux in the initial image.

Due to the dependence of the parameter on the CoR, Conselice et al. (2000) motivated for implementing a robust algorithm which would determine the rotation point at which the asymmetry of a galaxy is minimised. We refer to this point as the centre of symmetry, or CoS. With reference to optical studies, this was particularly important as a 1 pixel offset in the CoR chosen could result in a difference of up to 50% for the A parameter measured, depending on the size of the galaxy. However, in extending this work to HI images (see Holwerda et al. 2011b; Giese et al. 2016), the optical centre has been used as the CoR. Below we motivate the decision to follow the approach outlined in Conselice et al. (2000) to compute the minimised A parameter by searching for the CoS in the HI images.

Consider a galaxy involved in a major merger or galaxy-galaxy interaction such that the system is not in dynamic equilibrium. The optical centre of the galaxy is likely to be misaligned from the galaxy's dark matter potential as a result of the interaction and thus bears little relation to the physical distribution of the HI in the galaxy. In this scenario it becomes difficult to disentangle what fraction of the high A value returned for a galaxy is due to the choice of rotation centre and what fraction can be attributed to the HI distribution itself.

It is crucial to establish what the A parameter is expected to be a measure of; if the focus of research is on using the parameter as an indicator of the misalignment of the gas from the stellar distribution of a galaxy, it follows that the optical centre would be an appropriate choice for the CoR. However, the work in this thesis is focussed primarily on the behaviour of A over the duration of a merger, as well as its relation to the 1D measures of anti-symmetry discussed in §2.1. Using the CoS in place of the optical centre as the CoR reduces the likelihood of measuring an inflated A value as a consequence of the CoR chosen. In this way we are measuring the intrinsic asymmetry of a galaxy due

to its shape and light distribution.

Furthermore, determining the deviation between the centres of symmetry for the stellar and HI distributions in galaxies could also serve as an additional quantitative measure to more effectively display the misalignment of these distributions than using the A parameter, measured at the optical centre, in isolation.

Lastly, it is consistent with the work done in optical studies and is the most robust approach to calculate A. Although this thesis focusses primarily on HI data, we would like to consider a multi-wavelength approach to this topic in the long-term. If we intend on calculating various non-parametric measurements across a range of different wavelengths, it is imperative to use the same procedure for each wavelength range.

2.2.1.1 The algorithm

We employ a branching gradient descent algorithm to locate the CoS and compute A. This algorithm is similar to that described in Conselice et al. (2000), but implements an additional step to ensure that the CoS found is the global minimum for the galaxy.

1. **Calculate A at the initial CoR and eight surrounding pixels.** The algorithm begins by computing A at the specified initial CoR. The pixel chosen at the start must lie within the central region of the galaxy. It then calculates A using the eight neighbour pixels as a new rotation centre.
2. **Identify pixel with lowest A and re-centre local neighbourhood.** The nine A values are compared to determine which pixel returns the lowest A within this neighbourhood. This pixel is set as the new reference CoR and step 1 is repeated on the pixels within the new neighbourhood which have not previously been used. This is to avoid re-calculating A and considerably shortens the process.
3. **Locate local CoS.** Steps 1 and 2 are repeated until the central pixel of the neighbourhood is the rotation centre yielding the minimum asymmetry, i.e. the CoS. This is where the algorithm used by Conselice et al. (2000) ends.
4. **Find other possible local minima.** To verify if the CoS found in step 3 is the centre resulting in the global minimum asymmetry of the galaxy, the algorithm branches off to eight distant pixels, equidistant from the CoS, and repeats steps 1-3. If the CoS previously found results in the global minimum asymmetry, the branches from the eight distant pixels should converge.
5. **Compare local minima and repeat step 4 if necessary.** This step is only necessary if more than one local minimum has been found in step 4. Suppose that two branches located a second local CoS. The code compares the values of A for these centres and if the second CoS is the lower of the two, step 4 is repeated. If this is not the case, the process is complete because the branching step has already been performed on the global minimum.

The right panels of Figures 2.3 and 2.4 illustrate how the algorithm performs for WHISP galaxies UGC 7989 and UGC 4862 respectively. With respect to UGC 7989, we can see that the algorithm performed step 4 once, whereas it was performed twice for UGC 4862. For both galaxies it is apparent that the optical centre does not correspond to the CoS.

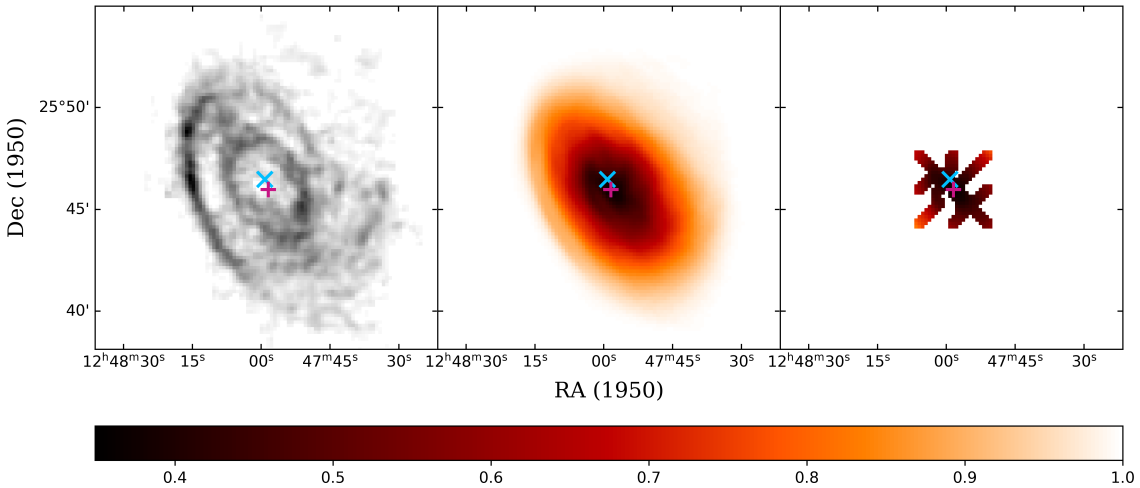

Figure 2.3: HI image of WHISP galaxy UGC 7989 (left panel), asymmetry map of the galaxy (middle) and the region mapped out using our algorithm (right). The blue cross marker corresponds to the starting point and the pink plus marker corresponds to the CoS where the asymmetry is minimised. The colour bar shows the range of asymmetry values in the asymmetry map.

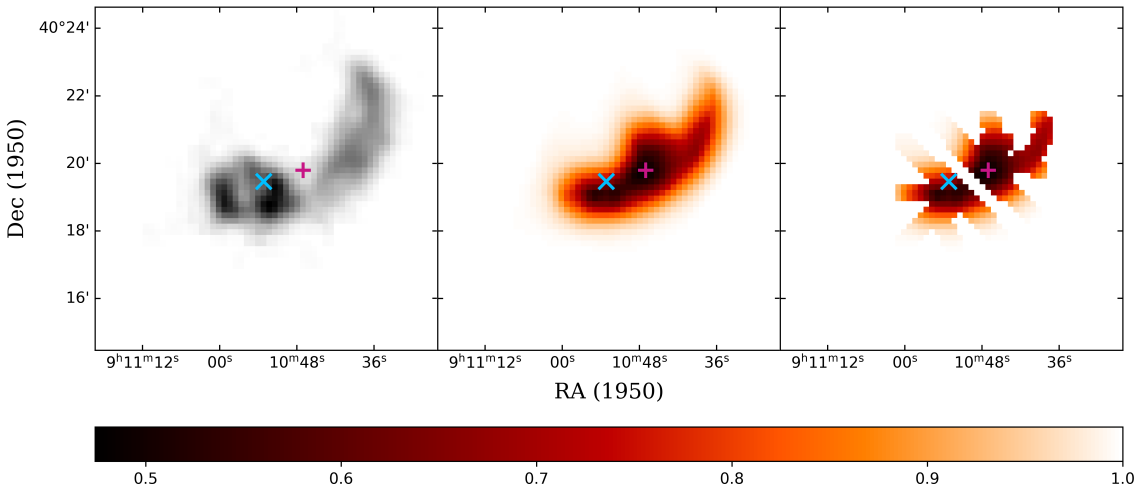

Figure 2.4: HI image of WHISP galaxy UGC 4862 (left panel), asymmetry map of the galaxy (middle) and the region mapped out using our algorithm (right). The blue cross marker corresponds to the starting point and the pink plus marker corresponds to the centre of symmetry where the asymmetry is minimised. The colour bar shows the range of asymmetry values in the asymmetry map.

2.2.2 Outer asymmetry

Although A has been shown in literature to successfully identify major mergers at low redshift (e.g. Conselice 2003; Lotz et al. 2008b; Abruzzo et al. 2018, and references therein),

it is important to note the limitations of the parameter. Due to the fact that A is, by definition, a flux-weighted measurement, the parameter is often dominated by asymmetric features in the bright regions of a galaxy. Fainter features on the outskirts of galaxies, such as tidal tails which are visual indicators of a galaxy-galaxy interaction, tend to have negligible contributions when calculating A due to their low surface brightness. This is because the current formulation of A normalises the difference between the original image and its rotated counterpart by the sum of the flux in the total image. For this reason, Lelli et al. (2014) introduced a new equation to up-weight the outskirts of the galaxy, given by:

$$\mathcal{A} = \frac{1}{N}\sum_{i,j}^{N}\frac{|I(i,j) - I_{180}(i,j)|}{|I(i,j) + I_{180}(i,j)|}. \tag{2.4}$$

Lelli et al. (2014) defined N to be the total number of pixels in the image, but we have adopted the convention of Starkenburg et al. (2016), where N is instead given by the total number of non-zero pixels in the additive image $|I(i,j) + I_{180}(i,j)|$. Equation 2.4 up-weights the contribution of low column density asymmetries because the residual image is now normalised to the local flux density. The intensity-weighted A parameter is essentially a ratio of the sum of the flux in the residual image to the sum of the flux in the original image, whereas the outer asymmetry $\mathcal{A}$ is a sum of the ratio of the residual image to the additive image. Figure 2.5 shows the difference in the asymmetry maps for UGC 4862 using A (left panel) and $\mathcal{A}$ (right panel).

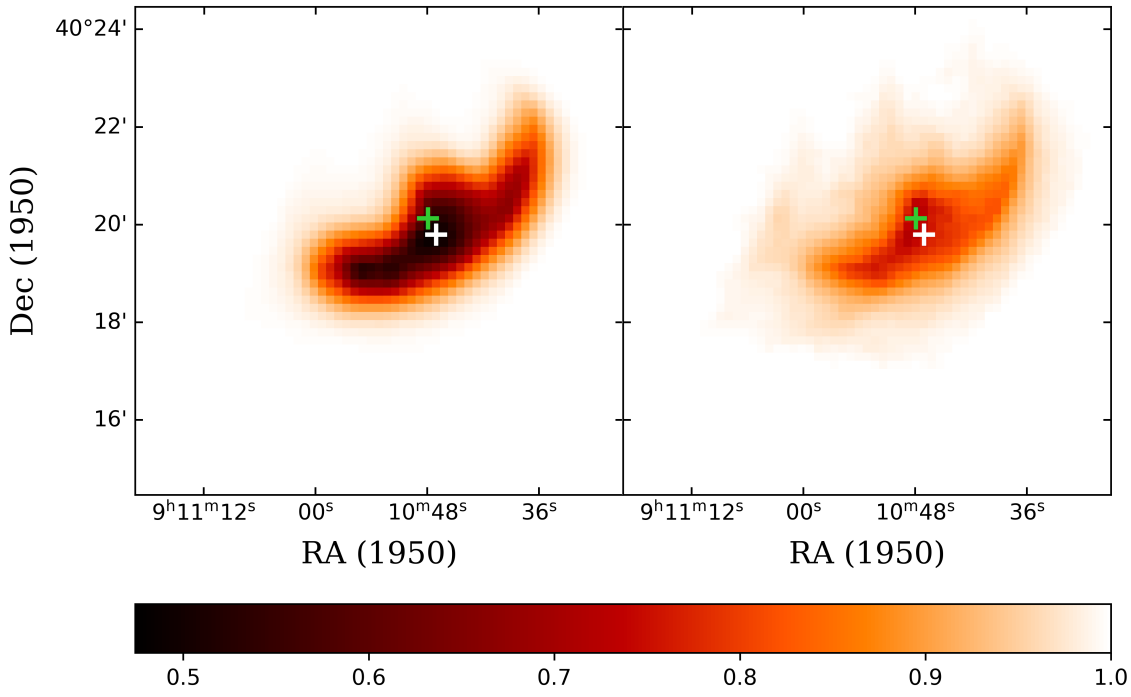

Figure 2.5: Asymmetry maps of the HI distribution of UGC 4862, constructed using Equation 2.3 (left) and Equation 2.4 (right). The white plus corresponds to the CoS for the intensity-weighted asymmetry A and the green plus corresponds to the CoS for the outer asymmetry $\mathcal{A}$. The colour bar shows the range of values in the maps.

From Figure 2.5, it is apparent that the map of outer asymmetry (right panel) extends further than the map of intensity-weighted asymmetry (left panel), and also that the lowest possible value for $\mathcal{A}$ is ~0.2 higher than the minimum for A. It should be noted that this formulation for the outer asymmetry is more susceptible to noise (Lelli et al. 2014).

Chapter 3

Data and simulations

In order to address the questions posed in Chapter 1, this thesis makes use of an idealised simulated galaxy merger event, provided by N. Deg, and archival radio data from the Westerbork HI survey of irregular and Spiral galaxies (WHISP; Kamphuis et al. 1996; van der Hulst et al. 2001). The use of simulations and observations will enable us to investigate galaxy asymmetries from various avenues.

3.1 Galaxy Initial ConditionS (GalactICS)

At present, currently developed 1D and 2D asymmetry parameters suffer from observational effects such as inclination and viewing angle. This is shown in Giese et al. (2016), where the measured 2D asymmetry of a galaxy is found to decrease with increasing inclination for $i > 50 - 60°$. Similarly in the 1D spectral domain, the lopsidedness of a galaxy's 1D global HI profile varies considerably depending on the viewing angle at which the galaxy is observed (Deg et al. 2020). These effects cannot be corrected for in real data, but can be controlled and accounted for in simulations. Furthermore, a galaxy merger cannot be observed in its entirety given the astronomical timescales of such an event. For these reasons, we consider a simulation of an equal-mass galaxy merger event.

3.1.1 Setting conditions

The initial conditions of the simulation are generated using the code GalactICS (Galaxy Initial ConditionS, Deg et al. 2019; Widrow et al. 2008; Widrow & Dubinski 2005; Kuijken & Dubinski 1995) and run using the Gadget-2 N-body code (Springel 2005). While GalactICS was originally designed to construct galaxy models with a bulge, stellar disk and dark matter halo, the most recent version of the code (Deg et al. 2019) builds on its predecessor by incorporating a second stellar disk and an exponential gas disk. The gas disk is implemented using a technique similar to that of the "Potential Method" employed in Wang et al. (2010).

The code begins with initial estimates for the density-potential pairs of the various

components and employs an iterative scheme to obtain a numerical distribution function for the entire system. The total distribution function of the system is given as

$$f(E, L_z, E_z) = f_{halo}(E) + f^*_{bulge}(E) + f^*_{disc}(E, L_z, E_z) + f_{gas}(E, L_z, E_z) \tag{3.1}$$

where E is the energy of the system, L_z is the angular momentum of the axis of symmetry and E_z is the energy associated with the vertical motions of the system (Kuijken & Dubinski 1995; Widrow & Dubinski 2005). The total distribution function and the total density of the system are related via

$$\rho(R, z, \Phi) = \int d^3v f(E, L_z, E_z) \tag{3.2}$$

where the volume density of the system, ρ, can be obtained by integrating Equation (3.1) over all velocities and is expressed in terms of the total potential, Φ, and cylindrical coordinates, R and z. The density of the system can be used to solve for the gravitational potential of the system using Poisson's equation:

$$\nabla^2\Phi = 4\pi G\rho(R, z, \Phi) \tag{3.3}$$

where G is Newton's gravitational constant. In essence, Equations (3.1) and (3.2) are used in an iterative method to solve Poisson's equation until a self-consistent potential-density pair has been obtained for the system.

Since GALACTICS is rooted in constructing galaxies with a specified density profile, it is important to briefly describe the initial density profiles of the components in our model. The target density profile of the bulge is given by:

$$\rho_b(r) = \rho_b \left(\frac{r}{r_b}\right)^{-p} e^{-b(r/r_b)^{1/n}}, \tag{3.4}$$

where r is the spherical radius, n is the Sérsic index and b depends on n. The above equation results in the Sérsic profile for $p = 1 - 0.6097/n + 0.5563/n^2$ (Prugniel & Simien 1997). GALACTICS re-parametrises ρ_b with a one-dimensional velocity dispersion, σ_b, defined as

$$\sigma_b = \sqrt{4\pi n b^{n(p-2)}\Gamma[n(2-p)]r_b^2\rho_b}. \tag{3.5}$$

where Γ is the Gamma function. The advantage of using this definition in place of ρ_b is that σ_b^2 corresponds to the depth of the bulge's associated gravitational potential (Widrow et al. 2008). GALACTICS uses an exponential surface density and a sech^2 vertical profile for the stellar disk. This is given by

$$\rho_d(R, z) = \frac{M_d}{4\pi R_d^2 z_d} e^{(-R/R_d)}\,\mathrm{sech}^2(z/z_d)C(R, R_d, \delta R_d), \tag{3.6}$$

where M_d is the mass of the disc, R_d is the disk scale length, z_d is the disk scale height

and C is a truncation factor described by

$$C(R, R_d, \delta R_d) = \frac{1}{2}\,\mathrm{erfc}\left(\frac{R - R_d}{\sqrt{2}\delta R_d}\right). \tag{3.7}$$

The dark matter halo is modelled using a double-power law:

$$\rho_h(r) = \frac{2^{2-\alpha}\sigma_h^2}{4\pi r_h^2}\frac{C(r, r_h, \delta r_h)}{(r/r_h)^\alpha(1 + r/r_h)^{3-\alpha}} \tag{3.8}$$

where σ_h is the halo scale velocity, r_h is the halo scale radius and α controls the shape of the halo. For $\alpha = 1$, Equation (3.8) produces a Navarro-Frenk-White profile (Navarro et al. 1997).

The gas disk is somewhat more complicated than the other collisionless components as the physics governing the gas must be taken into account when constructing an equilibrium disk. As mentioned earlier in the section, GALACTICS generates the gas disk using the "Potential" method described in Wang et al. (2010). This method creates isothermal disks where the disk scale height increases with radius. The density of the gas disk is given by

$$\rho_g(R, z) = \rho_{g,0}(R)\exp\left(-\frac{\Phi_z(R, z)}{\epsilon(\gamma - 1)}\right), \tag{3.9}$$

where $\Phi_z(R, z) = \Phi(R, z) - \Phi(R, z = 0)$ is the potential difference in the z-direction, γ is the adiabatic index, and ϵ is the specific internal energy. The mid-plane density, $\rho_{g,0}(R)$ can be expressed in terms of the surface density of

$$\rho_{g,0}(R) = \frac{\Sigma_0 e^{(-R/R_g)}}{\displaystyle\int_{-\infty}^{\infty}\exp\left(-\frac{\Phi_z(R, z)}{\epsilon(\gamma - 1)}\right)\mathrm{d}z} \tag{3.10}$$

where Σ_0 is the surface density at the galactic centre. The scale height of the disk, $h(R) = \Sigma(R)/(2\rho_0(R))$, is then calculated using the disk temperature and total potential of the model.

3.1.2 Details of the model

The model we investigate is an idealised equal-mass galaxy merger and so the galaxies are modelled as identical. While GALACTICS can construct galaxy models with two stellar disks (and five components altogether), our model has been generated with one stellar disk and four components in total. The temperature of the gas disk is set to 10^4 K, which is in agreement with the estimated temperature of the warm atomic HI in the Milky Way (Dickey et al. 1978; Ferrière 2001, and references therein). The values of the model parameters described in Equations (3.4) - (3.10) are given in Table 3.1. Each galaxy consists of 8.5×10^5 particles which are distributed as follows: 5×10^5 are halo particles, 5×10^4 are bulge particles, 2×10^5 are stellar disk particles and 10^5 are gas particles. The galaxies are initialised on an approximately radial orbit. At the start of the merger, galaxy

1 is initialised in the xy-plane with zero velocity. Galaxy 2 is initialised with its center at $(50, 280, 0)$ kpc, a velocity of $(10, -50, 0)$ km s^{-1} relative to galaxy 1 and is inclined by 30° from the xy-plane.

The initial conditions of the model were evolved over 5 Gyr using GADGET-2, with the timestep between snapshots set to 0.01 Gyr. Code provided by N. Deg (private communication) was used to create mock data cubes and moment-0 images for the gas and stellar distributions, as well as velocity profiles for the model at each snapshot.

Table 3.1: Model parameters

Parameter	Units	Value
Halo scale velocity, σ_h	km s^{-1}	430
Halo scale radius, r_h	kpc	20
Inner slope, α	-	1
Disk Mass, M_d	M_u	17.2
Disk scale length, R_d	kpc	2.5
Disk scale height, z_d	kpc	0.276
Bulge scale velocity, σ_b	km s^{-1}	204
Bulge scale radius, r_b	kpc	0.64
Bulge Sersic index, n	-	2
Gas disk mass, M_g	M_u	2.5
Gas disk scale length, R_g	kpc	7
Gas temperature	K	10^4

In GALACTICS, a mass unit, $M_u = 2.325 \times 10^9 M_\odot$.

This code allows for the data cubes (and thus moment-0 images) to be centred on a specific component of one (or both) of the galaxies. This is done by iteratively calculating the centre of mass (CoM) using the particles assigned to the chosen component. For this work, all data cubes were centred on the CoM of galaxy 1's gas distribution. The images have been convolved with a point spread function which has been modelled as a 2D Gaussian distribution.

Figure 3.1 shows the moment-0 images of the stellar distributions of galaxies in the model at various snapshots over the 5 Gyr merger event, from the pre-merger galaxies to the post-merger remnant. Figure 3.2 shows the moment-0 images of the gas distributions at the same snapshots shown in Figure 3.1. For both Figures 3.1 and 3.2, galaxy 1 (the central galaxy) is viewed face-on.

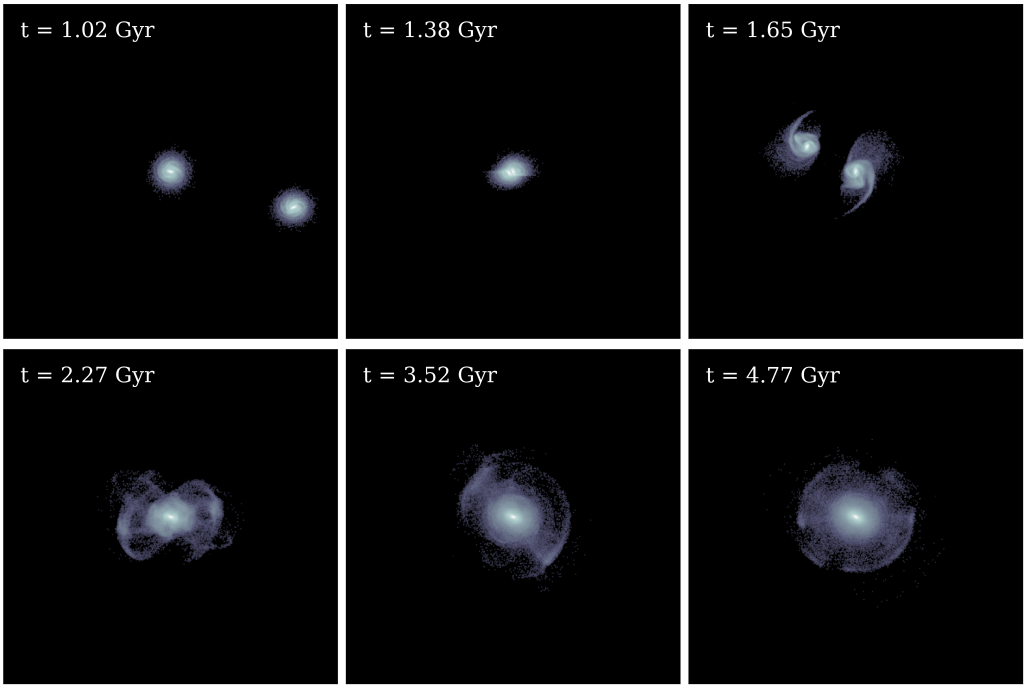

Figure 3.1: Moment-0 images showing the stellar distributions of the galaxies in the GalactICS merger model. Time since the start of the simulation is quoted in the top left corner of each panel. The top row shows the initial pre-merger galaxies (left), the first pass (middle) and the maximal separation after the first pass (right). Shown in the bottom row is the merger of the nuclei (left), the merger remnant 1.25 Gyr after the merger (middle) and the merger remnant 2.5 Gyr after the merger (right).

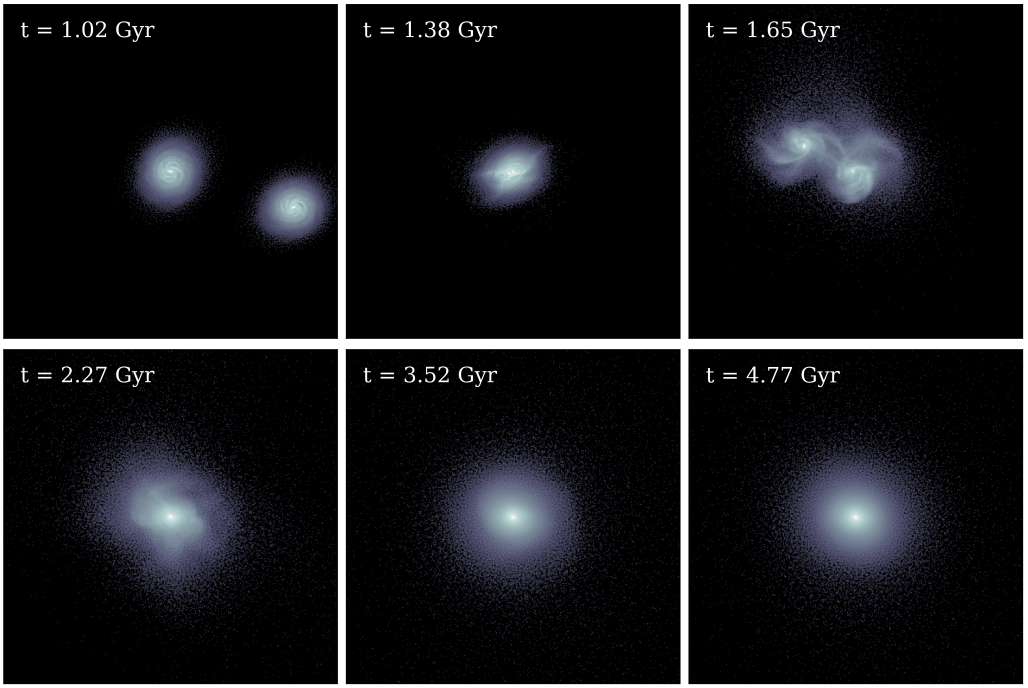

Figure 3.2: Moment-0 images showing the gas distributions of the galaxies in the GalactICS merger model. Time since the start of the simulation is quoted in the top left corner of each panel. The points in the simulation are the same as those shown in Figure 3.1.

3.1.3 Caveats

It is important to take note of the limitations of the simulated merger event. This simulation does not implement star formation or any gas feedback mechanisms. While these are physical processes that would affect the asymmetry of a galaxy's gas and stellar distributions, we are currently focussed on the dynamic scale over which these asymmetries are observed in the extended gas disk and the stellar disk, as well as the difference in reaction times between these distributions. Furthermore, we do not anticipate that these processes will significantly alter these timescales and leave this investigation for future work.

Another limitation is that we are unable to distinguish the species of gas. So while the gas is modelled to be hydrogen, we are unable to distinguish between how the neutral hydrogen (HI) in our model would behave in comparison to the molecular hydrogen (H_2).

Lastly, none of the cubes (and thus images) have been degraded to match real galaxy observations. The degradation of the images would affect the asymmetry measurements calculated but not the behaviour of the measurements over time. Once again, investigating this topic is left for future work.

3.2 The Westerbork HI survey of Irregular and SPiral galaxies (WHISP)

As inferred by the name of the survey, WHISP was an ambitious endeavour to map the HI distribution and its velocity structure of hundreds of nearby galaxies (Kamphuis et al. 1996; van der Hulst et al. 2001) using the Westerbork Synthesis Radio Telescope (WSRT). Prior to WHISP, HI synthesis imaging surveys were limited by necessity to samples smaller than 30 galaxies. The desire to create a documented database of the HI distributions and velocity fields of several hundred galaxies with various morphologies, luminosities and environments served as the scientific motivation for the survey. The main objectives, as articulated in van der Hulst et al. (2001), were to study various aspects of the HI component, such as its structure and kinematical properties, in the local galaxy population and additionally to use HI as a proxy to investigate the dark matter in galaxies, as well as other topics not directly related to HI.

Galaxies in the survey were selected from the Uppsala General Catalogue of Galaxies (UGC, Nilson 1973). The selection criteria for the main observing list were as follows for all targets:

1. declination $\delta(1950) > 20°$. This requirement was to avoid the elongation of the synthesised beam at low declinations because WSRT is an east-west array.
2. major axis apparent size $a > 1.5'$ (B band) to ensure the structure of the HI is sufficiently resolved.

3. The HI flux density $f = F_{\rm HI}/w_{50} > 100$ mJy, where $F_{\rm HI}$ is the integrated HI flux density and w_{50} is the profile width at 50% the peak flux density. Additionally, HI fluxes must have been catalogued in the Third Reference Catalogue of Bright Galaxies (de Vaucouleurs et al. 1991).

At the survey's conclusion in 2002, 375 galaxies had been observed. WHISP is currently the largest targeted HI survey to make its data publicly available.

3.2.1 Data acquisition

The WSRT (Figure 3.3) is a radio interferometer consisting of fourteen steerable parabolic dish antennas, each 25 m in diameter, which are linearly arranged in an East-West configuration. Ten dishes are fixed and four dishes are movable on a railway track to result in a maximum baseline of 2.7 km. WSRT has been subjected to various major upgrades over the years which has enabled the facility to continue contributing to radio astronomy for more than 50 years*.

Figure 3.3: Westerbork Synthesis Radio Telescope (Jackson 2018). In the image, all 14 dishes can be seen from West (bottom left) to East (top right).

* The 50^{th} anniversary of the telescope's completion was celebrated in September 2018 (Jackson 2018).

As already mentioned, data for the WHISP survey have been made publicly available for astronomers around the world to access. Located on the "Westerbork on the Web" (WoW) archive[†], the available data products for each galaxy include radio continuum subtracted data cubes, total HI images and velocity fields at three resolutions: full (~$12'' \times 12''/\sin(\delta)$), intermediate ($30'' \times 30''$) and low ($60'' \times 60''$) resolution.

A full description of the steps necessary to produce data cubes and total intensity maps on the WoW archive can be found on the WHISP webpages. Briefly, the first stage of data reduction is the (u,v) reduction phase, which consists of a self-calibration, a Fourier transform step and re-weighting the (u,v) data in order to obtain different resolution cubes. Table 3.2 lists the map size and pixel size corresponding to each cube resolution. Following the (u,v) reduction of the data, radio continuum is subtracted from the cubes using GIPSY[‡] routines. Next, masks are created using a Hanning smoothed version of the $60''$ cubes. These masks are used to produce the HI images available on the archive. The $60''$ masks are interpolated to fit the full and $30''$ resolution data cubes in order to produce the corresponding images.

Table 3.2: Summary of the three resolutions of data available in the WHISP survey.

Resolution	Map size	Pixel size
$12'' \times 12''$	512×512	$5'' \times 5''$
$30'' \times 30''$	512×512	$10'' \times 10''$
$60'' \times 60''$	256×256	$20'' \times 20''$

3.2.2 Sample selection

The starting sample of galaxies studied in this work is first constructed by an amalgamation of the samples studied by Swaters et al. (2002) and Noordermeer et al. (2005). This sample of 141 galaxies has been used in Holwerda et al. (2011b) and Giese et al. (2016), who were interested in extending the use of the intensity-weighted asymmetry (A) and other non-parametric morphologies to HI data. Swaters et al. (2002) and Noordermeer et al. (2005) visually classified the degree of asymmetry in the global HI profiles and 2D HI distributions of the galaxies in their respective samples, but did not quantify the asymmetries. In contrast, Holwerda et al. (2011b) and (Giese et al. 2016) measured the 2D asymmetries for these samples but used the optical centre as a rotation point. Thus, we chose to study the same sample in order to consolidate and further build on the work in the literature. However, this sample is further reduced to 115 galaxies based on the data preparation steps outlined in §3.2.3. We briefly describe the sample selection criteria used by Swaters et al. (2002) and Noordermeer et al. (2005) in the following sections.

[†] http://wow.astron.nl/

[‡] Documentation on GIPSY (Grongingen Image Processing SYstem) can be found at https://www.astro.rug.nl/~gipsy/

The Swaters et al. sample

Swaters et al. (2002) studied the HI content in a sample of 73 late-type dwarf galaxies, which at the time had been under-represented in HI imaging surveys, and how various HI properties compared to luminous properties. In addition to the 3 selection criteria of the WHISP survey's primary sample, several other restrictions were applied:

- Galaxies with Hubble type later than Sd were chosen. Additionally, galaxies of Hubble Type earlier than Sd but with absolute B magnitude M_b > -17 were then added to the sample.
- Flux density restrictions were imposed to only consider galaxies with $f > 200$ mJy and galactic latitudes $|b| > 10°$.
- The sample was supplemented with galaxies satisfying all the above criteria as well as the first and third criteria of the WHISP sample, which resulted in the inclusion of 4 galaxies and a total sample of 113 galaxies.

In the resulting sample, 40 of the galaxies had HI data obtained by other researchers and thus were excluded, resulting in the final Swaters et al. (2002) sample of 73 late-type dwarf galaxies. The majority of these galaxies were observed in single 12 hour observations between 1992 and 1996, with the exception of large galaxies which required multiple observations.

The Noordermeer et al. sample

The Noordermeer et al. (2005) sample consists of 68 early-type disk galaxies. Due to the morphological type-dependence of the HI of disk galaxies (Roberts & Haynes 1994), the majority of galaxies observed at the start of the WHISP survey were late-type galaxies. Of the ~300 galaxies that had been observed between 1992 and 1998, only 11 systems were early-type galaxies. However, the WSRT underwent a major upgrade in 1999, which improved the sensitivity of the telescope considerably. With the new system, the HI flux limit criterion was reduced to $f > 20$ mJy, which allowed for observations of an additional 57 early-type disk galaxies between 2000 and 2002. This resulted in the final Noordermeer et al. (2005) sample of 68 galaxies. The distribution of morphological types for this sample as well as the sample of late-type dwarf galaxies is shown in Figure 3.4.

3.2.3 Data preparation

In order to calculate the various asymmetry parameters discussed in Chapter 2, we require the 2D images of the galaxies, which are provided on the WoW archive, and the 1D global HI profiles, which need to be extracted from the data cubes. Here we describe the process of preparing the 2D images and extracting the 1D global profiles from the data cube.

When deciding on which resolution of data would be best for this topic, several factors were taken into consideration. Swaters et al. (2002) and Noordermeer et al. (2005) used

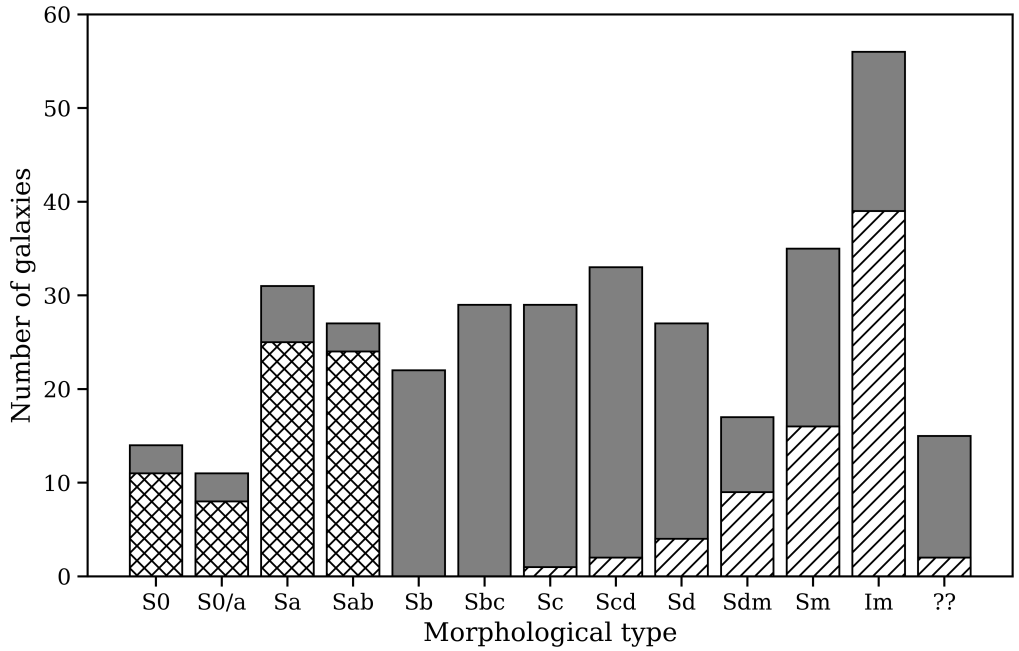

Figure 3.4: Histogram of Hubble types in the full WHISP sample (grey). The cross-hatched area shows the distribution of the sample of early-type disk galaxies presented in Noordermeer et al. (2005) and the diagonally-hatched area shows the distribution of the sample of late-type dwarf galaxies presented in Swaters et al. (2002).

the 60″ data when obtaining the HI profiles since the S/N ratio of extended HI emission is greatly improved at this resolution. In contrast, Holwerda et al. (2011b) and Giese et al. (2016) made use of the full resolution data when calculating the 2D asymmetries. Giese et al. (2016) also found that the measured asymmetry of a galaxy decreases for lower resolutions. Given this dependence on resolution, we want to ensure that we are not artificially inflating the asymmetry as a consequence of the resolution or the per pixel S/N of the data, but also require the HI images to be sufficiently resolved to reliably measure asymmetries in the galaxies. For these reasons, we have chosen to use the 30″ data.

3.2.3.1 Integrated HI maps

The integrated HI maps obtained from the WoW archive required little preparation as the flux not attributed to the galaxies had been preset to NaN. However, a number of galaxies in the sample were observed in the same pointing. In this instance, the HI flux not associated with the galaxy of interest was manually masked out.

In order to isolate a galaxy from the background noise, we had to apply a sigma cut to the image. However, this step of applying a sigma cut is not straightforward, due to the fact that we did not have access to the original masks used to create the HI images and the majority of flux not attributed to the galaxy was set to NaN, as mentioned above. To calculate σ, the rms noise in the image, we only considered the flux below zero in the image. This flux was assumed to be attributed to the noise because the HI emission of the galaxy would only contribute to the positive flux. The modulus of the negative flux was appended to an array containing the negative flux to create a psuedo-Normal

distribution, from which σ was calculated as the standard deviation of this distribution. After all NaN-valued pixels were set to zero, a 1σ cut was applied to the image to exclude any noise from the image. The resulting images were used to calculate the 2D asymmetry as described in Chapter 2.

3.2.3.2 Global HI profiles

Due to the fact that the 1D spectra of the galaxies are not available on the WOW archive, we had to extract the spectra from their HI data cubes before we could measure their asymmetries. This process is described below.

1. To determine any "bad" channels and calculate the rms noise in each cube, 4 random pixels were chosen towards the edges of each cube, where they were guaranteed to contain no HI flux from the galaxy. The flux of these pixels were plotted as a function of channel number. In most cases, the channels toward the beginning and end of the cube displayed erratic behaviour and as a result were excluded from the data. Figure 3.5 displays the spectra of the four locations from the data cube of UGC 5721, before and after cropping the channels. For each galaxy, the number of channels excluded from each end of the cube was chosen individually, depending on the spectra of the pixels.

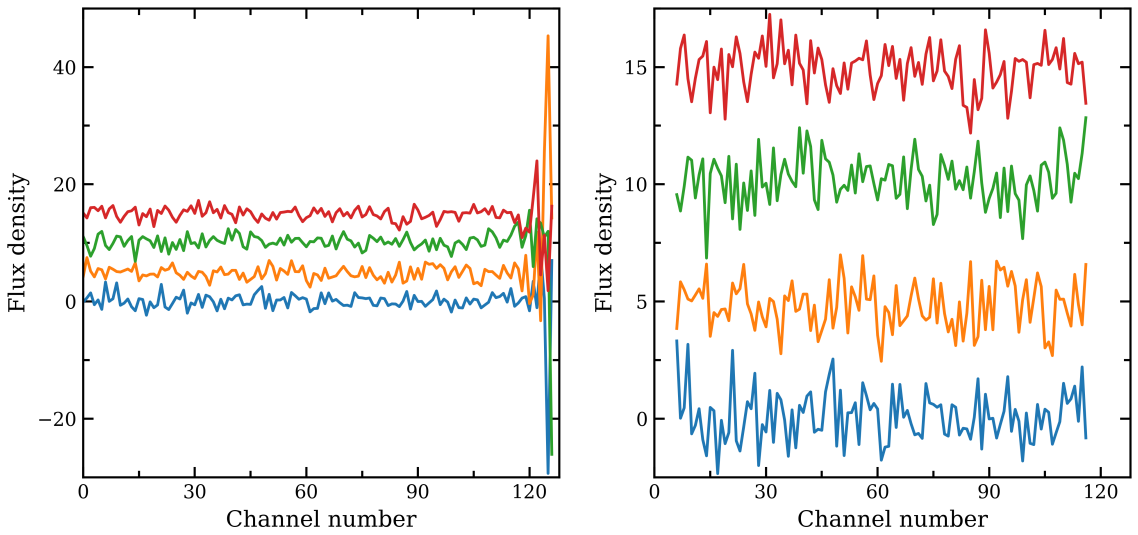

Figure 3.5: Spectra of the four locations in the cube of UGC 5721 as a function of channel number. The left panel displays the spectra across all the channels in the cube, and the right panel displays the result after cropping the channels from the start and end of the cube. In both panels, the spectra have been offset from each other vertically for clarity.

2. The rms noise in the cube, σ_{cube}, was determined by calculating the standard deviation of the distribution of flux in these four reference pixels. Using this result, we created a mask that would only consider voxels with an intensity $> 2\sigma_{cube}$, as used in Noordermeer et al. (2005). While this mask removed most of the noise from the

cube, there were still some noise peaks which were included with the emission from the galaxy.

3. The initial 3D masks used by WHISP are not made available on the WoW archive. As such, we generated our own masks in order to extract the HI spectra. This was done using the 2D image as a spatial mask on the 3D cube and extending it through all channels. This mask was then applied to the cube to exclude any flux that did not fall within the regions of flux in the HI image. This result is shown in Figure 3.6 for UGC 5721. As observed in the figure, the left panel contains extra flux from the cube that is not present in the right panel, but this low level flux will be accounted for in step 5.

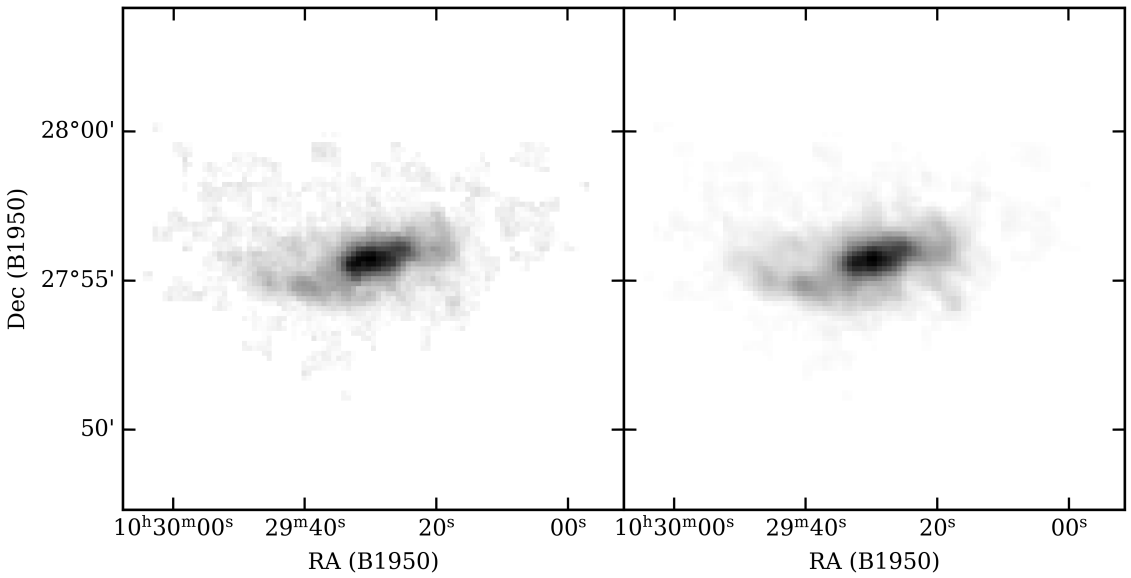

Figure 3.6: Comparison between the moment-0 image of the cube of UGC 5721 after all masks have been applied by us (left panel) and the published image of the same galaxy (right panel).

4. Using the region shown in the left panel of Figure 3.6, the spectrum was extracted by summing the flux in each channel. The result is shown in the left panel of Figure 3.7 for UGC 5721. For reference, the horizontal zero flux line has been included in the figure.
5. The final step was to correct for any offset of the spectrum. With reference to the left panel of Figure 3.7, upon close inspection, the spectrum appears to lie on a linear baseline above zero. This is due to voxels being included in the 3D mask which are not necessarily associated with the galaxy (as mentioned in step 3). For certain galaxies, this correction was done manually, by selecting regions of the spectrum outside the peak positions, and fitting a straight line to these regions. This average flux value was then subtracted from the spectrum so that the baseline of the spectrum was set to zero. For the majority of galaxies, the outer regions were selected using the w_{50} values provided in Swaters et al. (2002) and Noordermeer et al. (2005). The result of the subtraction for UGC 5721 is shown in the right panel of Figure 3.7.

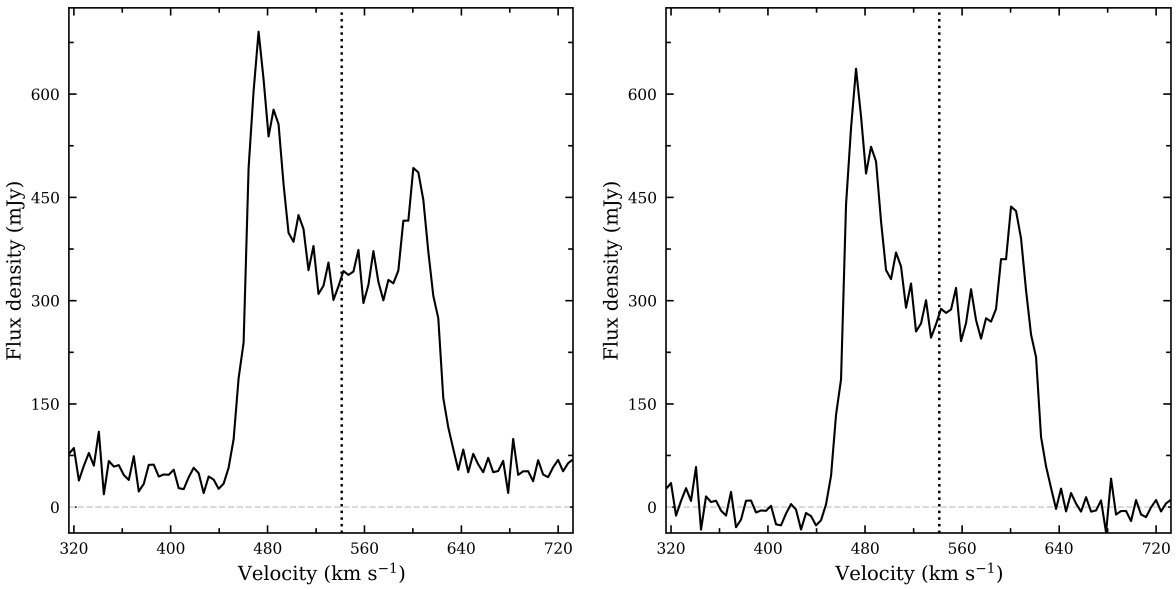

Figure 3.7: Extracted HI spectrum of WHISP galaxy UGC 5721 before (left) and after (right) the pedestal subtraction described in step 5. The zero flux line is shown by the dashed grey horizontal line. The dotted black vertical line corresponds to the calculated systemic velocity.

These steps were performed for all galaxies in the sample. If it was not possible to separate interacting galaxies in §3.2.3.1, the spectra of the galaxies were not extracted. Similarly, if there was no discernible profile in the spectrum when it was extracted, or the pedestal subtraction could not be performed in a reliable manner, the galaxy was removed from the sample and no attempt was made to calculate the 1D lopsidedness parameters. Of the 130 galaxies studied by Giese et al. (2016), 15 galaxies were excluded based on these conditions, leaving us with a sample of 115 galaxies which are listed in Table A.1.

Chapter 4

The evolution of asymmetry during a simulated merger

This chapter presents the results of the simulated merger event described in Chapter 3. The first section pertains to the time-scales over which these asymmetries are observed in the gas and stellar distributions of the central galaxy and explores the difference in behaviour of the two 2D asymmetry measurements. In the second section we explore the relationship between the 1D and 2D asymmetry parameters for the gas distribution of the central galaxy.

4.1 Evolution of the gas and stellar distributions

In this section we explore two questions: how do the 2D asymmetry parameters evolve for the gas and stellar distributions of a disk galaxy undergoing an equal mass galaxy merger, and which of these parameters is better at tracing the various stages of the merger?

Separation of the galaxies

It is important to briefly describe how the galaxies in the simulation were separated over the 5 Gyr merger event. With observations, an ideal approach would be to use spatial and spectral information about the interacting galaxies in order to separate them. For the merger model considered in this thesis, the velocity vector is perpendicular to the line-of-sight of the observers. As a result, there is no spectral separation between the galaxies and so we can only utilise spatial separation.

The method used in this work takes advantage of the fact that the galaxies are identical in mass and light distribution. The centre of brightness (CoB), or barycentre, of a system is located at position

$$x_{CoB} = \frac{\sum_{i,j} I(i,j) \cdot x_i}{\sum_{i,j} I(i,j)}, \; y_{CoB} = \frac{\sum_{i,j} I(i,j) \cdot y_j}{\sum_{i,j} I(i,j)}. \tag{4.1}$$

For two identical galaxies in an image, the CoB should lie at the midpoint between the galaxies depending on the distribution of their light. At each snapshot, the CoB for the specific distribution (gas or stars) was calculated. A straight line was constructed joining the CoB of the system and the brightest pixel of galaxy 1, since this was the galaxy on which the images were centered. A second straight line, perpendicular to the first and passing through the CoB, was used to separate the galaxies and is shown in Figure 4.1 at T = 1.1 Gyr, prior to the interaction when the galaxies are still clearly separated, and at T = 1.6 Gyr, after the first pericentric passage of the galaxies. The lines separating the galaxies can be different for the gas and stellar distributions as they depend on the CoB and brightest pixel of the specific distribution.

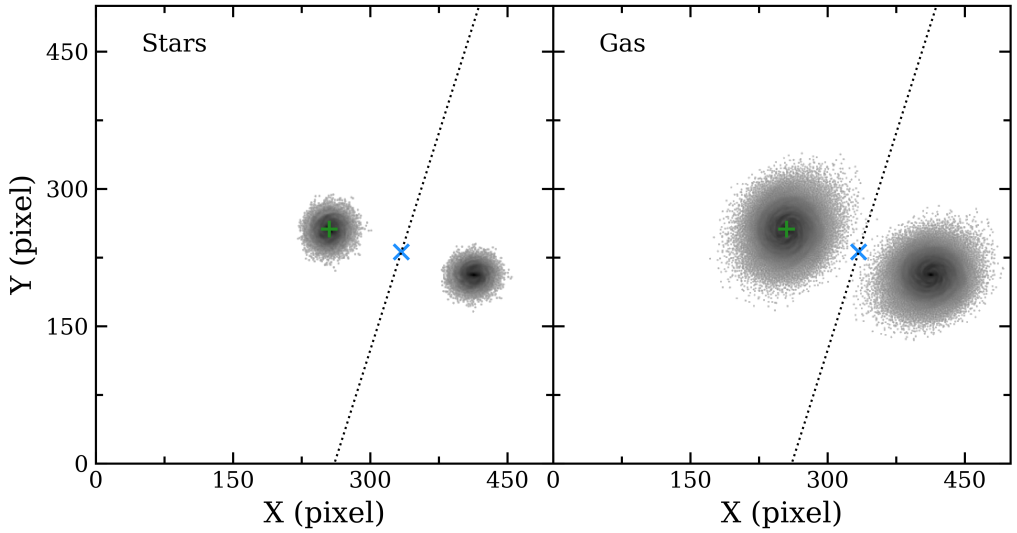

(a)

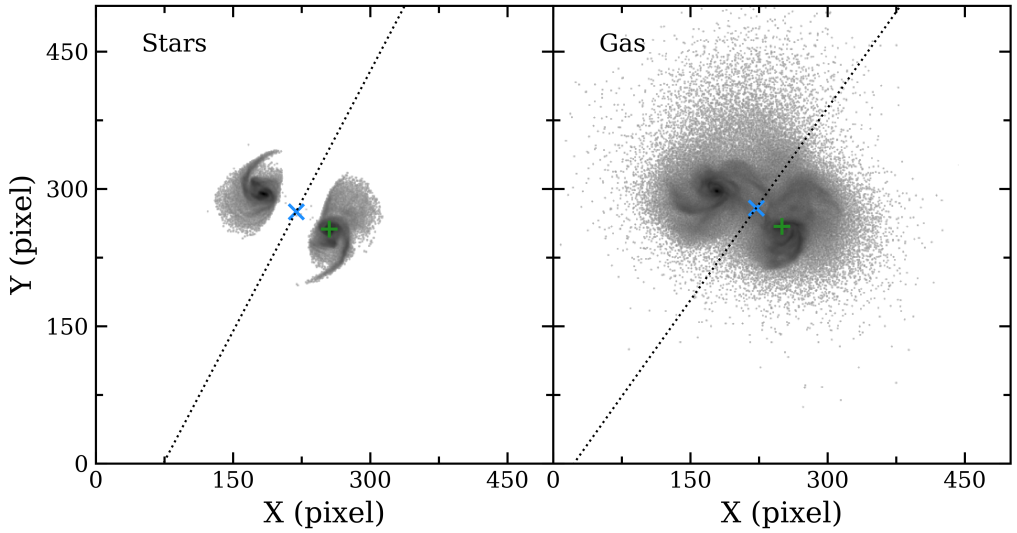

(b)

Figure 4.1: (a) Moment-0 images of the stellar (left) and gas (right) distributions of the galaxies in the merger model at T = 1.1 Gyr. (b) Same as (a) but at a time-step of T = 1.6 Gyr. The green plus markers show the brightest pixels in the gas or stellar distributions of the central galaxy, and the blue cross markers indicate the CoB for the respective systems.

In the early stages of the merger, save for the periods leading up to and shortly after the first and second passes, the stellar distributions of the two galaxies are clearly distinguishable prior to the merger of the nuclei at T = 2.27 Gyr. As such, our method of separating the galaxies is for the most part acceptable as a first attempt. In contrast, it is evident from the right panel of Figure 4.1b that the gas distributions of the galaxies in the stages after the first pass are more difficult to divorce from one another. However, we believe that this technique is still appropriate given the data available and separates the galaxies in a consistent manner. Furthermore, the decision to implement this separation as opposed to considering a galaxy's individual gas component, as tagged in the simulations output, is that it is more realistic from an observational perspective. This is important because as the merger progresses, gas on the outskirts of either galaxy gets captured by its companion and in real observations, this captured gas would not be spatially distinguishable from the other galaxy. Although tailored simulations enable us to look at the gas components of these galaxies in isolation, doing so would lead us to consider stripped gas which is no longer a part of the galaxy.

4.1.1 2D asymmetries as diagnostics for merger stages

In order to investigate how the gas and stellar distributions behave over the duration of the merger, we make use of the intensity-weighted asymmetry and outer asymmetry parameters (A and $\mathcal{A}$ respectively) to measure the disturbances in their morphologies. In this section, we are particularly interested in the performance of the 2D parameters and their ability to quantify the asymmetries formed in these distributions during the merger.

The 2D parameters were calculated at their centres of symmetry for the two distributions of both galaxies at all snapshots where the nuclei of the galaxies could be clearly identified. Where the nuclei of the galaxies could not be distinguished, the asymmetry parameters were not calculated. This occurred between time-steps of 1.36 – 1.45 Gyr and again at 1.93 – 2 Gyr, which correspond to the periods during the first and second passes of the galaxies respectively. In these two regions, we opted to not calculate the parameters instead of treating the two galaxies as a single object. Since the galaxies are modelled as identical objects, re-introducing the stellar or gas distributions of the companion galaxy and treating the galaxies as a single object will result in a drastic decrease in the measured parameters. This is because A and $\mathcal{A}$ are calculated at the centres at which they are minimised and so asymmetric features mirrored in both galaxies will effectively cancel each other out.

From T = 2 Gyr, the parameters are calculated for the entire system despite the coalescence of the nuclei, which we define to occur when the nuclei are within 1 kpc of each other (Lotz et al. 2008a; Abruzzo et al. 2018), only taking place at T = 2.27 Gyr. Although this appears to be in contradiction to what was stated regarding the periods of the first and second passes, this decision was made for a number of reasons. With reference to the far right panels in the first rows of Figure 3.1 and Figure 3.2, which

show the stellar and gas distributions of the galaxies at maximal separation after the first pass, the nuclei of the galaxies are separated by distances greater than 60 kpc. In contrast, the maximal separation between the galaxies is less than 5 kpc between $2-2.27$ Gyr. Furthermore, we would like to explore any considerable change in the measured parameters at the time-step corresponding to the coalescence of the nuclei, which requires us to measure the parameters for the same system leading up to the nuclei merging.

Shown in Figure 4.2 is the evolution of the intensity-weighted asymmetry A and the outer asymmetry $\mathcal{A}$, represented by the solid and dotted lines respectively, with time for galaxy 1. The colour of the lines indicate the distribution used to measure the parameters: the red lines show the asymmetry parameters measured for the stellar distribution, and the blue lines show the parameters measured for the gas distribution. The vertical black dashed lines demarcate the time periods where the asymmetry parameters were not computed due to the indistinguishability of the galactic nuclei.

Before examining the overall behaviour of the measured 2D parameters, it is important to take stock of several features present in Figure 4.2 and the possible causes of these features. We adopt the convention used in Lotz et al. (2008a) and Abruzzo et al. (2018) to divide the merger event into six stages: pre-merger, first pass, maximal separation, final merger, post-merger and lastly, merger remnant. Table 4.1 provides the definitions of the starting time-step for each merger stage as well as the corresponding time-steps in our merger event. With the exception of the pre-merger stage, which starts at T = 0 Gyr, and the final stage which ends at T = 5 Gyr, the remaining stages begin at the time-step listed in Table 4.1 and end at the time-step of the succeeding stage. The limits of the merger stages, as described in Lotz et al. (2008a), are dependent on one or more of the following time-steps when pivotal events in the merger take place:

- t_{fp} - the moment of closest approach during the first pass of the galaxies,
- t_{max} - the maximal separation of the galactic nuclei after the first pass, and
- t_{merg} - the coalescence of the nuclei.

For this specific merger event, we find that $t_{fp} = 1.38$ Gyr, $t_{max} = 1.65$ Gyr and $t_{merg} = 2.27$ Gyr. The definitions of the various stages have been specified in such a way so as to ensure that the event (or period) after which the stage is named occurs during the stage. For example, while the first pass stage in this merger is defined as the period from 0.69 Gyr $<$ T $<$ 1.52 Gyr, the first pass itself takes place at T = 1.38 Gyr. The starting time-steps of the merger stages listed in Table 4.1 are indicated by black arrows in Figure 4.2.

Let us consider the first two stages of the merger, which occur in the first 1.52 Gyr of the merger event. One prominent feature in Figure 4.2 is the apparent series of peaks and troughs in the intensity-weighted asymmetry parameter measured for the stellar distribution, A_S. This trend begins 0.38 Gyr into the merger and is fairly regular in amplitude until the first pass of the galaxies, after which it continues but is considerably more erratic.

Table 4.1: Definitions of the merger stages and their corresponding time-steps in the simulated merger event.

Merger Stage	Definition	Time (Gyr)
First Pass	$0.5(t_{fp})$	0.69
Maximal Separation	$0.5(t_{fp}+t_{max})$	1.52
Merger	$0.5(t_{max}+t_{merg})$	1.96
Post-merger	t_{merg}+0.5 Gyr	2.77
Remnant	t_{merg}+1 Gyr	3.27

With reference to A measured for the gas distribution, A_G, a similar trend is observed in that A_G also appears to experience numerous peaks and troughs, but these occur over a longer cycle and are less regular with time than those observed in A_S. In contrast, there is considerably less variability in the amplitude of the outer asymmetry parameters for the gas and stellar distributions, $\mathcal{A}_G$ and $\mathcal{A}_S$ respectively, prior to the first pass of the galaxies. Although there appears to be slightly periodic behaviour in $\mathcal{A}_G$, this occurs over a much longer timescale than what we observe in A_G and A_S. This suggests that the cause of the oscillatory behaviour lies in the central regions of the two distributions.

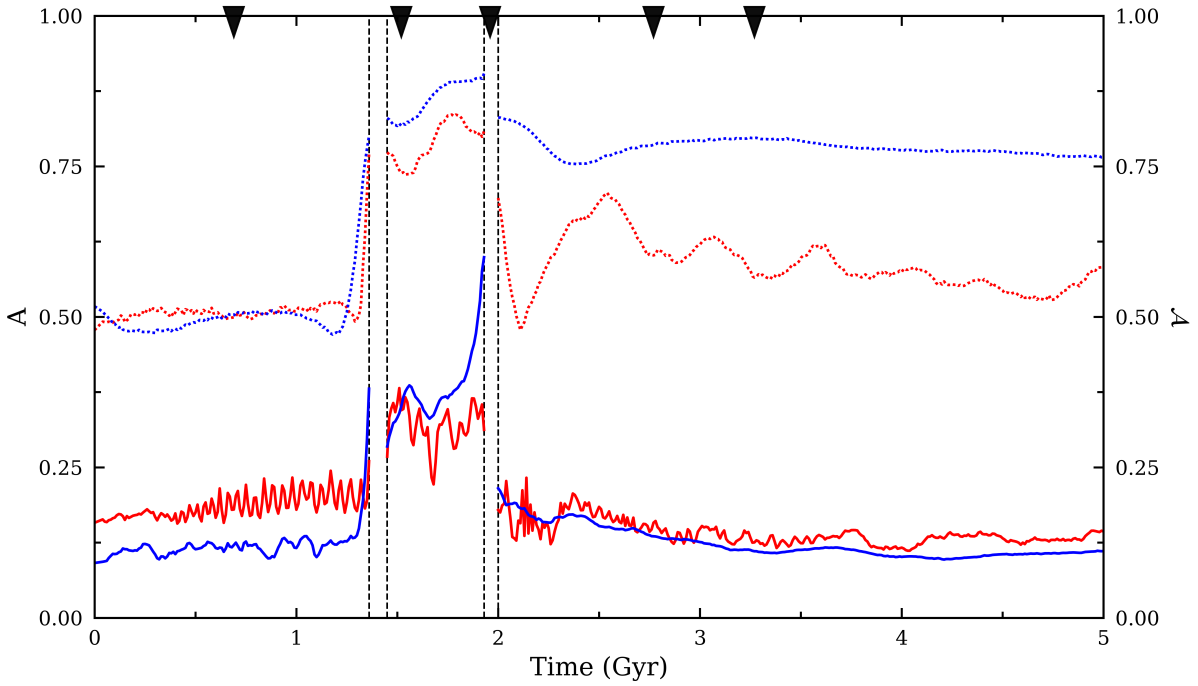

Figure 4.2: Temporal evolution of the 2D asymmetry parameters A (solid lines) and $\mathcal{A}$ (dotted lines) for the central galaxy of the simulated merger model. The red lines correspond to the asymmetry parameters measured for the stellar distribution at each time-step and the blue lines to the gas distribution. The black dashed lines indicate the periods leading up to, and shortly after, the first and second passes in the merger event where the galaxies could not be separated. The black arrows mark the transitions between the merger stages listed in Table 4.1.

These attributes are likely due to the formation of the spiral arms in the inner regions of the galaxy, as well as the formation of the bar in the stellar distribution. Upon inspecting

the images of both distributions, we find that the stellar bar forms around the same time-step at which A_S begins to exhibit this behaviour. The bar completes one rotation about the galactic centre in ~0.18 Gyr, and in that same time period A_S has 4 cycles. We can infer that the peaks in A_S correspond to time-steps when the bar is maximally antisymmetric relative to the spiral arms of the galaxy and the troughs to time-steps when the bar is minimally antisymmetric relative to the spiral arms. Although there appears to be a bar-like structure in the centre of the gas disk, it is relatively short-lived and less pronounced compared to the stellar bar. The irregularity in A_G as well as $\mathcal{A}_G$ is likely due to the spiral structure in the gas disk, which is more extended, rotates over a longer period, and is subject to small-scale changes prior to the first pass.

Another prominent feature in this period of the merger is the drastic increase in value seen with all four parameters shortly before the first pass of the galaxies. The outer asymmetry parameters experience a slight dip in value prior to this increase, which occurs when the edges of the gas and stellar disks of the galaxies make physical contact with one another. The discrepancy in response times for $\mathcal{A}_G$ (1.2 Gyr) and $\mathcal{A}_S$ (1.29 Gyr) is due to the gas disk being more extended than the stellar disk and as a result, $\mathcal{A}_G$ registers the oncoming interaction 0.09 Gyr before $\mathcal{A}_S$. Since the centres of the gas and stellar distributions are aligned and the intensity-weighted asymmetry has been shown to be dominated by the central regions, we would expect A_G and A_S to register the first pass around the same time. Nevertheless, we observe the same trend in differential response times with the intensity-weighted A, where A_G also begins its steep increase before A_S (1.28 Gyr vs. 1.34 Gyr), although the difference in response times for these parameters is 0.06 Gyr. However, it is important to take into consideration that the dependence of A_S on the stellar bar period is possibly responsible for the late response of A_S to the first pass. Of the four parameters, $\mathcal{A}_G$ experiences the most drastic increase leading to the first pass, followed by $\mathcal{A}_S$, A_G and lastly, A_S. At this point of the merger event, the behaviour of A and $\mathcal{A}$ indicates that the gas distribution shows the effects of the first pass before the stellar distribution. Additionally, Figure 4.2 shows that the gas distribution becomes more asymmetric than the stellar distribution as the interaction continues.

Proceeding to the maximal separation stage, which takes place from 1.52 - 1.96 Gyr, it is evident that these parameters exhibit substantially more erratic behaviour than they did during the two previous stages. Given the continued variability of A_S, we can infer that the bar is still present in the stellar distribution. We also find that the parameters experience a local minimum during the maximal separation stage, which occurs at an earlier time-step for $\mathcal{A}$ of both distributions than A (1.54 Gyr vs. 1.65 Gyr). Shortly after the first pass, the gas and stellar distributions are more asymmetric than they were in the pre-merger stage, but are still relatively compact in shape. However, as the galaxies advance towards the time-step where their nuclei are maximally separated, these distributions become more extended. Recall that $\mathcal{A}$ is formulated to normalise the flux density of the outer emission. Thus, it is unsurprising that the local minima of $\mathcal{A}_G$ and $\mathcal{A}_S$ occurs earlier in this stage when there are fewer non-zero pixels to consider, whereas

A_G and A_S experience their minima at a later point because these extended, asymmetric outer regions are more diffuse and lower in surface brightness, and therefore contribute less to the calculation of A.

Beyond these local minima, both A and $\mathcal{A}$ indicate that the gas distribution is more asymmetric than the stellar distribution for the remainder of this stage. Leading up to the second pass, A_G is the only parameter that registers the interaction in the same manner as the first pass. In comparison, A_S does not appear to be affected, $\mathcal{A}_S$ displays its global maximum at 1.78 Gyr before decreasing, and $\mathcal{A}_G$ has a more subdued increase preceding the second pass. Moreover, the global maxima of A_G and $\mathcal{A}_G$ occur at the final time-step in this stage*, which suggests that the gas distribution is at its most asymmetric state leading up to the second pass.

We observe a decrease in the measured parameters at the start of the merger stage (1.96−2.77 Gyr). This decrease is especially severe with the intensity-weighted asymmetry parameters. Recall that in this stage (and the succeeding stages) of the merger, the parameters are calculated for the entire system, although the coalescence of the nuclei takes place later in the stage. Treating the system as a single object is also suspected to be the cause of the behaviour of $\mathcal{A}_S$ at the start of this stage. Since the galaxies are modelled identically, asymmetric outer regions are likely mirrored in both stellar distributions and are minimised when computing $\mathcal{A}_S$ for the whole system. As a result, the value of $\mathcal{A}_S$ leading up to T = 2.1 Gyr suggests that the outer stellar distribution becomes relatively symmetric when the visual appearance indicates otherwise. Likewise, A_S appears to be considerably more unsettled than the other measured parameters at this point of the interaction. It is possible that the bar, albeit weaker in strength, is still present in the stellar distributions of both galaxies, and that the variability of A_S is then due to the orientation of the bars relative to one another.

As expected, the intensity-weighted parameters are most affected by the merging of the nuclei at T = 2.27 Gyr, given that both parameters display a local minimum at this time-step. In contrast, $\mathcal{A}_G$ continues to steadily decrease from the start of this stage and exhibits a local minimum 0.1 Gyr after the coalescence, whereas $\mathcal{A}_S$ displays the opposite behaviour to $\mathcal{A}_G$ and has a local maximum at 2.54 Gyr. Surprisingly, we find that A_S continues to display oscillatory behaviour in this stage, despite the destruction of the bar. This trend, which we observe to be irregular with time, is noticeably weaker in amplitude compared to what was observed in the first two stages of the merger event. To investigate whether this behaviour is possibly due to transitory asymmetric features present in the central region of the stellar distribution, we inspected the moment-0 images and their residual images at three time-steps where A_S displayed a local minimum or maximum: T = 2.47, 2.5 and 2.53 Gyr. The images at these time-steps, shown in Figure 4.3, as well as those in between, have the same CoS in pixel space and so we can eliminate the

* Recall that the final time-step in this stage at which the parameters are calculated is at 1.93 Gyr, despite the stage ending at 1.96 Gyr.

position of the CoS moving as a possible cause for this behaviour.

From inspecting the residual images, it is apparent that the shell-like structure observed in the mock images is slightly asymmetric relative to the CoS because it is still present in the residual images at the three time-steps shown in Figure 4.3. However, the row of pixels that stretches across the centre of the nucleus is the likely cause for the variation in A_S. This row of 4/5 pixels, which is seen in the residual images at T = 2.47 and 2.53 Gyr, is on average an order of magnitude lower than those in the residual image at T=2.5 Gyr. To confirm if this is the cause for the discrepancy in value, we applied a circular mask with a radius of 5 pixels and centred on the CoS at these time-steps, to exclude any flux contained within this region. This radius size, shown by the red circle in Figure 4.3, was chosen so as to avoid excluding too much of the central region. After applying this mask, A_S was recalculated at the three time-steps in the same manner as previously. Despite excluding the brightest region of the galaxy, we find that that CoS remains at the same pixel for each time-step considered. We also find that the value for A_S decreases, but that the absolute differences in A_S for these three time-steps decrease from ~0.018 to ~0.002. Thus, these small variations in A_S are due to pixel variations in the galactic centre of the merger system.

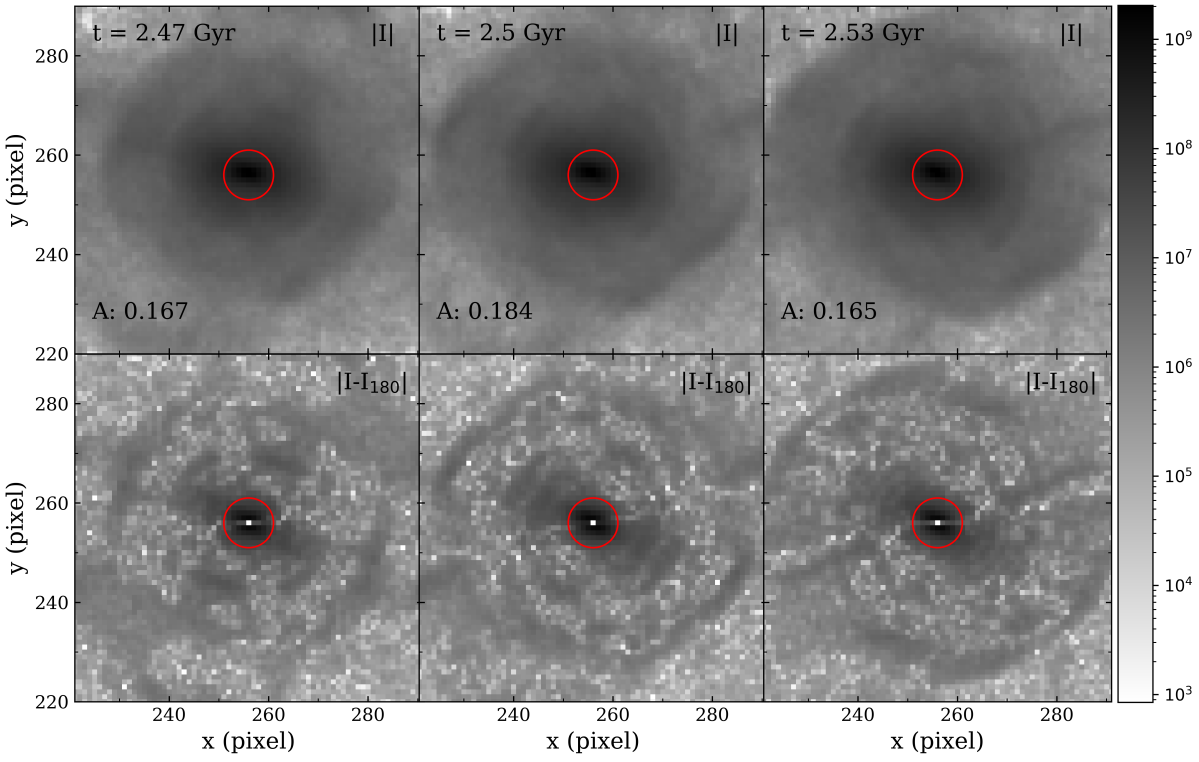

Figure 4.3: Moment-0 images of the central region (top row) in the stellar distribution of the system at three time-steps in the merger stage, and their corresponding difference images (bottom row). The time-step of each snapshot is quoted in the top left corner of each moment-0 image and the intensity-weighted A parameter is quoted in the bottom left corner. The red circle represents the boundary of the circular mask.

Lastly, we consider the post-merger and merger remnant stages together, as the param-

eters do not appear to exhibit significantly different behaviour in these final stages of the merger event. We observe the irregular variations in A_S continue throughout both stages, although it becomes far less frequent with time after ~T = 3.7 Gyr. We also find that $\mathcal{A}_S$ exhibits what appears to be damped oscillatory behaviour, beginning in the merger stage and subsiding shortly before T = 4 Gyr. This trend, which occurs over a fairly long cycle (~0.52 Gyr), is due to various tidal features which materialise in the outer regions of the stellar distribution as the system recovers from the merger. These tidal debris, shown in Figure 4.4 for three time-steps corresponding to two local minima (2.8 Gyr and 3.32 Gyr) and a local maximum (3.06 Gyr) in $\mathcal{A}_S$, experience periods in which they are more pronounced and asymmetric relative to the CoS. These features become less asymmetric as the average value of $\mathcal{A}_S$ appears to decrease with time.

It is apparent that the average values of these parameters decrease over the course of these two stages. This is not a surprising result as we expect the parameters to approach a constant amplitude once the merger remnant has settled. At the end of the merger event, the intensity-weighted parameters are much closer in amplitude than they were at the start of the merger, whereas the outer asymmetry parameters are distinctly separated in amplitude in the final stages of the merger.

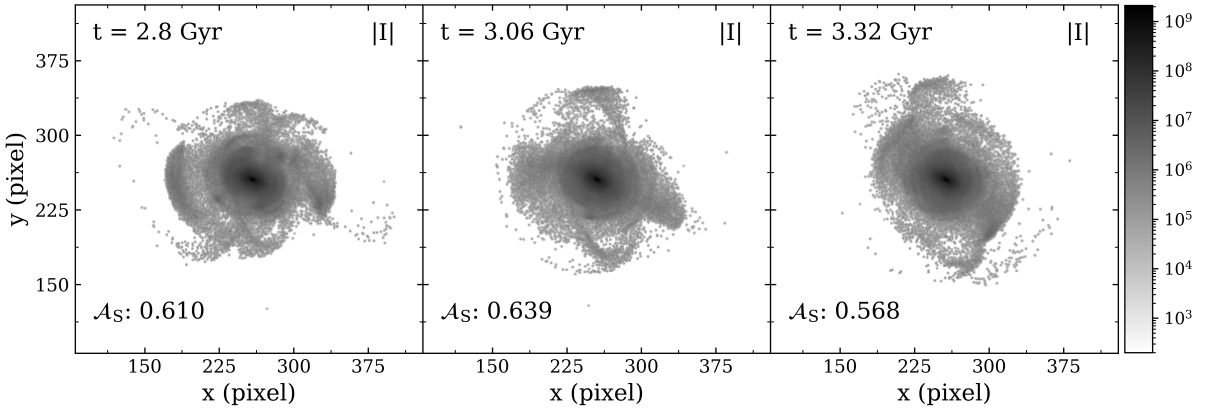

Figure 4.4: Moment-0 images of the stellar distribution of the system in the post-merger stage at three time-steps. The time-step of each snapshot is quoted in the top left corner of each moment-0 image and the outer asymmetry parameter $\mathcal{A}$ is quoted in the bottom left corner.

Having assessed the various features present in Figure 4.2, we are now in a position to examine the general behaviour of the four parameters over the entirety of the merger event. At every time-step in the merger, the outer asymmetry measured for a particular distribution is higher than the intensity-weighted asymmetry measured for that same distribution. This could possibly be the result of not applying any column density cuts when computing the parameters. Nevertheless, these results suggest that the outer asymmetry generally returns higher values than the intensity-weighted asymmetry.

At the start of the merger event, $\mathcal{A}_G$ and $\mathcal{A}_S$ begin with similar values and this continues until the lead up to the first pass. After this first interaction, and for the

remainder of the merger event, these two parameters are distinctly separated. On the contrary, A_G and A_S exhibit an average absolute difference of $\delta A \approx 0.06$ during this same period of the merger. Prior to the first pass, the average amplitudes of all parameters are fairly constant with time, with the stellar distribution appearing more asymmetric than the gas distribution.

The behaviour of both A and $\mathcal{A}$ parameters suggests that the gas distribution registers the passes before the stellar distribution is affected. With both distributions, $\mathcal{A}$ reacts to the first pass at least 0.05 Gyr before A, and only the gas distribution appears to effectively register the second pass. We also find that all parameters are, on average, higher in value than they were before the first pass, and that they display their global maximum during the maximal separation stage.

All the parameters exhibit a decrease in amplitude after the second pass, which is primarily due to the inclusion of particles from the second galaxy involved in the merger. However, it is crucial to note that despite this decrease, the average outer asymmetry for both distributions remains at a higher signal during (and post-) merger, whereas the average intensity-weighted asymmetries return to their pre-merger values. As a result, $\mathcal{A}$ is better at distinguishing between the pre-merger galaxy and the post-merger remnant. In particular, $\mathcal{A}_G$ appears to be a good tracer of this equal mass galaxy merger event as it is able to register the oncoming interaction before any of the other parameters and it displays noticeably different values in the merger remnant than in the pre-merger stage.

The joint use of A and $\mathcal{A}$ could be used as a diagnostic tool for which merger stage a galaxy might be in if we consider three stages: pre-merger, interacting, and post-merger. Specifically with reference to the gas distribution in this galaxy, low values for both parameters indicate that the galaxy is in the pre-merger stage, high values for both indicate the galaxy is involved in an ongoing interaction, and low values for A with high values for $\mathcal{A}$ suggest the galaxy is a post-merger remnant.

4.2 Comparison of asymmetries in two merger stages

The work presented in §4.1 examined the general behaviour of the 2D asymmetry parameters, A and $\mathcal{A}$, for the gas and stellar distributions. In this section, we opt to focus on the gas distribution of the central galaxy, and extend this work to investigate the 1D lopsidedness parameters, L and $\mathcal{L}$. This decision to only consider the gas distribution is made for two reasons: (1) the 1D parameters described in §2.1, are specific to quantifying the asymmetry in HI spectra, and (2) this allows us to compare our results obtained for the simulations to the work using archival data, which will be addressed in Chapter 5.

In particular, we are interested in building on the work done in §4.1.1, which only considered the merger event when viewed face-on, by exploring the effects of viewing angle and inclination on these asymmetry parameters. To do so, we generate mock observations with various orientations at two time-steps: T = 1.26 Gyr, shortly after the gas disks have

come into contact, and T = 1.65 Gyr, the time-step when the nuclei of the galaxies are maximally separated. Recall that at this first time-step, $\mathcal{A}^{\dagger}$ has begun its increase due to the imminent first pass, but A has yet to register the interaction. At the second time-step, A displays a local minimum. We would like to examine the extent to which the results observed at these time-steps depend on the orientation of the observation.

One issue arising from introducing multiple orientations is that it becomes more difficult to implement the separation of galaxies employed in §4.1 in a consistent manner. For some orientations, such as nearly edge-on systems, it is no longer suitable to separate the galaxies spatially and a method using spectral separation must be used. With real observations, we would need to use a generalised spatial-spectral separation approach for consistency. However, since this work deals with simulations, we can circumvent this issue by only considering the gas particles that belong to the central galaxy at the start of the merger. It should be noted that this is less realistic than our previous approach, but allows us to consider each orientation in a consistent manner.

For each snapshot, the selected gas particles are rotated using Euler angles, which in turn alter the inclination and viewing angle of the gas distribution. Mock gas images and velocity profiles were generated for 131 observations at the two time-steps of interest. This number was based on the size of the WHISP sample described in Chapter 3. Figure 4.5 shows the lopsidedness parameters as a function of the 2D asymmetry parameters, where the colour of each data point indicates the inclination of the galaxy. In each panel of the figure, the closed circle markers correspond to the observations at 1.26 Gyr and the cross markers to the observations at 1.65 Gyr.

For convenience, we will refer to the 1.26 Gyr sample as the FP (First Pass) sample and the 1.65 Gyr sample as the MS (Maximal Separation) sample. Before analysing the results shown in Figure 4.5, we first motivate for applying an inclination cut to these samples. One of the most noticeable trends in the figure is the observed horizontal 'tail' of data points from the FP sample which return low values for both 1D parameters, but varying values of the 2D parameters. Given their colour, it is evident that these are all nearly edge-on systems.

The likely cause of this trend is that the interaction has pushed gas particles out the plane of the central galaxy. Although these particles are much lower in surface brightness since they originate from the edges of the gas disk, the rest of the disk is still relatively thin when viewed edge-on. As a result, the contribution of these 'extraplanar' particles is doubled in the residual images of the galaxies. It should be noted that this effect can likely be lessened with the implementation of a segmentation map, but we leave this investigation for future work.

Giese et al. (2016) noted that the inclination of a galaxy begins to have a significant effect on the measured A parameter for inclinations $i > 60°$ and found that beyond these values, the measured A decreases as inclination increases. It should be noted that while

† We drop the subscripts from the parameters since we are only looking at the gas distribution.

we observe the inverse relationship between inclination and A, the trend observed by Giese et al. (2016) is due to a loss of detail, whereas our observed increase is due to the impact of the interaction. Nevertheless, since our measurements are affected over the same range of inclinations, we adopt the upper inclination limit recommended by Giese et al. (2016) and consider observations with $i \leq 60°$.

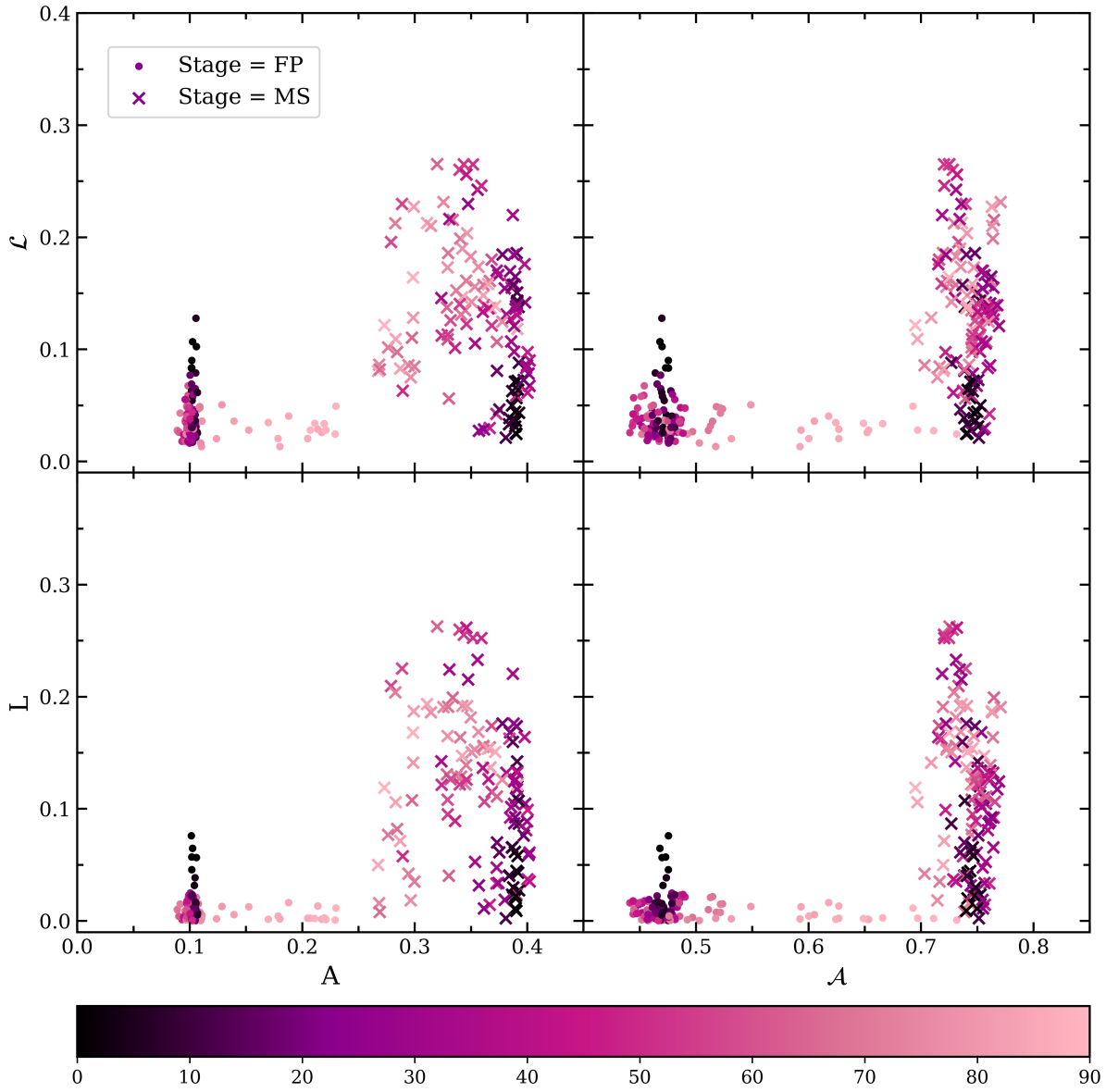

Figure 4.5: The 1D parameters $\mathcal{L}$ (top row) and L (bottom row) as a function of the 2D parameters A (left panels) and $\mathcal{A}$ (right panels) for the simulated mock observations. The closed circle markers represent the observations at T = 1.26 Gyr during the 'First Pass' stage and the x markers represent the observations at T = 1.65 Gyr during the 'Maximal Separation' stage. All data points are coloured according to their inclination, which are shown in degrees in the colour bar.

The 1D parameters also tend to suffer from inclination effects at low inclinations. Due to a loss of information regarding the radial velocity component, nearly face-on galaxies generally result in narrow single peak HI profiles. To account for the effect of inclination on the 1D parameters, we adopt a somewhat generous lower inclination cut and exclude

all observations with $i < 10°$.

Figure 4.6 shows the 1D parameters as a function of the 2D parameters for all mock observations with inclinations $10° \leq i \leq 60°$. After imposing the inclination cuts, 66 observations remain from the FP sample and 76 observations from the MS sample. By comparing Figures 4.5 and 4.6, we find that the lower inclination cut has considerably reduced the range of L and $\mathcal{L}$ in the FP sample. It is also apparent that nearly face-on galaxies, which are coloured black in Figure 4.5, generally result in higher 1D parameter values in the FP sample, while galaxies with similar inclinations in the MS sample have considerably lower measured 1D parameters. This is likely due to the profile widths of the velocity profiles and the number of channels available to calculate L and $\mathcal{L}$.

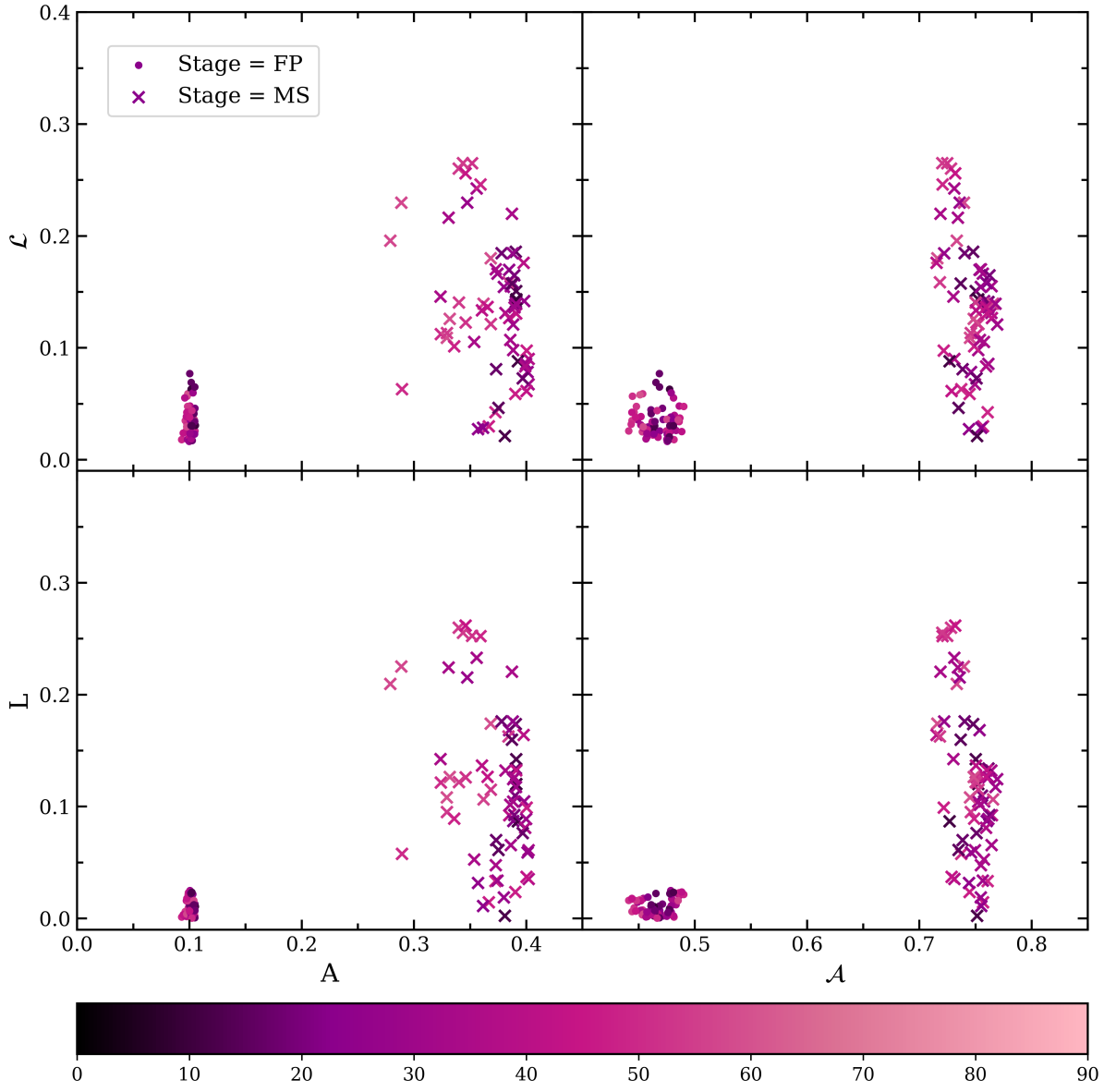

Figure 4.6: The 1D parameters $\mathcal{L}$ (top row) and L (bottom row) as a function of the 2D parameters A (left panels) and $\mathcal{A}$ (right panels) for the reduced samples of simulated mock observations. The closed circle markers represent the observations in the FP sample and the x markers represent the observations in the MS sample. All data points are coloured according to their inclination.

Consider the velocity profiles of one galaxy from each sample, as shown in Figure 4.7. Although these galaxies both have an inclination of $i = 1°$, as well as similar viewing angles, their velocity profiles have vastly different profile widths. In particular, $\mathcal{L}$ is more sensitive to the profile width of a velocity profile and is more prone to returning inflated values for very narrow profiles. For this reason, we believe it is acceptable to keep this lower inclination cut to avoid inflating our results due to the profile widths of the velocity profiles.

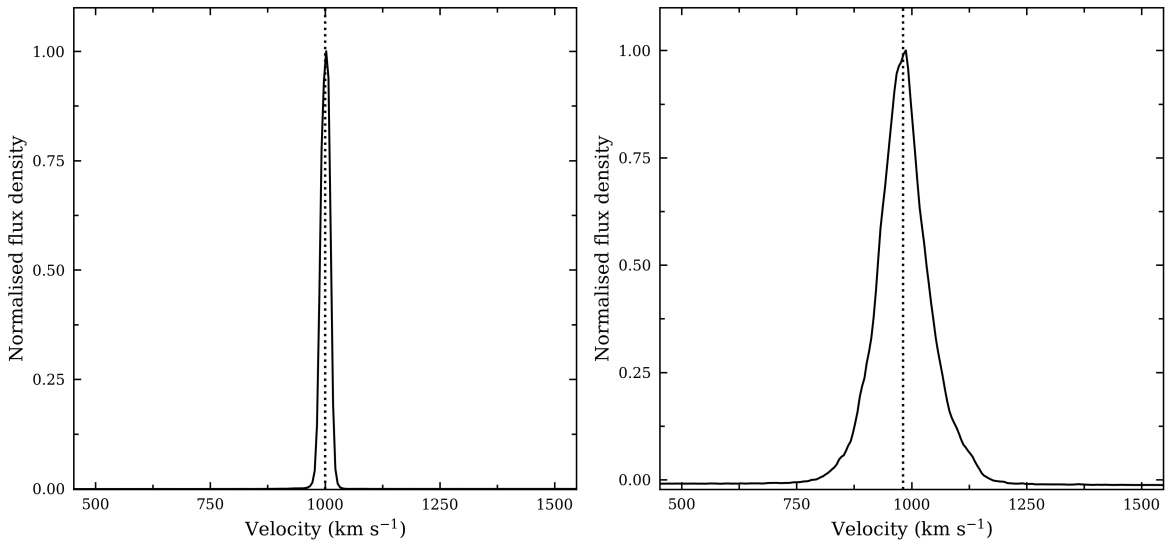

Figure 4.7: HI spectra of two approximately face-on observations from the FP sample (left) and the MS sample (right). In each panel, the black dotted line corresponds to the measured systemic velocity.

With the upper inclination limit, we observe both samples shown in Figure 4.6 to be clearly separated in A and $\mathcal{A}$. For each sample, it is evident that A of the FP sample has the smallest spread in distribution, with a standard deviation of $\sigma_{A,FP} = 0.003$. In contrast, A of the MS sample has a considerably wider spread, with a standard deviation of $\sigma_{A,MS} = 0.03$, a factor of 10 greater than $\sigma_{A,FP}$. With the FP sample, the central region of the gas distribution is still relatively unaffected by the interaction and so it is unsurprising that we see little spread in the possible values for A. With the MS sample, we see that observations with intermediate inclinations $10°\leq i \leq 60°$ are dispersed towards lower values of A and that observations with lower inclinations appear to be densely packed near $A = 0.38$. These results suggest that the measured value of A is sensitive to the orientation of the distribution depending on which stage of a merger the distribution is being observed at. Interestingly, the standard deviation of $\mathcal{A}$ for both samples is the same at $\sigma = 0.01$. While we have only considered two time-steps, this suggests that the $\mathcal{A}$ parameter is less sensitive to the orientation of the galaxy, provided the inclination of the galaxy is within the specified limits.

We do not observe the same distinct separation between the two samples when considering the 1D spectral lopsidedness parameters. With the MS sample, we still observe low

measured values for L and $\mathcal{L}$, despite the gas distribution having a disturbed morphology as indicated by the 2D parameters. It appears that the main differences between L and $\mathcal{L}$ occur at low values ($L, \mathcal{L} \leq 0.1$) and are most apparent in the FP sample. Relatively speaking, the distribution of $\mathcal{L}$ for this sample is noticeably more spread than that of L. This is likely due to small variations in the channel pairs closest to the systemic velocity, which result in slightly higher values for $\mathcal{L}$.

The spread of L and $\mathcal{L}$ in the MS sample show that the 1D parameters are much more sensitive to the orientation of the galaxy than the 2D parameters. This is due to the fact that the 1D parameters are affected by the viewing angle of the observation in addition to the inclination, whereas we see that the 2D parameters are affected by the inclination more than the viewing angle.

It is crucial to remember that these results are specific to our simulations, as well as the time-steps considered. Nevertheless, we can remark on a number of findings. Firstly, the 2D asymmetry parameters appear to be the preferred parameters to distinguish between these two time-steps in the merger event. While both parameters suffer from inclination effects, the outer asymmetry $\mathcal{A}$ appears to be less sensitive to the orientation of the galaxy than the intensity-weighted asymmetry A. Lastly, in the absence of pointing error offsets and noise, we find that a high measured value for L or $\mathcal{L}$ suggests a high 2D asymmetry, and thus a disturbed spatial distribution.

Chapter 5

The 1D and 2D HI asymmetries in WHISP galaxies

In the previous chapter, it was shown that the 1D lopsidedness parameters, depending on the orientation of a galaxy, display a relatively wide range of values in comparison to the 2D asymmetry parameters. No clear relationship between the 1D and 2D parameters could be discerned, but our results were limited in that we only considered random orientations of the central galaxy at two time-steps of one simulated merger event. Thus, we turn to using archival data to further investigate if a relationship exists between the 1D and 2D parameters, measured in the HI global profiles and integrated HI maps respectively, for a sample of 115 galaxies from WHISP. In the first section, we examine how well the 1D and 2D parameters correspond to visual classifications of asymmetry in the profiles and images. The second section builds on the work discussed in §4.2 by exploring the relation between the 1D and 2D parameters for this sample. We investigate which combination of parameters results in the strongest linear correlation, identify optimal inclination limits for the sample, and examine where interacting galaxies reside on the 1D-2D asymmetry diagram.

5.1 The visual classification of WHISP galaxies

To establish the efficacy of the parameters in quantifying a galaxy's asymmetry, we visually classified all galaxies in the WHISP sample, described in §3.2.2, according to the degree of asymmetry observed in their HI profiles and HI images. Three classifiers were tasked with individually categorising HI profiles and images of the galaxies, as well as answering supplementary questions on features present in the profile or image. The profiles and images were inspected separately so as to avoid potentially biasing the degree assigned to a galaxy image based on the appearance of its line profile or vice versa.

Due to the subjectivity of visual classifications, one stipulation was that we required 100% agreement between the classifiers on the degree of asymmetry assigned to an image/profile. For all galaxies with differing assignments, the classifiers met to re-classify

those galaxies with differing assignments and re-answer the additional questions. In the event that there were any disagreements regarding the answers for the supplementary questions but the galaxies were assigned the same degree of asymmetry, the most common answer was chosen. However, it should be noted that this was seldom the case and there was often high agreement between the classifiers regarding the supplementary questions.

5.1.1 The 1D global HI profiles

The classifiers were presented with the following questions when inspecting the HI spectra:

Q1. Does the HI spectrum have a double-horn profile?

Q2. What is the degree of asymmetry in the profile? Classify as follows:
- ◇ 0 - symmetric
- ◇ 1 - slightly asymmetric
- ◇ 2 - moderately asymmetric
- ◇ 3 - severely asymmetric

Q3. Do the peaks of the profile have different widths?

Q4. Does the central dip of the profile lie above f_{50}, the intensity level corresponding to 50% of the peak flux?

For each question except Q2, a galaxy is allocated a value of 1 if the answer is 'yes', and a value of 0 otherwise. Any profile that does not have two clearly-defined peaks with a central dip is classified as a single peak. Although this is a relatively broad definition, it is appropriate for this work. Regarding Q3, single peak profiles were allocated a value of 2 if the peak of the profile is lopsided relative to the calculated systemic velocity. Table 5.1 provides a summary of our classifications for the profiles. It should be noted that the values in parentheses in the last two columns of Table 5.1 signify the number of single peak profiles which are allocated a value of 1 or 2, and are not to be confused for subsets from the other values quoted in those columns.

Table 5.1: Visual classification summary of the 1D HI profiles of the WHISP sample. In the last two columns, values in parentheses indicate the number of single peak profiles which have been allocated a value of 1 or 2, depending on the question.

Classification	N	Q1	Q3	Q4
Symmetric	28	13	0 (0)	8 (15)
Slightly asymmetric	43	24	18 (18)	17 (19)
Moderately asymmetric	38	27	23 (11)	13 (11)
Severely asymmetric	6	4	4 (2)	2 (2)
Total	115	68	45 (31)	40 (47)

5.1.1.1 Comparison of lopsidedness parameter results

Using the methods outlined in Chapter 2, the 1D lopsidedness parameters were measured for the sample and are tabulated in Table A.1, along with the asymmetry classification for each profile. The distribution of measured 1D parameters, grouped according to the visually classified degrees of 1D asymmetry, is presented in Figure 5.1. The 25^{th} and 75^{th} percentiles (P_{25} and P_{75}) of each category are represented by the boundaries of the box, while the mean and median are shown by the black triangle and dashed line respectively. Data points are regarded as suspected outliers if they lie outside the range ($P_{25} - 1.5{\cdot}$IQR, $1.5{\cdot}$IQR$+P_{75}$), where IQR $= P_{75} - P_{25}$ is the interquartile range. These data points are shown as black diamonds in Figure 5.1. Lastly, the black errorbars, or whiskers, on either side of each box show the minimum and maximum data points of each group that fall within this range.

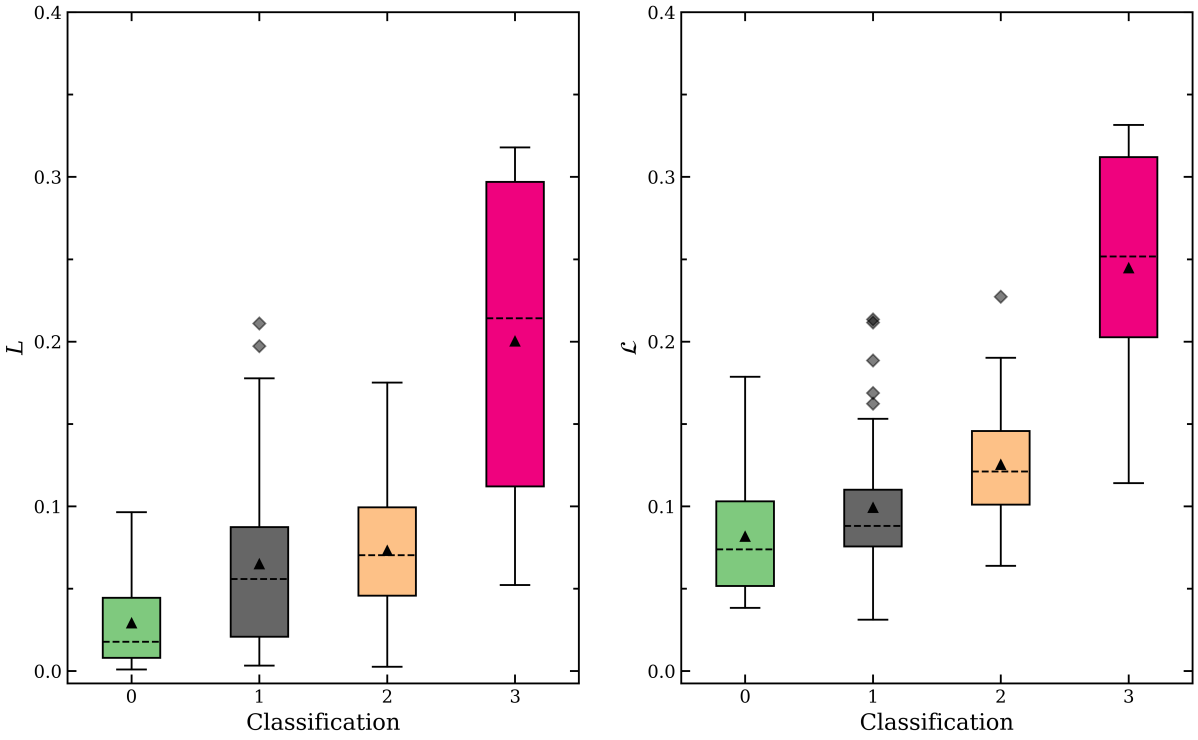

Figure 5.1: Box-plot of the 1D lopsidedness parameters L (left panel) and $\mathcal{L}$ (right panel) measured for the WHISP sample and grouped according to the visual classifications of asymmetry present in the HI spectra. Within each box, the black triangle markers represent the mean of the class and the dashed lines represent the median. The black diamond markers represent suspected outliers.

By comparing the panels in Figure 5.1, it appears that the folding difference lopsidedness, $\mathcal{L}$, is in better agreement with our visual classifications than the traditional lopsidedness parameter, L. Let us first consider the minimum measured values of L and $\mathcal{L}$ for each category, which are shown as horizontal lines at the ends of the bottom whiskers in the figure. We find that it is possible to return a value close to zero for L, despite the visual asymmetry observed in the HI profiles of the slightly asymmetric (grey) and

moderately asymmetric (peach) samples. It is not particularly surprising or concerning that we observe this with the slightly asymmetric (grey) category, given that these classifications are subjective and there is bound to be some overlap. However, the fact that we also observe this with the moderately asymmetric (peach) sample suggests that L is less sensitive to the observed asymmetries in some of the profiles in this category. Although we find the minimum value of $\mathcal{L}$ of the slightly asymmetric (grey) sample to be less than that of the symmetric (green) sample, the IQR of both samples appear more separated in the right panel than in the left. However, it is important to take into consideration the general distribution of these categories and not focus solely on the minimum and maximum data points as an indicator of how these parameters perform.

We find that the symmetric (green) sample is the only sample where the IQR, which is indicative of the distribution of the central 50% of the data, and standard deviation, σ, of L is smaller than that of $\mathcal{L}$. For the other samples, especially the slightly asymmetric (grey) and moderately asymmetric (peach) samples, the spread for L is greater than $\mathcal{L}$. The short bottom whiskers on the symmetric, slightly asymmetric and moderately asymmetric samples in the left panel of the figure, in addition to the positions of the median lines, demonstrate that there is less variation in the low values of L and that the mean is skewed to higher values of L. This implies that L is able to reliably quantify the degree of asymmetry (or lack thereof) in symmetric profiles, but is more likely to underestimate small-scale asymmetries in profiles that are visually asymmetric.

When analysing this data, it is crucial to remember that the severely asymmetric (pink) sample only consists of 6 galaxies, which amounts to ~5% of the full sample. In comparison, the second smallest sample, accounts for ~21%. Thus, the large length of the pink boxes in Figure 5.1 is a consequence of the small sample size. Even so, we still observe less variation in the values of $\mathcal{L}$ for this sample than for L. The HI profile causing the extended bottom whisker in the severely asymmetric (pink) sample belongs to UGC 5060, whose profile and HI image can be found in Appendix B. While the single peak profile is clearly asymmetric with an extended profile wing on one side, the reason why this is not being reflected in either measurement is because this profile wing extends beyond w_{20} and so it is not included when calculating L or $\mathcal{L}$.

The suspected outliers shown in both panels of Figure 5.1 suggest that we have visually under-classified the degree of asymmetry in these profiles. The reason we observe more outliers in the right panel than in the left is likely due to the lower spread in $\mathcal{L}$ for each sample. However, these data points are not concerning because as mentioned, visual classifications are inherently subjective.

An additional method of comparison would be to perform two-sample Kolmogorov-Smirnov (K-S) tests to examine each parameter's ability to distinguish between the various classification categories. For two samples of size m and n, with cumulative distribution functions described by $F_m(x)$ and $G_n(x)$ respectively, the K-S statistic D calculates the maximum difference between the samples' distribution functions and is given by

$$D_{m,n} = \sup_x |F_m(x) - G_n(x)|. \tag{5.1}$$

At a chosen significance level α, the null hypothesis that the two samples are drawn from the same distribution is rejected if

$$D_{m,n} > \sqrt{-ln\Big(\frac{\alpha}{2}\Big) \cdot \Big(\frac{n+m}{2n \cdot m}\Big)}. \tag{5.2}$$

Table 5.2 gives the K-S statistic D and the associated p-value for each of the samples being compared. These results suggest that L is only able to distinguish between the symmetric (green) and slightly asymmetric (grey) samples. For the other samples, we cannot reject the null hypothesis that these populations have the same distribution when using L. However, the converse is true with $\mathcal{L}$; the results from Table 5.2 suggest that $\mathcal{L}$ is more successful at separating the distributions according to their visual classifications for asymmetric profiles, but is less successful at distinguishing between the symmetric (green) and slightly asymmetric (grey) samples.

Table 5.2: K-S test statistics for the 1D parameters and the visual classification categories for the HI profiles of the WHISP sample.

Samples	D		p-value	
	L	$\mathcal{L}$	L	$\mathcal{L}$
S_0 and S_1	0.46	0.29	8.5×10^{-4}	0.09
S_1 and S_2	0.23	0.50	0.19	3.9×10^{-5}
S_2 and S_3	0.57	0.81	0.04	8.3×10^{-4}

Note: S_0, S_1, S_2 and S_2 refer to the symmetric, slightly asymmetric, moderately asymmetric and severely asymmetric samples respectively.

5.1.1.2 Lopsidedness vs. other profile properties

We now review if there is any observable trend between the measured values of these parameters and the widths of the peaks or the depth of the central dip observed in double-horn profiles. Figures C.1 and C.2, provided in Appendix C, can be considered complementary plots to Figure 5.1. In these figures, the data are still grouped according to their visual classifications, but have been separated into single peak profiles and double-horn profiles, represented by circle and triangle markers respectively. Due to how condensed some of the categories are, we have opted to plot the data without their errorbars. The data in Figure C.1 are coloured according to the answers for Q3, and the data in Figure C.2 are coloured according to the answers for Q4.

With reference to Figure C.1, it is apparent that of all single peak profiles classified as having some degree of asymmetry, only one profile is observed to be symmetric relative to the systemic velocity. Recall that we have defined the systemic velocity as the mid-point

between the velocities measured at the 20% peak flux level. This result suggests that the position of the peak relative to the systemic velocity plays a notable role in the values measured for L and $\mathcal{L}$ for single peak profiles. We don't observe any notable trend with the peak widths in the double-horn profiles, but this is not surprising given that the 1D parameters measured for double-horn profiles are dependent on the peak widths as well as the peak heights.

As provided in Table 5.1, double-horn profiles with central dips below f_{50} account for ~48% of double-horn profiles in our sample. By comparing the panels of Figure C.2, we find that profiles with large central dips tend to cluster at the higher values of $\mathcal{L}$ in each sample. In contrast, we don't observe any noticeable trend in L. The reason we don't observe any trend between central dip depth and L is likely due to the fact that asymmetries in this central region of the profile have a smaller contribution when computing L because it is a measure of the areal flux ratio. However, it should be noted that the majority of profiles whose peaks are significantly different in height will result in an average f_{50} that lies above one of the peaks and this would count as a central dip below f_{50}. After cross-comparing the results for Q3 and Q4, we find that 20 of the 28 profiles with steep central dips also have differing peak widths. Thus this trend seen in the right panel of Figure C.2 may not necessarily be related to the depth of the central dip, but rather other features that are demonstrated in these profiles.

In summary, these categories of visual asymmetry appear to be more clearly separated in $\mathcal{L}$ than in L. The standard deviation of $\mathcal{L}$ for the asymmetric samples is smaller in value than the standard deviation of L for these same samples. Additionally, we find that L is more likely to underestimate the lopsidedness in visually asymmetric profiles and that values of L tend to be more concentrated at lower values. However, we also find that $\mathcal{L}$ tends to return slightly inflated values for profiles classified as symmetric, which is possibly due to the S/N of the profiles or the widths of the profiles.

5.1.2 The 2D HI images

As mentioned at the start of this chapter, we have also visually classified the HI images of our sample. The decision was made to reduce the number of possible asymmetric classes, but we also consider more supplementary questions which examine the inner and outer asymmetry of the HI distributions. The questions presented were as follows:

Q1. Is the galaxy edge-on?

Q2. Is there a depression (1) or hole (2) in the central region?

Q3. Does the HI distribution have any spiral/ring structure?

Q4. Are there tidal tails present?

Q5. What is the degree of overall asymmetry in the image? Classify according to:

- ◇ 0 - symmetric
- ◇ 1 - mildly asymmetric

- ◇ 2 - severely asymmetric

Q6. Is the inner region of the galaxy asymmetric?

Q7. Is the outer region asymmetric?

Q8. Is the HI distribution clumpy?

Q9. Do you think the CoS is offset from the CoB of the galaxy?

In the same fashion as the classifications for the HI profiles, a galaxy is allocated 1 for 'yes' and 0 for 'no' to the supplementary questions. A summary of the classifications is provided in Table 5.3. The values in parentheses in the fourth column indicate the number of galaxies which are found to have a central hole in the HI distribution.

Table 5.3: Visual classification summary of the 2D HI images of the WHISP sample.

Classification	N	Q1	Q2	Q3	Q4	Q6	Q7	Q8	Q9
Symmetric	13	5	4 (2)	5	0	0	0	2	1
Mildly asymmetric	80	11	23 (4)	20	2	47	65	37	24
Severely asymmetric	22	0	4 (1)	7	6	21	21	8	20
Total	115	16	31 (7)	32	8	68	86	47	45

It should be noted that is possible for a galaxy to be classified as mildly or severely asymmetric overall but have either their inner or outer region classified as symmetric. However, if a galaxy is classified as symmetric overall, we expect that visually, the inner and outer regions must be symmetric. As indicated in Table 5.3, the mildly asymmetric category is by far the largest category and accounts for ~70% of the sample.

5.1.2.1 Comparison of asymmetry parameters results

The measured 2D parameters and visual classifications of asymmetry for each galaxy are provided in Table A.1. Similarly to what was done in §5.1.1, box-plots have been used in Figure 5.2 to represent the distribution of measured values grouped according to the galaxies' visual classifications.

As can be be seen in both panels of Figure 5.2, the 2D parameters correspond well with our visual classifications. A clear increase in the median and mean is observed with each successive category in both panels. Although there are several suspected outliers observed in the left panel and none in the right, the biggest difference between A and $\mathcal{A}$ appears to be the spread in their distributions. It is evident that there is far more overlap between the boxes and their whiskers in the right panel, which infers a spread in the $\mathcal{A}$ values measured across all samples. In contrast, while there is overlap in the bottom whiskers of the symmetric (green) and mildly asymmetric (grey) samples in the left panel, the boxes of these samples appear more separated in A. Furthermore, the spread of A, as indicated by the IQR as well as σ, is consistently less than the spread of $\mathcal{A}$ for the

symmetric (green) and mildly asymmetric (grey) samples: the differences in the standard deviations of $\mathcal{A}$ and A for these samples are 0.05 and and 0.03 respectively.

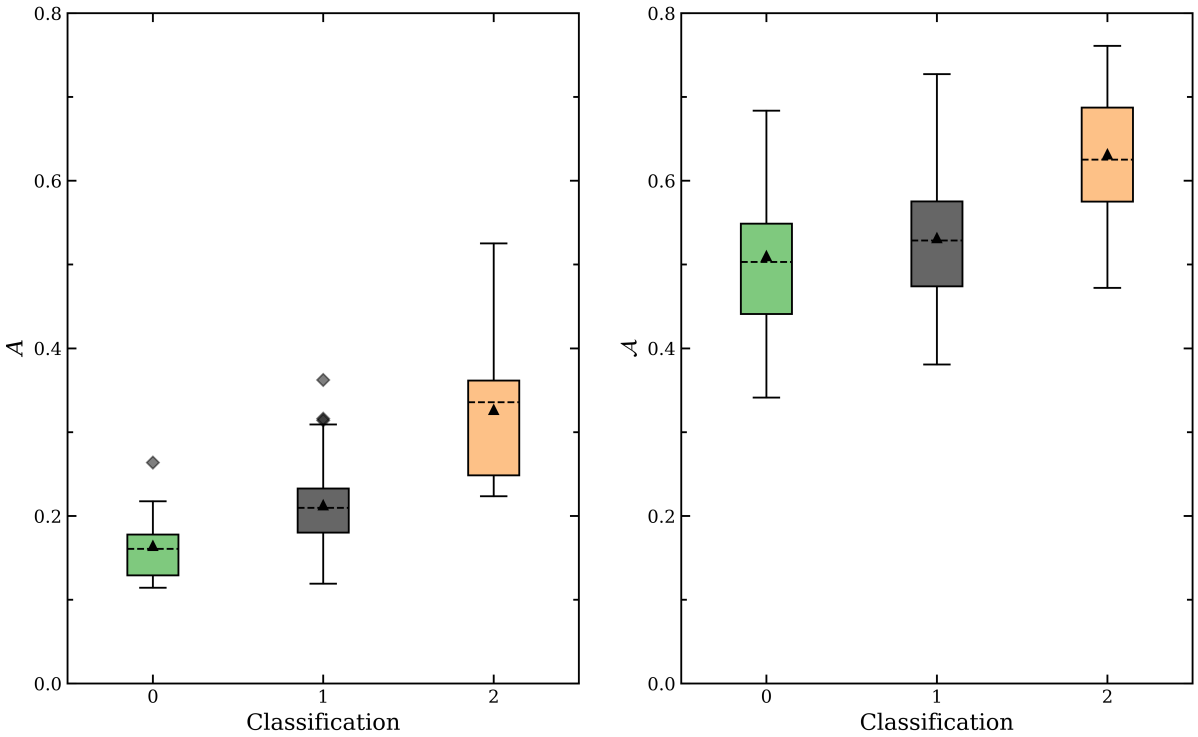

Figure 5.2: Box-plot of the 2D asymmetry parameters A (left panel) and $\mathcal{A}$ (right panel) measured for the WHISP sample and grouped according to the visual classifications of asymmetry present in the HI images. Within each box, the black triangle markers represent the mean of the class and the dashed lines represent the median. The black diamond markers represent suspected outliers.

We find that the severely asymmetric (peach) sample is the only sample where the differences between the IQR and standard deviation of A and $\mathcal{A}$ are negligible; we measure absolute differences of 0.001 and 0.009 for the IQR and standard deviations respectively, which suggests that the parameters exhibit the same spread in the severely asymmetric sample. Once again, we implement two-sample K-S tests and the results are given in Table 5.4 for the 2D parameters measured for these three samples.

Table 5.4: K-S test statistics for the 2D parameters and the visual classification categories for the HI images of the WHISP sample.

Samples	D		p-value	
	A	$\mathcal{A}$	A	$\mathcal{A}$
S_0 and S_1	0.53	0.20	0.002	0.740
S_1 and S_2	0.66	0.54	1.78×10^{-7}	3.48×10^{-5}

Note: S_0, S_1 and S_2 refer to the symmetric, mildly asymmetric and severely asymmetric samples respectively.

The results from Table 5.4 suggest that the distributions of A for all classification categories are statistically different. This is not the case for $\mathcal{A}$; we cannot reject the null

hypothesis that the distributions of $\mathcal{A}$ for the symmetric and mildly asymmetric galaxies are statistically different. Thus, we can infer that A is in better agreement with our visual classifications of asymmetry in the HI images.

5.1.2.2 2D asymmetry vs. other observed spatial features

Proceeding to the other visual classifications, Figures C.3 - C.10 in Appendix C show the distributions of A and $\mathcal{A}$, grouped according to the classification categories and coloured according to the supplementary questions given earlier in this section. Before analysing these figures, it should be noted that there is considerable overlap in the data points shown in these figures, particularly in the distributions of A (left panels of these figures). To help visualise any possible trends, the order of data points has been specified according to their colour in some of the figures. However, as a result it can be misleading to compare the various figures at face value.

To demonstrate this issue, we compare the severely asymmetric sample of galaxies (given classification 2) shown in Figures C.7 and C.8. In the left panel of both figures, the only green data point occurs at the lowest measured value of A, which would lead one to conclude that they are the same data point. However, the right panels of the same figures show the data point at different measured values of $\mathcal{A}$. In actuality, these data points correspond to two galaxies, UGC 94 and UGC 7047, which have the same measured A (0.22) but different values for $\mathcal{A}$ (0.69 vs 0.47). Thus, it is important to keep in mind that some data points have been brought to the foreground to help with visualising the data in the panels of the same figure.

Let us briefly consider the figures, and thus questions, where we do not observe a notable trend. We do not find any clustering of edge-on galaxies at certain values of A or $\mathcal{A}$ in Figure C.3. Although we find that no edge-on galaxies have been classified as severely asymmetric, this is not surprising since the full extent of the galaxies' spatial distribution cannot be observed. Figure C.4 shows that galaxies with central depressions or holes in their HI distributions return a range of values for both A and $\mathcal{A}$. Given that A is dominated by the bright central regions of galaxies, one would expect these galaxies to return higher values of A since their central regions are no longer the largest contributions when calculating A. However, this does not appear to be the case.

We find that galaxies exhibiting some form of ring or spiral structure in their HI distribution, shown as grey markers in Figure C.5, generally return low and intermediate values of $\mathcal{A}$ but have a wide spread of values for A. With reference to the symmetric and mildly asymmetric galaxies, this suggests that the outer regions of these galaxies are not the main cause of asymmetry.

From Figure C.9, there does not appear to be any relation between the clumpiness observed in galaxies and the values of A or $\mathcal{A}$. We also do not observe any discernible pattern between the parameters and whether there is an expected offset between the CoB and the CoS, although this question is subjective because it requires the classifier

to predict where the position of these centres would lie based on the distribution. It is important to be cognizant of the fact that these features, such as the clumpiness and the presence of spiral structure in the HI gas, do not occur in isolation and that there is likely a relation between many of these various features. However, investigating the relation between these features and how that affects the measured 2D asymmetry parameters is the topic of further research.

Let us now review Figures C.6, which shows the data coloured according to the answers of Q4 (on whether there are any tidal tails present). We find that the spread of $\mathcal{A}$ for galaxies with tidal tails is much smaller than the spread of A. Furthermore, all galaxies with tidal tails return a value of $\mathcal{A} > 0.6$, whereas we observe values as low as 0.22 for A. This is not surprising as these tidal tails generally have low surface brightnesses. However, this figure clearly illustrates that $\mathcal{A}$ is the more suitable parameter to quantify these tidal features. If we were to use one of these parameters to set a threshold when searching for possible merger candidates presenting tidal features, $\mathcal{A} \geq 0.6$ would result in a much smaller sample of possible candidates than $A \geq 0.2$.

Lastly, let us consider Figures C.7 and C.8. According to the mildly asymmetric categories in both panels of C.7, there does not appear to be any relation between the visual classification of inner asymmetry and the parameters. This is not a concern regarding $\mathcal{A}$ since we expect $\mathcal{A}$ to correspond more closely with the visual classification of outer asymmetry, as shown in Figure C.8. However, we would expect the galaxies with asymmetric inner regions to return higher values of A.

Both panels of Figure C.8 illustrate that galaxies with visually symmetric outer regions tend to result in lower values measured for A and $\mathcal{A}$ to a lesser extent. We find that galaxies classified as mildly and severely asymmetric overall, but with visually symmetric outer regions (green markers) return much lower values of $\mathcal{A}$ than those galaxies with visually asymmetric outer regions (grey markers) in those same samples. However, due to the spread of the visually symmetric sample in $\mathcal{A}$, we find that it is possible to measure a value of $\mathcal{A} > 0.6$ despite having both the inner and outer regions classified as symmetric. This is the case for galaxies UGC 3966 and UGC 8286, which have both been classified as visually symmetric but have high values of $\mathcal{A}$ (0.61 and 0.68 respectively). Upon inspecting their images, we find that UGC 3966 has a reasonably clumpy HI distribution and was likely visually classified as symmetric due to the relative size of the beam being comparable to the size of the galaxy, and UGC 8286 is highly inclined. These two galaxies show that it is possible to measure high asymmetry parameters for galaxies which are presumably not undergoing active interactions. This is an important consideration if we are to use these parameters when identifying possible merger candidates.

5.2 The correlation between 1D and 2D asymmetry parameters

The previous section presented a comprehensive comparison of the visual classifications of asymmetry in the HI images and profiles of galaxies with the various parameters formulated to quantify these asymmetries. In the context of high redshift data where the HI distribution of galaxies cannot be resolved spatially using the radio telescopes currently available, can we deduce anything about the condition of the underlying HI distribution if we only have the galaxy's 1D global profile? We attempt to address this question by exploring the relationship between the measured 1D and 2D parameters in this sample.

To investigate this relation, we make use of the Pearson correlation coefficient, which quantifies how well two variables are associated and the direction of this relationship. The coefficient is described by the equation below,

$$r = \frac{\sum_{i=1}^{n}(x_i - \overline{x}) \cdot (y_i - \overline{y})}{\sqrt{\sum_{i=1}^{n}(x_i - \overline{x})^2}\sqrt{\sum_{i=1}^{n}(y_i - \overline{y})^2}} \tag{5.3}$$

where n is the sample size, x_i, y_i are the ith variables of interest, and $\overline{x}$ and $\overline{y}$ are the sample means of x and y respectively. Possible values of r range from -1 to 1, where 1(-1) indicates a perfectly positive (negative) linear relationship between x and y, and 0 infers no linear relation.

Figure 5.3 presents the measures of 1D lopsidedness and 2D asymmetry for the WHISP sample considered in this work. The calculated r and its corresponding p-value for the various pairs of parameters are quoted in the upper left corner of each panel. The data are coloured according to the visual 1D classifications of asymmetry in the global profiles in order to explore if there is a possible relation between the 2D measured parameters and the classifications of the profiles. The uncertainties for the 1D parameters of each galaxy, as explained in Chapter 2, are calculated as the standard deviation of the parameters measured for 100 profiles with Gaussian noise. The uncertainties for the 2D parameters are calculated as the standard deviation of the parameters measured using the CoS and the 8 pixels surrounding it as the centre of rotation.

Let us first examine the right panels of Figure 5.3, which present the 1D parameters as a function of the 2D outer asymmetry $\mathcal{A}$. From the distribution of the data in the bottom right panel, there does not appear to be a relationship between L and $\mathcal{A}$. Recall from the results in §5.1 that these two parameters displayed a weaker correlation with our visual classifications than the other available parameters. Thus, it is not entirely surprising that the pairing of L and $\mathcal{A}$ returns the lowest r with the largest p-value, and so we do not have enough evidence to reject the null hypothesis that these two parameters are not related. With reference to the top right panel of the figure, we find that $\mathcal{A}$ fares slightly better when paired with the folding difference lopsidedness $\mathcal{L}$. Although there is still a

substantial overlap between the visual classification categories, it is observed that galaxies whose profiles are classified as moderately and severely asymmetric are generally more separated from the symmetric and slightly symmetric galaxies in $\mathcal{L}$ than they are in L. However, there appears to be no discernible relation between the visual 1D classifications and the measured $\mathcal{A}$ for galaxies as we find the majority of galaxies whose profiles were classified as moderately and severely symmetric display $\mathcal{A} \leq 0.6$. Nonetheless, a weak correlation of $r = 0.21$ with $p = 0.02$ is calculated for $\mathcal{A}$ and $\mathcal{L}$, inferring a weak positive linear correlation between $\mathcal{A}$ and $\mathcal{L}$.

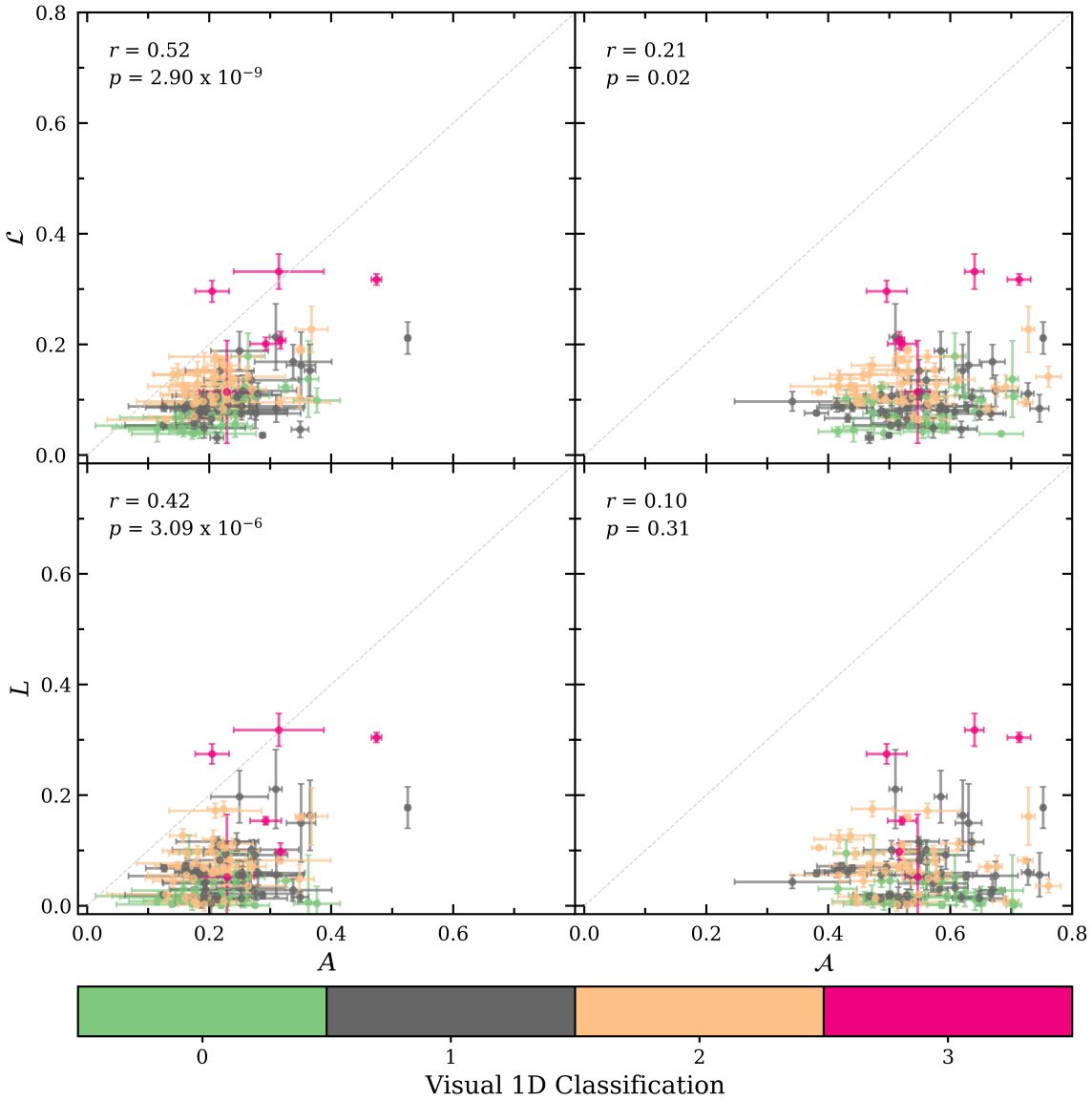

Figure 5.3: The 1D parameters $\mathcal{L}$ (top row) and L (bottom row) as functions of the 2D parameters A (left panels) and $\mathcal{A}$ (right panels) measured from the 1D global profiles and 2D HI images of 115 WHISP galaxies. The colour of the data indicates the visual classification assigned to the HI profiles of the galaxies where green is symmetric, grey is slightly asymmetric, peach is moderately asymmetric and pink is severely asymmetric. The vertical errorbars show the standard deviation of the 1D parameters for 100 measurements and the horizontal errorbars show the uncertainty due to error in the CoS.

In contrast, we observe substantially different results in the left panels of the figure, which display the 1D parameters as a function of the 2D intensity-weighted asymmetry A. Both panels show a clear horizontal shift towards the 1:1 reference line, but this is to be expected since it was shown in both §4.2 and §5.1.2 that $\mathcal{A}$ preferentially returns higher values than A for both simulated and real galaxies. Additionally, because the standard deviation of A is less than that of $\mathcal{A}$ for the sample, this results in higher correlation coefficients for the left panels.

There are a number of observations to be made from comparing the relation between A and L, shown in the bottom left panel, and the relation between A and $\mathcal{L}$ shown in the top left panel. It appears that within each visual classification category, $\mathcal{L}$ generally increases with A in the top panel. While we observe a similar trend in the bottom panel with A and L, it appears less pronounced at lower L values due to the overlap of the classification categories. In particular, if we examine the lower right region of these two panels beyond $A \geq 0.3$, it appears that there are fewer data points populating this region with low values of $\mathcal{L}$ than there are in this same region in the bottom panel. This suggests that galaxies with higher values of A will generally return higher values of $\mathcal{L}$, but this is not necessarily true with L.

With reference to the correlation coefficients measured for the various 1D-2D asymmetry pairings, it is clear that A and $\mathcal{L}$ have the strongest correlation with $r = 0.52$ and $p = 2.9 \times 10^{-9}$, indicating a moderate positive linear correlation between these two parameters. Recall from §5.1 that A and $\mathcal{L}$ were both found to be in better agreement with our visual classifications of the asymmetry observed in the images and profiles of the galaxies than the other parameters.

To further probe the difference in the correlations between the 1D parameters and A, since these pairings resulted in the two highest r coefficients with the smallest p-values, we have plotted these distributions side by side in Figure 5.4. The colour of the data points has been changed to correspond to the outer asymmetry $\mathcal{A}$, which allows us to examine how the 2D parameters relate to one another. Due to the concentration of data points, the data presented in this figure and the remaining figures in this section are plotted without their error bars.

The discrepancies between L and $\mathcal{L}$ for high values of A are much more conspicuous in Figure 5.4. Focussing once again on the region of both figures where $0.3 < A < 0.4$, we find that the average galaxy displays a value of $\mathcal{L} \gtrsim 0.1$, whereas a considerable number of these galaxies have L values close to zero in the left panel. To briefly explore what could be the cause for these differences between the two parameters, Figure C.11 presents the ratio of $\mathcal{L}/L$ against the integrated signal-to-noise (S/N) ratio of the 1D profiles, with the colour of the data indicating the profile width w_{20} for profiles in this sample. It appears that the discrepancies between $\mathcal{L}$ and L are not related to the S/N of the profiles or the profile widths, and that the majority of galaxies appear to lie along the $\mathcal{L}/L = 1$ line. However, this topic requires further investigation on a larger sample and we leave this for

future work.

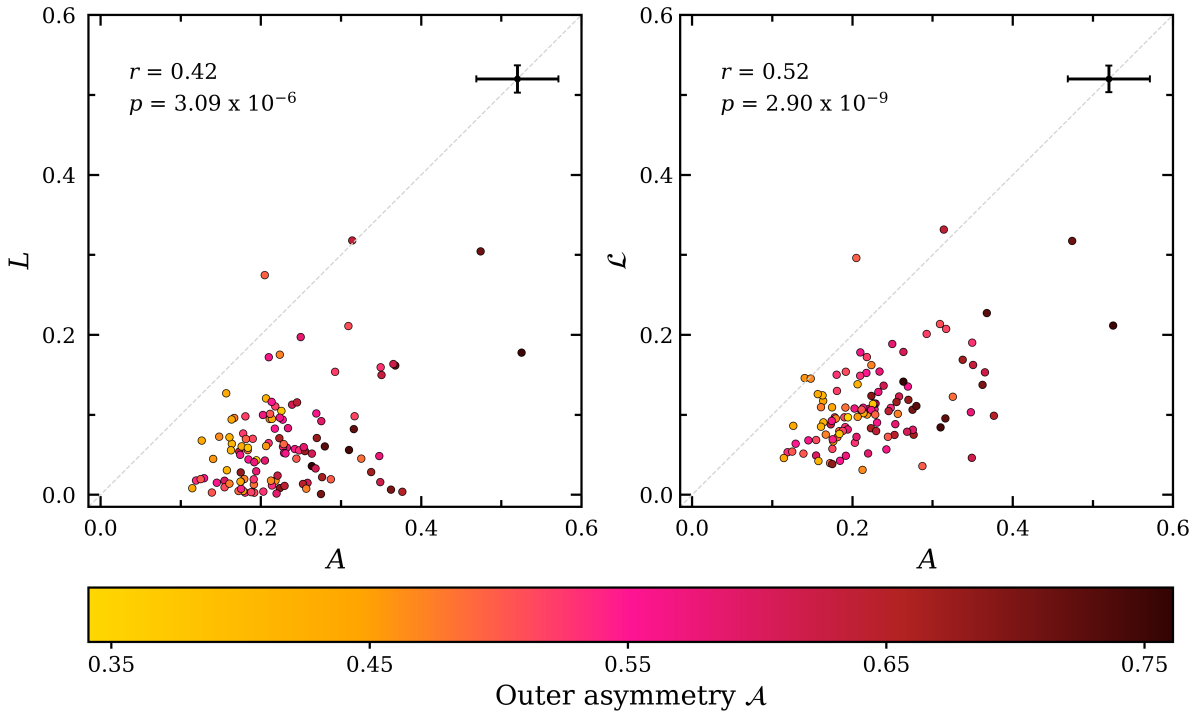

Figure 5.4: The 1D parameters L (left) and $\mathcal{L}$ (right) as a function of the 2D intensity-weighted asymmetry A for the sample of 115 WHISP galaxies. The colour of the data indicates the measured outer asymmetry $\mathcal{A}$ of the galaxies. The Pearson correlation coefficient and associated p-value are quoted in the upper left corner of each panel. The mean uncertainties associated with the parameters are shown

We also observe that $\mathcal{A}$, indicated by the colour of the data in Figure 5.4, appears to be relatively well correlated with A. We find that galaxies with low measured $\mathcal{A}$, shown as yellow and light orange markers, tend to have low A, but the inverse is not necessarily true in that it is possible for galaxies with intermediate and high values of $\mathcal{A}$ to have low A. This is not a surprising observation given that the primary motivation for formulating $\mathcal{A}$ as an additional parameter, explained in §2.2.2, was to up-weight the outer regions of galaxies which can have a negligible contribution in the computation of A due to their flux densities relative to the central regions of these galaxies (Lelli et al. 2014). Thus, the pink and brown data points occupying the bottom left regions of both panels in Figure 5.4 with $A \lesssim 0.2$ infer that the diffuse outskirts of these galaxies are considerably asymmetric. We also find that galaxies with high A tend to have high $\mathcal{A}$, which suggests that galaxies returning high intensity-weighted asymmetries are likely to have highly asymmetric outer regions.

5.2.1 The effect of inclination

Thus far, all results presented in this chapter have utilised the full sample of 115 WHISP galaxies. Given how the measured 1D and 2D lopsidedness and asymmetry parameters of a galaxy can be influenced by its inclination, it is important to consider reducing this

sample. The task of implementing an inclination cut is relatively uncomplicated when studying asymmetries in either the global profiles or the images of galaxies. However, when considering these 1D and 2D parameters jointly, there is an unavoidable trade-off between ensuring that galaxies suffering from inclination effects have been removed from the sample and retaining a substantial sample size for statistically reliable results.

For any real or simulated galaxy sample, the most conservative lower and upper inclination limits which could be applied are 30° and 60° respectively, as we assume that the 1D and 2D parameters measured for galaxies with intermediate inclinations between $30° \leq i \leq 60°$ have not been underestimated. Recall that in §4.2, any simulated galaxy with an inclination outside the range $10° \leq i \leq 60°$ was subsequently disregarded. While partly motivated by the findings of Giese et al. (2016), this decision was also made due to the trends observed in Figure 4.5 which were specific to our merger model. To investigate if any clustering occurs for face-on and edge-on galaxies in 1D-2D asymmetry parameter space (hereafter referred to as parameter space), Figure 5.5 shows the same sample as Figure 5.4, except the colour of each data point is now indicative of its inclination taken from literature. Additionally, galaxies which would be excluded under the conservative cut previously described have been given different markers: galaxies with moderately low inclinations ($15° \leq i < 30°$) are shown as diamond markers, galaxies with moderately high inclinations ($60° < i \leq 75°$) are shown as square markers and highly inclined ($75° < i \leq 90°$) galaxies are shown as triangle markers. It is worth mentioning that there are no galaxies in this sample with inclinations below 16°, which is why there are no markers for low inclination ($0° \leq i < 15°$) galaxies. The remaining galaxies with intermediate inclinations ($30° \leq i \leq 60°$) are represented by circle markers.

Regarding galaxies with low inclinations, it is apparent that the majority of these galaxies display relatively low measured values ($\lesssim 0.1$) of L and $\mathcal{L}$, but are not distinctly grouped in the parameter spaces shown in both panels of Figure 5.5. Comparing the left and right panels of the figure, we find that there are slightly more orange diamond markers with $\mathcal{L} > 0.1$ than there are those with $L > 0.1$. The two diamond markers shown to have $\mathcal{L} > 0.2$ in the right panel of Figure 5.5 represent galaxies UGC 4862 and UGC 7166, where the former is the only diamond marker present in the same region ($L > 0.2$) of the left panel. Both of these galaxies have an inclination of $i = 20°$ and have double-horn profiles that were visually classified as severely asymmetric. This outcome is not surprising given the results of Figure 5.1, which demonstrated that the mean values of $\mathcal{L}$ for the four 1D visual classification categories were greater than the mean values of L for the same categories. We do not observe any trends with the measured 2D A parameter of the galaxies with moderately low inclinations, but this is expected because A is not at risk of suffering from inclination effects when measured for nearly face-on galaxies.

When interpreting the absence of any clustering of low inclination galaxies, it is important to remember that we are somewhat constrained by the inclination range of our sample and that we cannot ascertain where galaxies more face-on than 16° will reside in

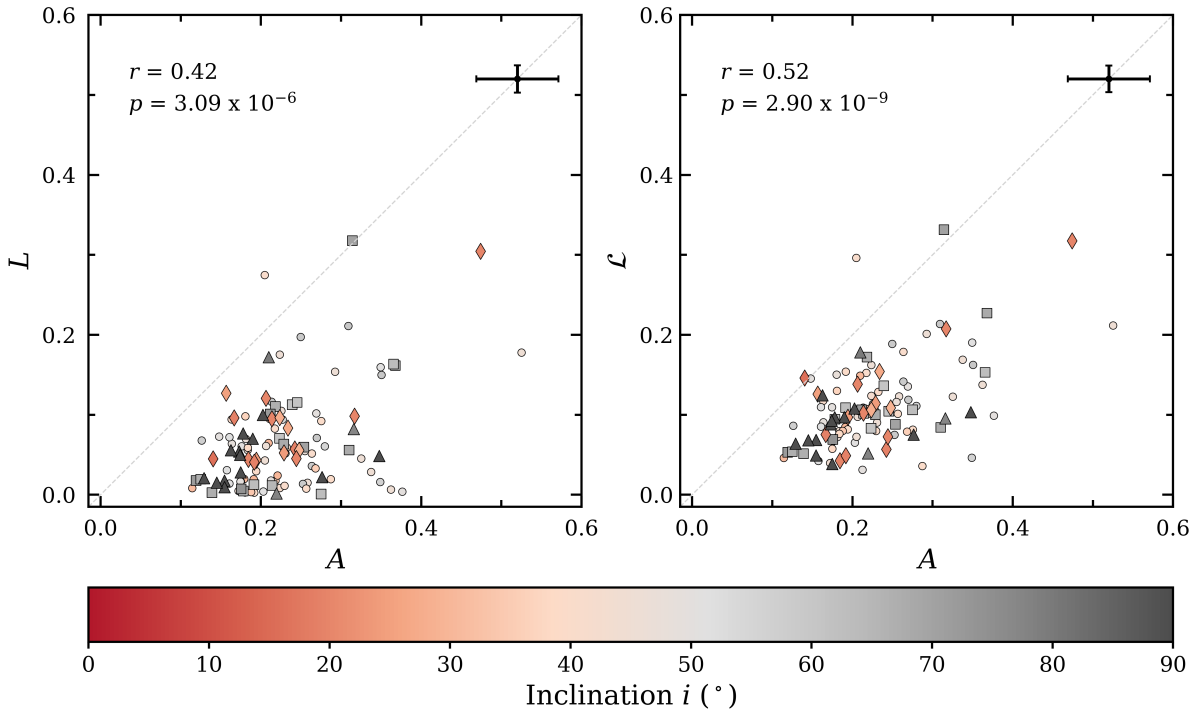

Figure 5.5: The 1D parameters L (left) and $\mathcal{L}$ (right) as a function of the 2D intensity-weighted asymmetry A for the sample of 115 WHISP galaxies. The colour of the data represents the inclination. The Pearson correlation coefficient and associated p-value for the entire sample are quoted in the upper left corner of each panel.

parameter space. While it is possible to make use of simulated data to explore this topic, a larger sample must be used in future work.

Proceeding to galaxies with moderately high inclinations, shown as grey square markers in Figure 5.5, we find that these galaxies display a wide range of values for both the 1D parameters and A. In both panels of the figure, there appears to be great overlap between the square and circle markers in terms of their placement in parameter space. This suggests that the measured A parameters for these galaxies have not started to suffer from inclination effects at $60^\circ < i \leq 75^\circ$, given that the square markers in the right panel of Figure 5.5 appear to emulate the linear trend observed with the circle markers in the same panel.

Nearly edge-on galaxies display quite different trends compared to the subcategories of galaxies discussed in the previous paragraphs. These galaxies are observed residing on what appears to be two 'branches' of triangle markers that connect at A~0.13 in both panels. Of the 16 galaxies with inclinations in the range $75^\circ < i \leq 90^\circ$, 12 galaxies have relatively low measured A values ($A \lesssim 0.21$) and are located on the leftmost branch closest to the 1:1 reference line. This branch appears to have a steeper slope in the left panel than in the right panel, although in both cases it extends to $L, \mathcal{L} \approx 0.18$. The grouping of galaxies on this branch at moderately low A values suggests that the 2D parameters are being underestimated because the full spatial extent of the galaxies cannot be observed, which is in agreement with the findings of Giese et al. (2016). The second branch of

highly inclined galaxies has a much flatter slope and only consists of 4 galaxies which all measure $A \gtrsim 0.21$ despite returning relatively low values for L and $\mathcal{L}$. These galaxies are UGC 2141, 5960, 7603 and 8331. Upon inspecting their HI images, we find that these galaxies all have some form of extra-planar HI emission. Recall the discussion from §4.2 regarding the trend of inflated A values for nearly edge-on simulated galaxies; the likely reason these 4 galaxies do not cluster with the other edge-on galaxies is because the presence of extra-planar gas increases the A value measured for an otherwise thin gas disk. It should be noted that the use of segmentation maps could exclude this extra-planar gas from the calculation of the 2D parameters, in which case these galaxies would likely cluster with galaxies in the first branch. However, as previously mentioned, this will be investigated in future work.

Having examined where low and high inclination galaxies reside in parameter space, we now direct our attention to establishing the optimal inclination limits for this sample. We opt not to use the limits applied in §4.2 since our simulated sample and our WHISP sample are spread differently in parameter space, as evidenced in Figure 5.5 and the left panels of Figure 4.5. Suppose we postulate that an intrinsic linear relationship exists between the 2D A parameter and the 1D L and $\mathcal{L}$ parameters, and that galaxies suffering from inclination effects deviate from this relationship. If this is the case, then the Pearson correlation coefficient, which has been used to quantify the linear relation between the 1D and 2D parameters, should presumably increase with the removal of these affected galaxies. To explore this further, we have applied various cuts to the sample by stepping through possible lower and upper inclination limits, in 5° increments, below 30° and above 60° respectively. For each limit pairing, the Pearson correlation coefficient and corresponding p-value are calculated between A and L (r_{AL}), and A and $\mathcal{L}$ ($r_{A\mathcal{L}}$). These results and the remaining sample size are presented in Table 5.5, where the lower and upper inclination limits are given in the row and column headers.

From the last columns of subtables 5.5a and 5.5c, it is evident that both correlation coefficients decrease if lower limits of 25° or 30° are used. This is due to the removal of UGC 4862 which was mentioned when analysing the placement of low inclination galaxies in Figure 5.5. To verify this, we recalculated the correlation coefficients with UGC 4862 removed from the sample and find that $r_{AL} = 0.34$, $p = 2.09 \times 10^{-4}$, and $r_{A\mathcal{L}} = 0.45$, $p = 3.89 \times 10^{-7}$. This illustrates that our measured correlation coefficients are inflated due to the presence of UGC 4862 in our sample and in its absence, a strict lower inclination limit does not significantly change the correlation coefficients. However, it is not sensible to exclude UGC 4862 from the sample simply because it returns high 1D and 2D parameters, given that it has been visually classified as severely asymmetric in both its spatial distribution and global HI profile. Furthermore, Deg et al. (2020) demonstrated that the lopsidedness parameters are measured fairly accurately for galaxies with $i > 15° - 20°$, provided the profiles meet the resolution element prerequisite (~20 channels at low S/N).

Table 5.5: Pearson correlation coefficients measured between the 2D intensity-weighted asymmetry parameter A and 1D lopsidedness parameters, L and $\mathcal{L}$, for various lower and upper inclination cuts imposed on the WHISP sample.

i (°)	60	65	70	75	80	85	90
15	0.36	0.38	0.42	0.43	0.42	0.42	0.42
20	0.37	0.39	0.43	0.44	0.42	0.42	0.42
25	0.23	0.27	0.34	0.35	0.34	0.34	0.35
30	0.26	0.3	0.36	0.37	0.36	0.36	0.36

(a) Pearson correlation coefficient measured for A and L.

i (°)	60	65	70	75	80	85	90
15	9.2×10^{-4}	2.1×10^{-4}	1.8×10^{-5}	8.6×10^{-6}	1.2×10^{-5}	1.2×10^{-5}	3.1×10^{-6}
20	1.1×10^{-3}	2.4×10^{-4}	2.2×10^{-5}	1.1×10^{-5}	1.5×10^{-5}	1.5×10^{-5}	3.6×10^{-6}
25	5.4×10^{-2}	1.6×10^{-2}	1.5×10^{-3}	8.3×10^{-4}	1.0×10^{-3}	1.0×10^{-3}	3.5×10^{-4}
30	3.7×10^{-2}	1.1×10^{-2}	1.0×10^{-3}	5.5×10^{-4}	6.9×10^{-4}	6.9×10^{-4}	2.4×10^{-4}

(b) Corresponding p-values for table (a).

i (°)	60	65	70	75	80	85	90
15	0.49	0.50	0.52	0.53	0.51	0.51	0.52
20	0.51	0.51	0.53	0.54	0.52	0.52	0.53
25	0.39	0.40	0.44	0.46	0.44	0.44	0.46
30	0.40	0.41	0.45	0.47	0.45	0.45	0.46

(c) Pearson correlation coefficient measured for A and $\mathcal{L}$.

i (°)	60	65	70	75	80	85	90
15	3.3×10^{-6}	8.6×10^{-7}	6.5×10^{-8}	1.7×10^{-8}	3.6×10^{-8}	3.6×10^{-8}	2.9×10^{-9}
20	2.8×10^{-6}	6.9×10^{-7}	5.8×10^{-8}	1.4×10^{-8}	3.0×10^{-8}	3.0×10^{-8}	2.1×10^{-9}
25	1.1×10^{-3}	3.9×10^{-4}	2.3×10^{-5}	6.9×10^{-6}	1.3×10^{-5}	1.3×10^{-5}	1.3×10^{-6}
30	1.1×10^{-3}	3.9×10^{-4}	2.6×10^{-5}	7.7×10^{-6}	1.4×10^{-5}	1.4×10^{-5}	1.4×10^{-6}

(d) Corresponding p-values for table (c).

i (°)	60	65	70	75	80	85	90
15	80	88	96	99	102	102	115
20	76	84	92	95	98	98	111
25	68	76	84	87	90	90	103
30	64	72	80	83	86	86	99

(e) Remaining sample size.

There is generally little variation in r_{AL} and $r_{A\mathcal{L}}$ when most of the upper inclination limits are imposed on the sample, with the exception of the strict limits of 60° and 65°, where both correlation coefficients decrease. Similar to what happened with the strict lower

limits, this reduction is linked to the exclusion of three galaxies: UGC 5351, 5935 and 8201, which have inclinations of 70°, 68° and 63° respectively, and are shown as the grey square markers with $A > 0.3$ and $L, \mathcal{L} > 0.15$ in Figure 5.5. When these galaxies are removed from the sample, we find that $r_{AL} = 0.37$, $p = 5.89 \times 10^{-5}$ and $r_{A\mathcal{L}} = 0.49$, $p = 4.05 \times 10^{-8}$. This indicates that the measured correlation coefficients are particularly sensitive to the presence of galaxies with high 1D and 2D parameters, which are scarce in comparison to the remainder of galaxies in the sample.

Taking these observed trends into consideration, we propose 20° and 70° as the inclination limits to be applied to the sample. Although r_{AL} and $r_{A\mathcal{L}}$ both measure slightly stronger correlations when considering galaxies within the range $20° \leq i \leq 75°$, as shown in Table 5.5, we opt for a marginally stricter upper limit that allows us to ensure that nearly-edge on galaxies have been removed while still retaining 80% of the sample.

5.3 Interacting galaxies in WHISP

One aspect we have yet to explore is the location of interacting galaxies in parameter space, and whether the joint use of the 1D and 2D lopsidedness and asymmetry parameters can be used as a diagnostic tool to identify interacting and merging galaxies. Of the 92 galaxies remaining in the sample after applying the inclination cut proposed in §5.2.1, 21 were visually identified in Swaters et al. (2002) or Noordermeer et al. (2005) to be involved in ongoing interactions (see Table A.1). The term non-interacting, as used in the mentioned literature, refers to galaxies that do not display signs of an interaction. Given the subjectivity of visual classifications, it is possible that some galaxies classified as non-interacting may be involved in minor interactions. However, for the purpose of this work, interacting and non-interacting galaxies will be treated as separate subsamples.

Before examining parameter space, it is important to investigate how these samples are distributed for the individual parameters. Figure 5.6 shows the normalised distributions of parameter values for interacting and non-interacting galaxies, shown as hatched and grey histograms respectively. We once again make use of the K-S test statistic D, quoted in the top right corner of each panel along with the p-value, to quantitatively compare the distributions of these samples. At the 1% significance level, we find that L is the only parameter where we cannot reject the null hypothesis that interacting and non-interacting galaxies are drawn from the same distribution, as the 1% critical value for sample sizes of 21 and 71 is 0.4. This is not surprising given the large overlap between the distributions of L for both subsamples, as shown in the top left panel of Figure 5.6. The majority of galaxies in both subsamples have low values of L (~57% of interacting galaxies and ~85% of non-interacting galaxies have $L < 0.1$).

A similar trend is observed with $\mathcal{L}$, shown in the top right panel, in that the majority of galaxies (~52% and ~86% of interacting and non-interacting galaxies respectively) have $\mathcal{L} < 0.15$. Because such a large percentage of non-interacting galaxies have low-

intermediate measured values of L and $\mathcal{L}$, we find that there is a higher percentage of interacting galaxies at higher 1D values than there are non-interacting galaxies. However, this does not necessarily translate to more galaxies as there are ~3.4 times as many non-interacting galaxies as there are interacting in our sample. While the general shape of the L and $\mathcal{L}$ distributions is the same for both subsamples, the distribution of both parameters extends to higher values for the interacting galaxies.

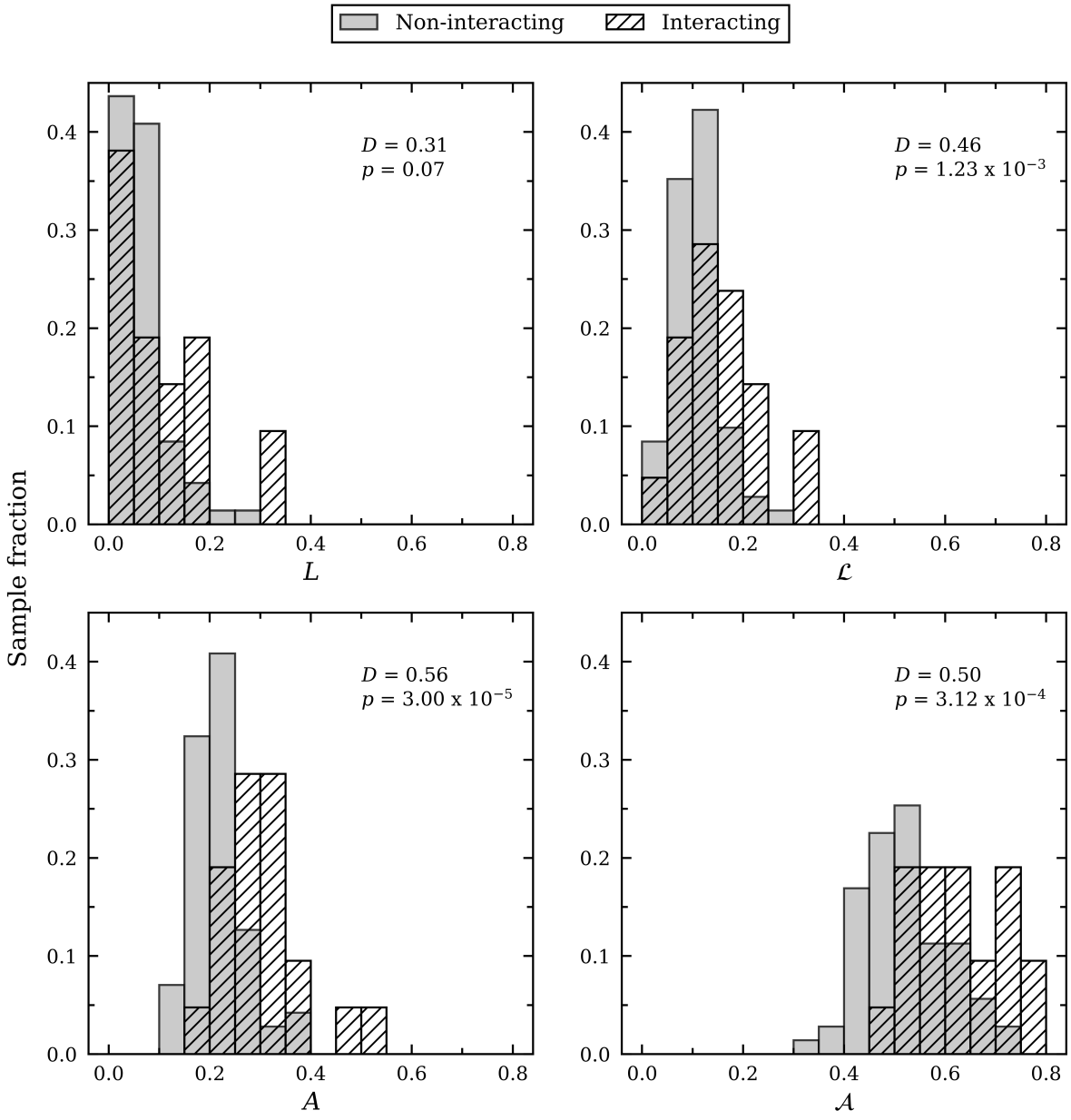

Figure 5.6: Normalised distributions of the 1D lopsidedness (top row) and 2D asymmetry (bottom row) parameters for interacting (hatched histogram) and non-interacting (grey histogram) galaxies. The K-S statistic D and p-value are quoted in the upper right corner of each panel.

Regarding the distributions of 2D parameters, shown in the bottom row of Figure 5.6, there is a clear shift towards higher values for the interacting subsample, resulting in less overlap at low values of A and $\mathcal{A}$, as well as extended distribution tails towards high 2D

values. This is especially noticeable with A, where we find that ~80% of non-interacting galaxies have $A < 0.25$ in comparison to just ~24% of interacting galaxies. Despite the considerable overlap with the distributions of $\mathcal{A}$, this trend is still observed, with ~43% and ~80% of interacting and non-interacting galaxies measuring $\mathcal{A} < 0.6$. These findings in combination with the results of the K-S tests suggest that the 2D parameters are more effective than the 1D parameters at roughly separating the two subsamples without inadvertently excluding a large percentage of interacting galaxies.

We return to parameter space to determine if a combination of these parameters may be more successful in separating the two subsamples than the use of a single parameter. Figure 5.7 shows the correlations between the four parameters for galaxies in the WHISP sample, where interacting and non-interacting galaxies are represented by red star and grey circle markers respectively. While the work presented in §5.2 focussed specifically on the correlations between the 1D and 2D parameters, it is also worth examining the placement of interacting galaxies when the 1D (and 2D) parameters are plotted against each other. The distribution of galaxies in the $A - \mathcal{A}$ (top left) and $\mathcal{L} - L$ (bottom right) panels of Figure 5.7 show that the parameters are strongly correlated. In the case of the 2D parameters, this relation is expected as this observation was made in §5.2 when discussing Figure 5.4. This panel shows that galaxies with high intensity-weighted asymmetry ($A \geq 0.3$) are likely to have high outer asymmetry ($\mathcal{A} \geq 0.6$).

Interestingly, the $\mathcal{L}-L$ panel shows a broadened cone-like distribution at low L values that appears to converge at higher values of L. This broad distribution at low values of L hints at the inability of L to effectively quantify small-scale asymmetries in some profiles. For 26 galaxies (28% of the sample), the absolute difference between the 1D parameters is < 0.02 (see Figure C.12). While this illustrates that the majority of galaxies have non-negligible differences between the parameters, it also shows that galaxies with small differences between the measured parameters occur at various values of L. This is of particular importance as it confirms the assertion from §2.1.2 that for truly symmetric and asymmetric profiles, there should be no substantial difference between L and $\mathcal{L}$.

Although Holwerda et al. (2011b) and Giese et al. (2016) identified a number of selection criteria, we have chosen not to adopt these criteria and briefly motivate this decision below. Although this work uses the same sample* as the mentioned literature, A is the only common parameter and so it it necessary to establish selection criteria using the other parameters in this work. Giese et al. (2016) also showed that for galaxies in the WHISP sample and for model galaxies, a decrease in angular resolution results in a decrease in the measured A parameter. Thus, it is unsuitable to adopt the selection criteria proposed in Holwerda et al. (2011b) or Giese et al. (2016), as both papers used HI images constructed from the highest resolution WHISP data cubes in order to calculate A. Lastly, Holwerda et al. (2011b) and Giese et al. (2016) both used the optical centre as the rotation point

* Recall that our sample is smaller due to the removal of galaxies with complex HI images or spectra (discussed in Chapter 3), as well as our imposed inclination cut.

when calculating A which, as discussed in §2.2.1, affects the measured value of A.

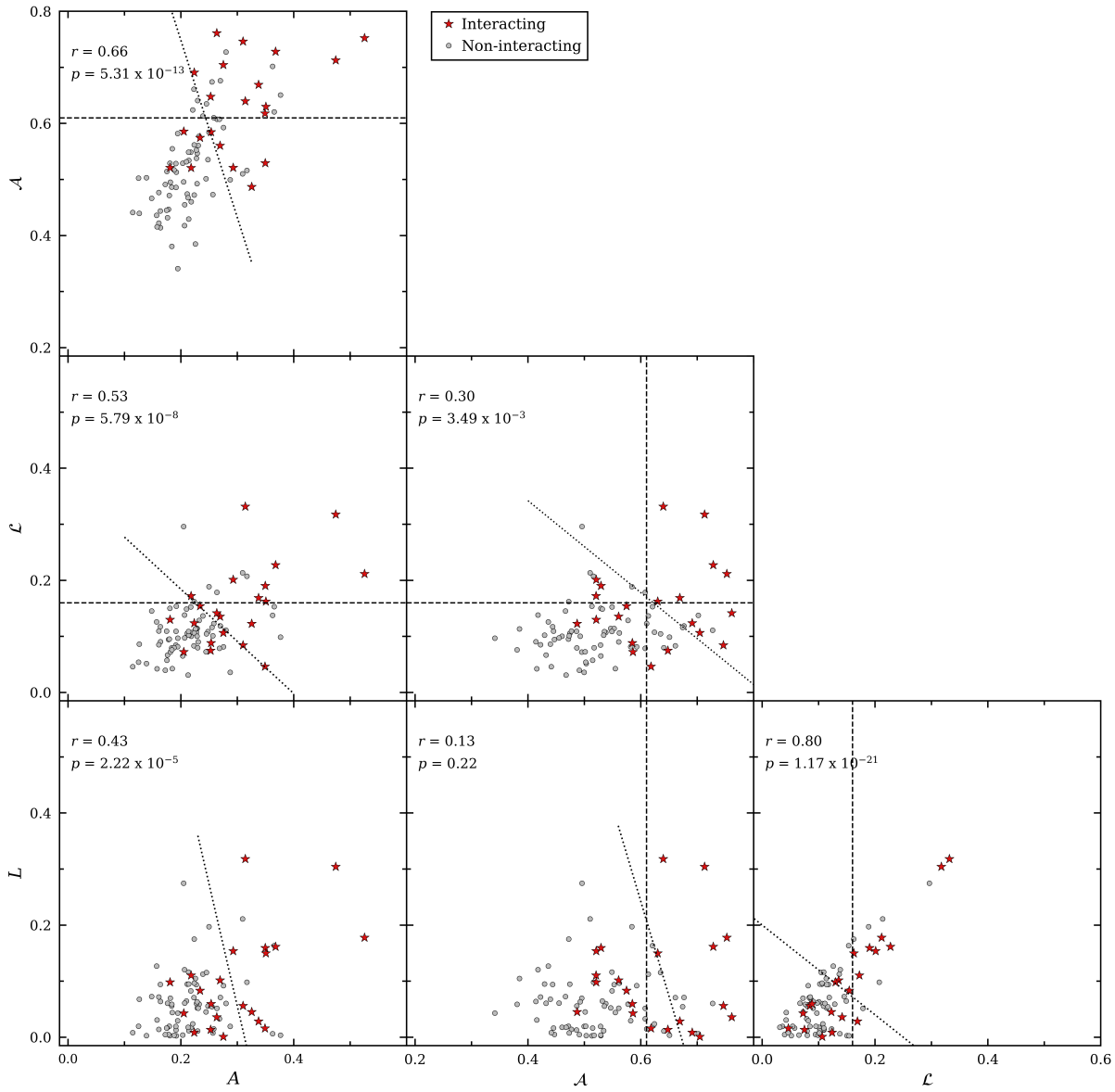

Figure 5.7: Relations between the 1D lopsidedness (L and $\mathcal{L}$) and 2D asymmetry (A and $\mathcal{A}$) parameters for the interacting (red stars) and non-interacting (grey circles) galaxies in the WHISP sample with inclinations $20° \leq i \leq 70°$. The Pearson correlation coefficient and associated p-value are quoted in the upper left corner of each panel. The dotted lines in each panel indicate regions where interacting and non-interacting galaxies are well separated, and the dashed lines in certain panels correspond to criteria (h) and (j).

For each pair of parameters, we define a criterion that maximises the number of interacting galaxies identified. Due to the difference in the subsample sizes and the general overlap in all panels of Figure 5.7, we impose a condition that the number of non-interacting galaxies incorrectly identified by the criterion cannot exceed the number of interacting galaxies. These criteria are illustrated as dotted lines in Figure 5.7 and are listed (a) - (f) in Table 5.6. Four additional criteria, listed (i) - (j) in Table 5.6, are identified based on the distributions of the parameters shown in Figure 5.6. For each criterion, as well as a combination of the various criteria, we calculate the completeness as well as

the purity. We find that criteria (a), (b) and (g) perform moderately well and are able to correctly identify more than 70% of interacting galaxies in the sample. However, these criteria end up including a substantial number of non-interacting galaxies.

Table 5.6: Number of interacting (N_{int}) and non-interacting (N_{non}) galaxies classified as interacting using the specified criterion.

Selection criterion	N_{int}	N_{non}	Completeness (%)	Purity (%)
Visual classification	21	71	–	–
(a) $\mathcal{A} \geq -3.16 \times A + 1.38$	17	14	81	55
(b) $\mathcal{L} \geq -0.93 \times A + 0.37$	15	10	71	60
(c) $\mathcal{L} \geq -0.82 \times \mathcal{A} + 0.67$	10	5	48	67
(d) $L \geq -4.35 \times A + 1.36$	11	5	52	69
(e) $L \geq -3.38 \times \mathcal{A} + 2.27$	10	5	48	67
(f) $L \geq -0.8 \times \mathcal{L} + 0.2$	11	11	52	50
(g) $A \geq 0.25$	16	14	76	53
(h) $\mathcal{A} \geq 0.61$	12	12	57	50
(i) $L \geq 0.12$	7	7	33	50
(j) $\mathcal{L} \geq 0.16$	9	6	43	60
(b) $\cap$ (e)	8	2	38	80
(c) $\cap$ (d)	7	1	33	87
(g) $\cap$ (h)	11	7	52	61
(h) $\cap$ (j)	6	0	29	100
(i) $\cap$ (j)	7	4	33	64

All criteria that feature the intensity-weighted A parameter are able to recover at least 50% of the interacting galaxies in the reduced WHISP sample. This comes as no surprise given the results of the K-S tests, which indicated that A is more effective than the other three parameters at separating the two subsamples. Criteria (c) - (f) and (h) - (j) are generally less successful at correctly identifying interacting galaxies and still experience considerable contamination.

When used separately, none of the criteria are able to completely separate interacting and non-interacting galaxies in parameter space. While numerous combinations of the criteria were considered, only five of the best performing combinations have been included in Table 5.6. Interestingly, we find that the combined criteria of $\mathcal{A} \geq 0.61$ and $\mathcal{L} \geq 0.16$ is the only pairing where no non-interacting galaxies are incorrectly identified (i.e. 100% purity). Consequently, it is only able to correctly identify ~29% of interacting galaxies, which is the lowest success rate of all the criteria. However, we find that that all 6 galaxies which meet criteria (h) and (j) have $A > 0.3$, and 5 have $L > 0.15$, surpassing the conditions of criteria (g) and (i). This indicates that galaxies which measure high $\mathcal{A}$ and $\mathcal{L}$ values are likely to measure high values for A and L.

Regarding the use of the 2D parameters, and optimising for completeness, criterion (a) appears to be of more value than the combined use of criteria (g) and (h). Furthermore, the use of criterion (g) or (h) in combination with (a) does little to increase the purity.

Of the criteria pertaining solely to the 1D parameters (f, i and j), criterion (f) appears to return the highest completeness, while criterion (j) gives a sample with a higher purity. The combined use of (i) and (j) slightly increases the purity, but significantly reduces the completeness.

Chapter 6

Discussion and future prospects

6.1 Discussion

As referenced in Chapters 1 and 2, a considerable amount of work on non-parametric spectral and morphological measurements exists in the literature. What follows is a brief comparison of the results in this thesis with key findings of 1D and 2D asymmetries using observations and simulations.

6.1.1 Comparison to theoretical studies

Numerous studies have used idealised merger simulations (e.g. Lotz et al. 2008a; Holwerda et al. 2011c; Starkenburg et al. 2016) and cosmological simulations (e.g. Snyder et al. 2015a,b; Bignone et al. 2017; Abruzzo et al. 2018) to explore 2D non-parametric morphological measurements. For this comparison, we focus on studies that have examined the temporal evolution of 2D asymmetry.

We find that the general behaviour of the intensity-weighted A parameter measured for the stellar distribution (A_S) over the course of the merger event and shown by the solid red line in Figure 4.2, is in agreement with the temporal evolution of A for the Sbc radial orbit merger investigated by Lotz et al. (2008a) (see the last column of Figure 11 from Lotz et al. 2008a). In both simulations, the stellar distribution is most asymmetric shortly after the initial encounter of the galaxies but measures relatively low values of A during the final merger. This agreement in the evolution of A_S is not surprising as the galaxies in our simulation are also initialised on an approximately radial orbit, as mentioned in §3.1.2, and it was shown in Lotz et al. (2008a) that the orbital parameters of a merger can significantly affect the time-scales as well as the strength of these morphological disturbances.

With respect to the intensity-weighted A parameter measured for the gas distribution (A_G), we do not find much agreement with the results of Holwerda et al. (2011c), who studied the non-parametric morphologies measured for H I in passively evolving galaxies and merging systems. This could be due to the difference in orbital parameters of our

simulations and the fact that we minimise A_G using the CoS of the gas distribution, whereas Holwerda et al. (2011c) use the centre of the dark matter halo when rotating the galaxy image.

Interestingly, we observe some similar trends to that of Starkenburg et al. (2016), who studied minor mergers between dwarf galaxies and dark satellites. In both simulations, we observe the first increase in A_G leading up to the initial encounter, and a greater increase leading up to the second encounter. The evolution of the gas distributions in our simulations differ hereafter, as we observe a sharp decrease in A_G before the final coalescence of the nuclei, whereas Starkenburg et al. (2016) measure a heightened A_G until after the minor merger. We suspect that this is due to the intrinsic difference between our merger events. As mentioned in §4.1, after the second pass of the galaxies in our merger event, the merging system is treated as a single object and the inclusion of gas and stellar particles from the second galaxy has an effect on the measured values of A_G and A_S. However, because the merger investigated in Starkenburg et al. (2016) occurs between a dwarf galaxy and a dark satellite, there is no sudden inclusion of gas particles from the satellite galaxy at later stages of the merger.

Starkenburg et al. (2016) also identified upper limits for the intensity-weighted asymmetry (A) and the outer asymmetry ($\mathcal{A}$) measured for the gas and stellar distributions of isolated systems. The authors remark that it is easier to delineate regions of parameter space where isolated systems are likely to reside, as merging systems occupy a much larger region due to the time variability of these parameters. However, it follows that galaxies with asymmetry parameters greater than these limits are more likely to be merging. The identified limits are $A_G < 0.19$, $A_S < 0.15$ and $\mathcal{A} < 0.4$ for both distributions. It should be noted that we have adjusted the limits for A as there is a factor of 2 difference between the asymmetry equation used in this work (Equation 2.3) and the one used by Starkenburg et al. (2016). Applying these limits to our simulation, we find that A_G is only above this limit during the interaction* while A_S lies above the limit during both the pre-merger and interaction stages. In contrast, the outer asymmetry of both distributions lies above the limit for the entirety of the simulation. There are a variety of reasons why our results may differ from Starkenburg et al. (2016), the chief of which is that we have not implemented any column density or surface brightness cuts to our distributions. This points to the importance of evaluating the sensitivity of observations (and simulations) before applying limits on the classification of an object.

When considering the effects that inclination and viewing angle have on the 1D and 2D asymmetry parameters of our simulation at two time-steps prior to the merger stage, we found that inclination limits of $10^\circ \leq i \leq 60^\circ$ were required. The upper inclination limit is the same as the recommendation by Giese et al. (2016). In our simulations, edge-on galaxies measured inflated 2D parameters due to extra-planar gas particles. We

* In this context, interaction refers to the first pass, maximal separation and merger stages as defined in Chapter 4.

also required a lower inclination limit of 10° to account for the inclination effects on the extracted 1D spectra. Below this limit, the profiles are too narrow for a reliable calculation of the 1D lopsidedness parameters.

6.1.2 Comparison to observational studies

From an observational perspective, we studied the 1D lopsidedness and 2D asymmetry parameters for 115 WHISP galaxies. As outlined in Chapter 3, our initial sample of 130 galaxies, which has been studied previously in Holwerda et al. (2011b) and Giese et al. (2016), was first reduced due to our requirements that the HI spectra be clearly measured with an appropriate pedestal subtraction. The sample was reduced further to 92 galaxies after imposing inclination cuts to remove galaxies with inclinations outside the range $20° \leq i \leq 70°$.

Using this inclination-reduced sample, we are able to compare the lopsidedness parameter, L, for both an interacting and non-interacting sample of galaxies with results from the literature. Table 6.1 summarises the comparison to spectral lopsidedness for a variety of studies, organised by galaxy environment. As mentioned previously, Espada et al. (2011) found that the distribution of A_{1D}, measured for a sample of isolated galaxies, could be described by a half-Gaussian with a width of $\sigma_{A_{1D}} = 0.13$. The authors then classified a galaxy as asymmetric if $A_{1D} > 2\sigma_{A_{1D}}$ (1.26), which corresponds to $L > 0.12$ in our notation. This threshold has been commonly used in the literature to calculate an HI lopsidedness rate and we provide these values in the third column of Table 6.1 for various studies.

We find that the lopsidedness rate in our non-interacting subsample (10%) is in good agreement with that of other isolated samples (e.g. Haynes et al. 1998; Matthews et al. 1998; Espada et al. 2011; Bok et al. 2019). We also observe that our interacting subsample has a higher fraction of galaxies with $L > 0.12$ (33%) than the non-interacting subsample, which is consistent with the findings of samples in high density environments (e.g. Scott et al. 2018; Bok et al. 2019). In the context of this work, this result corroborates the findings of Bok et al. (2019), in that galaxy-galaxy interactions appear to be responsible for the increase in the lopsidedness rate of the interacting sample.

In Chapter 2, we introduced the folding difference lopsidedness, $\mathcal{L}$, which is a precursor to the 1D asymmetry statistic used in Deg et al. (2020). They found, as previously mentioned in §2.1.2, that a background subtraction term is necessary for lower S/N spectra. However, the WHISP data used have sufficient S/N ratios that the background term is small. The $\mathcal{L}$ parameter is similar to the flipped spectrum residual defined by Reynolds et al. (2020), although it should be noted that there is a difference in the normalisation of the two parameters. Reynolds et al. (2020) found that the flipped spectrum residual was better than the lopsidedness at distinguishing between samples in different density environments. Although our work didn't investigate environment directly, we find a similar

Table 6.1: Comparison between the HI lopsidedness rates of the interacting and non-interacting subsamples examined in this work, and other samples in the literature.

Galaxy sample	Sample size	$L > 0.12$ (%)
Low density/isolated samples		
Haynes et al. (1998)	104	9
Espada et al. (2011)	166	9
Matthews et al. (1998)	30	17
HI isolated sample (Bok et al. 2019)	304	18
Medium density/field samples		
HALOGAS subsample (Reynolds et al. 2020)	18	0
LVHIS subsample (Reynolds et al. 2020)	73	8
Bournaud et al. (2005)	76	22
High density/interacting pair samples		
VIVA subsample (Reynolds et al. 2020)	45	20
HI-optical pair sample (Bok et al. 2019)	304	27
Scott et al. (2018)	43	40
This work		
Non-interacting WHISP subsample	71	10
Interacting WHISP subsample	21	33

result, in that $\mathcal{L}$ is the preferred 1D lopsidedness parameter for separating the interacting and non-interacting subsamples.

In §5.3 we also explored the use of the 2D asymmetry parameters to distinguish between the interacting and non-interacting samples. We find that the criterion using both the 2D asymmetry parameters ($\mathcal{A} \geq -3.16 \times A + 1.38$, see Table 5.6) provides a good balance of completeness and purity. Our criteria results are not directly comparable to those found by Giese et al. (2016), who optimised for sample purity. Furthermore, it should be noted that their preferred criteria use other non-parametric morphological measures that we have not studied in this work.

Lastly, the inclination-reduced WHISP sample was used to investigate the correlation between the 1D and 2D asymmetry measures. We found that both 1D lopsidedness parameters correlate moderately with the intensity-weighted A parameter and the strongest correlation was measured for A and $\mathcal{L}$ ($r = 0.53$). This is similar to, but stronger than, the result found by Reynolds et al. (2020), when comparing their flipped spectrum residual with their moment-0 asymmetry ($r = 0.34$). Our linear correlations measured between A and L are also in agreement ($r = 0.43$ in our work vs. $r = 0.38$ in Reynolds et al. 2020). One possible reason for the stronger correlations is that we minimise A, whereas Reynolds et al. (2020) rotate the image around the galaxy's HI flux centre of mass. Another reason could be due to the fact that we imposed inclination cuts on our sample, which resulted in a marginal increase in the calculated correlation.

6.2 Thesis summary and conclusion

In this thesis, we used idealised equilibrium simulations and archival HI data to study the applicability of various 1D and 2D asymmetry measures. There were four primary aims to this work: (1) investigate the time evolution of the 2D parameters over a simulated major merger, (2) examine the agreement between various statistics and visual classifications of asymmetry, (3) investigate whether the 1D and 2D parameters are linearly correlated, and (4) explore if interacting and non-interacting samples have statistically different asymmetry distributions.

The main results from the simulations are:

- At both the start and end of the merger event, $A_S > A_G$, suggesting that the central region of the gas distribution is only more asymmetric than that of the stellar distribution in between the first pass of the galaxies and the eventual coalescence of the nuclei.
- Conversely, $\mathcal{A}_S > \mathcal{A}_G$ at the start of the merger but the outer asymmetry of the gas distribution becomes more asymmetric at ~T = 1.26 Gyr during the First Pass stage. For the remainder of the merger, $\mathcal{A}_G > \mathcal{A}_S$, indicating that the merger leaves the outskirts of the gas distribution more asymmetric. Despite this observation, this has little effect on the measured value of A_G because the outskirts of the gas distribution have lower column densities than the central region.
- The outer asymmetry of both distributions is statistically different and higher than the intensity-weighted asymmetries in the post-merger stage compared to the pre-merger stage. This trend is particularly evident with the gas distribution. However, the implementation of column density and surface brightness cuts would affect this observation.
- When comparing the gas distributions of the central galaxy at two different time-steps in the merger, the 2D parameters are distinctly different, whereas there is marginal overlap of the 1D parameters at low values (L, $\mathcal{L} < 0.1$). However, we find that we only measure high values for L and $\mathcal{L}$ in the time-step after the first pass, when the galaxies are approaching maximal separation. In the absence of noise, this result suggests that a high 1D lopsidedness is indicative of some external process, in this case a major merger, taking place.
- The 2D asymmetry parameters, within a defined inclination range ($10^\circ \leq i \leq 60^\circ$ in the case of our simulations), display less variation than the 1D lopsidedness parameters when viewing angle and inclination are altered for a single galaxy.

From the analysis of the WHISP sample, the key findings are:

- The folding difference lopsidedness, $\mathcal{L}$, better corresponds to visual classifications of asymmetry in the HI spectra than the lopsidedness. Similarly, the intensity-weighted

asymmetry parameter A better corresponds to visual classifications of asymmetry in the HI images than the outer asymmetry.

- After inclination cuts have been applied, we measure a moderate linear relation between A and L ($r = 0.42$), and A and $\mathcal{L}$ ($r = 0.53$). Additionally, we find that galaxies with high 1D values are likely to have high 2D values, but the inverse is not true. This implies that galaxies with highly asymmetric HI spectra have disturbed HI morphologies. This result is particularly important for future work where we cannot spatially resolve the HI distributions of galaxies.
- The joint use of the 2D parameters is moderately successful at distinguishing between interacting and non-interacting galaxies (see Table 5.6). The combination of 1D and 2D parameters can also be used to separate these samples, but with less success. However, the 1D statistics alone cannot effectively classify interacting and non-interacting galaxies.

In summary, asymmetry measures are powerful tools for studying the HI in large surveys of galaxies. There are many processes that may disturb the morphology of a galaxy and, as we have shown, these statistics can help to identify disturbed galaxies. The 2D asymmetry parameters should be preferred over 1D parameters when studying mergers. However, the spectral lopsidedness parameters presented in this work can still be used with a great deal of success. We have shown that highly asymmetric HI spectra broadly correspond to disturbed HI morphologies. And, while not studied in this thesis, spectral asymmetries may be sensitive to processes that may not be easily detected in HI images, like gas accretion. Moreover, there are orders of magnitude more HI spectra than there are HI images, which enables the study of these processes in large samples across different environments. The study of asymmetries is particularly exciting in the context of upcoming surveys on the SKA pathfinder telescopes, which will observe thousands of spatially resolved galaxies and millions of spectra. The wealth of HI data to come from these instruments will enable the use of asymmetries to investigate the underlying processes that govern galaxy evolution in different galaxy populations across different epochs of the Universe.

6.3 Future prospects

There are various aspects of this work that can be built on and investigated further. The outer asymmetry parameter ($\mathcal{A}$) used in this thesis is a relatively recent statistic that requires further investigation. It is important to explore the effect of realistic column density limits on the measurement of $\mathcal{A}$ and whether the trends seen in its evolution remain in more realistic observations. It is also worth exploring, in greater detail, the effects of observational biases on $\mathcal{A}$ in order to better understand the virtues and limitations of using the parameter in conjunction with A in larger HI imaging studies.

More generally, many theoretical studies that have used non-parametric morphological measurements on galaxies from cosmological simulations have focussed their investigations on the optical morphologies of these galaxies. Studying the HI morphologies of galaxies modelled in the cosmological environment will complement the first portion of this work as our simulations did not include physical processes, such as star formation and feedback mechanisms, which would affect a galaxy's HI distribution. The large samples obtainable with cosmological simulations allow the investigation of different mechanisms for causing asymmetric morphologies. They also enable the study of population asymmetries in different environments and different redshifts. Most importantly, the study of HI asymmetries in cosmological simulations can be used to relate observational results from upcoming HI surveys to the dynamical astrophysical processes that govern galaxy evolution over cosmic time.

In the near future, upcoming HI surveys with large volumes of galaxies in the local Universe (e.g. MIGHTEE and/or WALLABY) can be used to study and cement the statistical connection between the spectral and morphological asymmetries in spatially resolved galaxies. These results can then be related to the spectral asymmetries measured for the spatially unresolved distant galaxies that will be observed in the LADUMA survey.

Bibliography

Abraham R. G., Tanvir N. R., Santiago B. X., Ellis R. S., Glazebrook K., van den Bergh S., 1996, Monthly Notices of The Royal Astronomical Society, 279, L47

Abraham R. G., van den Bergh S., Nair P., 2003, The Astrophysical Journal, 588, 218

Abruzzo M. W., Narayanan D., Davé R., Thompson R., 2018, preprint, (arXiv:1803.02374)

Angiras R. A., Jog C. J., Omar A., Dwarakanath K. S., 2006, Monthly Notices of The Royal Astronomical Society, 369, 1849

Angiras R. A., Jog C. J., Dwarakanath K. S., Verheijen M. A. W., 2007, Monthly Notices of The Royal Astronomical Society, 378, 276

Arp H., 1966, Astrophysical Journal, Supplement Series, 14, 1

Baldwin J. E., Lynden-Bell D., Sancisi R., 1980, Monthly Notices of The Royal Astronomical Society, 193, 313

Barnes J. E., 2004, Monthly Notices of The Royal Astronomical Society, 350, 798

Barnes J. E., Hernquist L., 1992, Annual Review of Astronomy and Astrophysics, 30, 705

Barnes D. G., et al., 2001, Monthly Notices of The Royal Astronomical Society, 322, 486

Bignone L. A., Tissera P. B., Sillero E., Pedrosa S. E., Pellizza L. J., Lambas D. G., 2017, Monthly Notices of The Royal Astronomical Society, 465, 1106

Bloom J. V., et al., 2017, Monthly Notices of The Royal Astronomical Society, 465, 123

Bloom J. V., et al., 2018, Monthly Notices of The Royal Astronomical Society, 476, 2339

Bluck A. F. L., Conselice C. J., Buitrago F. o., Grützbauch R., Hoyos C., Mortlock A., Bauer A. E., 2012, The Astrophysical Journal, 747, 34

Blyth S., et al., 2016, in MeerKAT Science: On the Pathway to the SKA. p. 4

Bok J., Blyth S. L., Gilbank D. G., Elson E. C., 2019, Monthly Notices of The Royal Astronomical Society, 484, 582

Boomsma R., Oosterloo T. A., Fraternali F., van der Hulst J. M., Sancisi R., 2008, Astronomy & Astrophysics, 490, 555

Bournaud F., Combes F., Jog C. J., Puerari I., 2005, Astronomy & Astrophysics, 438, 507

Broeils A. H., Rhee M. H., 1997, Astronomy & Astrophysics, 324, 877

Bundy K., Fukugita M., Ellis R. S., Kodama T., Conselice C. J., 2004, Astrophysical Journal, Letters, 601, L123

Cappellari M., et al., 2011, Monthly Notices of The Royal Astronomical Society, 413, 813

Catinella B., et al., 2018, Monthly Notices of The Royal Astronomical Society, 476, 875

Chung A., van Gorkom J. H., Kenney J. D. P., Crowl H., Vollmer B., 2009, The Astronomical Journal, 138, 1741

Combes F., Foy F. C., Gottesman S. T., Weliachew L., 1980, Astronomy & Astrophysics, 84, 85

Conselice C. J., 2003, Astrophysical Journal, Supplement Series, 147, 1

Conselice C. J., Bershady M. A., Jangren A., 2000, The Astrophysical Journal, 529, 886

Cox T. J., Jonsson P., Somerville R. S., Primack J. R., Dekel A., 2008, Monthly Notices of The Royal Astronomical Society, 384, 386

Crain R. A., et al., 2015, Monthly Notices of The Royal Astronomical Society, 450, 1937

Davé R., Rafieferantsoa M., 2016, in Proceedings of MeerKAT Science: On the Pathway to the SKA. 25-27 May. p. 25

Davé R., Anglés-Alcázar D., Narayanan D., Li Q., Rafieferantsoa M. H., Appleby S., 2019, Monthly Notices of The Royal Astronomical Society, 486, 2827

Deg N., Widrow L. M., Randriamampandry T., Carignan C., 2019, Monthly Notices of The Royal Astronomical Society, 486, 5391

Deg N., Blyth S. L., Hank N., Kruger S., Carignan C., 2020, Monthly Notices of The Royal Astronomical Society, 495, 1984

Dickey J. M., Salpeter E. E., Terzian Y., 1978, Astrophysical Journal, Supplement Series, 36, 77

Ellison S. L., Viswanathan A., Patton D. R., Bottrell C., McConnachie A. W., Gwyn S., Cuillandre J.-C., 2019, Monthly Notices of The Royal Astronomical Society, 487, 2491

Espada D., Verdes-Montenegro L., Huchtmeier W. K., Sulentic J., Verley S., Leon S., Sabater J., 2011, Astronomy & Astrophysics, 532, A117

Ewen H. I., Purcell E. M., 1951, Nature, 168, 356

Fakhouri O., Ma C.-P., Boylan-Kolchin M., 2010, Monthly Notices of The Royal Astronomical Society, 406, 2267

Ferrière K. M., 2001, Reviews of Modern Physics, 73, 1031

Gajda G., Łokas E. L., Athanassoula E., 2018, The Astrophysical Journal, 868, 100

Genel S., Genzel R., Bouché N., Naab T., Sternberg A., 2009, The Astrophysical Journal, 701, 2002

Giese N., van der Hulst T., Serra P., Oosterloo T., 2016, Monthly Notices of The Royal Astronomical Society, 461, 1656

Gottlöber S., Klypin A., Kravtsov A. V., 2001, The Astrophysical Journal, 546, 223

Grand R. J. J., et al., 2017, Monthly Notices of The Royal Astronomical Society, 467, 179

Gunn J. E., Gott J. Richard I., 1972, The Astrophysical Journal, 176, 1

Haynes M. P., van Zee L., Hogg D. E., Roberts M. S., Maddalena R. J., 1998, The Astronomical Journal, 115, 62

Haynes M. P., et al., 2018, The Astrophysical Journal, 861, 49

Hayward C. C., Narayanan D., Kereš D., Jonsson P., Hopkins P. F., Cox T. J., Hernquist L., 2013, Monthly Notices of The Royal Astronomical Society, 428, 2529

Heald G., et al., 2011, Astronomy & Astrophysics, 526, A118

Henriques B. M. B., Thomas P. A., Oliver S., Roseboom I., 2009, Monthly Notices of The Royal Astronomical Society, 396, 535

Holwerda B. W., Pirzkal N., de Blok W. J. G., Bouchard A., Blyth S. L., van der Heyden K. J., Elson E. C., 2011a, Monthly Notices of The Royal Astronomical Society, 416, 2401

Holwerda B. W., Pirzkal N., de Blok W. J. G., Bouchard A., Blyth S. L., van der Heyden K. J., Elson E. C., 2011b, Monthly Notices of The Royal Astronomical Society, 416, 2415

Holwerda B. W., Pirzkal N., Cox T. J., de Blok W. J. G., Weniger J., Bouchard A., Blyth S. L., van der Heyden K. J., 2011c, Monthly Notices of The Royal Astronomical Society, 416, 2426

Hopkins P. F., Cox T. J., Hernquist L., Narayanan D., Hayward C. C., Murray N., 2013, Monthly Notices of The Royal Astronomical Society, 430, 1901

Jackson C., 2018, in Westerbork Telescope 50th Anniversary. p. 1

Jarvis M., et al., 2016, in MeerKAT Science: On the Pathway to the SKA. p. 6 (arXiv:1709.01901)

Jog C. J., Combes F., 2009, Physics Reports, 471, 75

Jogee S., et al., 2009, The Astrophysical Journal, 697, 1971

Kamphuis J. J., Sijbring D., van Albada T. S., 1996, Astronomy & Astrophysics, Supplement, 116, 15

Kerr F. J., Hindman J. V., 1953, The Astronomical Journal, 58, 218

Kim J.-h., Wise J. H., Abel T., 2009, Astrophysical Journal, Letters, 694, L123

Klypin A. A., Trujillo-Gomez S., Primack J., 2011, The Astrophysical Journal, 740, 102

Koribalski B. S., et al., 2018, Monthly Notices of The Royal Astronomical Society, 478, 1611

Koribalski B. S., et al., 2020, Astrophysics and Space Science, 365, 118

Kornreich D. A., Haynes M. P., Lovelace R. V. E., van Zee L., 2000, The Astronomical Journal, 120, 139

Kuijken K., Dubinski J., 1995, Monthly Notices of The Royal Astronomical Society, 277, 1341

Lagos C. d. P., Tobar R. J., Robotham A. S. G., Obreschkow D., Mitchell P. D., Power C., Elahi P. J., 2018, Monthly Notices of The Royal Astronomical Society, 481, 3573

Lelli F., Verheijen M., Fraternali F., 2014, Monthly Notices of The Royal Astronomical Society, 445, 1694

Lotz J. M., Primack J., Madau P., 2004, The Astronomical Journal, 128, 163

Lotz J. M., Jonsson P., Cox T. J., Primack J. R., 2008a, Monthly Notices of The Royal Astronomical Society, 391, 1137

Lotz J. M., et al., 2008b, The Astrophysical Journal, 672, 177

Lotz J. M., Jonsson P., Cox T. J., Primack J. R., 2010a, Monthly Notices of The Royal Astronomical Society, 404, 575

Lotz J. M., Jonsson P., Cox T. J., Primack J. R., 2010b, Monthly Notices of The Royal Astronomical Society, 404, 590

Lu Y., Mo H. J., Weinberg M. D., Katz N., 2011, Monthly Notices of The Royal Astronomical Society, 416, 1949

Mapelli M., Moore B., Bland-Hawthorn J., 2008, Monthly Notices of The Royal Astronomical Society, 388, 697

Matthews L. D., van Driel W., Gallagher J. S. I., 1998, The Astronomical Journal, 116, 1169

Meurer G. R., Carignan C., Beaulieu S. F., Freeman K. C., 1996, The Astronomical Journal, 111, 1551

Mihos J. C., Hernquist L., 1996, The Astrophysical Journal, 464, 641

Moore B., Katz N., Lake G., Dressler A., Oemler A., 1996, Nature, 379, 613

Muller C. A., Oort J. H., 1951, Nature, 168, 357

Mundy C. J., Conselice C. J., Duncan K. J., Almaini O., Häußler B., Hartley W. G., 2017, Monthly Notices of The Royal Astronomical Society, 470, 3507

Namumba B., Carignan C., Foster T., Deg N., 2019, Monthly Notices of The Royal Astronomical Society, 490, 3365

Navarro J. F., Frenk C. S., White S. D. M., 1997, The Astrophysical Journal, 490, 493

Nilson P., 1973, Nova Acta Regiae Soc. Sci. Upsaliensis Ser. V, p. 0

Noordermeer E., van der Hulst J. M., Sancisi R., Swaters R. A., van Albada T. S., 2005, Astronomy & Astrophysics, 442, 137

Patton D. R., Carlberg R. G., Marzke R. O., Pritchet C. J., da Costa L. N., Pellegrini P. S., 2000, The Astrophysical Journal, 536, 153

Pearson W. J., et al., 2019, Astronomy & Astrophysics, 631, A51

Peterson S. D., Shostak G. S., 1974, The Astronomical Journal, 79, 767

Pillepich A., et al., 2018, Monthly Notices of The Royal Astronomical Society, 473, 4077

Privon G. C., Barnes J. E., Evans A. S., Hibbard J. E., Yun M. S., Mazzarella J. M., Armus L., Surace J., 2013, The Astrophysical Journal, 771, 120

Prugniel P., Simien F., 1997, Astronomy & Astrophysics, 321, 111

Reichard T. A., Heckman T. M., Rudnick G., Brinchmann J., Kauffmann G., 2008, The Astrophysical Journal, 677, 186

Reynolds T. N., Westmeier T., Staveley-Smith L., Chauhan G., Lagos C. D. P., 2020, Monthly Notices of The Royal Astronomical Society, 493, 5089

Richter O. G., Sancisi R., 1994, Astronomy & Astrophysics, 290, L9

Rix H.-W., Zaritsky D., 1995, The Astrophysical Journal, 447, 82

Roberts M. S., Haynes M. P., 1994, Annual Review of Astronomy and Astrophysics, 32, 115

Robotham A. S. G., et al., 2014, Monthly Notices of The Royal Astronomical Society, 444, 3986

Ruiz A. N., et al., 2015, The Astrophysical Journal, 801, 139

Saitoh T. R., Daisaka H., Kokubo E., Makino J., Okamoto T., Tomisaka K., Wada K., Yoshida N., 2009, Publications of the ASJ, 61, 481

Sancisi R., Fraternali F., Oosterloo T., van der Hulst T., 2008, Astronomy and Astrophysics Reviews, 15, 189

Sanders D. B., Mirabel I. F., 1996, Annual Review of Astronomy and Astrophysics, 34, 749

Sawala T., et al., 2016, Monthly Notices of The Royal Astronomical Society, 457, 1931

Schade D., Lilly S. J., Crampton D., Hammer F., Le Fevre O., Tresse L., 1995, Astrophysical Journal, Letters, 451, L1

Schaye J., et al., 2015, Monthly Notices of The Royal Astronomical Society, 446, 521

Scott T. C., Brinks E., Cortese L., Boselli A., Bravo-Alfaro H., 2018, Monthly Notices of The Royal Astronomical Society, 475, 4648

Semczuk M., Łokas E. L., Salomon J.-B., Athanassoula E., D'Onghia E., 2018, The Astrophysical Journal, 864, 34

Shapiro K. L., et al., 2008, The Astrophysical Journal, 682, 231

Skillman S. W., Warren M. S., Turk M. J., Wechsler R. H., Holz D. E., Sutter P. M., 2014, arXiv e-prints, p. arXiv:1407.2600

Snyder G. F., Lotz J., Moody C., Peth M., Freeman P., Ceverino D., Primack J., Dekel A., 2015a, Monthly Notices of The Royal Astronomical Society, 451, 4290

Snyder G. F., et al., 2015b, Monthly Notices of The Royal Astronomical Society, 454, 1886

Somerville R. S., Davé R., 2015, Annual Review of Astronomy and Astrophysics, 53, 51

Springel V., 2005, Monthly Notices of The Royal Astronomical Society, 364, 1105

Springel V., et al., 2005, Nature, 435, 629

Starkenburg T. K., Helmi A., Sales L. V., 2016, Astronomy & Astrophysics, 595, A56

Steinmetz M., Navarro J. F., 2002, New Astronomy, 7, 155

Swaters R. A., van Albada T. S., van der Hulst J. M., Sancisi R., 2002, Astronomy & Astrophysics, 390, 829

Tifft W. G., Cocke W. J., 1988, Astrophysical Journal, Supplement Series, 67, 1

Toomre A., 1977, in Tinsley B. M., Larson D. Campbell R. B. G., eds, Evolution of Galaxies and Stellar Populations. p. 401

Toomre A., Toomre J., 1972, The Astrophysical Journal, 178, 623

Verdes-Montenegro L., Sulentic J., Lisenfeld U., Leon S., Espada D., Garcia E., Sabater J., Verley S., 2005, Astronomy & Astrophysics, 436, 443

Vogelsberger M., et al., 2014, Monthly Notices of The Royal Astronomical Society, 444, 1518

Vogelsberger M., Marinacci F., Torrey P., Puchwein E., 2020, Nature Reviews Physics, 2, 42

Walter F., Brinks E., de Blok W. J. G., Bigiel F., Kennicutt Robert C. J., Thornley M. D., Leroy A., 2008, The Astronomical Journal, 136, 2563

Wang H.-H., Klessen R. S., Dullemond C. P., van den Bosch F. C., Fuchs B., 2010, Monthly Notices of The Royal Astronomical Society, 407, 705

Wang J., et al., 2013, Monthly Notices of The Royal Astronomical Society, 433, 270

Watts A. B., Catinella B., Cortese L., Power C., 2020, Monthly Notices of The Royal Astronomical Society, 492, 3672

Wetzel A. R., Hopkins P. F., Kim J.-h., Faucher-Giguère C.-A., Kereš D., Quataert E., 2016, Astrophysical Journal, Letters, 827, L23

White S. D. M., Frenk C. S., 1991, The Astrophysical Journal, 379, 52

White S. D. M., Rees M. J., 1978, Monthly Notices of The Royal Astronomical Society, 183, 341

Widrow L. M., Dubinski J., 2005, The Astrophysical Journal, 631, 838

Widrow L. M., Pym B., Dubinski J., 2008, The Astrophysical Journal, 679, 1239

Yun M. S., Ho P. T. P., Lo K. Y., 1994, Nature, 372, 530

Zaritsky D., Rix H.-W., 1997, The Astrophysical Journal, 477, 118

de Vaucouleurs G., de Vaucouleurs A., Corwin Herold G. J., Buta R. J., Paturel G., Fouque P., 1991, Third Reference Catalogue of Bright Galaxies

van Driel W., et al., 2016, Astronomy & Astrophysics, 595, A118

van Eymeren J., Jütte E., Jog C. J., Stein Y., Dettmar R. J., 2011, Astronomy & Astrophysics, 530, A30

van der Hulst J. M., van Albada T. S., Sancisi R., 2001, in Hibbard J. E., Rupen M., van Gorkom J. H., eds, Astronomical Society of the Pacific Conference Series Vol. 240, Gas and Galaxy Evolution. p. 451

Appendix A

Additional tables: the WHISP sample

Table A.1 is a complete list of the asymmetry and lopsidedness parameters measured for the WHISP sample, along the visual classifications of asymmetry in the HI images and profiles, and visual classification of interacting systems from the literature. The columns in Table A.1 are:

(1) UGC number.
(2) spectral lopsidedness L
(3) uncertainty associated with L
(4) folding difference lopsidedness $\mathcal{L}$
(5) uncertainty associated with $\mathcal{L}$
(6) intensity-weighted asymmetry A
(7) uncertainty associated with A
(8) outer asymmetry $\mathcal{A}$
(9) uncertainty associated with $\mathcal{A}$
(10) visually classified degree of asymmetry in the global profile
(11) visually classified degree of overall asymmetry in the HI image
(12) evidence for current galaxy-galaxy interaction. Taken from Swaters et al. (2002) and Noordermeer et al. (2005).

Table A.1: The asymmetry and lopsidedness parameters for 115 WHISP galaxies.

UGC	L	σ_L	$\mathcal{L}$	$\sigma_{\mathcal{L}}$	A	σ_A	$\mathcal{A}$	$\sigma_{\mathcal{A}}$	Asymmetries		
									prof.	morph.	int.
(1)	(2)	(3)	(4)	(5)	(6)	(7)	(8)	(9)	(10)	(11)	(12)
89	0.102	0.017	0.135	0.017	0.269	0.078	0.560	0.037	1	1	$\star$
94	0.008	0.008	0.124	0.021	0.224	0.044	0.691	0.022	2	2	$\star$
232	0.003	0.006	0.150	0.019	0.180	0.031	0.529	0.024	2	1	
499	0.045	0.012	0.123	0.010	0.325	0.012	0.487	0.012	0	2	$\star$

Table A.1. continued.

UGC	L	σ_L	$\mathcal{L}$	$\sigma_{\mathcal{L}}$	A	σ_A	$\mathcal{A}$	$\sigma_{\mathcal{A}}$	Asymmetries		
									prof.	morph.	int.
(1)	(2)	(3)	(4)	(5)	(6)	(7)	(8)	(9)	(10)	(11)	(12)
624	0.036	0.012	0.141	0.019	0.264	0.061	0.761	0.020	2	2	⋆
731	0.068	0.006	0.086	0.007	0.126	0.030	0.440	0.034	1	0	
798	0.003	0.012	0.154	0.031	0.192	0.043	0.513	0.046	2	1	
1249	0.001	0.003	0.106	0.005	0.275	0.024	0.704	0.012	0	2	⋆
1281	0.018	0.010	0.049	0.010	0.155	0.114	0.595	0.050	0	0	
1541	0.275	0.018	0.296	0.02	0.205	0.028	0.496	0.033	3	1	
2023	0.057	0.021	0.057	0.024	0.242	0.021	0.564	0.02	0	1	
2034	0.096	0.032	0.075	0.022	0.167	0.016	0.474	0.017	0	1	
2045	0.071	0.009	0.083	0.008	0.223	0.051	0.661	0.014	2	1	
2053	0.059	0.021	0.129	0.014	0.232	0.028	0.577	0.025	2	1	
2141	0.022	0.012	0.075	0.012	0.276	0.074	0.666	0.021	1	1	
2183	0.070	0.004	0.097	0.004	0.190	0.058	0.515	0.018	2	1	
2455	0.004	0.019	0.065	0.009	0.203	0.019	0.529	0.012	1	1	
2487	0.018	0.008	0.100	0.010	0.218	0.015	0.460	0.018	0	1	
2916	0.154	0.007	0.201	0.012	0.293	0.026	0.521	0.023	3	1	⋆
2941	0.043	0.011	0.072	0.010	0.205	0.036	0.586	0.025	0	1	⋆
3137	0.077	0.008	0.097	0.008	0.178	0.097	0.525	0.055	2	0	
3205	0.003	0.004	0.051	0.005	0.139	0.091	0.503	0.079	0	0	
3354	0.021	0.004	0.064	0.004	0.129	0.096	0.549	0.051	2	0	
3371	0.064	0.013	0.091	0.013	0.164	0.020	0.414	0.029	1	1	
3382	0.045	0.011	0.146	0.011	0.140	0.033	0.458	0.039	2	1	
3407	0.028	0.02	0.169	0.031	0.338	0.063	0.669	0.021	1	1	⋆
3546	0.072	0.006	0.085	0.006	0.161	0.040	0.422	0.041	1	0	
3580	0.013	0.008	0.109	0.015	0.191	0.026	0.486	0.024	1	1	
3698	0.092	0.026	0.081	0.033	0.275	0.053	0.593	0.037	1	1	
3711	0.071	0.02	0.119	0.013	0.270	0.023	0.676	0.009	2	2	
3817	0.024	0.026	0.107	0.020	0.221	0.019	0.624	0.017	0	1	
3966	0.052	0.042	0.179	0.042	0.264	0.028	0.608	0.018	0	0	
3993	0.121	0.017	0.138	0.015	0.206	0.017	0.418	0.041	2	1	
4173	0.060	0.022	0.107	0.011	0.228	0.013	0.538	0.018	2	1	
4278	0.054	0.007	0.088	0.008	0.173	0.105	0.626	0.041	1	1	
4305	0.019	0.007	0.036	0.003	0.287	0.004	0.499	0.003	1	1	
4325	0.094	0.011	0.117	0.013	0.164	0.030	0.444	0.030	2	1	
4458	0.083	0.009	0.154	0.012	0.234	0.025	0.575	0.016	2	1	⋆
4499	0.061	0.009	0.067	0.008	0.176	0.032	0.432	0.038	1	1	
4543	0.015	0.014	0.123	0.015	0.258	0.022	0.61	0.013	0	2	
4605	0.056	0.003	0.124	0.004	0.163	0.063	0.416	0.078	2	1	

Table A.1. continued.

UGC	L	σ_L	$\mathcal{L}$	$\sigma_{\mathcal{L}}$	A	σ_A	$\mathcal{A}$	$\sigma_{\mathcal{A}}$	Asymmetries		
									prof.	morph.	int.
(1)	(2)	(3)	(4)	(5)	(6)	(7)	(8)	(9)	(10)	(11)	(12)
4666	0.005	0.004	0.095	0.011	0.178	0.049	0.447	0.038	2	1	
4862	0.304	0.009	0.317	0.01	0.474	0.008	0.713	0.019	3	2	⋆
5060	0.052	0.113	0.114	0.093	0.229	0.045	0.546	0.02	3	1	
5272	0.014	0.013	0.075	0.011	0.253	0.076	0.648	0.043	1	1	⋆
5351	0.318	0.029	0.332	0.032	0.314	0.074	0.64	0.016	3	1	⋆
5414	0.094	0.017	0.114	0.012	0.227	0.037	0.553	0.04	1	2	
5721	0.113	0.01	0.136	0.009	0.239	0.033	0.613	0.027	2	2	
5829	0.095	0.028	0.105	0.016	0.211	0.016	0.474	0.019	2	1	
5846	0.02	0.017	0.095	0.014	0.179	0.035	0.472	0.038	0	1	
5906	0.056	0.026	0.109	0.034	0.248	0.07	0.535	0.031	1	1	
5918	0.052	0.023	0.09	0.017	0.231	0.016	0.561	0.027	1	2	
5935	0.162	0.052	0.227	0.041	0.368	0.027	0.728	0.011	2	2	⋆
5960	0.082	0.006	0.095	0.008	0.316	0.083	0.723	0.013	2	1	
6001	0.055	0.026	0.116	0.029	0.255	0.088	0.674	0.037	1	1	
6118	0.043	0.012	0.097	0.018	0.194	0.072	0.341	0.095	1	0	
6283	0.009	0.006	0.069	0.009	0.155	0.062	0.512	0.03	0	1	
6446	0.031	0.009	0.042	0.009	0.158	0.023	0.416	0.032	0	1	
6628	0.044	0.012	0.043	0.012	0.184	0.027	0.555	0.032	0	1	
6742	0.033	0.018	0.079	0.013	0.268	0.057	0.608	0.022	1	1	
6786	0.012	0.005	0.102	0.005	0.214	0.037	0.534	0.018	1	1	
6787	0.111	0.006	0.172	0.006	0.218	0.015	0.521	0.015	2	1	⋆
6817	0.211	0.071	0.214	0.06	0.309	0.01	0.51	0.01	1	1	
6944	0.056	0.04	0.084	0.025	0.31	0.045	0.746	0.016	1	2	⋆
7047	0.175	0.014	0.162	0.014	0.224	0.027	0.472	0.034	2	2	
7125	0.1	0.009	0.108	0.009	0.203	0.079	0.572	0.041	2	1	
7151	0.05	0.008	0.092	0.011	0.174	0.079	0.564	0.043	2	1	
7166	0.098	0.015	0.207	0.016	0.317	0.009	0.516	0.009	3	2	
7199	0.004	0.032	0.099	0.023	0.376	0.038	0.651	0.007	0	2	
7232	0.197	0.047	0.189	0.034	0.25	0.047	0.584	0.01	1	1	
7261	0.019	0.011	0.085	0.019	0.191	0.018	0.529	0.024	1	1	
7323	0.07	0.011	0.072	0.011	0.181	0.021	0.495	0.026	1	1	
7399	0.06	0.023	0.111	0.019	0.28	0.023	0.727	0.01	1	1	
7408	0.006	0.086	0.137	0.069	0.362	0.017	0.702	0.01	0	1	
7490	0.095	0.024	0.102	0.016	0.214	0.021	0.429	0.021	0	1	
7506	0.083	0.03	0.152	0.02	0.217	0.056	0.549	0.033	1	0	
7524	0.105	0.002	0.113	0.002	0.226	0.004	0.385	0.012	2	1	
7559	0.116	0.016	0.105	0.014	0.245	0.029	0.635	0.02	1	2	

Table A.1. continued.

UGC	L	σ_L	$\mathcal{L}$	$\sigma_{\mathcal{L}}$	A	σ_A	$\mathcal{A}$	$\sigma_{\mathcal{A}}$	Asymmetries		
									prof.	morph.	int.
(1)	(2)	(3)	(4)	(5)	(6)	(7)	(8)	(9)	(10)	(11)	(12)
7592	0.178	0.038	0.212	0.029	0.525	0.003	0.752	0.002	1	2	⋆
7603	0.002	0.006	0.052	0.011	0.22	0.052	0.586	0.024	0	1	
7608	0.127	0.012	0.126	0.018	0.157	0.022	0.436	0.033	2	1	
7690	0.011	0.019	0.08	0.017	0.23	0.037	0.641	0.018	0	1	
7704	0.116	0.008	0.109	0.009	0.213	0.068	0.549	0.033	1	1	
7866	0.005	0.012	0.04	0.011	0.172	0.024	0.491	0.028	0	1	
7916	0.007	0.009	0.069	0.008	0.175	0.074	0.54	0.051	2	1	
7971	0.017	0.017	0.057	0.012	0.175	0.03	0.514	0.044	1	1	
7989	0.159	0.007	0.19	0.007	0.349	0.007	0.529	0.006	2	2	⋆
8188	0.045	0.018	0.072	0.024	0.244	0.013	0.501	0.012	0	1	
8201	0.164	0.063	0.153	0.047	0.365	0.009	0.621	0.008	1	2	
8271	0.15	0.071	0.162	0.06	0.351	0.024	0.63	0.022	1	2	⋆
8286	0.028	0.004	0.038	0.004	0.175	0.102	0.684	0.036	0	0	
8331	0.048	0.027	0.103	0.019	0.348	0.025	0.577	0.019	2	2	
8490	0.018	0.005	0.031	0.01	0.213	0.011	0.467	0.007	1	1	
8550	0.015	0.011	0.068	0.01	0.145	0.091	0.559	0.047	0	1	
8683	0.096	0.022	0.106	0.029	0.224	0.026	0.562	0.029	0	1	
8699	0.018	0.007	0.053	0.007	0.119	0.106	0.534	0.064	0	1	
8837	0.172	0.013	0.178	0.011	0.21	0.076	0.563	0.054	2	1	
8863	0.014	0.008	0.11	0.008	0.161	0.041	0.477	0.042	2	0	
9128	0.029	0.01	0.082	0.009	0.194	0.058	0.582	0.014	1	1	
9211	0.056	0.009	0.08	0.009	0.184	0.027	0.486	0.023	1	1	
9644	0.041	0.016	0.049	0.018	0.192	0.067	0.572	0.057	1	1	
9992	0.065	0.02	0.149	0.02	0.21	0.025	0.532	0.019	2	1	
10310	0.003	0.007	0.08	0.012	0.188	0.044	0.517	0.026	1	1	
11269	0.016	0.009	0.046	0.015	0.349	0.014	0.618	0.026	1	2	⋆
11670	0.063	0.006	0.1	0.006	0.228	0.042	0.492	0.03	2	1	
11852	0.073	0.007	0.145	0.02	0.148	0.038	0.466	0.064	2	1	
11861	0.016	0.01	0.109	0.014	0.175	0.018	0.445	0.03	2	1	
11914	0.008	0.007	0.046	0.022	0.114	0.046	0.441	0.035	0	0	
11951	0.06	0.011	0.088	0.01	0.253	0.103	0.585	0.059	1	1	⋆
12043	0.02	0.005	0.054	0.004	0.125	0.063	0.502	0.062	1	0	
12060	0.008	0.011	0.101	0.019	0.257	0.012	0.473	0.015	0	1	
12276	0.098	0.011	0.13	0.013	0.181	0.042	0.521	0.033	2	1	⋆
12632	0.061	0.007	0.097	0.008	0.207	0.007	0.455	0.013	2	1	
12713	0.101	0.017	0.106	0.017	0.212	0.072	0.504	0.046	1	1	
12732	0.059	0.006	0.076	0.004	0.184	0.011	0.381	0.02	1	1	

Table A.2 is a consolidated list of the visual classifications for the global HI profiles and HI images of the WHISP sample studied in Chapter 5. Columns (2)−(5) correspond to the answers for the profiles and columns (6)−(14) correspond to the answers for the images. For convenience, the questions are re-stated below:

(2) Q1. Does the HI spectrum have a double-horn profile?

(3) Q2. What is the degree of asymmetry in the profile? Classify as follows:
- ◇ 0 - symmetric
- ◇ 1 - slightly asymmetric
- ◇ 2 - moderately asymmetric
- ◇ 3 - severely asymmetric

(4) Q3. Do the peaks of the profile have different widths?

(5) Q4. Does the central dip of the profile lie above f_{50}, the intensity level corresponding to 50% of the peak flux?

(6) Q1. Is the galaxy edge-on?

(7) Q2. Is there a depression (1) or hole (2) in the central region?

(8) Q3. Does the HI distribution have any spiral/ring structure?

(9) Q4. Are there tidal tails present?

(10) Q5. What is the degree of overall asymmetry in the image? Classify according to:
- ◇ 0 - symmetric
- ◇ 1 - mildly asymmetric
- ◇ 2 - severely asymmetric

(11) Q6. Is the inner region of the galaxy asymmetric?

(12) Q7. Is the outer region asymmetric?

(13) Q8. Is the HI distribution clumpy?

(14) Q9. Do you think the CoS is offset from the CoB of the galaxy?

Table A.2: The visually assigned classifications of asymmetry and other properties observed in the HI profiles and HI images of the WHISP sample.

UGC	Q1	Q2	Q3	Q4	Q1	Q2	Q3	Q4	Q5	Q6	Q7	Q8	Q9
(1)	(2)	(3)	(4)	(5)	(6)	(7)	(8)	(9)	(10)	(11)	(12)	(13)	(14)
89	1	1	1	0	0	0	0	0	1	1	1	0	0
94	1	2	1	1	0	0	0	1	2	0	1	0	1
232	1	2	1	0	0	0	0	0	1	1	0	0	0
499	0	0	0	1	0	0	1	0	2	1	1	1	1
624	1	2	1	0	0	0	0	0	2	1	1	0	1

Table A.2. continued.

UGC	Q1	Q2	Q3	Q4	Q1	Q2	Q3	Q4	Q5	Q6	Q7	Q8	Q9
(1)	(2)	(3)	(4)	(5)	(6)	(7)	(8)	(9)	(10)	(11)	(12)	(13)	(14)
731	1	1	1	1	0	0	0	0	0	0	0	1	0
798	1	2	1	0	0	0	0	0	1	1	1	1	0
1249	0	0	0	1	0	0	0	0	2	1	1	1	1
1281	0	0	0	1	1	0	0	0	0	0	0	0	0
1541	1	3	1	0	0	0	0	0	1	1	1	0	1
2023	1	0	0	1	0	0	0	0	1	1	1	1	1
2034	0	0	0	1	0	1	0	0	1	1	0	1	0
2045	1	2	1	1	1	0	0	0	1	0	1	0	0
2053	0	2	2	1	0	1	0	0	1	1	1	1	1
2141	1	1	1	1	0	0	0	1	1	0	1	0	1
2183	1	2	1	0	0	2	0	0	1	1	1	0	0
2455	0	1	2	1	0	1	0	0	1	1	0	1	1
2487	1	0	0	0	0	2	1	0	1	1	1	1	1
2916	1	3	1	1	0	0	0	0	1	1	1	0	1
2941	0	0	0	1	0	0	0	0	1	0	1	0	1
3137	1	2	1	1	1	0	0	0	0	0	0	0	0
3205	1	0	0	0	1	1	0	0	0	0	0	0	0
3354	1	2	1	0	1	0	1	0	0	0	0	0	0
3371	1	1	1	1	0	1	0	0	1	1	0	1	0
3382	1	2	1	1	0	1	1	0	1	0	1	0	0
3407	1	1	0	0	0	0	0	0	1	0	1	0	0
3546	1	1	1	0	0	2	1	0	0	0	0	0	1
3580	1	1	1	0	0	1	1	0	1	0	1	0	1
3698	0	1	2	1	0	0	0	0	1	0	1	1	1
3711	0	2	2	1	0	0	0	1	2	1	1	0	1
3817	0	0	0	1	0	1	0	0	1	1	1	1	1
3966	1	0	0	1	0	1	0	0	0	0	0	1	0
3993	1	2	1	0	0	1	1	0	1	0	1	1	0
4173	0	2	2	1	0	2	0	0	1	1	1	1	0
4278	1	1	1	0	1	0	0	0	1	0	1	0	0
4305	0	1	2	1	0	1	1	0	1	1	1	1	0
4325	1	2	1	1	0	0	0	0	1	1	0	0	0
4458	1	2	1	0	0	0	0	0	1	0	1	1	0
4499	1	1	1	1	0	1	0	0	1	1	0	1	0
4543	1	0	0	0	0	1	0	0	2	1	1	1	0
4605	1	2	1	0	1	0	0	0	1	1	1	0	0
4666	1	2	1	1	0	1	1	0	1	1	1	1	0
4862	1	3	1	0	0	1	1	1	2	1	1	1	1

Table A.2. continued.

UGC	Q1	Q2	Q3	Q4	Q1	Q2	Q3	Q4	Q5	Q6	Q7	Q8	Q9
(1)	(2)	(3)	(4)	(5)	(6)	(7)	(8)	(9)	(10)	(11)	(12)	(13)	(14)
5060	0	3	2	1	0	0	0	0	1	0	1	0	0
5272	0	1	2	1	0	0	0	1	1	1	1	0	1
5351	0	3	2	1	0	0	0	0	1	0	1	0	1
5414	0	1	2	1	0	0	0	0	2	1	1	0	1
5721	1	2	1	1	0	0	0	0	2	1	1	0	1
5829	0	2	2	1	0	1	0	0	1	1	1	1	1
5846	0	0	0	1	0	0	0	0	1	1	0	0	0
5906	1	1	1	0	0	0	0	0	1	0	1	0	0
5918	0	1	2	1	0	0	0	0	2	1	1	0	1
5935	0	2	2	1	0	0	0	1	2	1	1	0	1
5960	1	2	1	1	1	0	0	0	1	0	1	0	1
6001	1	1	1	1	0	0	0	0	1	0	1	0	1
6118	1	1	0	1	0	2	0	0	0	0	0	0	0
6283	1	0	0	1	1	0	0	0	1	0	1	0	1
6446	1	0	0	1	0	0	0	0	1	1	0	1	0
6628	0	0	0	1	0	1	0	0	1	1	1	1	1
6742	0	1	2	1	0	0	0	0	1	0	1	0	0
6786	1	1	1	0	0	1	1	0	1	0	1	0	1
6787	1	2	1	0	0	1	1	0	1	0	1	1	0
6817	0	1	2	1	0	0	1	0	1	1	0	1	0
6944	0	1	2	1	0	0	0	0	2	1	1	0	1
7047	0	2	2	1	0	0	1	0	2	1	0	1	1
7125	1	2	1	1	1	0	0	0	1	0	1	0	1
7151	1	2	1	1	1	1	0	0	1	1	1	0	0
7166	1	3	1	1	0	1	1	0	2	1	1	1	1
7199	0	0	0	1	0	0	0	0	2	1	1	1	1
7232	0	1	2	1	0	0	0	0	1	0	1	0	0
7261	1	1	1	1	0	1	0	0	1	1	1	1	0
7323	1	1	1	1	0	1	1	0	1	1	1	1	1
7399	1	1	1	1	0	0	0	0	1	1	1	0	0
7408	0	0	0	1	0	0	0	0	1	0	1	1	0
7490	0	0	0	1	0	2	1	0	1	1	1	1	0
7506	0	1	2	1	0	0	0	0	0	0	0	0	0
7524	1	2	0	1	0	0	1	0	1	1	0	1	0
7559	0	1	2	1	0	0	0	0	2	1	1	0	1
7592	0	1	2	1	0	1	1	0	2	1	1	0	0
7603	0	0	0	1	1	0	0	0	1	0	1	0	0
7608	0	2	2	1	0	0	0	0	1	1	0	1	0

Table A.2. continued.

UGC	Q1	Q2	Q3	Q4	Q1	Q2	Q3	Q4	Q5	Q6	Q7	Q8	Q9
(1)	(2)	(3)	(4)	(5)	(6)	(7)	(8)	(9)	(10)	(11)	(12)	(13)	(14)
7690	1	0	0	1	0	0	0	0	1	1	1	0	0
7704	0	1	2	1	0	0	0	0	1	0	1	0	1
7866	0	0	0	1	0	0	0	0	1	1	0	1	0
7916	0	2	2	1	0	0	0	0	1	1	1	1	0
7971	0	1	0	1	0	1	1	0	1	0	1	0	0
7989	1	2	1	0	0	2	1	0	2	1	1	1	1
8188	0	0	0	1	0	1	1	0	1	1	1	1	0
8201	0	1	2	1	0	0	0	0	2	1	1	0	1
8271	0	1	2	1	0	0	0	1	2	1	1	0	1
8286	1	0	0	1	1	0	0	0	0	0	0	0	0
8331	0	2	2	1	0	0	0	0	2	1	1	0	1
8490	1	1	0	1	0	0	1	0	1	1	1	1	0
8550	1	0	0	1	1	0	0	0	1	0	1	0	0
8683	0	0	0	1	0	1	0	0	1	1	1	1	0
8699	1	0	0	0	1	0	0	0	1	0	1	0	0
8837	0	2	2	1	0	0	0	0	1	0	1	0	0
8863	1	2	0	0	0	1	1	0	0	0	0	0	0
9128	0	1	2	1	0	0	0	0	1	0	1	0	0
9211	1	1	1	1	0	1	1	0	1	0	1	1	0
9644	1	1	0	1	0	0	0	0	1	0	1	0	0
9992	0	2	2	1	0	0	0	0	1	1	0	0	0
10310	1	1	1	1	0	0	0	0	1	1	1	1	0
11269	1	1	0	1	0	0	1	1	2	1	1	0	1
11670	1	2	0	0	0	0	1	0	1	0	1	0	0
11852	1	2	1	0	0	0	1	0	1	1	1	0	0
11861	1	2	1	0	0	1	0	0	1	1	0	1	0
11914	1	0	0	0	0	1	1	0	0	0	0	0	0
11951	1	1	1	1	1	0	0	0	1	1	1	0	1
12043	1	1	1	1	0	0	1	0	0	0	0	0	0
12060	1	0	0	1	0	0	1	0	1	1	1	1	0
12276	1	2	0	1	0	0	0	0	1	1	0	0	0
12632	1	2	1	1	0	0	0	0	1	1	1	1	0
12713	0	1	2	1	0	0	0	0	1	0	1	0	1
12732	1	1	0	1	0	0	1	0	1	1	1	1	0

Appendix B

HI atlas of the WHISP sample

The following pages present the HI images and the global HI profiles of the 115 WHISP galaxies studied. The blue ellipse in the bottom left corner of the panels containing the HI images illustrates the average beam size of the observations. The measured intensity-weighted asymmetry (A) and the outer asymmetry ($\mathcal{A}$) are quoted in the top left corners of these panels. In the panels containing the HI spectra, the blue dashed lines show the lower and upper velocities of the profiles, measured at 20% of the peak flux(es). The black dotted lines indicate the calculated systemic velocity. The measured lopsidedness (L) and the folding difference lopsidedness ($\mathcal{L}$) are quoted in the top left corners of these panels.

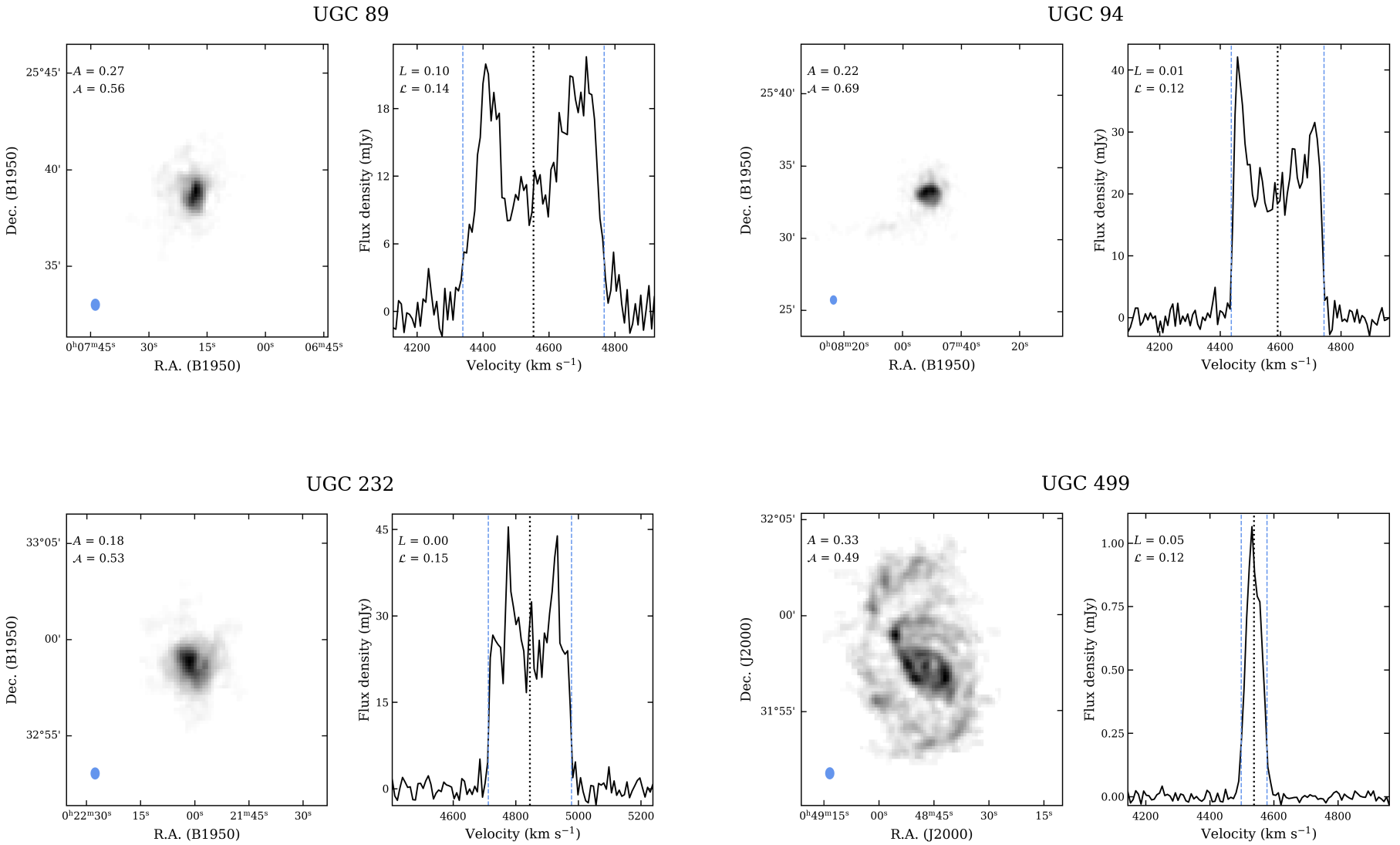

Figure B.1: HI images and HI spectra of galaxies in the WHISP sample. The measured asymmetry and lopsidedness parameters are quoted in the top left corners of the respective panels.

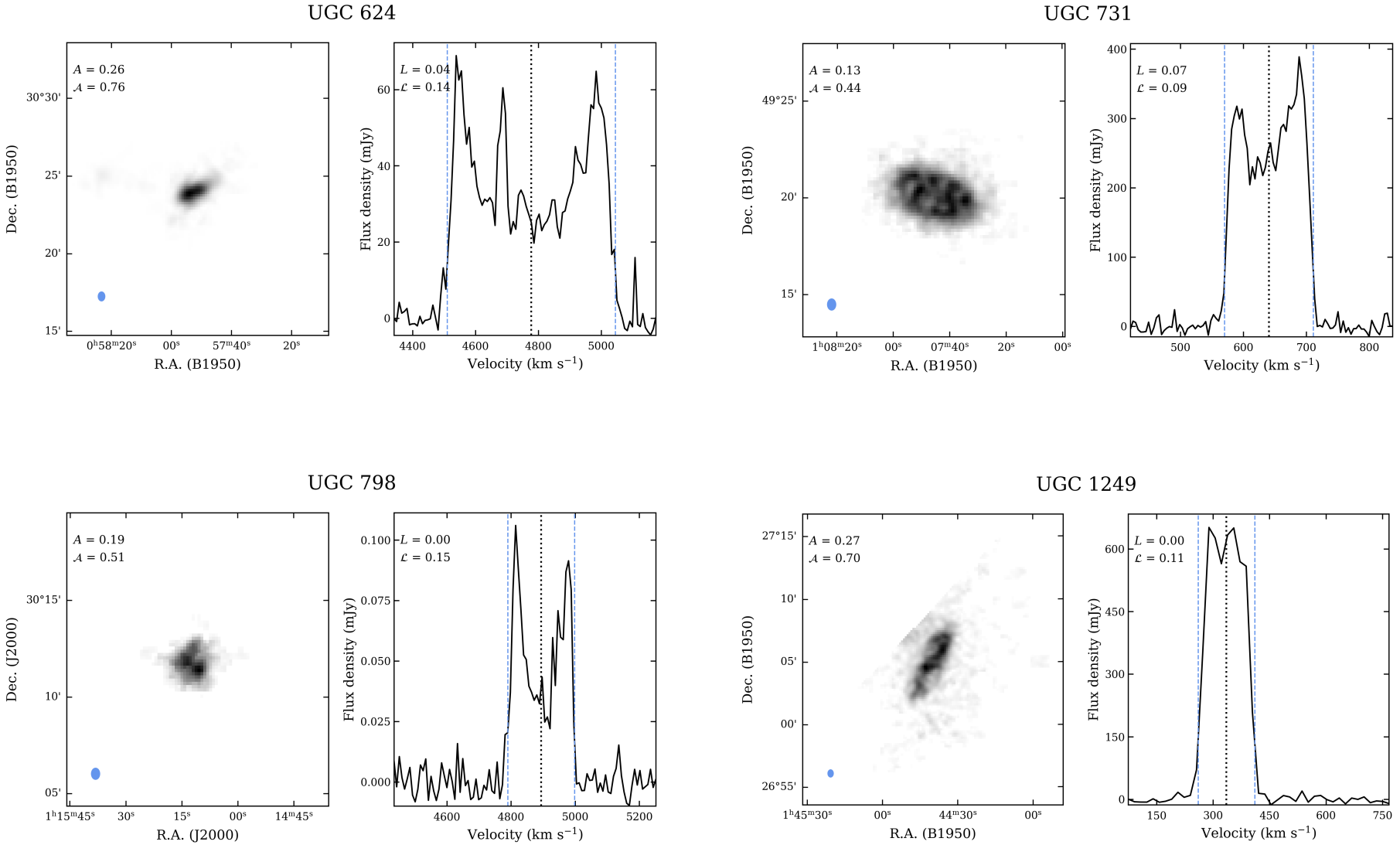

Figure B.1: continued.

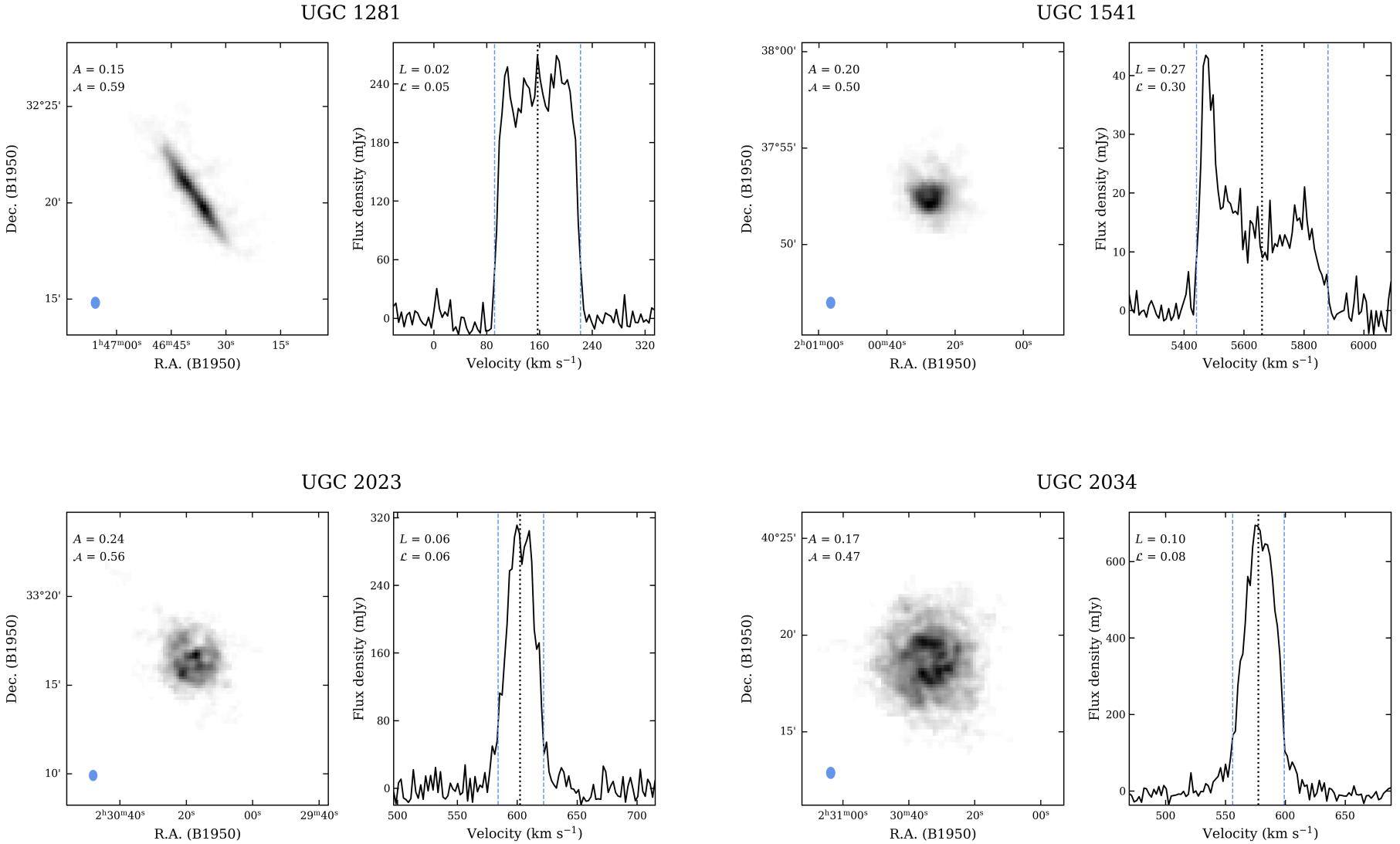

Figure B.1: continued.

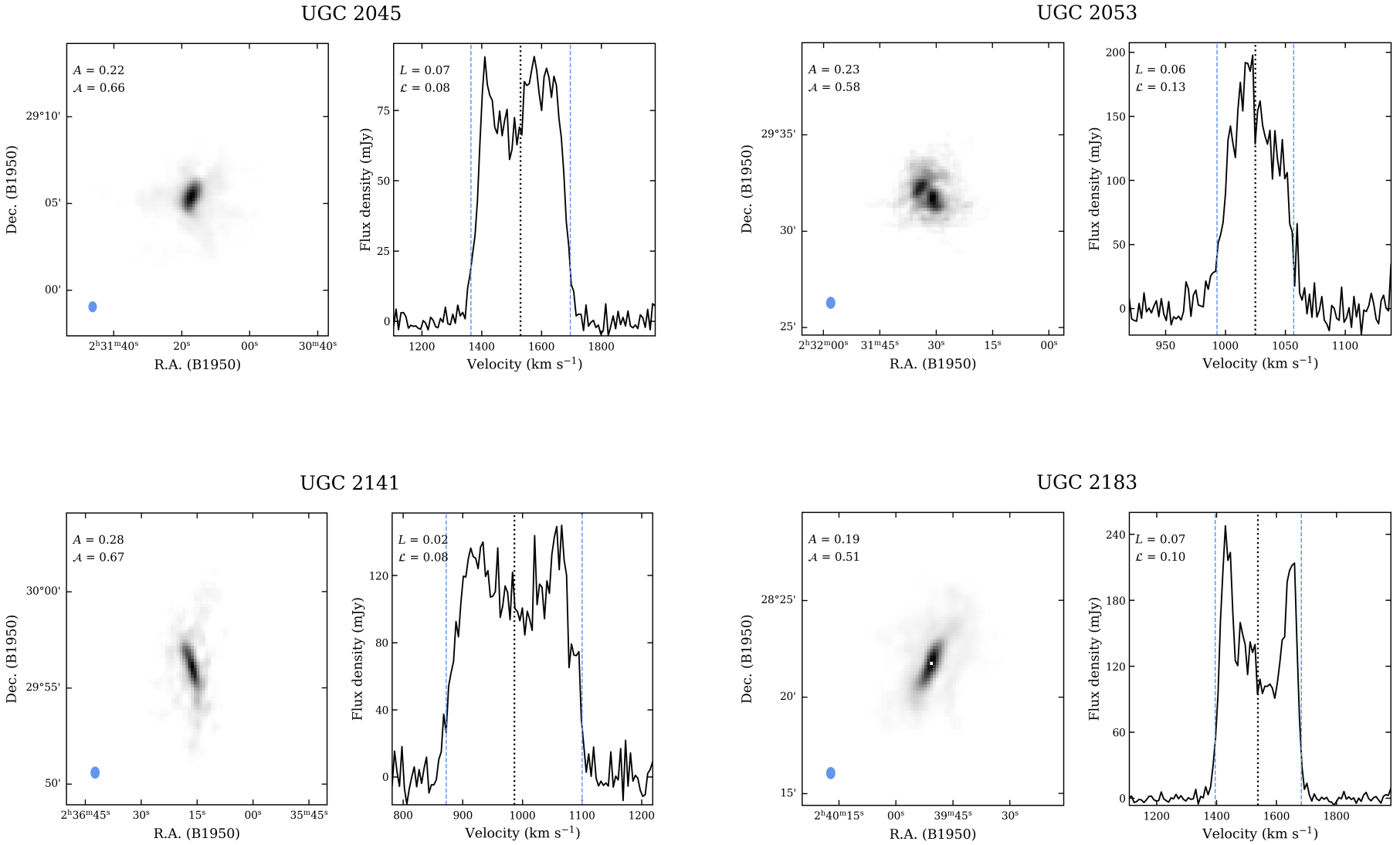

Figure B.1: continued.

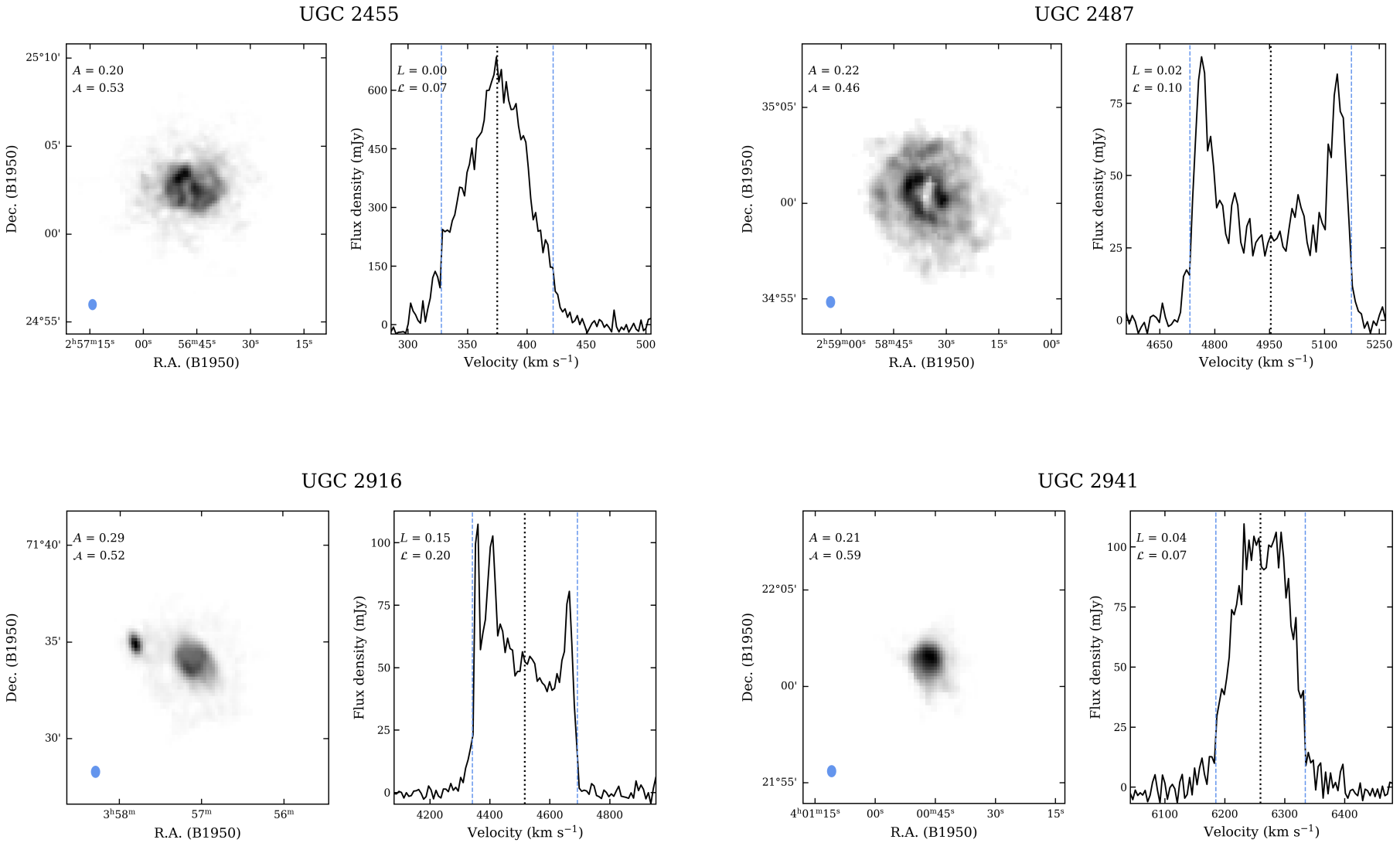

Figure B.1: continued.

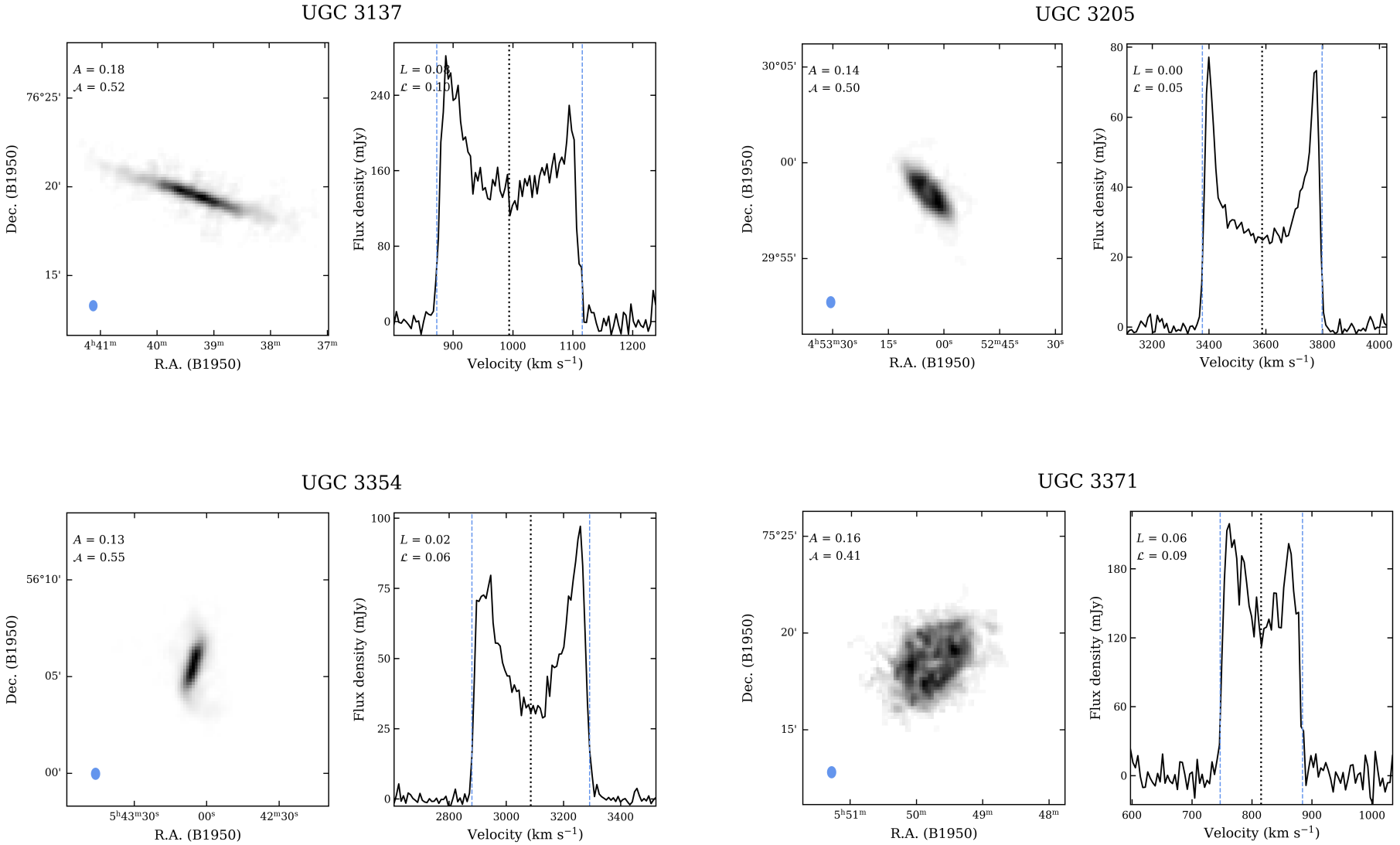

Figure B.1: continued.

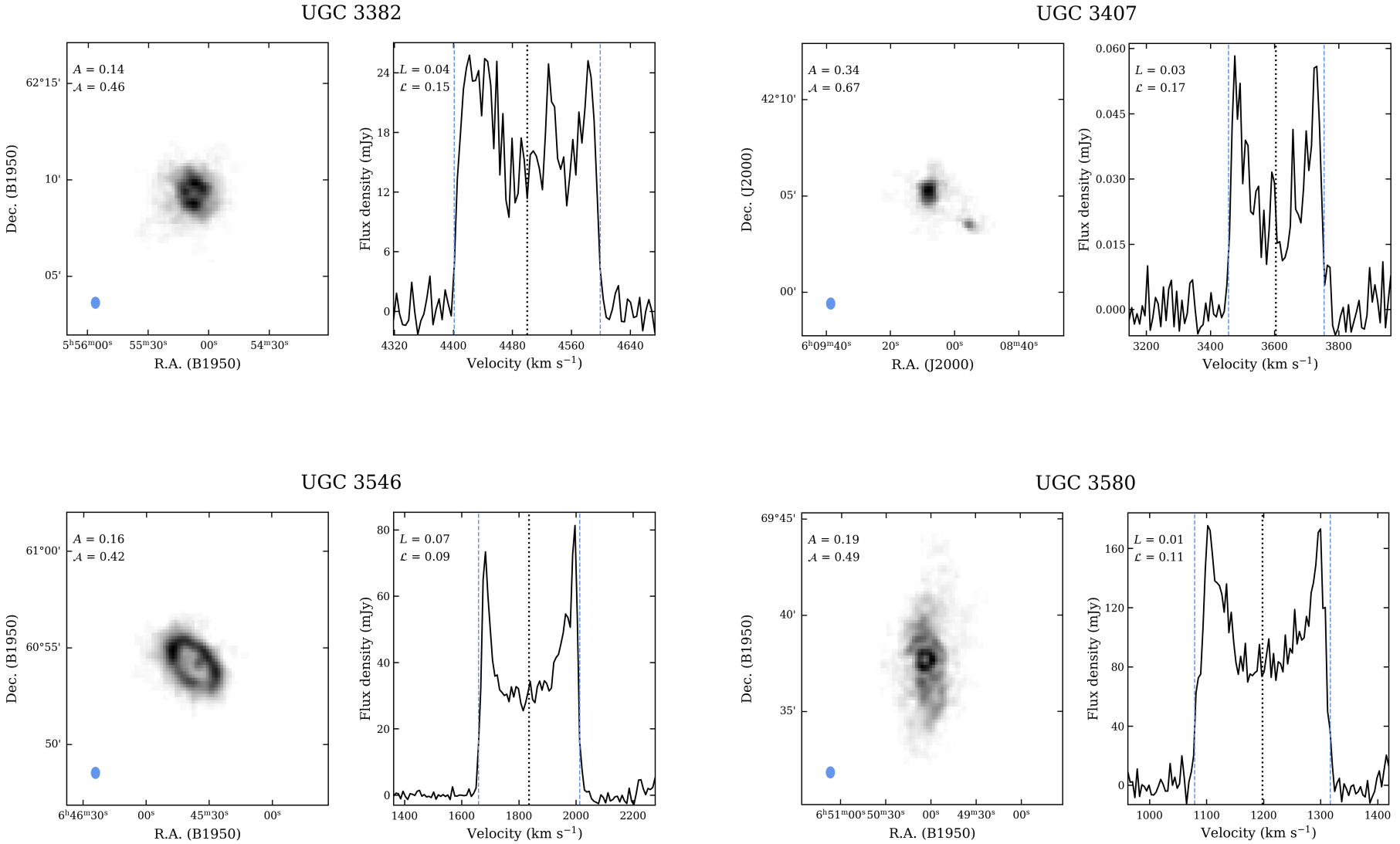

Figure B.1: continued.

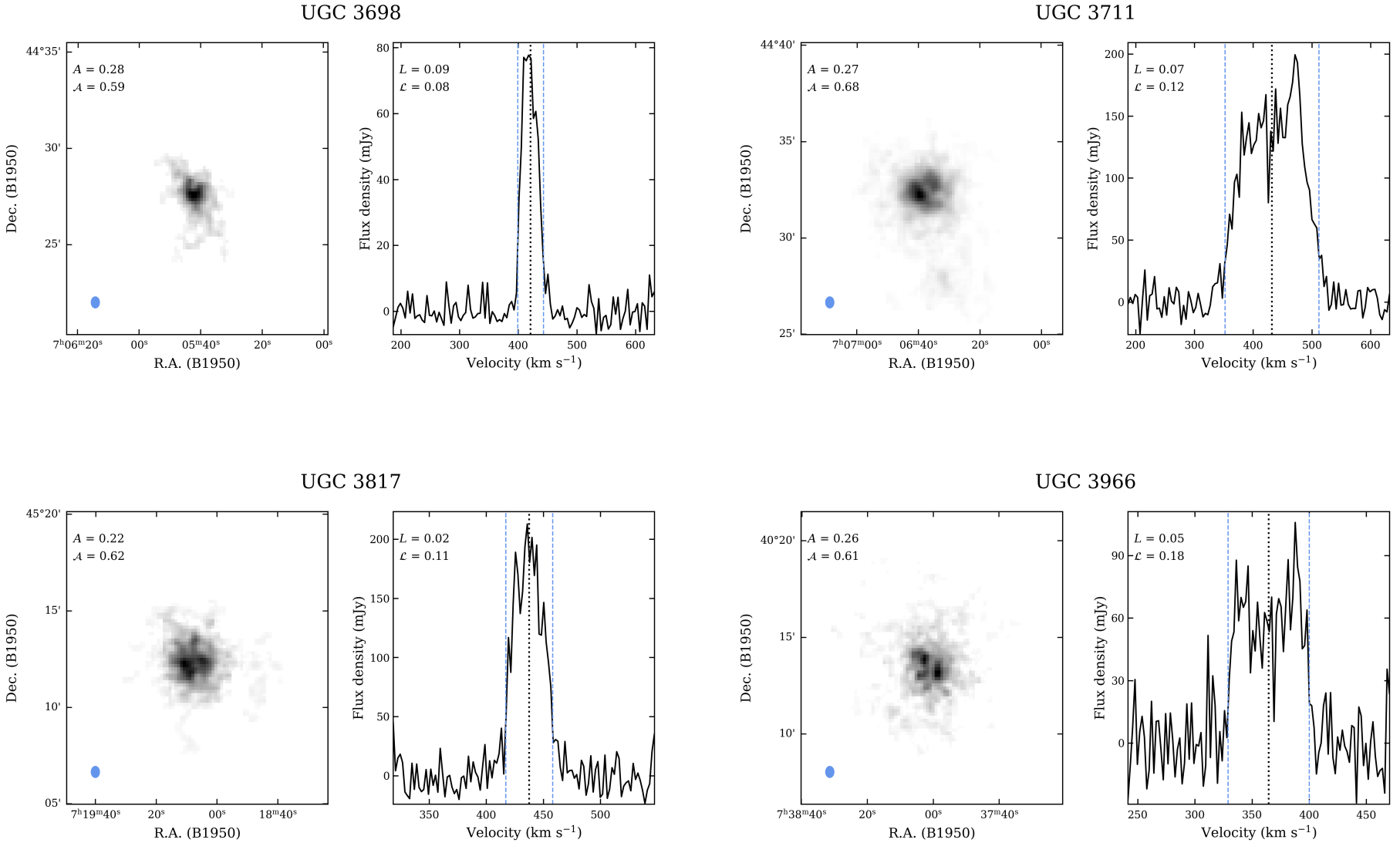

Figure B.1: continued.

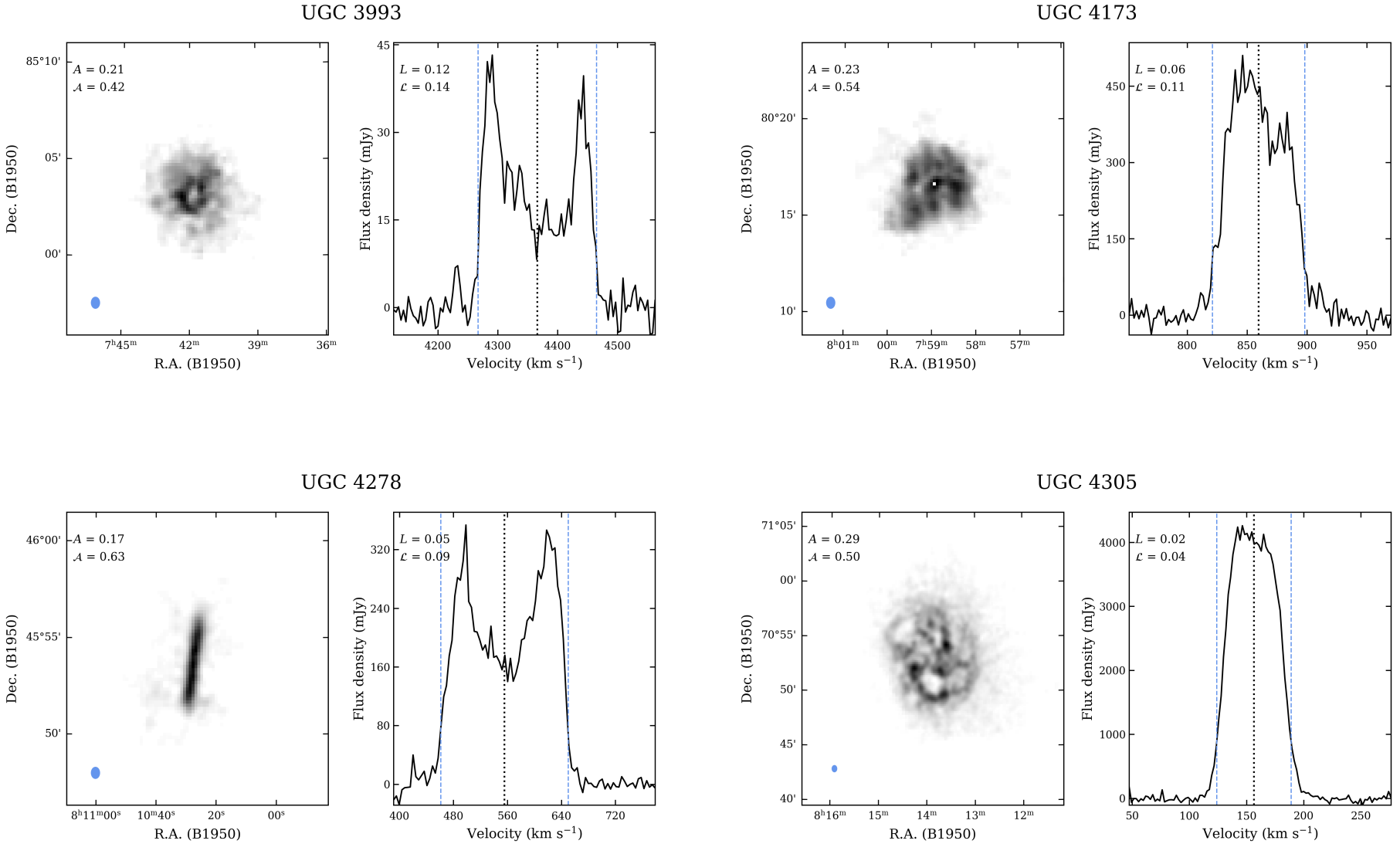

Figure B.1: continued.

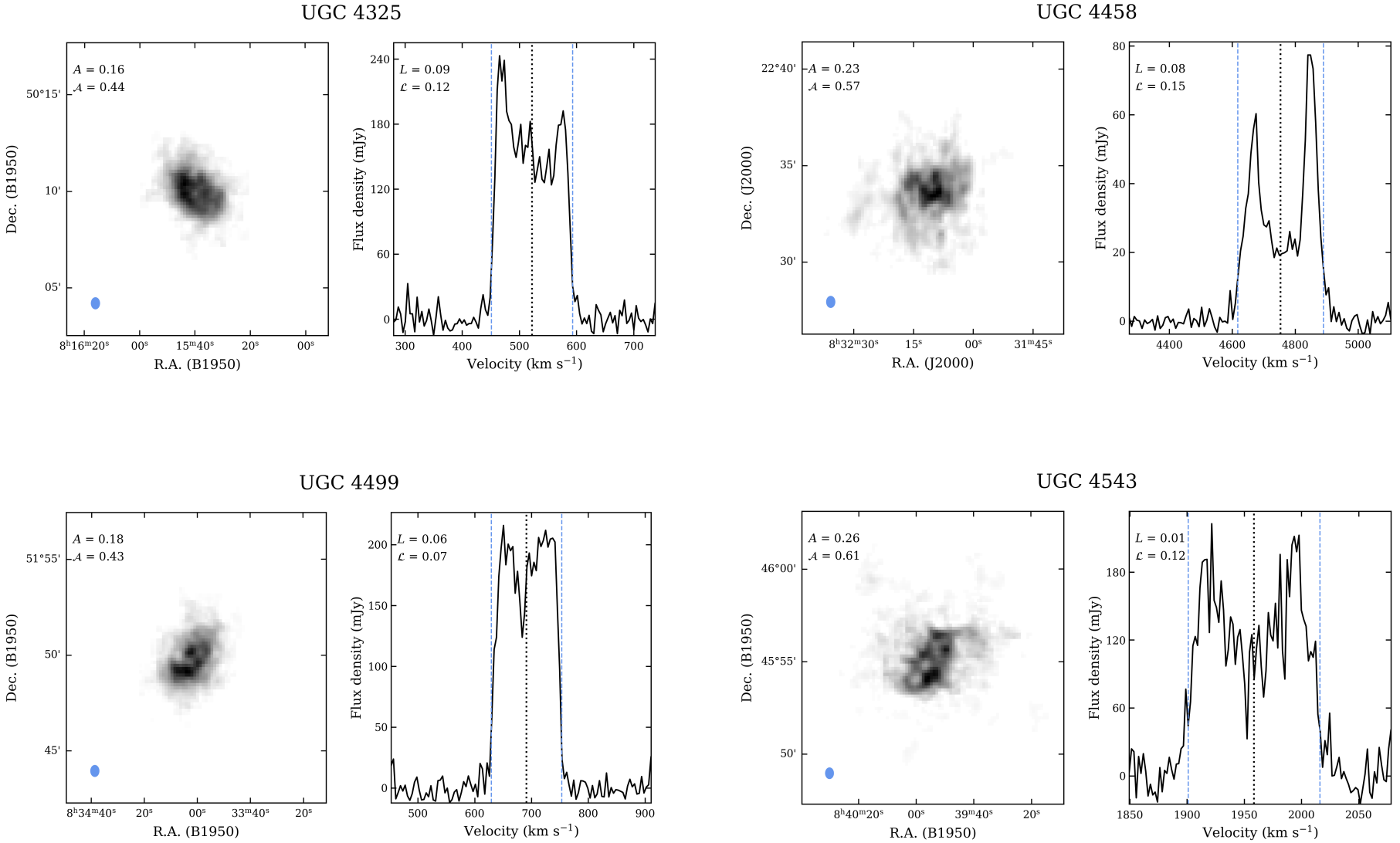

Figure B.1: continued.

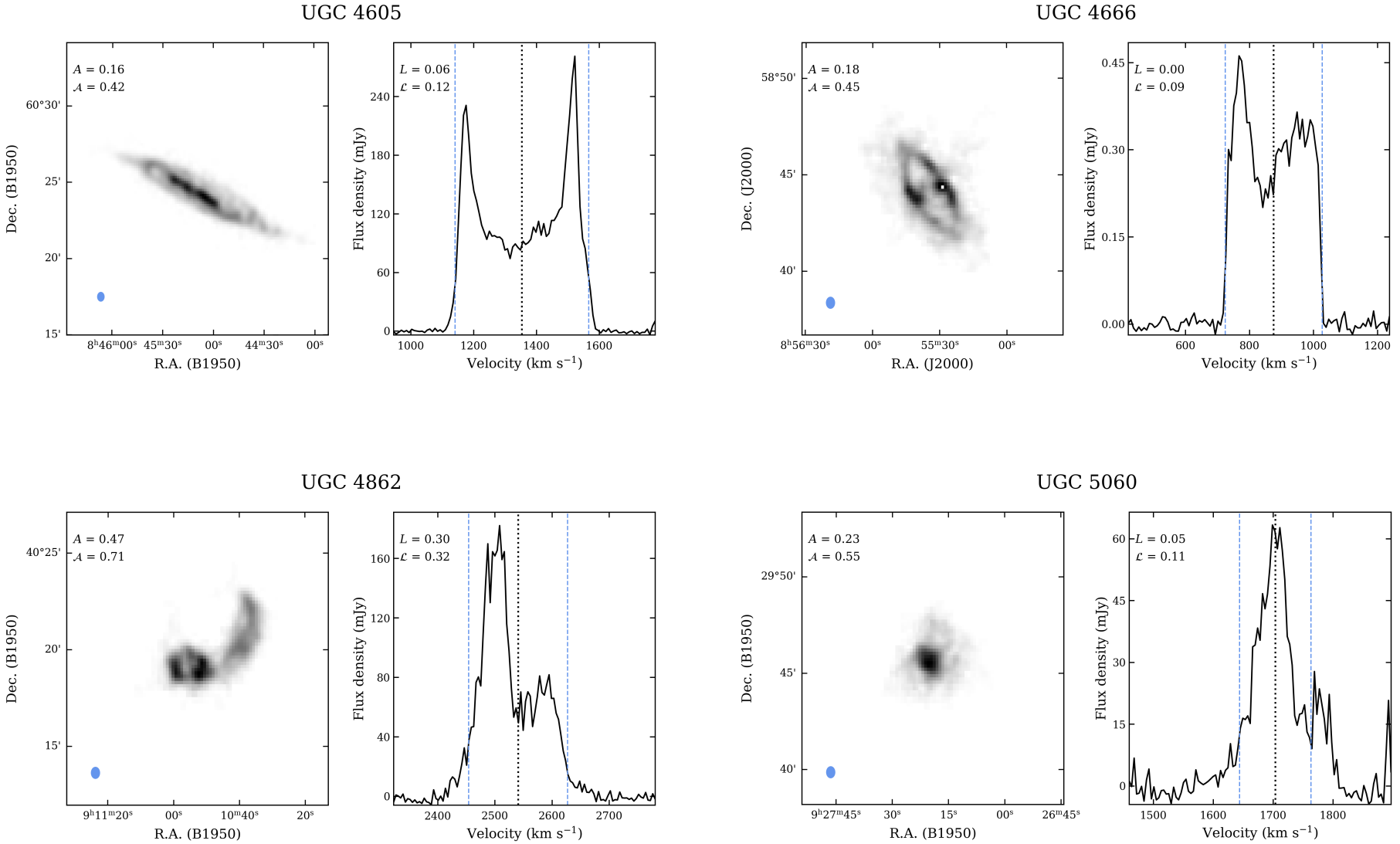

Figure B.1: continued.

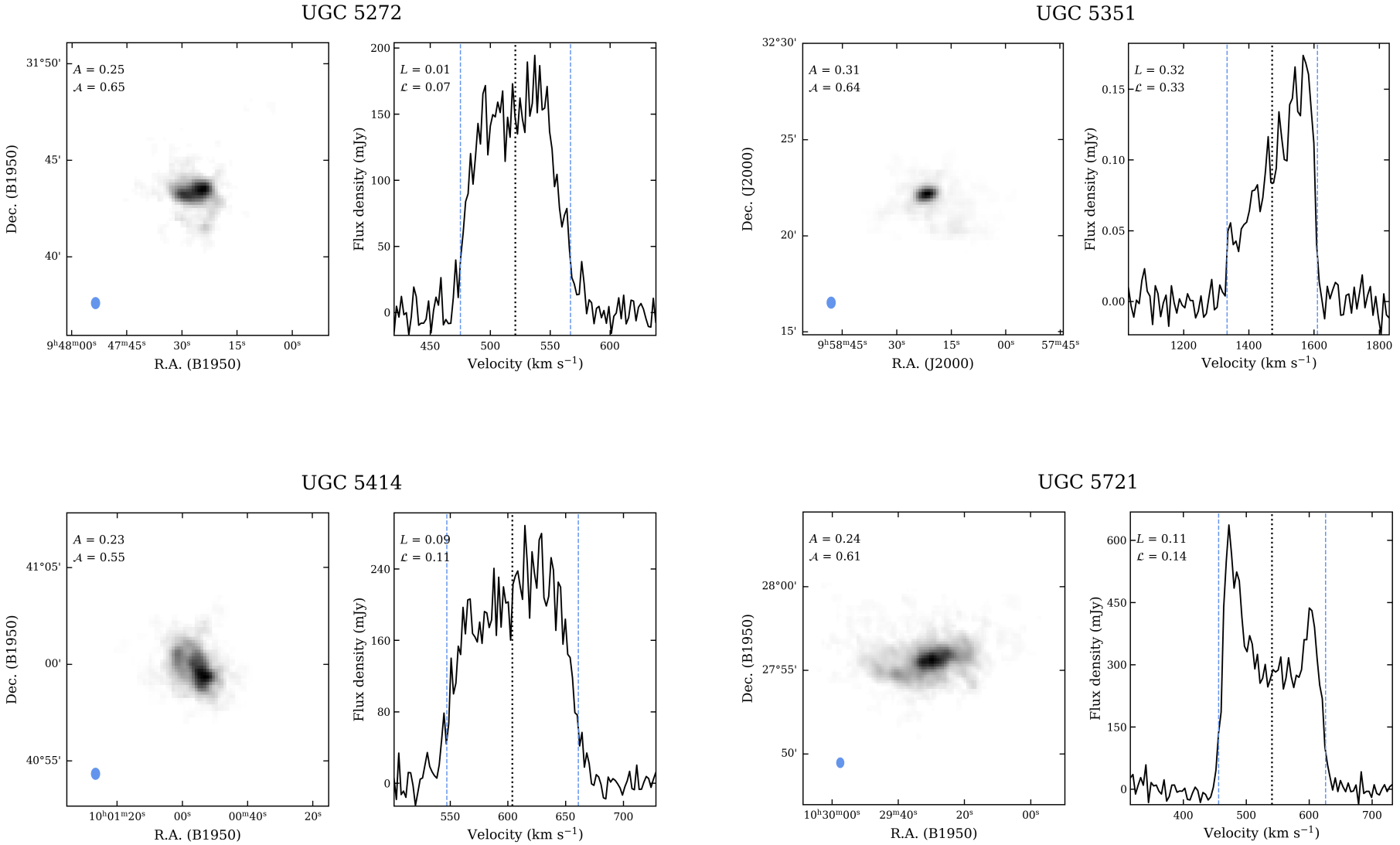

Figure B.1: continued.

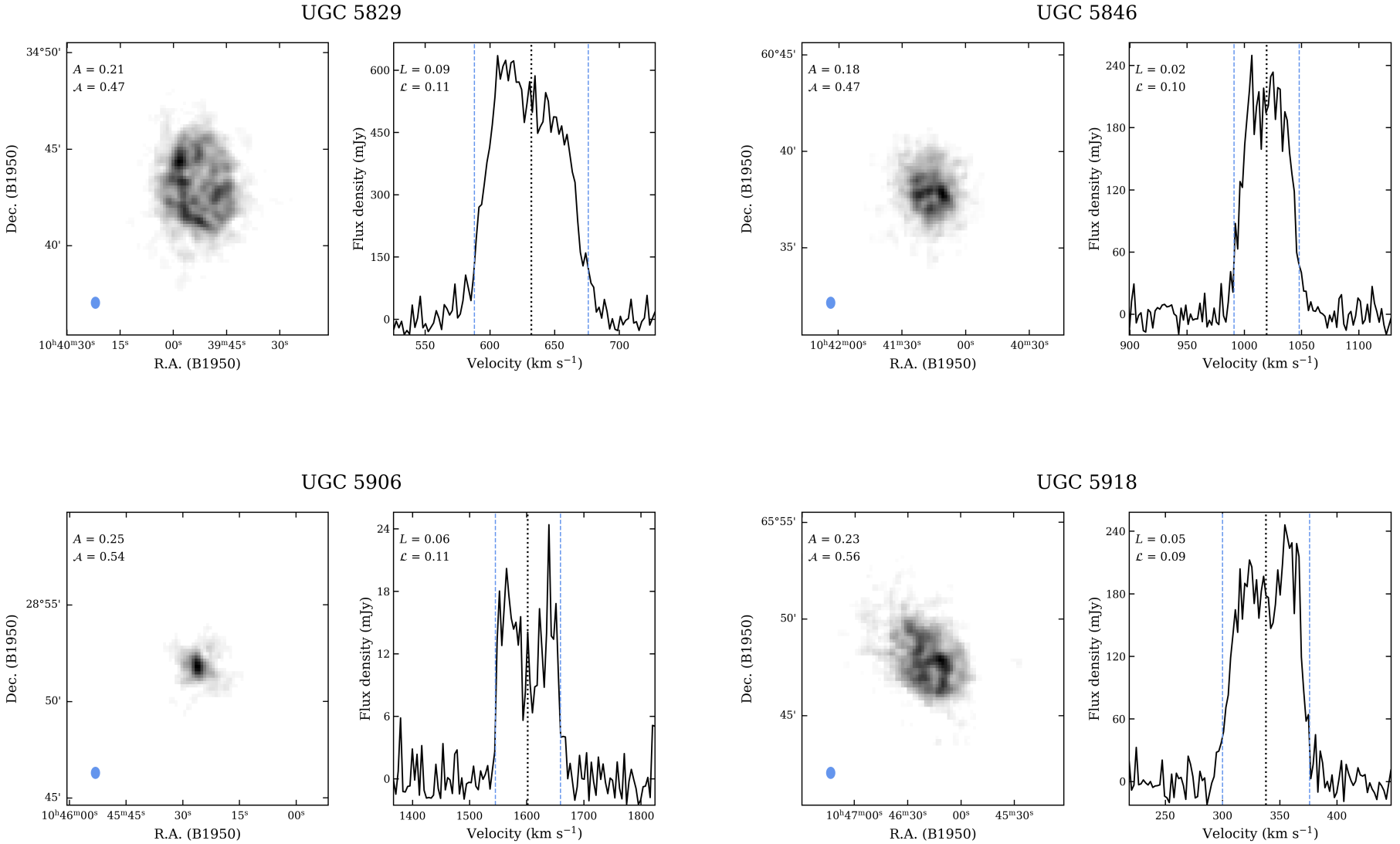

Figure B.1: continued.

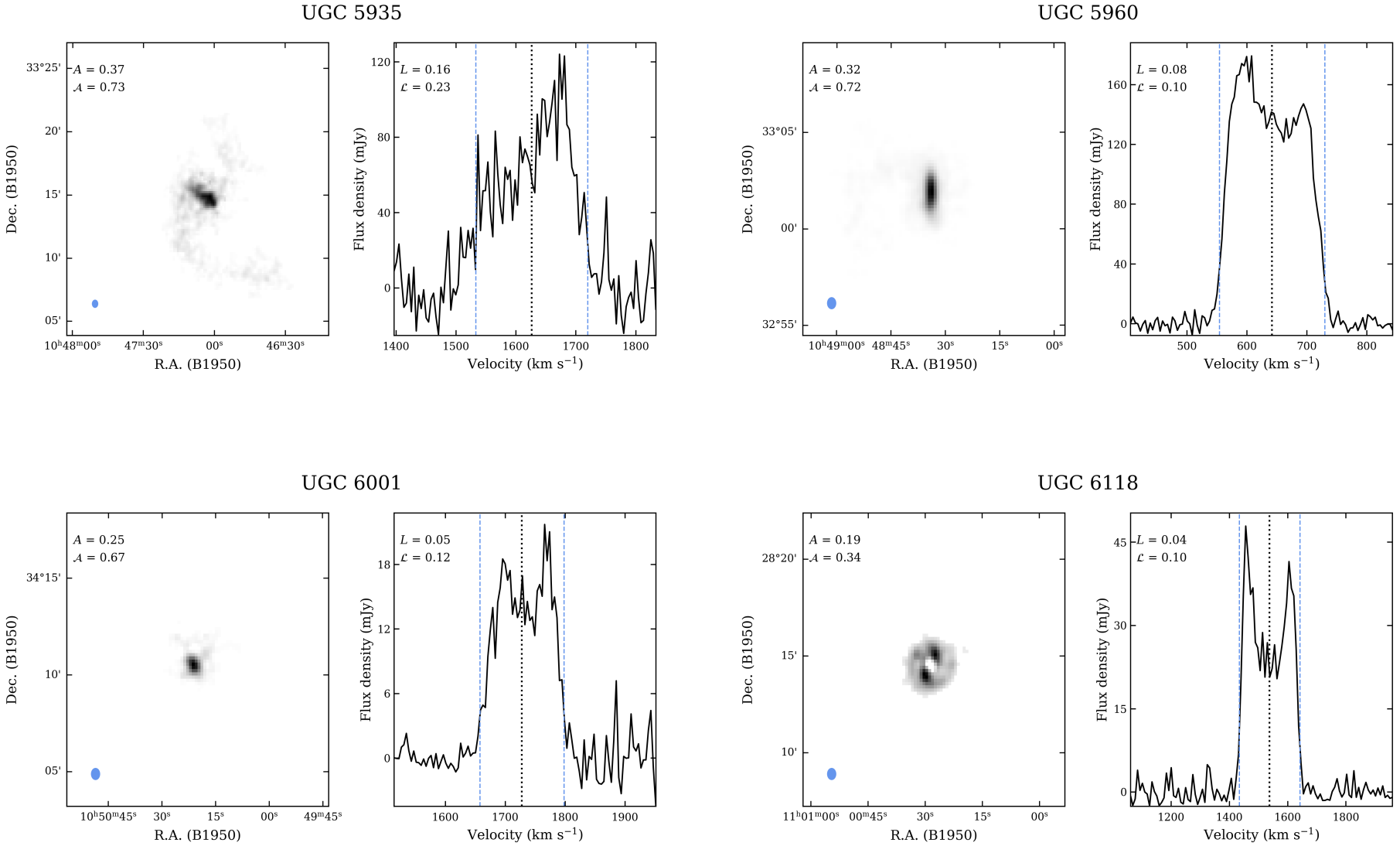

Figure B.1: continued.

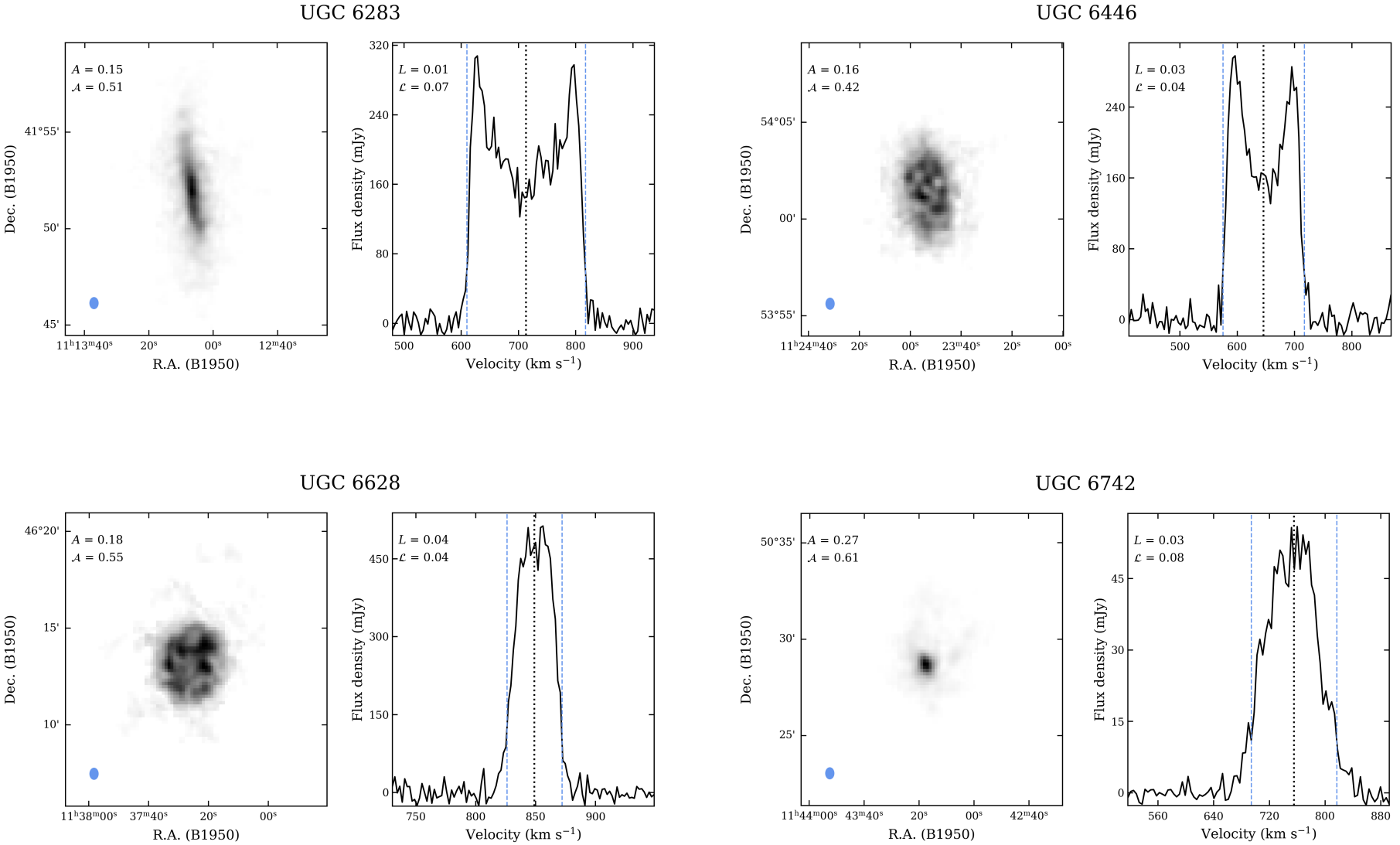

Figure B.1: continued.

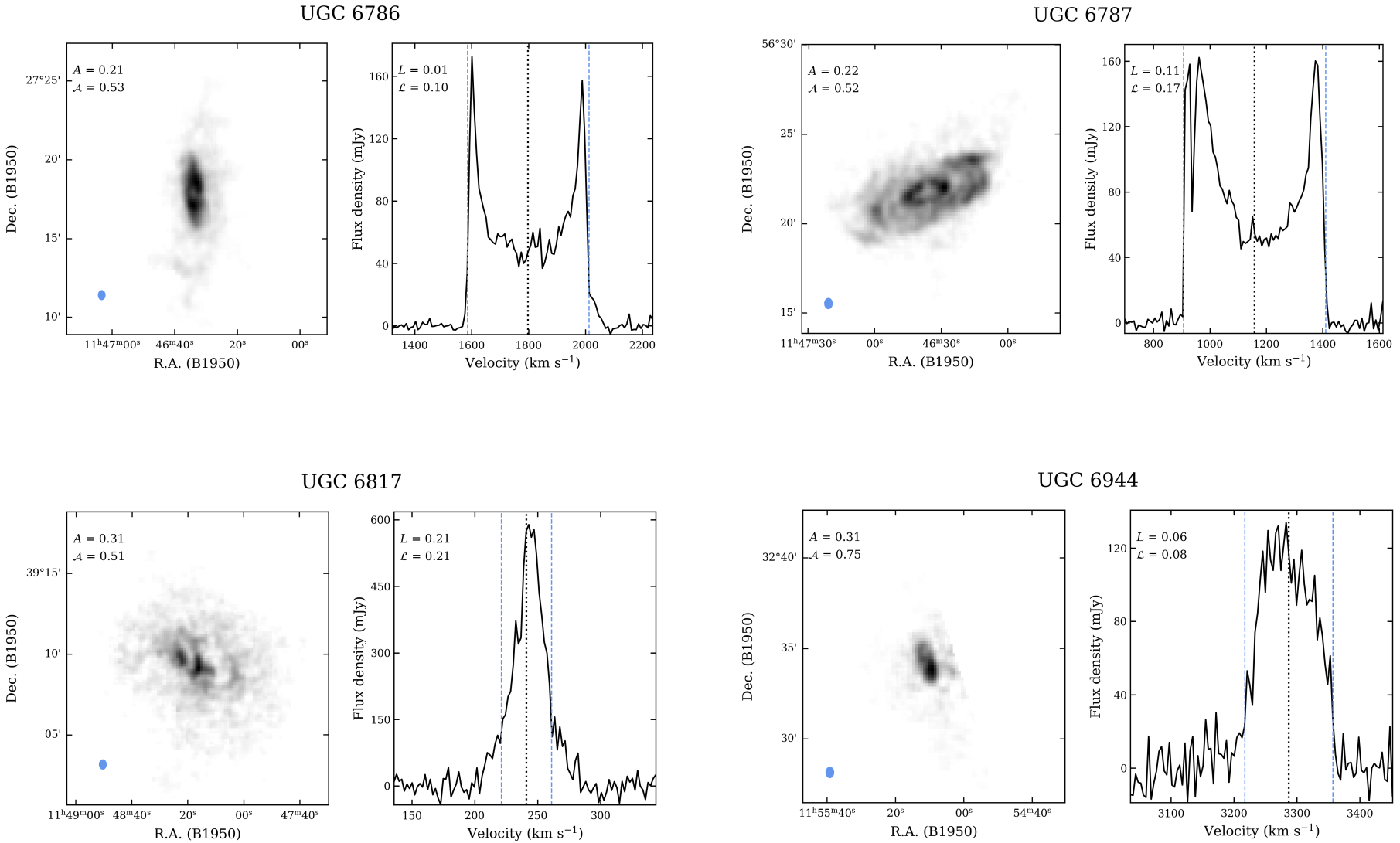

Figure B.1: continued.

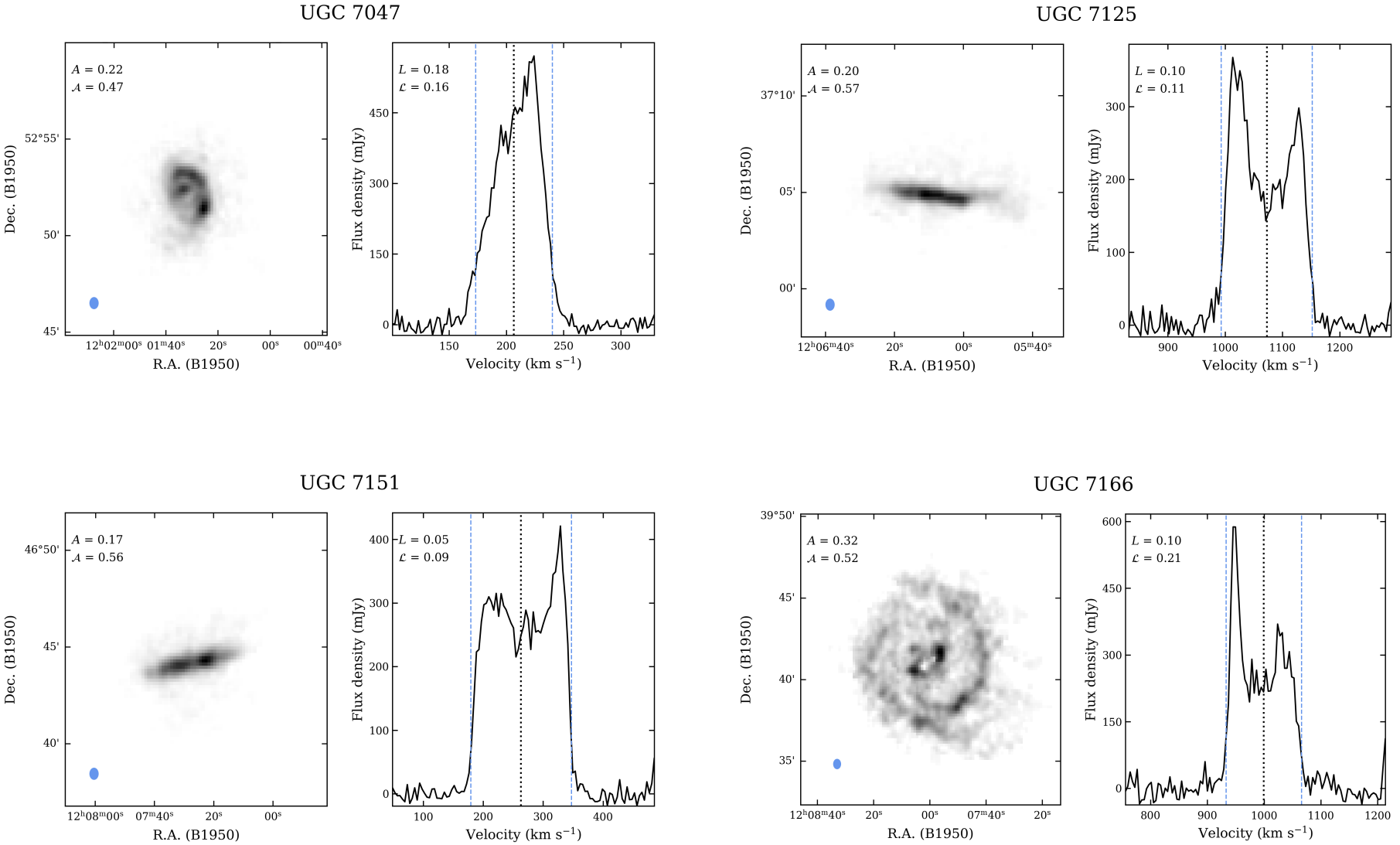

Figure B.1: continued.

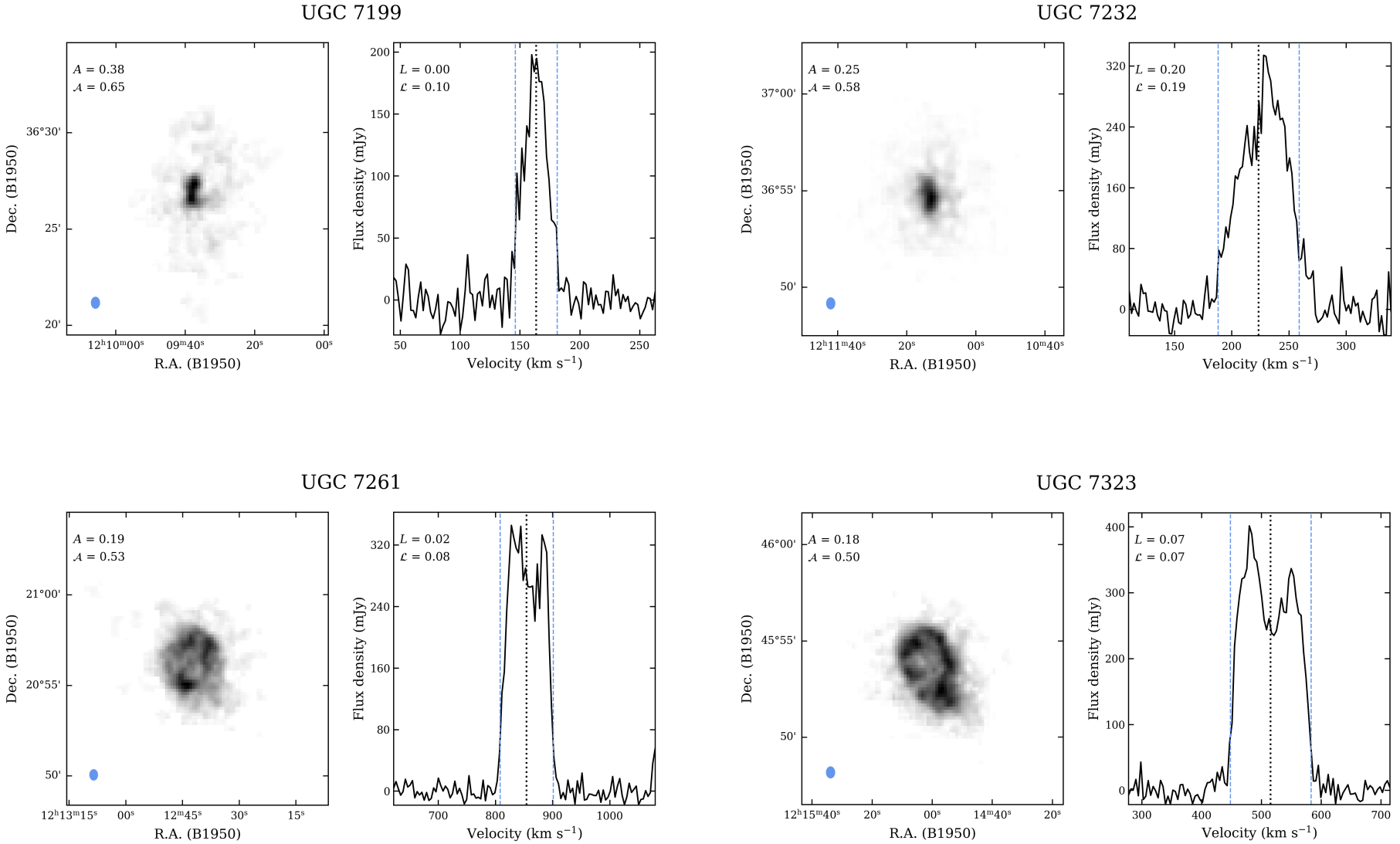

Figure B.1: continued.

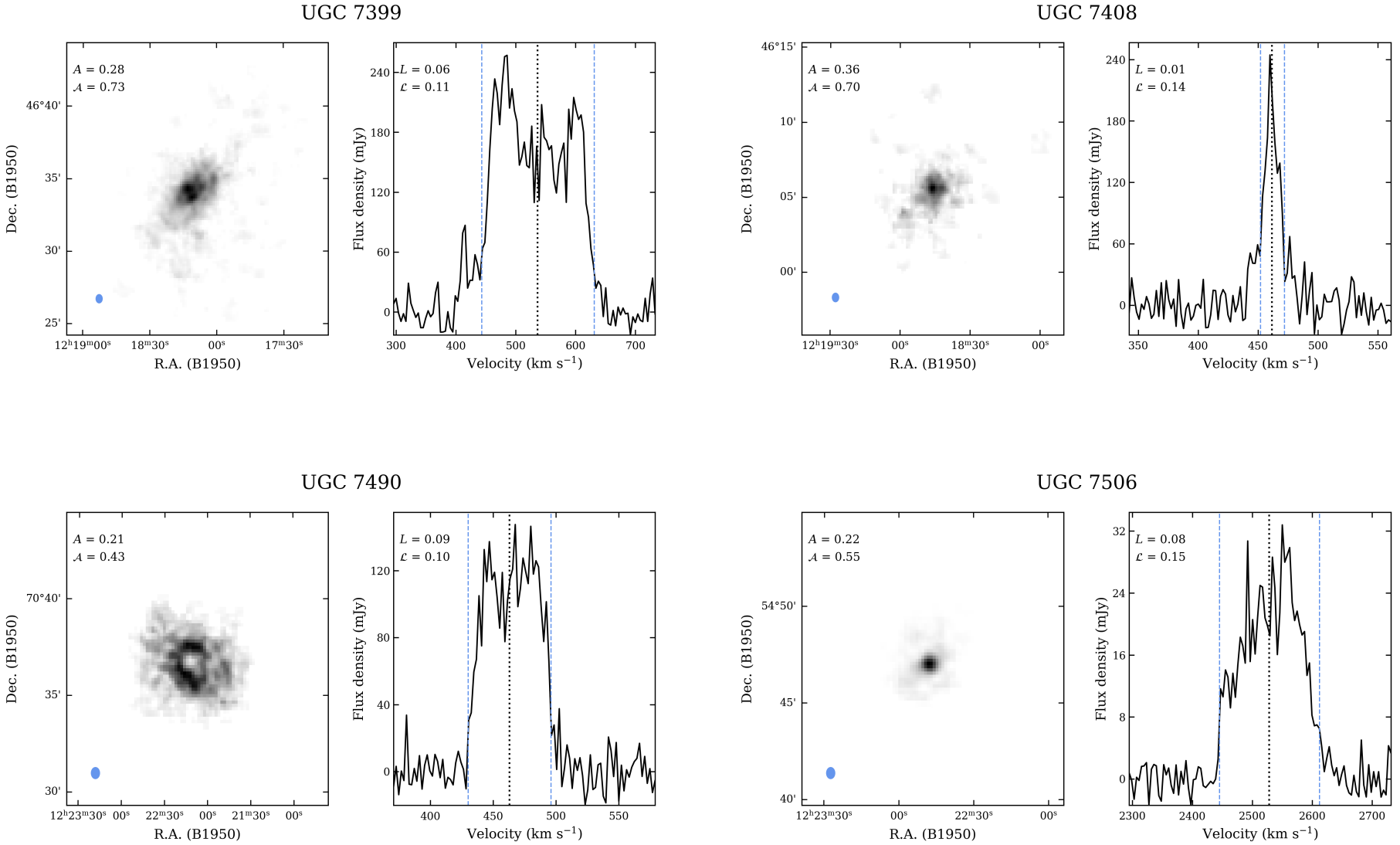

Figure B.1: continued.

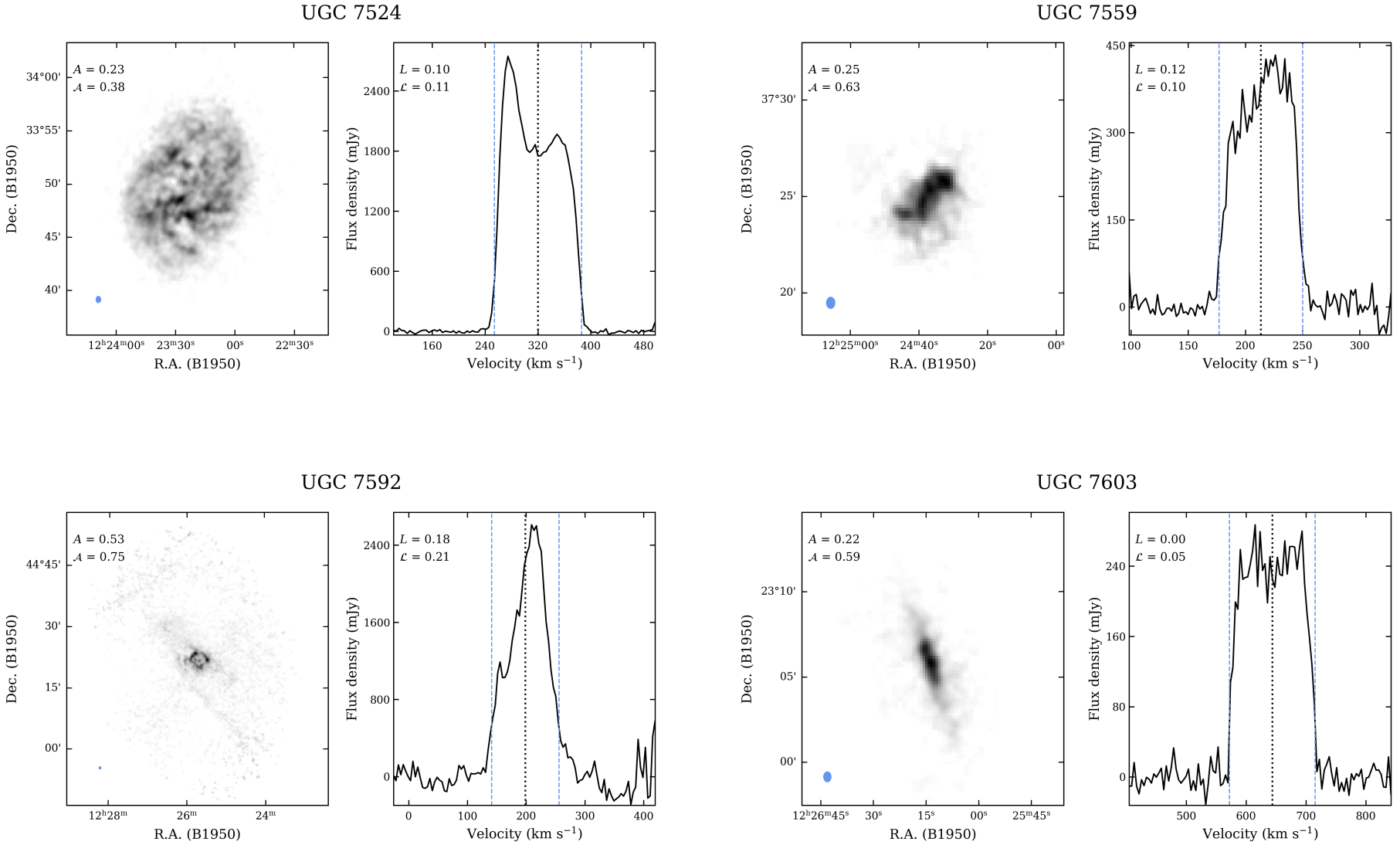

Figure B.1: continued.

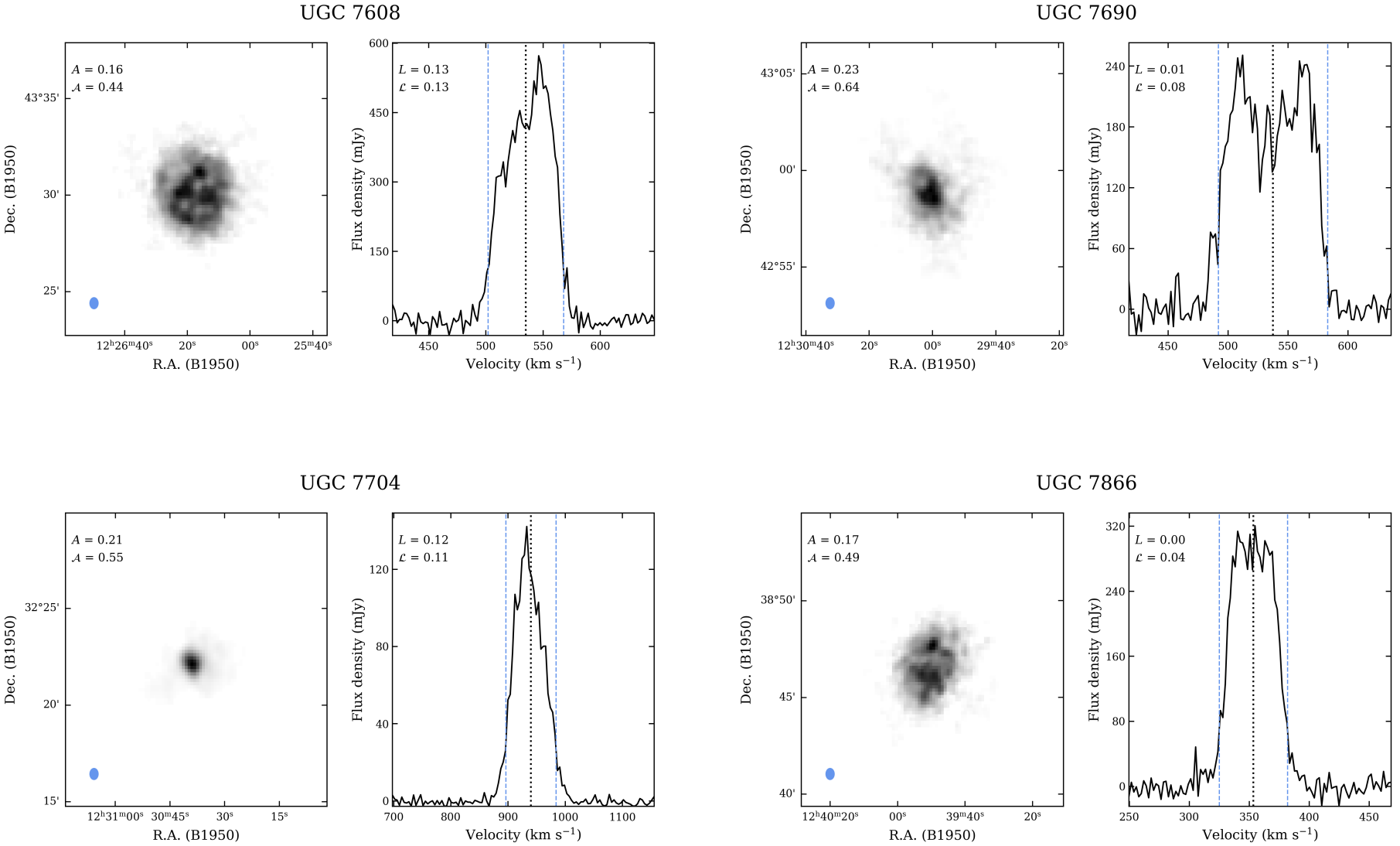

Figure B.1: continued.

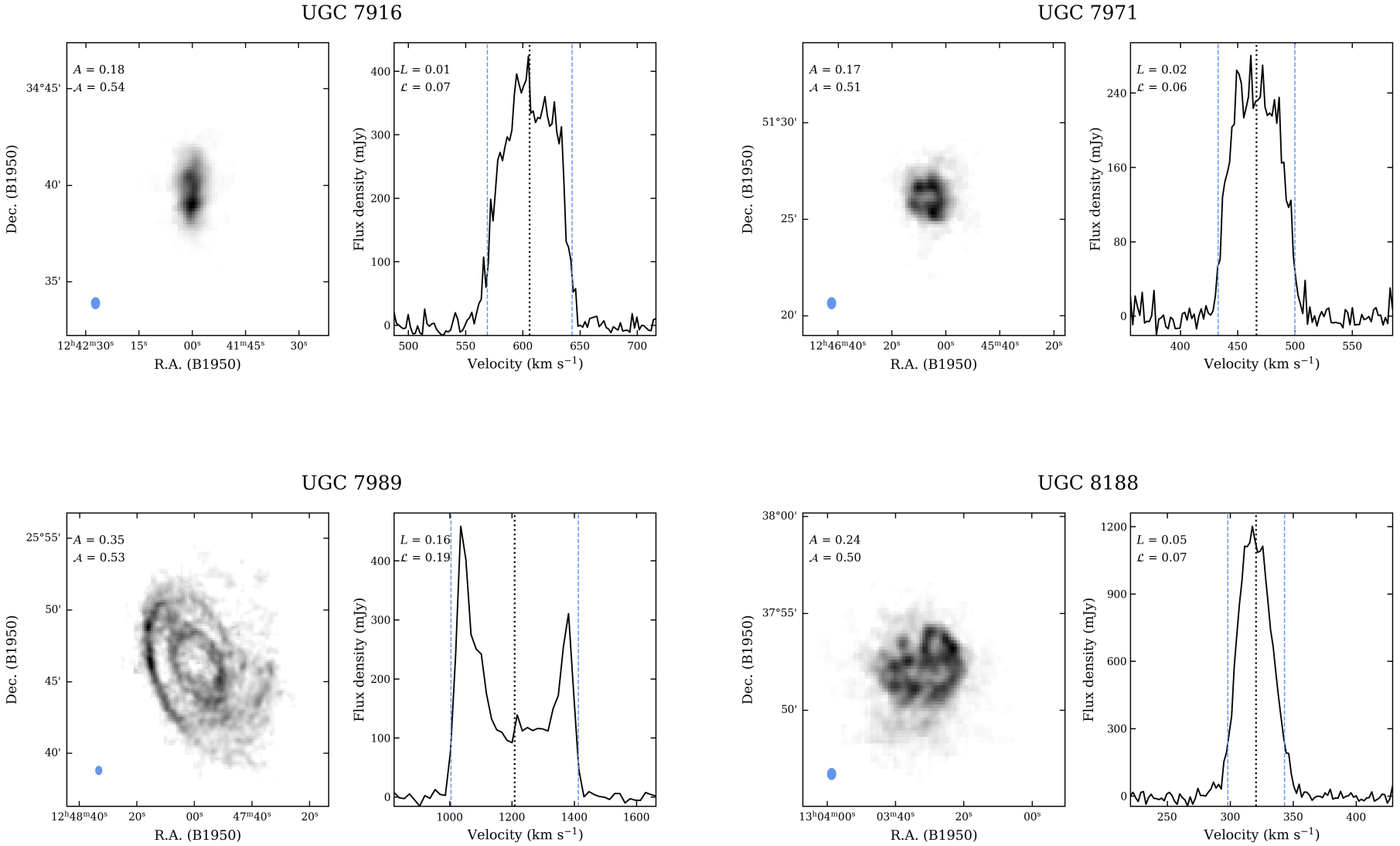

Figure B.1: continued.

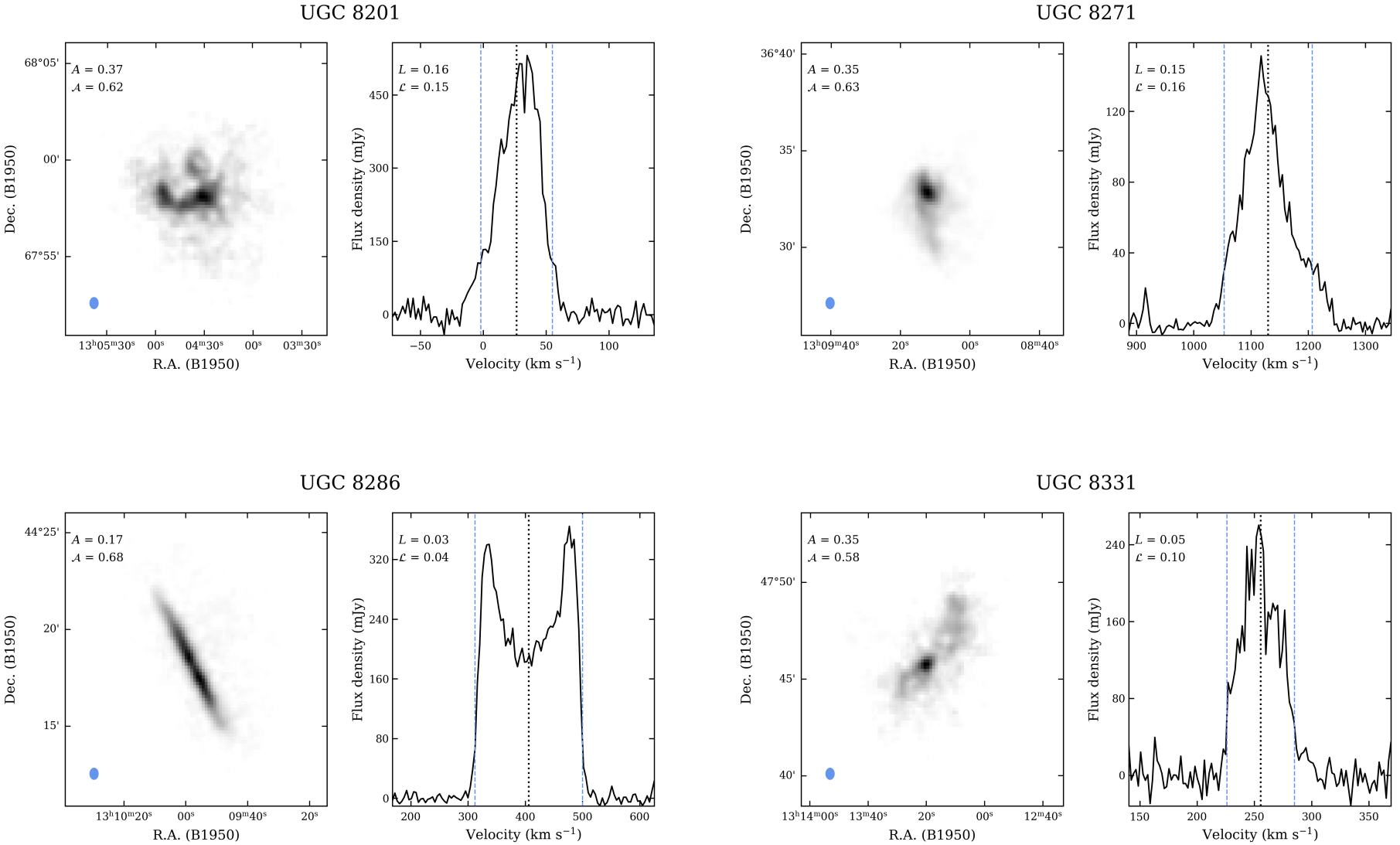

Figure B.1: continued.

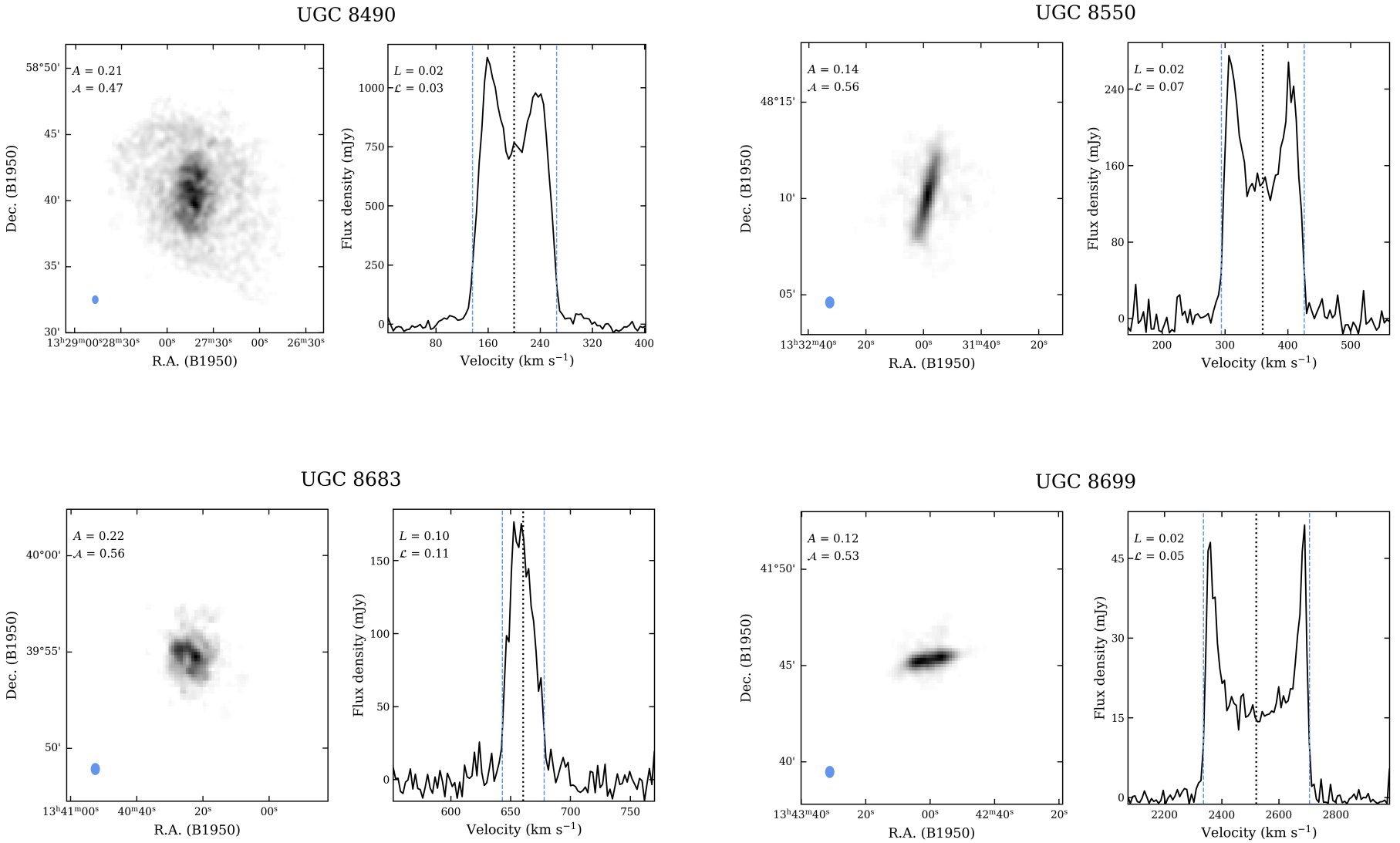

Figure B.1: continued.

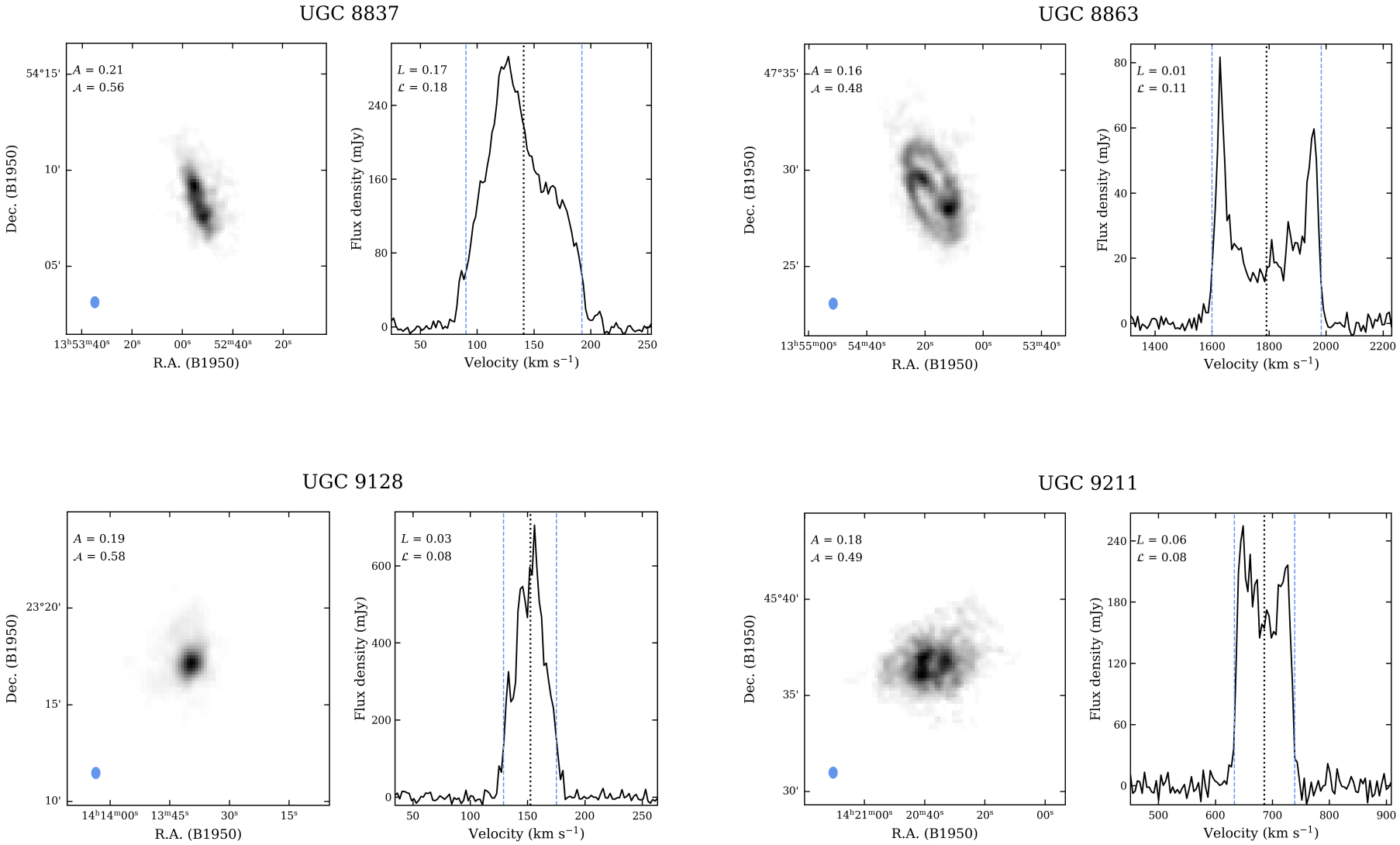

Figure B.1: continued.

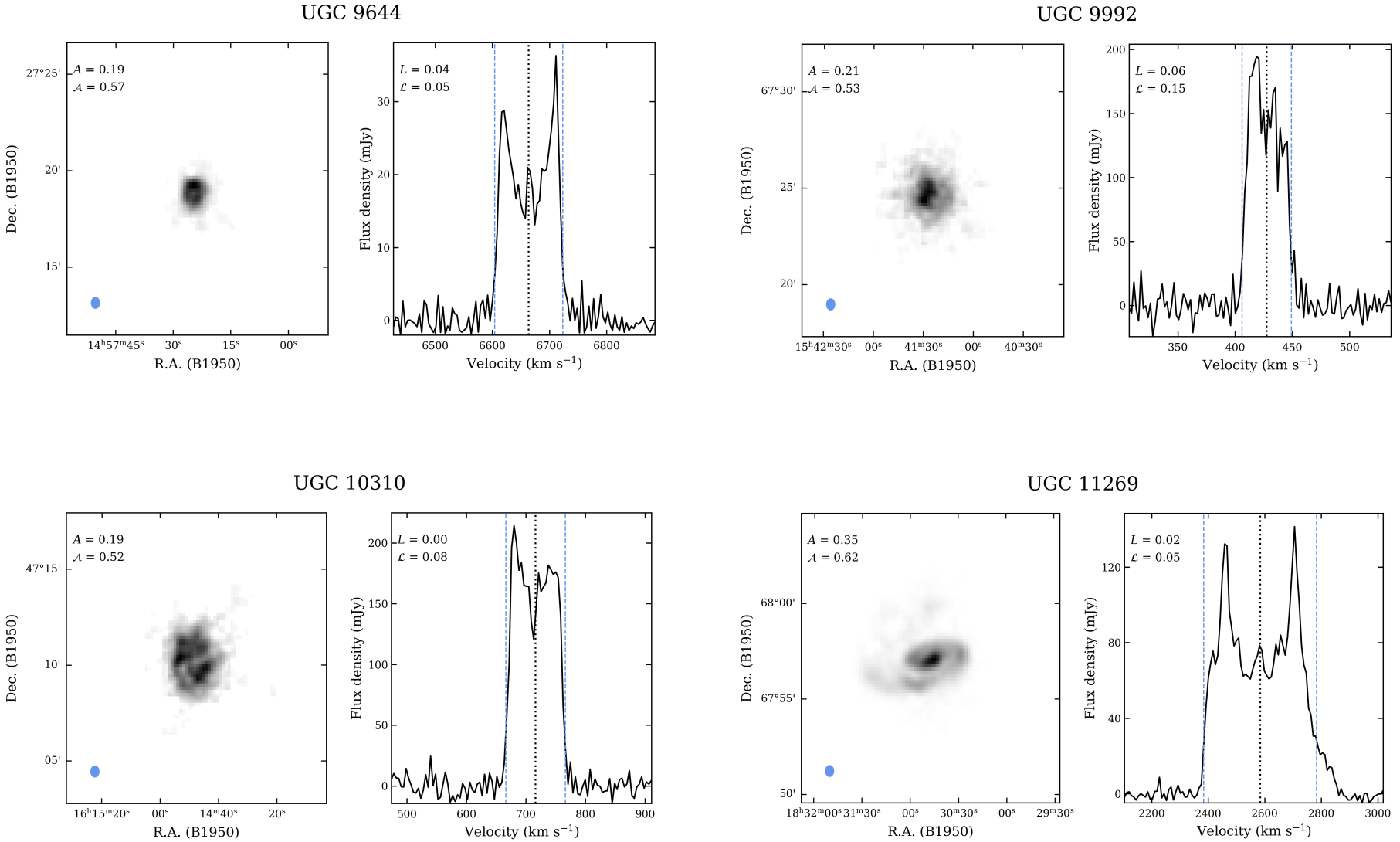

Figure B.1: continued.

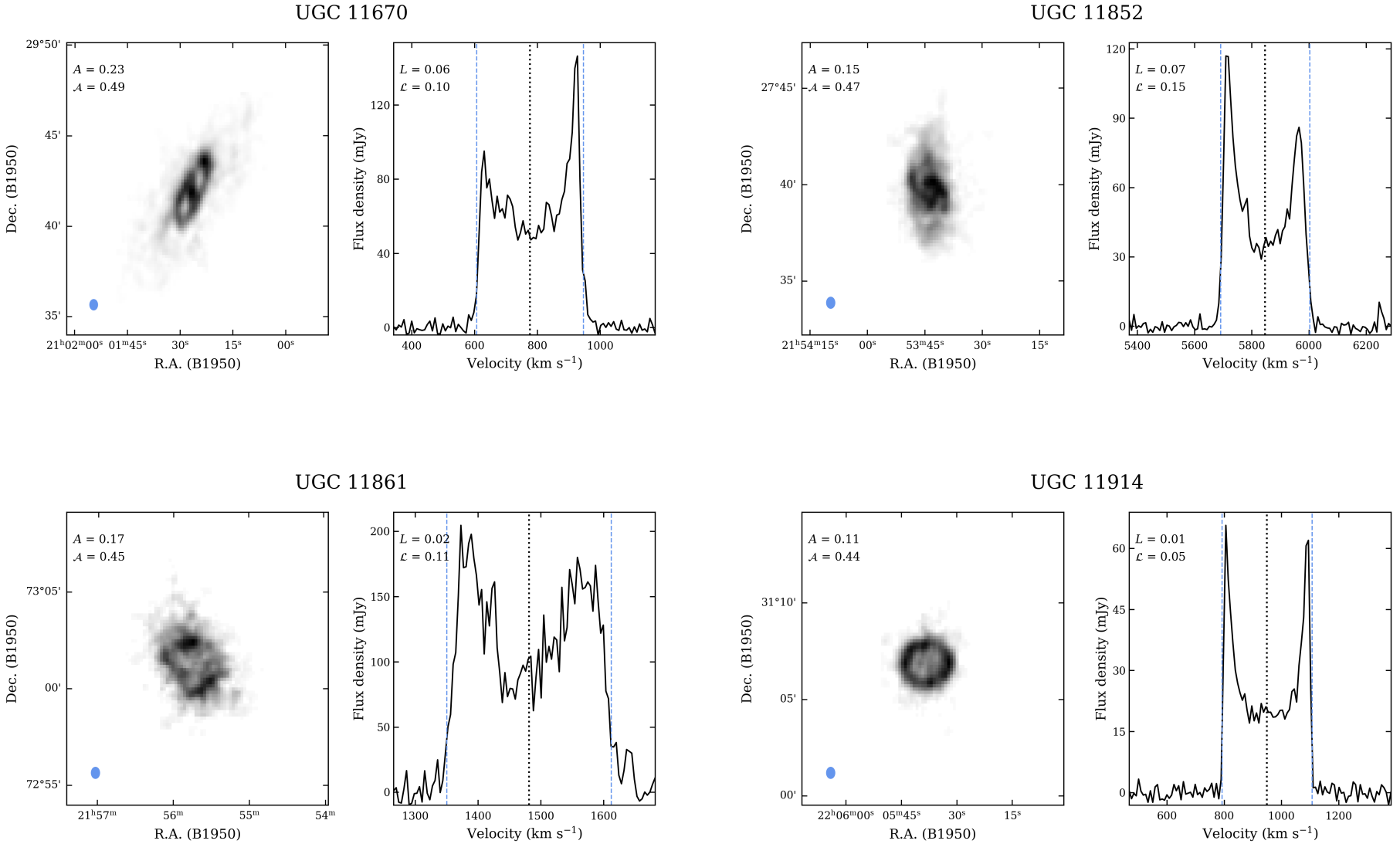

Figure B.1: continued.

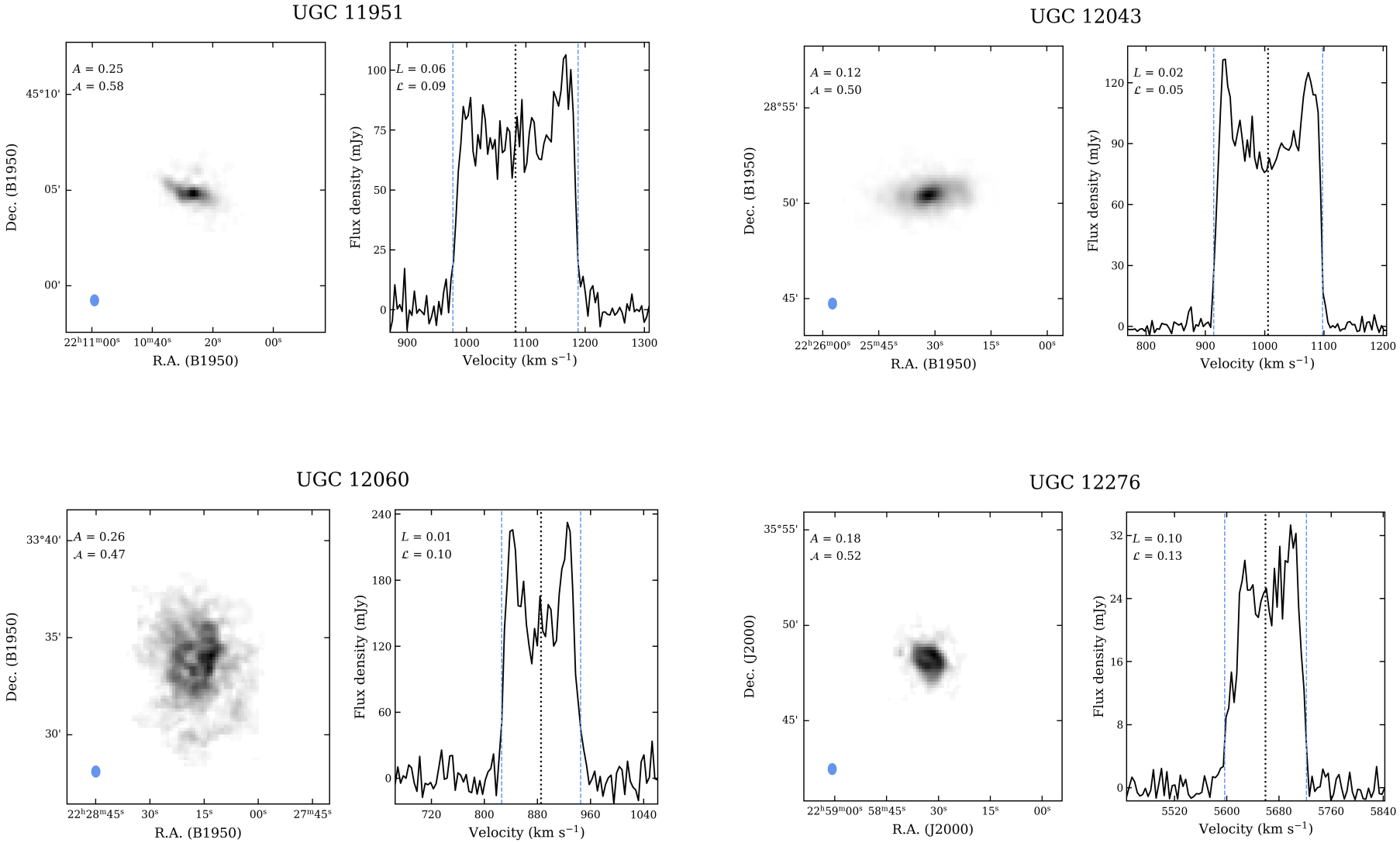

Figure B.1: continued.

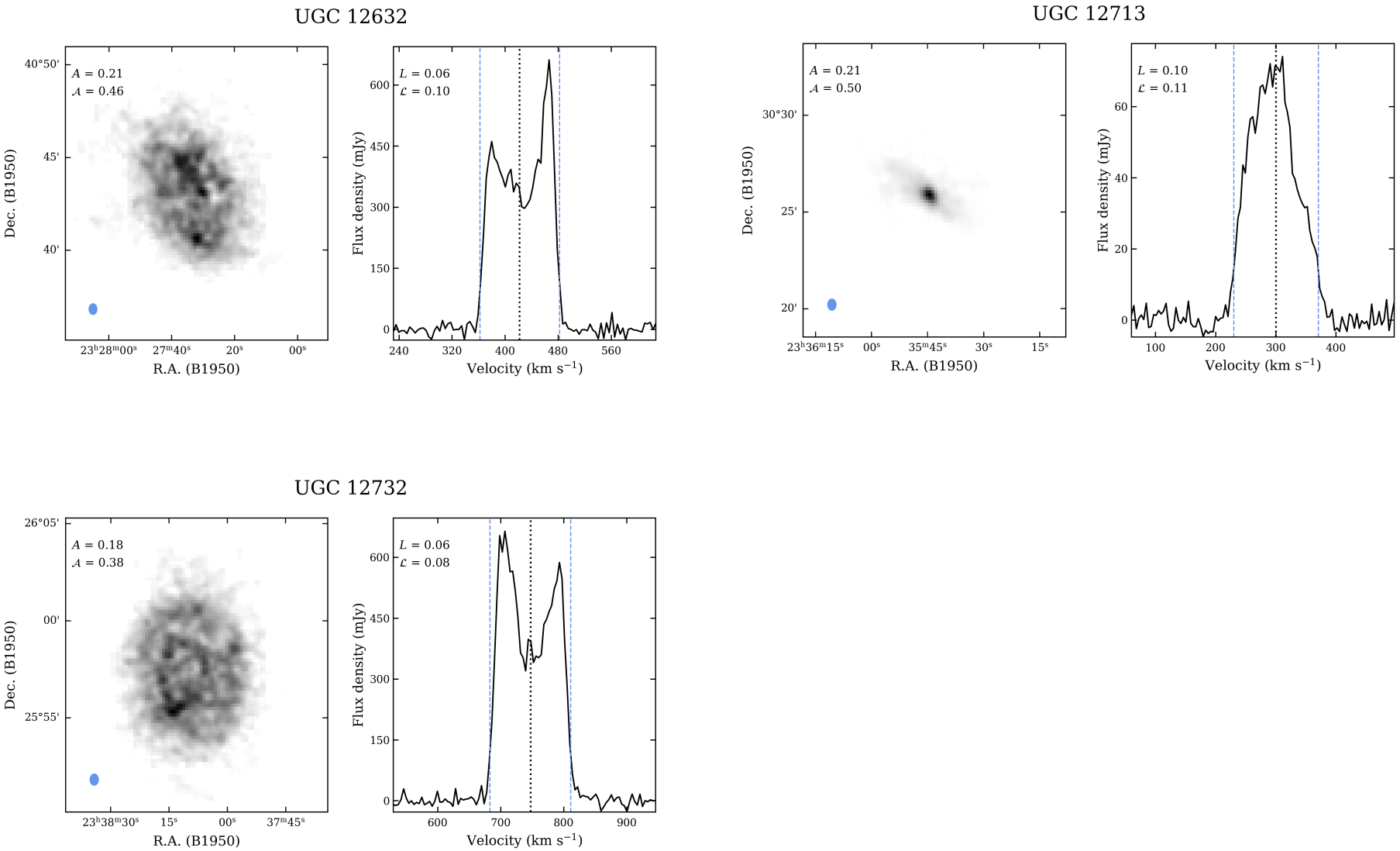

Figure B.1: continued.

Appendix C

Additional figures: WHISP

C.1 The 1D lopsidedness parameters vs. visual classifications

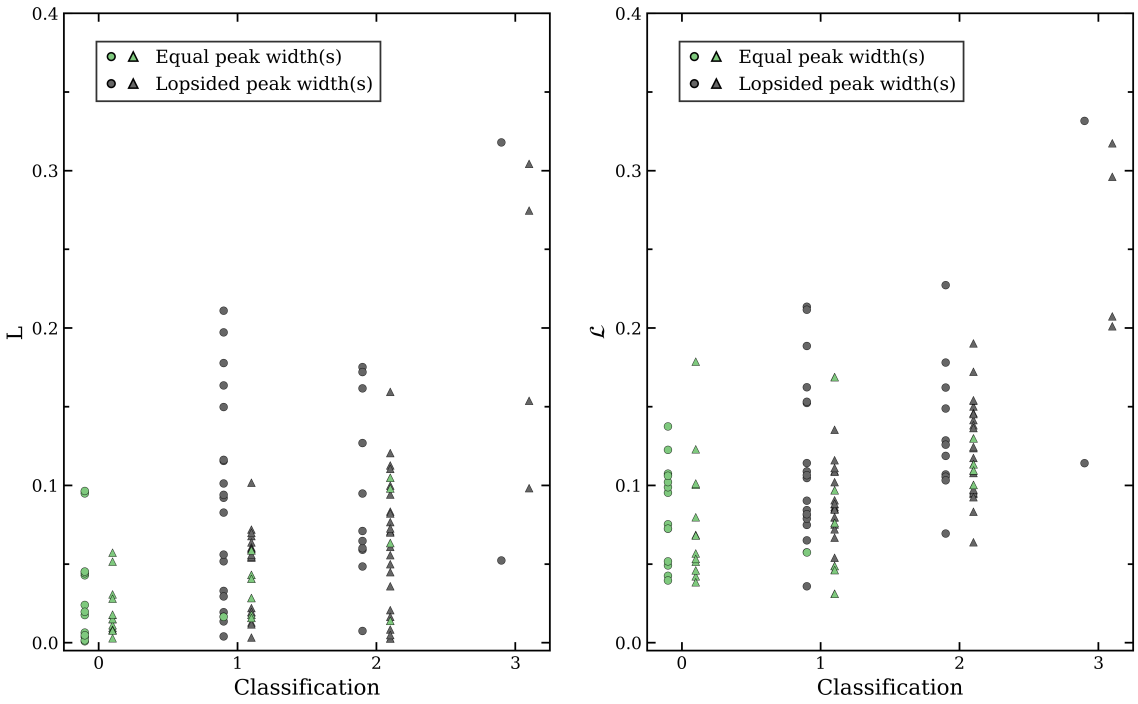

Figure C.1: Correlations between the visual classifications of asymmetry in the HI line profiles of WHISP galaxies and the measured 1D lopsidedness parameters L (left) and $\mathcal{L}$ (right). The triangle markers represent profiles identified to have two peaks and the circle markers represent single peak profiles. The markers are coloured according to whether the peak(s) of the profile have equal (green) or differing widths (grey).

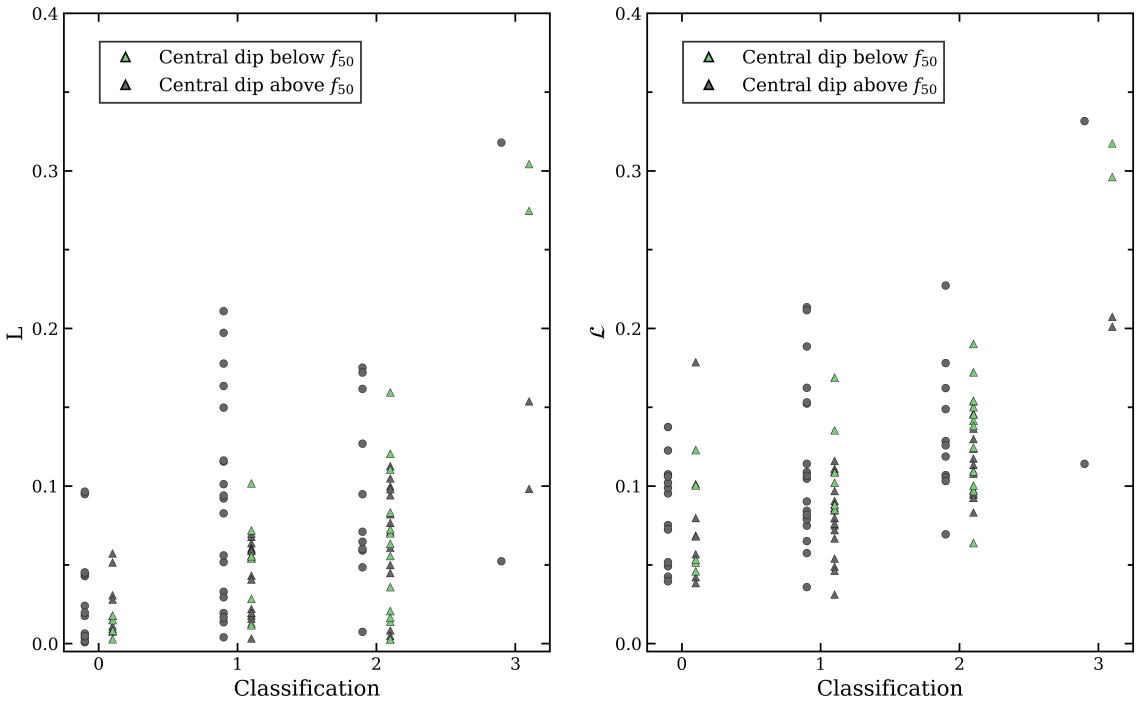

Figure C.2: Correlations between visual classifications and measured 1D lopsidedness parameters L (left) and $\mathcal{L}$ (right). The markers are the same as shown in Figure C.1. The markers are colour-coded according to whether the central dip in the profile lies above (grey) or below (green) f_{50}, the intensity level at 50% of the average peak flux.

C.2 The 2D asymmetry parameters vs. visual classifications

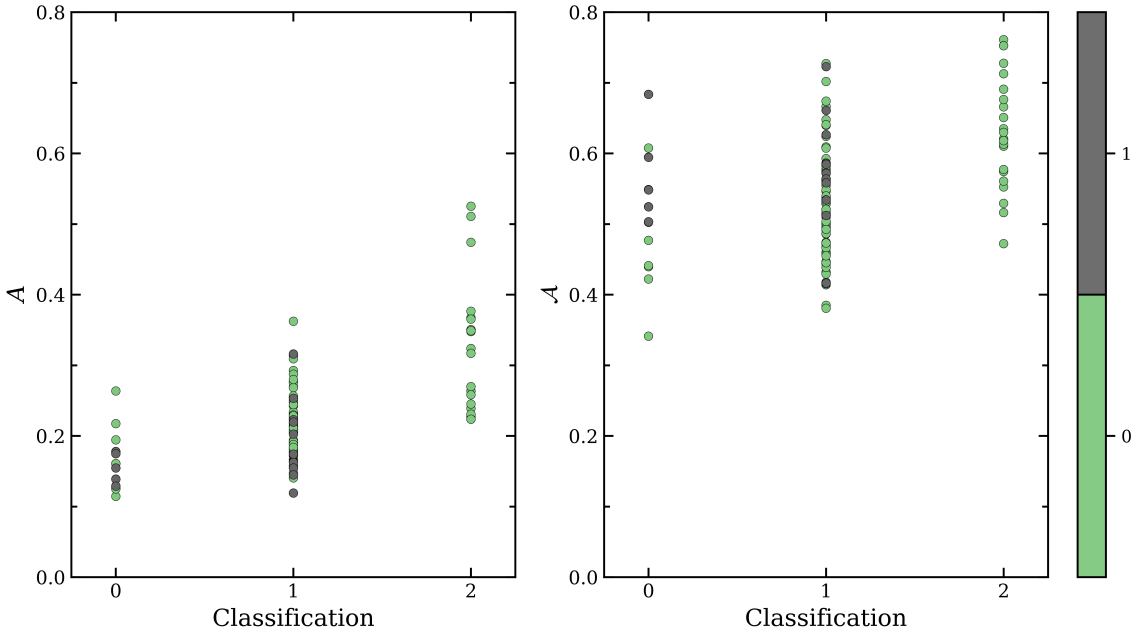

Figure C.3: Correlations between the visual classifications of asymmetry in the HI images of WHISP galaxies and the measured 2D parameters A (left) and $\mathcal{A}$ (right). The circle markers are coloured according to whether a galaxy is classified as edge-on (grey) or not (green).

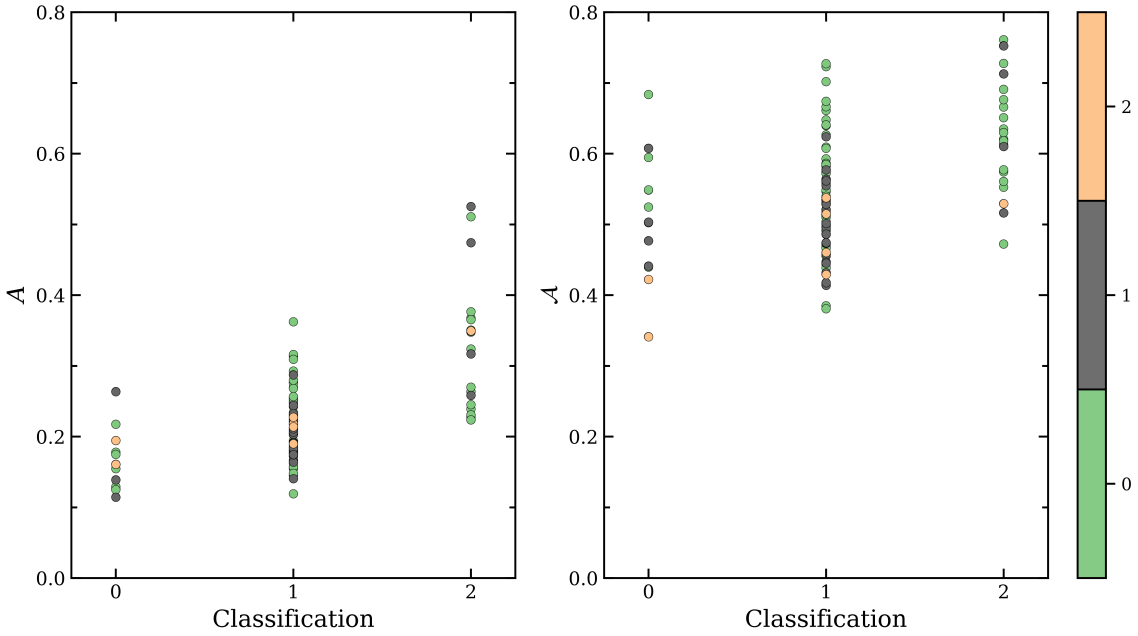

Figure C.4: Correlations between the visual classifications of asymmetry in the HI images of WHISP galaxies and the measured 2D parameters A (left) and $\mathcal{A}$ (right). The markers are coloured according to whether a depression (grey) or hole (peach) exists in the central region of the galaxy's HI distribution. Galaxies with none of these features present are represented by green markers.

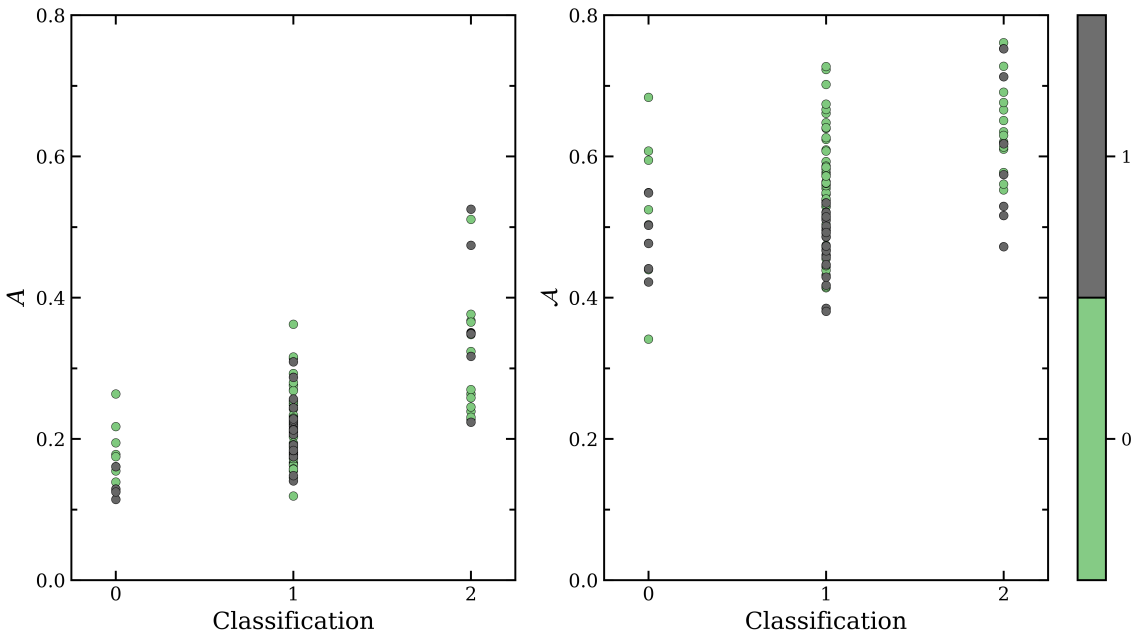

Figure C.5: Correlations between the visual classifications of asymmetry in the HI images of WHISP galaxies and the measured 2D asymmetry parameters A (left) and $\mathcal{A}$ (right). Grey markers represent galaxies that display spiral or ring structure in their HI distribution.

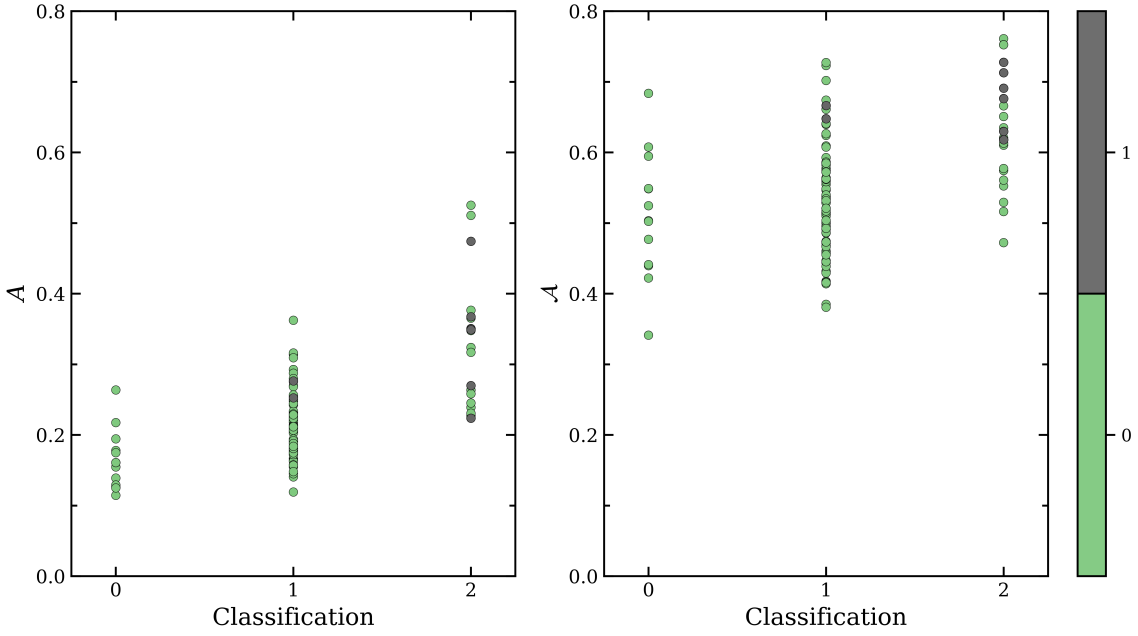

Figure C.6: Correlations between the visual classifications of asymmetry in the HI images of WHISP galaxies and the measured 2D asymmetry parameters A (left) and $\mathcal{A}$ (right). Grey markers represent galaxies that display tidal tails in their HI distribution.

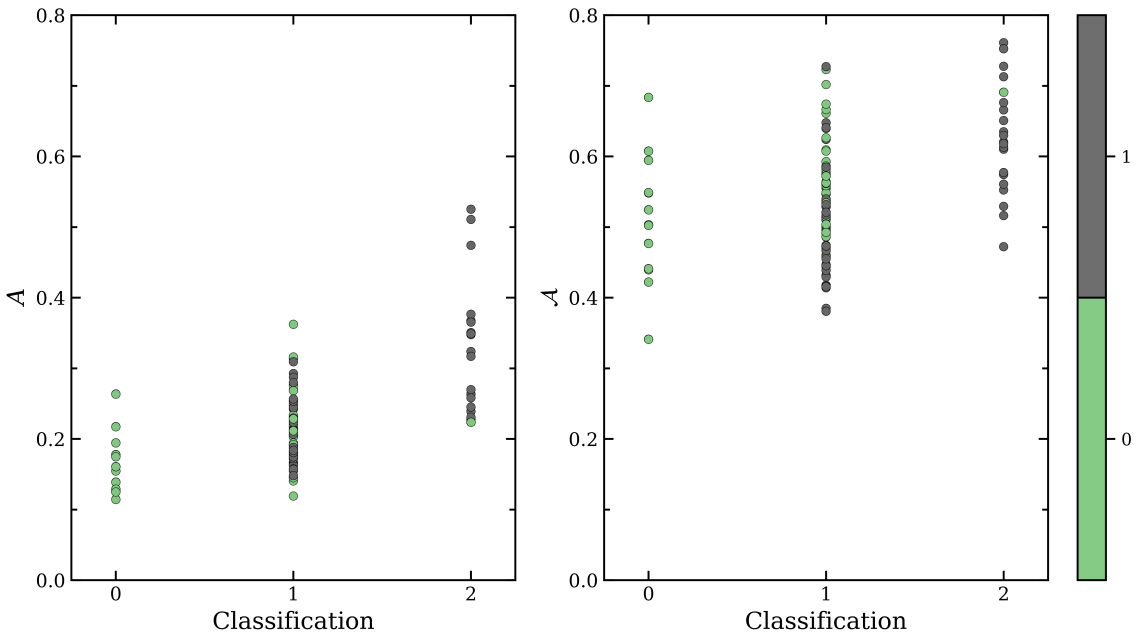

Figure C.7: Correlations between the visual classifications of asymmetry in the HI images of WHISP galaxies and the measured 2D asymmetry parameters A (left) and $\mathcal{A}$ (right). The markers are coloured according to whether the inner region of the galaxy's HI distribution has been classified as symmetric (green) or asymmetric (grey).

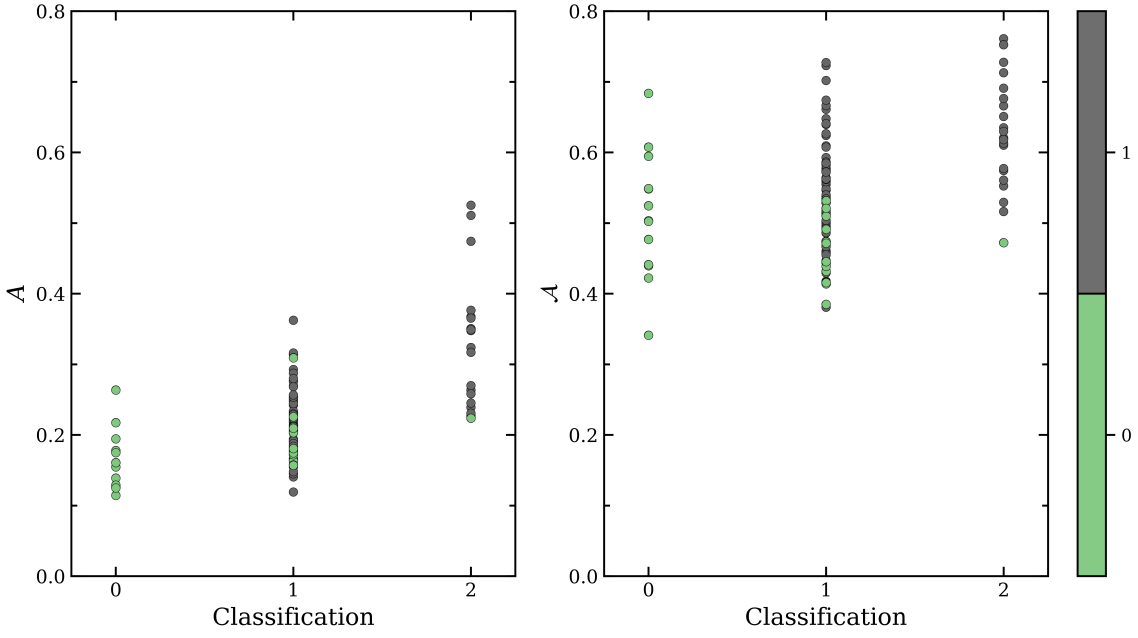

Figure C.8: Correlations between the visual classifications of asymmetry in the HI images of WHISP galaxies and the measured 2D asymmetry parameters A (left) and $\mathcal{A}$ (right). The green markers represent galaxies whose outer regions are considered symmetric and the grey markers indicate galaxies with asymmetric outer regions.

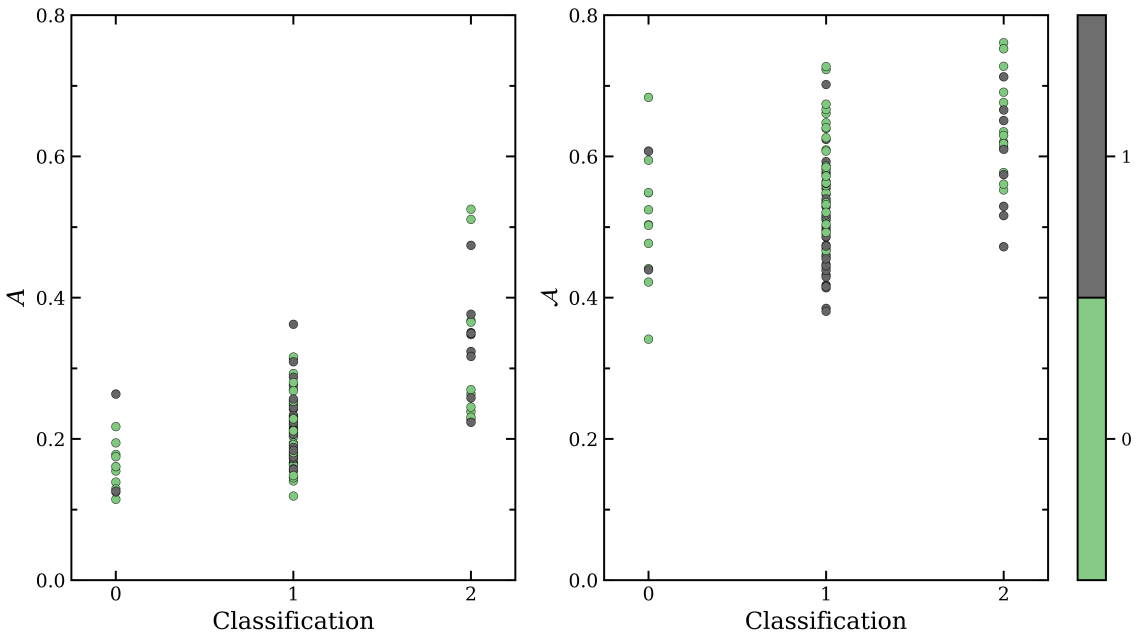

Figure C.9: Correlations between the visual classifications of asymmetry in the HI images of WHISP galaxies and the measured 2D asymmetry parameters A (left) and $\mathcal{A}$ (right). The markers are coloured according to whether the HI distribution of the galaxy is considered clumpy (grey) or smooth (green).

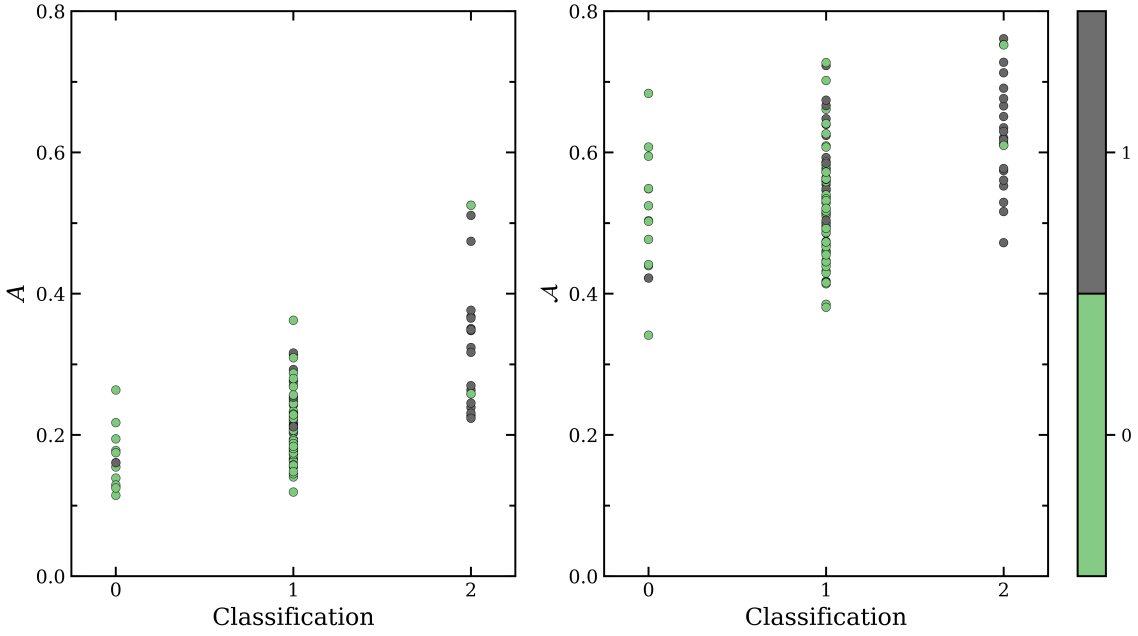

Figure C.10: Correlations between the visual classifications of asymmetry in the HI images of WHISP galaxies, and the measured 2D asymmetry parameters A (left) and $\mathcal{A}$ (right). The grey markers represent galaxies whose centre of symmetry is expected to deviate from the centre of brightness.

C.3 1D-2D asymmetry parameter space

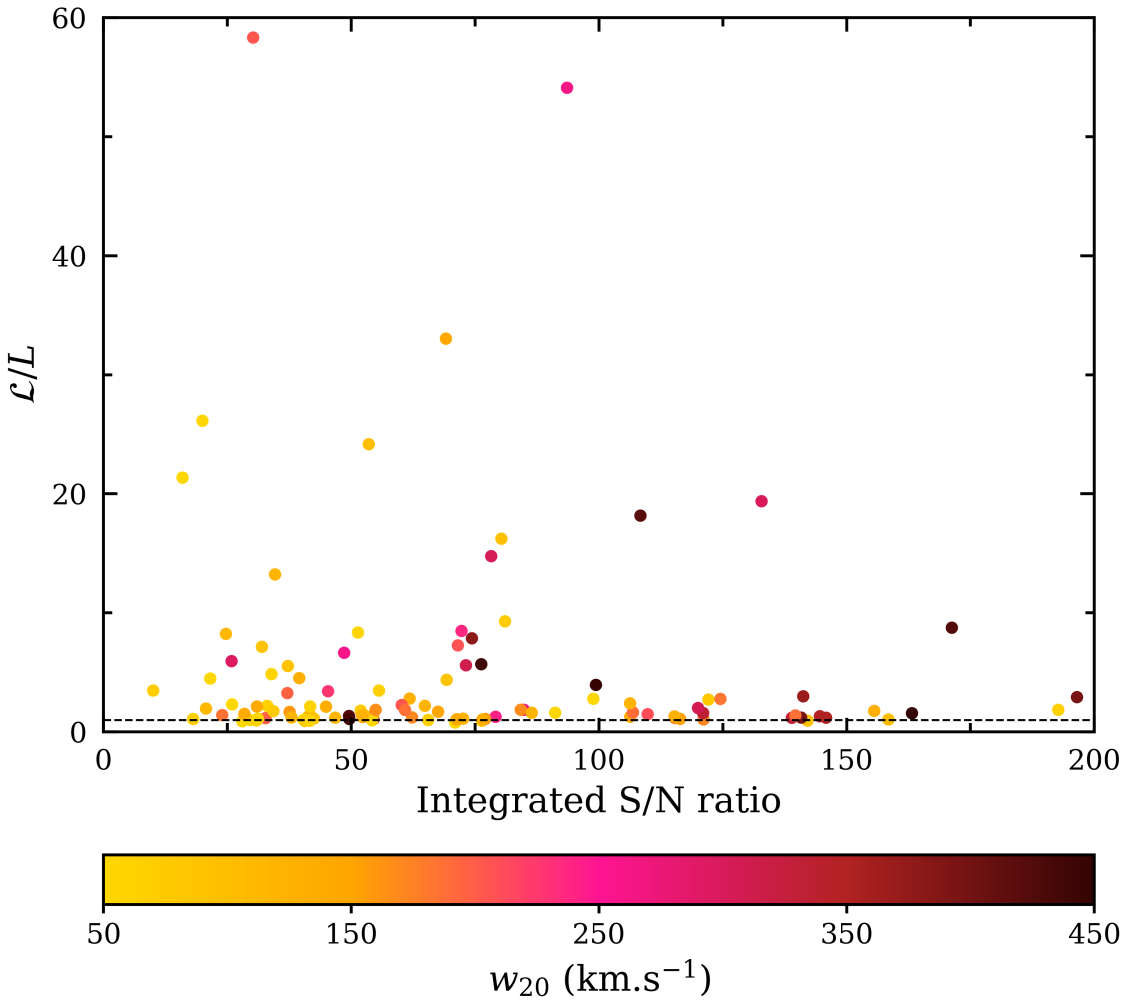

Figure C.11: Ratio of the 1D lopsidedness parameters $\mathcal{L}/L$ plotted against the integrated S/N for the WHISP profiles in this work. The data are coloured according to the profile width measured at 20% of the peak flux level. The black dashed line at $\mathcal{L}/L = 1$ indicates galaxies that return the same value for L and $\mathcal{L}$.

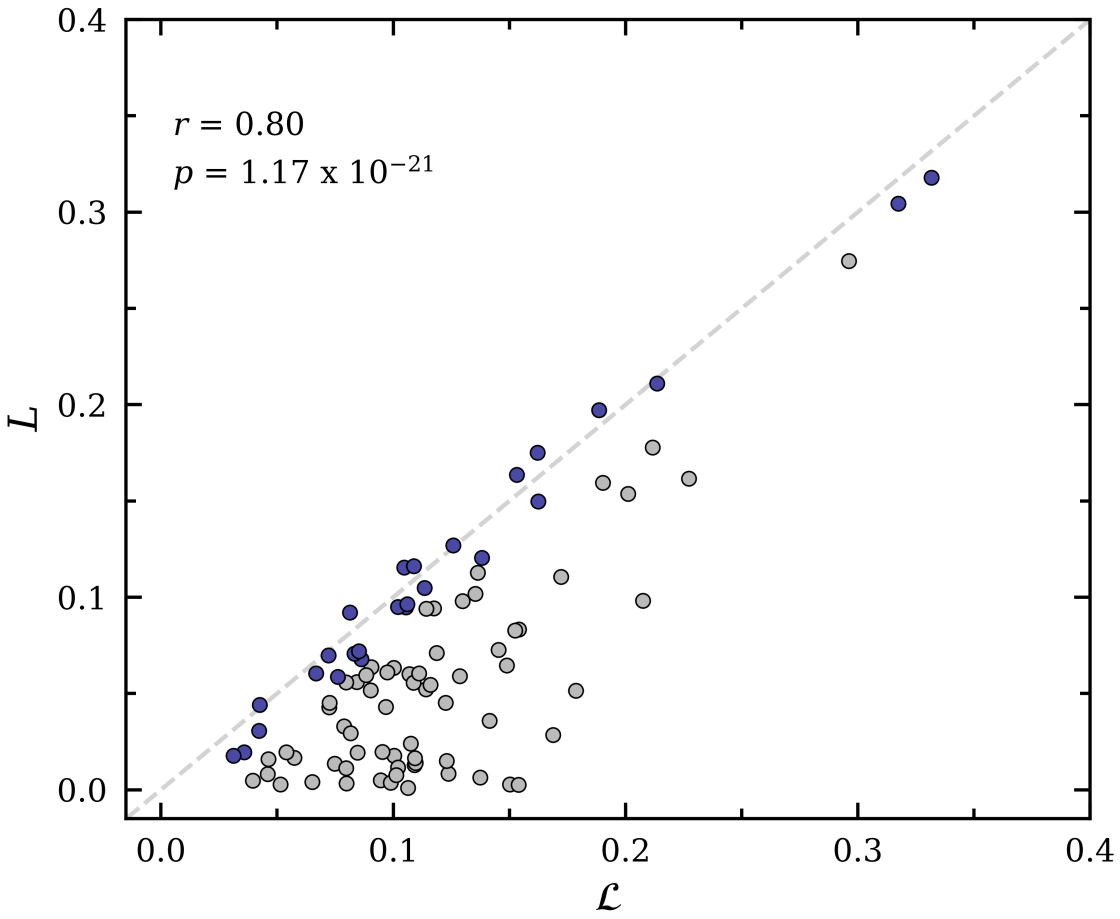

Figure C.12: Relation between the 1D lopsidedness parameters $\mathcal{L}$ and L. Blue circle markers indicate galaxies where the absolute $|\mathcal{L} - L| < 0.02$.